

CRANFIELD UNIVERSITY

OYEWOLE ADEDIPE

INTEGRITY OF OFFSHORE STRUCTURES

OFFSHORE RENEWABLE ENERGY ENGINEERING CENTRE

PhD

Supervisor: Professor Feargal Brennan
August 2015

CRANFIELD UNIVERSITY

OFFSHORE RENEWABLE ENERGY ENGINEERING CENTRE

PhD

OYEWOLE ADEDIPE

INTEGRITY OF OFFSHORE STRUCTURES

Supervisor: Professor Feargal Brennan
August 2015

This thesis is submitted in partial fulfilment of the requirements for
the degree of PhD

© Cranfield University 2015. All rights reserved. No part of this
publication may be reproduced without the written permission of the
copyright owner.

ABSTRACT

Corrosion and fatigue have been dominant degradation mechanisms in offshore structures, with the combination of the two, known as corrosion fatigue, having amplified effects in structures in the harsh marine environments. Newer types of structure are now being developed for use in highly dynamic, harsh marine environments, particularly for renewable energy applications. However, they have significantly different structural details and design requirements compared to oil and gas structures, due to the magnitude and frequency of operational and environmental loadings acting on the support structures. Therefore, the extent of corrosion assisted fatigue crack growth in these structures needs to be better understood.

In this research, fatigue crack growth in S355J2+N steel used for offshore wind monopile fabrications was investigated in air and free corrosion conditions. Tests were conducted on parent, HAZ and weld materials at cyclic load frequencies similar to what is experienced by offshore wind monopile support structures. The seawater used for testing was prepared according to ASTM D1141 specifications and was circulated past the specimens through a purpose designed and built corrosion rig at a rate of 3 l/min, at a temperature of 8-10⁰C and at a pH of 7.78-8.1. A new crack propagation method accompanied by constant amplitude loading was used. Crack growth rates in parent, HAZ and weld materials were significantly accelerated under free corrosion conditions, at all the stress ratios used compared to in air environment. However, in free corrosion conditions, crack growth rates in the parent, HAZ and weld materials were similar, particularly at a lower stress ratio. The results are explained with respect to the interaction of the loading condition, environment and the rate of material removal by corrosion in the weldments. A new model was developed to account for mean stress effects on crack growth rates in air and in seawater, and was found to correlate well with experimental data as well as with the other mean stress models tested.

Keywords: Corrosion fatigue, monopiles, crack growth, mean stress, free corrosion

ACKNOWLEDGEMENTS

Glory and honour to God Almighty for his endless blessings and protection.

First of all, I would like to thank my Supervisor, Professor Feargal Brennan for his guidance, patience, motivation and support throughout the period of this research. His encouragement and ideas are greatly appreciated.

My special appreciation goes to Dr. Athanasios Kolios for his guidance and immense contribution towards this research.

I would also like to thank my friends and colleagues: Dr. Payam Zargarzadeh, Dr. Wilson Vesga Rivera, Aliyu Aliyu and Matthew Pearce for their assistance and advice.

My appreciation goes to the staff of Cranfield University most importantly Mrs Sam Skears, Mrs Nicola Nally, Mr. Graham Lee, Mr. Antony Charnley, Mr. Derek Brown, Mr. Andrew Dyer, Mr. Kelvin White and Dr. Xianwei Liu for their support and advice during this research.

Thank you to my dear wife, Taiwo, and my beautiful daughters - Ronke, Temiloluwa and Marvelous for their patience and support throughout the period of this study. Also a special thanks to my Mum and siblings for their prayers and support throughout the period of this study.

I would like to thank Rev. Biyi Ajala, Dr. Sola Adesola and the members of Cranfield Pentecostal Assembly and Holding Forth the Word Ministry for their support and prayers towards the success of this research. God bless you all.

Finally, I would like to gratefully acknowledge the financial support provided for this research by the Petroleum Technology Development Fund (PTDF) Nigeria.

TABLE OF CONTENTS

ABSTRACT	i
ACKNOWLEDGEMENTS.....	iii
LIST OF FIGURES.....	ix
LIST OF TABLES	xvi
LIST OF EQUATIONS.....	xvii
LIST OF ABBREVIATIONS.....	xix
1 Introduction.....	1
1.1 Problem statement.....	1
1.2 Fatigue and corrosion fatigue	2
1.2.1 Corrosion mechanism	3
1.2.2 Free corrosion conditions.....	4
1.2.3 Cathodic protection	5
1.3 Fracture mechanics approach	6
1.3.1 Stress intensity factor	7
1.3.2 Elastic plastic fracture mechanics	10
1.3.3 Fatigue crack growth.....	10
1.4 Aim and Objectives	11
1.5 Scope of study	12
1.6 Thesis outline.....	12
1.7 Publications	13
2 Review of Corrosion Fatigue in Offshore Structures: Present Status and Challenges in the Offshore Wind Sector	15
2.1 Introduction	15
2.2 Offshore wind turbine structures	15
2.3 Offshore wind energy economics.....	20
2.4 Challenges in design of monopile support structures against corrosion fatigue damage	21
2.5 Seawater environmental conditions	23
2.5.1 Simulating service load conditions	24
2.6 Factors influencing fatigue crack growth in marine environments.....	25
2.6.1 Frequency effect on fatigue crack growth.....	28
2.6.2 Mean stress effects on fatigue crack growth	33
2.6.3 Effect of cathodic protection	40
2.6.4 Corrosion fatigue behaviour of high strength steels	45
2.6.5 Fatigue crack growth in weldments	47
2.7 Summary	51
3 Experimental Procedure and Data Acquisition	53
3.1 Introduction	53
3.2 Fatigue test machine.....	53
3.3 Alignment and loading fixtures.....	54

3.4	Material and specimen preparation.....	56
3.5	Test procedure.....	57
3.5.1	Pre-cracking.....	58
3.5.2	A new crack propagation methodology	60
3.6	Determination of crack length by back face strain (BFS) method	62
3.6.1	Strain gauge installation and strain measurements.....	62
3.6.2	Strain gauge coating	64
3.7	Procedures for crack length measurement using ACPD and DCPD methods.....	65
3.7.1	The alternating current potential drop (ACPD) method	65
3.7.2	The direct current potential drop (DCPD) method	66
3.8	Laboratory simulated seawater environment	67
3.9	Summary	70
4	Corrosion Fatigue Load Frequency Sensitivity Analysis.....	71
4.1	Introduction	71
4.2	Review of cyclic load frequency in offshore wind turbines	71
4.3	Methodology	76
4.3.1	Development of a new regression model for the prediction of crack lengths in corrosive environment.....	77
4.4	Fatigue crack growth results in air and discussion.....	82
4.4.1	Frequency effects on crack growth rates in air.....	88
4.4.2	Stress ratio effect on crack growth rates in air	89
4.5	Fatigue crack growth results in seawater and discussions	91
4.5.1	Stress ratio effect on fatigue crack growth in seawater	97
4.6	Comparison of test results with literature data	99
4.6.1	Discussion of medium strength steels data	101
4.6.2	Discussion of high strength steels data.....	102
4.6.3	Discussion of extra high strength steels data	104
4.6.4	Mean stress and cathodic protection.....	105
4.6.5	Results comparison with the BS7910 recommendations	109
4.7	Summary	109
5	Modelling Mean Stress Effects on Fatigue Crack Growth	113
5.1	Introduction	113
5.2	Fatigue crack propagation models.....	115
5.2.1	Paris model	115
5.2.2	Elber's model	117
5.2.3	Walker's model.....	118
5.2.4	Forman's model	118
5.2.5	Kujawski's model.....	119
5.2.6	Huang and Moan model.....	120
5.2.7	Zhan et al.'s model.....	122
5.3	Comparison of mean stress effects on fatigue crack growth in air	124

5.4 Comparison of the mean stress effects on fatigue crack growth in seawater	126
5.5 Prediction of low, medium and high cycle fatigue	128
5.6 A relative crack opening time correlation for corrosion fatigue crack growth in offshore structures.....	132
5.6.1 Model development methodology for positive R-ratios.....	134
5.6.2 Model development methodology for negative R-ratios	135
5.6.3 Experimental studies	138
5.7 Results and discussion of corrosion fatigue crack growth modelling	138
5.7.1 Model validation at positive R-ratios in seawater	140
5.7.2 Model validation at positive R-ratio in air.....	147
5.7.3 Discussion of negative R-ratio data.....	151
5.7.4 Model application to service life prediction.....	154
5.8 Model comparison with other fatigue crack propagation models	157
5.9 Summary	162
6 A Study of Fatigue Crack Growth in Offshore Wind Monopile Steel Weldments	165
6.1 Introduction	165
6.2 Material and welding procedure.....	165
6.3 Specimen preparation.....	166
6.3.1 Cutting.....	166
6.3.2 Grinding and polishing.....	167
6.4 Characterisation of the heat affected zone (HAZ).....	168
6.4.1 Etching	168
6.4.2 Specimen extraction.....	169
6.5 Experimental procedure.....	170
6.5.1 Metallurgical Examination	170
6.5.2 Fractography analysis	170
6.5.3 Scanning electron microscope (SEM) analysis	171
6.6 Fatigue crack growth of HAZ material in air and seawater.....	171
6.6.1 Results and discussion of HAZ materials crack growth data in air .	171
6.6.2 Results and discussion of HAZ materials crack growth data in seawater.....	176
6.6.3 Comparison of air and seawater data in HAZ materials	179
6.6.4 Mean stress effects on fatigue crack growth in HAZ materials.....	181
6.6.5 Comparison and discussion of crack propagation data in HAZ and parent materials	184
6.6.6 Discussion of HAZ material response with literature data	187
6.7 Fatigue crack growth of weld material in air and seawater	191
6.7.1 Results and discussion of Weld materials crack growth data in air	191
6.7.2 Results and discussion of weld materials crack growth data in seawater.....	194

6.7.3 Comparison of air and seawater data in weld materials	196
6.7.4 Discussion of weld material response with literature data	198
6.8 Comparison of parent, HAZ and weld materials	201
6.9 Implementation of model on HAZ materials	209
6.9.1 Discussion of fatigue test results with microstructural analysis	214
6.9.2 Discussion of fatigue test results with fractography analysis	217
6.10 Summary	221
7 Conclusions, Contribution and Recommendations for Future Work	223
7.1 Introduction	223
7.2 Conclusions	223
7.3 Contribution of this PhD	225
7.4 Recommendations for future work	226
REFERENCES	229
APPENDICES	241
Appendix A Crack growth results comparison	241
Appendix B Clevis and loading pins	243
Appendix C Material Certificate	245
Appendix D Welding procedure and specification	246
Appendix E Weld and HAZ specimens' orientation	248
Appendix F Hardness measurements	254
Appendix G Analysis of crack growth results with incremental polynomial and secant methods	256
Appendix H Experimental test matrix	258

LIST OF FIGURES

Figure 1-1 The three modes of loading experienced by crack [17].....	8
Figure 1-2 Stress field ahead of a crack tip [17]	9
Figure 1-3 Crack growth rates versus stress intensity factor range.....	11
Figure 2-1 Statistical breakdown of installed offshore wind capacity [31].....	16
Figure 2-2 Global growth of wind sector [33].....	17
Figure 2-3 Offshore wind support structures [40]	20
Figure 2-4 Corrosion fatigue crack growth in EH36 steel conducted under constant amplitude and spectrum loadings [63].....	25
Figure 2-5 Frequency effects on fatigue crack growth in X65 pipeline steel [74]	30
Figure 2-6 Frequency effects on corrosion fatigue crack growth [2].....	31
Figure 2-7 Crack growth rates of BS4360 50D steel in air and seawater [2]	34
Figure 2-8 R-ratio effect on crack growth rates in BS4360 50D steel [15].....	35
Figure 2-9 R-ratio effects on BS4360 50D steel at different temperatures [15]	36
Figure 2-10 Superimposed pattern of applied and residual stress [94]	38
Figure 2-11 Residual stress distribution in 316L stainless steel [96]	39
Figure 2-12 Fatigue crack growth rate for RQT501 steel [102].....	43
Figure 2-13 Fatigue crack growth rate of normalized steel [102].....	44
Figure 2-14 Crack growth rates comparison in HAZ and base materials [79] ..	49
Figure 2-15 Crack closure effects on fatigue crack growth [113].....	50
Figure 3-1 Instron 8801 100kN fatigue test machine.....	54
Figure 3-2 Loading fixtures.....	55
Figure 3-3 Load and alignment check	55
Figure 3-4 Results of load and alignment check.....	56
Figure 3-5 Compact Tension specimen design	57
Figure 3-6 Crack length monitoring by digital camera and travelling microscope	59
Figure 3-7 Wave matrix with envelopes	60
Figure 3-8 Single wave matrix	61

Figure 3-9 Loop type wave matrix	61
Figure 3-10 Left – Installed strain gauges, right – connection to P3 box	63
Figure 3-11 Crack length versus back face strain (BFS)	63
Figure 3-12 Strain gauge calibration procedure	64
Figure 3-13 Strain gauge protection	64
Figure 3-14 ACPD set-up	65
Figure 3-15 Crack length monitoring by DCPD method	66
Figure 3-16 DCPD calibration curve	67
Figure 3-17 CT specimen in laboratory simulated seawater	68
Figure 3-18 Corrosion fatigue test rig	69
Figure 3-19 Flow chart of experimental procedure	69
Figure 4-1 Design approaches for wind turbines [118]	73
Figure 4-2 Description of natural frequency against applied load [48]	74
Figure 4-3 Spectral analysis on response during power generation [119]	74
Figure 4-4 Compact tension specimen with BFS gauge	78
Figure 4-5 Calibration curve for crack length and back face strain	81
Figure 4-6 Fatigue crack growth in CT specimens ($\Delta P = 10.8 \text{ kN}$)	83
Figure 4-7 Crack growth rate in CT specimens ($\Delta P = 10.8 \text{ kN}$)	84
Figure 4-8 Fatigue crack growth for CT specimens ($\Delta P = 9 \text{ kN}$)	85
Figure 4-9 Crack growth rate for CT specimens ($\Delta P = 9 \text{ kN}$)	86
Figure 4-10 Comparison of fatigue crack growth in air at different loads	87
Figure 4-11 Crack growth rate in air at different load ranges	87
Figure 4-12 Frequency effect on fatigue crack growth in air	89
Figure 4-13 Frequency effect on crack growth rates in air	89
Figure 4-14 R-ratio effect on crack growth rates in air	90
Figure 4-15 Mean crack growth rates in air	91
Figure 4-16 Comparisons of crack measurement methods in air	92
Figure 4-17 Comparisons of DCPD and BFS responses	92
Figure 4-18 Fatigue crack growth in seawater under different loading conditions	93

Figure 4-19 Crack growth rates in seawater under different loading conditions	95
Figure 4-20 Comparison of crack growth rates in air and seawater	95
Figure 4-21 R-ratio effect on crack growth rates in seawater	97
Figure 4-22 Crack growth rates in air at R-ratio of 0.1 to 0.5.....	99
Figure 4-23 Crack growth rates in air and seawater at an R-ratio of 0.5	99
Figure 4-24 Comparison of crack growth rates in air and seawater with medium strength steels	101
Figure 4-25 Comparison of crack growth rates in air and seawater with high strength steels	103
Figure 4-26 Comparison of crack growth rates in air and seawater with extra high strength steels	104
Figure 4-27 Result comparison with Thorpe et al. data (-0.65V free corrosion potential).....	106
Figure 4-28 Result comparison with Thorpe et al. data (-0.85V cathodic protection).....	107
Figure 4-29 Result comparison with Thorpe et al. data (-1.1V cathodic protection).....	108
Figure 4-30 Result comparison with Thorpe et al. data (-1.3V cathodic protection).....	108
Figure 4-31 Comparison of crack growth rates in air and seawater with BS7910 recommendations	109
Figure 5-1 R-ratio effect on fatigue crack growth [89].....	117
Figure 5-2 Fatigue crack growth in CrMoV steel at R-ratios of $0.1 \leq R \leq 0.75$ [88]	121
Figure 5-3 Fatigue crack growth curves for 4340 steel at stress ratios $-1 \leq R \leq 0.7$ [88]	121
Figure 5-4 Fatigue crack growth curves for 300M steel $0.05 \leq R \leq 0.8$ [88]	122
Figure 5-5 Fatigue crack growth of medium carbon structural steel [89].....	123
Figure 5-6 Fatigue crack growth of CrMoV steel [89]	123
Figure 5-7 Predicted crack growth rates in air at R-ratios of 0.1 and 0.2.....	124
Figure 5-8 Predicted crack growth rates in air at R-ratios of 0.3 and 0.5.....	125
Figure 5-9 Predicted crack growth rates in air at R-ratios of 0.7 and -1	126
Figure 5-10 Predicted crack growth rates in seawater at R-ratios of 0.1 and 0.2	127

Figure 5-11 Predicted crack growth rates in seawater at R-ratios of 0.3 and 0.5	127
Figure 5-12 Predicted crack growth rates in seawater at R-ratios of 0.7 and -1	128
Figure 5-13 Prediction of low cycle fatigue (LCF).....	129
Figure 5-14 Prediction of medium cycle fatigue (MCF)	130
Figure 5-15 Prediction of high cycle fatigue (HCF).....	131
Figure 5-16 Superimposed stress patterns of positive and negative R-ratios	133
Figure 5-17 Schematic diagram of area ratio correlation.....	133
Figure 5-18 Representation of crack opening area at positive R-ratios.....	134
Figure 5-19 Area of loading cycle corresponding to R-ratio of 0.1.....	136
Figure 5-20 Damaging portion of the loading cycle corresponding to R-ratio of -1	136
Figure 5-21 Representation of crack opening area at negative R-ratios	137
Figure 5-22 Predicted crack growth rates at positive R-ratios	139
Figure 5-23 Comparison of predicted crack growth rates with experimental data in seawater	140
Figure 5-24 Observed versus predicted crack growth rates in seawater at an R- ratio of 0.1.....	141
Figure 5-25 Observed versus predicted crack growth rates in seawater at an R- ratio of 0.5.....	142
Figure 5-26 Model comparison with experimental data at an R-ratio of 0.1 and 0.2 in seawater	143
Figure 5-27 Model comparison with experimental data at R-ratio of 0.5 in seawater	144
Figure 5-28 Model comparison with Appleton data at an R-ratio of 0.5.....	145
Figure 5-29 Comparison of predicted crack growth in seawater with experimental data at R-ratio of 0.1	146
Figure 5-30 Comparison of predicted crack growth in seawater with experimental data at R-ratio of 0.5	146
Figure 5-31 Comparison of the predicted crack growth rates in air with experimental data	148
Figure 5-32 Observed versus predicted crack growth rates in seawater at an R- ratio of 0.1.....	149

Figure 5-33 Observed versus predicted crack growth rates in air at an R-ratio of 0.5	149
Figure 5-34 Comparison of predicted crack growth in air with experimental data at R-ratio of 0.1	150
Figure 5-35 Comparison of predicted crack growth in air with experimental data at R-ratio of 0.5.....	150
Figure 5-36 Crack growth rates in air	152
Figure 5-37 Fatigue crack growth in air	153
Figure 5-38 Comparison of the predicted crack growth rates in seawater with experimental data	154
Figure 5-39 Prediction of crack growth behaviour in service	156
Figure 5-40 Crack growth prediction for a 150mm thick structural member ...	156
Figure 5-41 Model comparison with other crack propagation models in air....	158
Figure 5-42 Model comparison with other crack propagation models in seawater	160
Figure 5-43 Comparison of predicted fatigue crack growth in seawater at an R-ratio of -1	161
Figure 6-1 (a) 90mm thick weld plate (b) weld plate dimensions.....	166
Figure 6-2 Cutting procedure.....	167
Figure 6-3 (a) Weld runs and HAZ (b) Weld and HAZ dimensions.....	169
Figure 6-4 Compact tension specimens extraction.....	169
Figure 6-5 Fatigue crack growth in HAZ materials in air at an R-ratio of 0.1 ..	172
Figure 6-6 Crack growth rates in HAZ materials in air at an R-ratio of 0.1	173
Figure 6-7 Closure effect due to residual stresses in HAZ	174
Figure 6-8 Fatigue crack growth in HAZ materials in seawater at an R-ratio of 0.1	177
Figure 6-9 Crack growth rates in HAZ materials in seawater at an R-ratio of 0.1	178
Figure 6-10 Fatigue crack growth in HAZ materials in air and seawater	179
Figure 6-11 Crack growth rates in HAZ materials in air and seawater	180
Figure 6-12 Crack growth rates in HAZ material in air at R-ratios of 0.1 to 0.7	182

Figure 6-13 Crack growth rates in HAZ materials in seawater at R-ratios of 0.1 and 0.7.....	183
Figure 6-14 Air and seawater data in HAZ materials at R-ratios of 0.5 and 0.7	184
Figure 6-15 Crack growth data comparison in HAZ and parent materials in air	185
Figure 6-16 Crack growth data comparison in HAZ and parent materials in seawater	186
Figure 6-17 Comparison of crack growth rates in HAZ materials in air with literature data.....	188
Figure 6-18 Comparison of crack growth rates in HAZ materials in seawater with literature data	189
Figure 6-19 Fatigue crack growth in weld materials in air at an R-ratio of 0.1	192
Figure 6-20 Crack growth rates in weld materials in air at an R-ratio of 0.1 ...	193
Figure 6-21 Fatigue crack growth in weld materials in seawater at an R-ratio of 0.1	194
Figure 6-22 Crack growth rates in weld materials in seawater at an R-ratio of 0.1	195
Figure 6-23 Fatigue crack growth in weld materials in air and seawater	197
Figure 6-24 Crack growth rates in weld materials in air and seawater	198
Figure 6-25 Comparison of crack growth rates in weld materials in air with literature data.....	199
Figure 6-26 Comparison of crack growth rates in weld materials in seawater with literature data	201
Figure 6-27 Crack growth rates in parent, HAZ and weld materials in air at an R-ratio of 0.1.....	202
Figure 6-28 Crack growth rates in parent and HAZ materials in air at an R-ratio of 0.5 and 0.7.....	203
Figure 6-29 Crack growth rates in parent, HAZ and weld materials in seawater at an R-ratio of 0.1	204
Figure 6-30 Crack growth rates in parent and HAZ materials in seawater at an R-ratio of 0.5 and 0.7	205
Figure 6-31 Comparison of Parent, HAZ and weld data with BS 7910 in air and seawater at an R-ratio of 0.1	207
Figure 6-32 Comparison of Parent and HAZ data with BS 7910 in air and seawater at an R-ratio of 0.5 and 0.7	209

Figure 6-33 Model application to HAZ materials in air at positive R-ratios	210
Figure 6-34 Model application to HAZ materials in seawater at positive R-ratios	212
Figure 6-35 Model application to HAZ material in air at negative R-ratio	213
Figure 6-36 Model application to HAZ materials in seawater at negative R-ratio	214
Figure 6-37 Microstructural variation from weld to parent materials (X5)	215
Figure 6-38 Crack growth in the Intercritical HAZ region (X5)	215
Figure 6-39 Crack growth in HAZ materials in air (X5)	216
Figure 6-40 Crack growth pattern in left: HAZ and right: weld materials (X20)	217
Figure 6-41 Mixture of ductile and brittle striations in parent materials in air at $\Delta K=20\text{MPa}\sqrt{m}$	217
Figure 6-42 Transition region in HAZ material in air at ΔK between $18\text{MPa}\sqrt{m}$ and $19\text{MPa}\sqrt{m}$	218
Figure 6-43 Mixture of ductile and brittle striation in weld materials in air at $\Delta K=20\text{MPa}\sqrt{m}$	219
Figure 6-44 Ductile striations on parent materials in seawater $\Delta K=19\text{MPa}\sqrt{m}$.	219
Figure 6-45 Mixture of brittle and ductile striation in HAZ materials in seawater $\Delta K=20\text{MPa}\sqrt{m}$	220
Figure 6-46 Brittle striations in weld materials in seawater $\Delta K=20\text{MPa}\sqrt{m}$	221

LIST OF TABLES

Table 2-1 United Kingdom commissioned offshore wind farms [31].....	16
Table 4-1 Back face strain parameter versus a/W	80
Table 4-2 Loading Scenarios and material constants for S355J2+N steel in air	88
Table 5-1 Comparison of experimental and predicted lives in air and seawater	151
Table 6-1 Material constants for HAZ materials in air.....	176
Table 6-2 Material constants for HAZ materials in seawater.....	178
Table 6-3 Materials constants in weld materials in air	193
Table 6-4 Material constants in weld materials in seawater	195
Table 6-5 Material constants for parent plate, HAZ and weld materials	206
Table 6-6 Model and experimental data material constants	211

LIST OF EQUATIONS

(1-1).....	4
(1-2).....	5
(1-3).....	5
(1-4).....	6
(1-5).....	6
(1-6).....	6
(1-7).....	6
(1-8).....	7
(1-9).....	7
(1-10).....	7
(1-11).....	7
(1-12).....	8
(1-13).....	8
(1-14).....	9
(1-15).....	9
(1-16).....	11
(1-17).....	11
(3-1).....	58
(3-2).....	58
(4-1).....	79
(4-2).....	79
(4-3).....	82
(5-1).....	116
(5-2).....	117
(5-3).....	117
(5-4).....	118
(5-5).....	119
(5-6).....	119

(5-7).....	119
(5-8).....	120
(5-9).....	120
(5-10).....	122
(5-11).....	123
(5-12).....	135
(5-13).....	135
(5-14).....	135
(5-15).....	135
(5-16).....	137
(5-17).....	137
(5-18).....	137
(5-19).....	155

LIST OF ABBREVIATIONS

ACPD	Alternating Current Potential Drop
BFS	Back Face Strain
CAPEX	Capital Expenditure
CCT	Centre Crack Tension
CMOD	Crack Mouth Opening Displacement
CP	Cathodic Protection
CT	Compact Tension
DCPD	Direct Current Potential Drop
EPFM	Elastic Plastic Fracture Mechanics
ERF	Environmental Reduction Factor
GWEC	Global Wind Energy Council
HAZ	Heat Affected Zone
HCF	High Cycle Fatigue
HSS	High Strength Steels
LCF	Low Cycle Fatigue
LEFM	Linear Elastic Fracture Mechanics
MCF	Medium Cycle Fatigue
MT	Middle Tension
PWHT	Post Weld Heat Treatment
SEM	Scanning Electron Microscope
SLIC	Structural Lifecycle Industry Collaboration
S-N	Stress Life

1 Introduction

In this chapter, background relating to fatigue and corrosion assisted fatigue damage in offshore structures is presented. The need for an understanding of the behaviour of offshore support structures with respect to the gap between the oil and gas structures and wind support structures are highlighted. The fracture mechanics approach to fatigue assessment is presented. The aim, objectives and scope of this study are also highlighted.

1.1 Problem statement

A significant number of offshore structures have been developed and installed for use in harsh marine environments over the years. The environmental influence on the damage mechanisms in these structures depends on the type of materials used for fabrication, site and loading conditions. The existing fatigue design guidance was developed based on studies conducted on oil and gas structures over 30 years ago. However, a significant number of the first offshore wind turbines monopile structures are operating based on these standards, which are well outside the scope of larger diameter monopiles [1] as well as their design requirements, due to the volume of manufacturing, and the magnitude and frequency of operational and environmental loadings acting on the support structures. Therefore, some of the important research areas that need to be addressed for a better understanding of behaviour of offshore monopile support structures include the following:

- The extent of corrosion assisted fatigue damage in monopile structures with respect to the operational loads envelope such as the effects of loading frequency,
- Environmental condition such as the free corrosion conditions, which have been a major threat to wind monopile supports, most importantly the internal section,
- The behaviour of the steels used for monopile fabrications with respect to currently used modern materials and manufacturing techniques,

- The behaviour of steel weldments with thicknesses similar to those used for offshore monopile support structures,
- The extent to which mean stress can enhance crack growth behaviour in monopile steels.

1.2 Fatigue and corrosion fatigue

Fatigue failure in offshore structures, such as oil and gas structures and structures for renewable energy applications can occur due to the magnitude of cyclic loadings which they experience in service. Fatigue cracks can develop from pre-existing defects which may be introduced into structures during manufacturing, transportation and installation etc. Fatigue cracks, if not controlled can grow into failure or collapse of the structures when an unstable stage of the crack growth is reached. Therefore, defects or cracks in offshore structures need to be discovered and sized by reliable inspection and monitoring techniques to ensure the economical and safe operation of the structures in service. Offshore structures are vulnerable to corrosion attacks due to the harsh marine environment and this may lead to significant levels of damage to the structures and hence a reduction in service life. The corrosion crack growth mechanisms can be amplified under fatigue loading due to the synergistic interaction of the applied cyclic loads and the influence of the corrosive environment. The extent of the damage is influenced by a significant number of variables, some of which are discussed in Chapter 2.

Crack growth behaviour of steels used for offshore oil and gas applications has been studied over the years, for example in [2] and [3], in order to understand the behaviour of the structures in marine environments. However, newer types of structure, such as wind turbine structures, are being developed and installed offshore. Monopile structures have been the most commonly used support structures. At the moment, there is deficit of information on corrosion fatigue crack growth behaviour in these large diameter structures and therefore this remains an area of study that needs to be addressed and better understood. The understanding of corrosion fatigue can only be achieved by testing [4], so that confidence can be gained regarding the behaviour of the steel structures

offshore. In this research, one of the primary objectives is to carry out experimental investigations on monopile steel materials in appropriate environments similar to what might be experienced by the real monopile support structures in service.

The two most commonly used fatigue assessment techniques are the stress life (S-N) approach and the fracture mechanics approach. The S-N approach has been widely used for fatigue assessments of components and structures; a review of the currently used S-N curves is provided in [4]. However, in this thesis, the fracture mechanics approach is employed to study fatigue crack growth in monopile steel materials both in air and free corrosion conditions. This approach is discussed in a later section.

1.2.1 Corrosion mechanism

In marine environments, corrosion occurs due to the release of electrons from the materials into the corrosive environment by oxidation. Corrosion has also been explained as a process of material damage which occurs when materials are exposed to harsh environments [5]. The degree of the interaction of materials with the seawater environment depends on the types of materials and the design [6]. However, the major interest of this research is not the chemistry of corrosion but the interaction of the corrosive environment on fatigue crack growth in offshore steels. In this thesis, results are presented of crack growth rates in monopile steel materials in a free corrosion condition.

As mentioned in Chapter 2, free corrosion conditions in offshore structures are never designed for, but may occur due to loss of corrosion protection or, on occasions, of corrosion threats particularly similar to what occur in the inner compartments of monopile support structures. A significant number of the first installed offshore monopile structures are not protected internally and were initially designed to be airtight in order to avoid corrosion. These compartments are flooded with water and it is possible for corrosion conditions accompanied by oxygen replenishment to occur, in the event that the airtight seals are damaged [7]. This would lead to a free corrosion condition which makes the

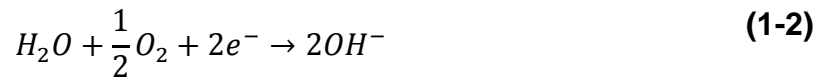
understanding of the real effect of corrosion important, so that useful knowledge regarding inspection and repair of the structures can be achieved.

Alternatives for corrosion protection in the inner section of future offshore wind installations are currently being researched on. For example, in the European Wind Energy Association (EWEA) offshore conference 2015, Tavares et al. [8] mentioned the need for an update to the existing design guidance with design requirements that accommodate the use of galvanic anodes for the inner sections of monopile structures. Pawsey [9] also cited an example of corrosion effects found in the monopile structures of 54 turbines installed at the Lynn and Inner Dowsing wind farms. Internal protection of the structures was suggested and it was concluded that the offshore wind industry needs to develop its standards instead of depending solely on those developed for oil and gas structures. Due to rapid development in the wind sector, internal protection for future wind turbine support structures is likely to be considered to be used from the design stage but this should be considered with respect to the cost of energy. Corrosion assisted fatigue damage has been studied under different environments [2] namely; air, free corrosion potential and under cathodic protections. These are discussed in the following section.

1.2.2 Free corrosion conditions

Steels used for offshore structures are exposed to harsh marine environments and are prone to corrosion fatigue failure. This failure mechanism has been characterised into three stages; pit formation, crack initiation from pit and crack propagation [10]. However, the damage mechanisms depend on the environment, exposure time and the magnitude of the applied cyclic stress. The reactions that occur within the crack during corrosion in relation to structural and high strength steels (HSS) in a seawater environment can be found in [11]. An example of corrosion reactions is described in Equations 1-1 to 1-3 [5], [12]:





The process of anodic dissolution which occurs under free corrosion conditions in seawater, when steels release electrons by oxidation (Equation 1-1), has also been described in [13] and [14]. In these studies, crack growth rates under a free corrosion condition have generally being described by material removal at the crack tip through the process of anodic dissolution. This implies that in a free corrosion condition, the corrosion mechanism is related to the test specimen dissolving into the environment by giving away electrons. However, cathodic protections have been applied to steels in marine environments to protect them from corrosion. The effect of cathodic protection is not within the scope of this research as all the tests reported in the later chapters are conducted under a free corrosion condition, but a brief description of the mechanism associated with cathodic protection is given in the following section. Some of the results obtained from previous tests conducted under both free corrosion potential and cathodic protection are compared with the results obtained from the present study in Chapters 4, 5 and 6.

1.2.3 Cathodic protection

Cathodic protection (CP) has been widely used for the protection against corrosion in offshore structures. In CP methods, the steel to be protected is made the cathode in order to prevent it from oxidation. Two CP methods have been described in the literature; the sacrificial anode and the impressed current types. These methods are described in [14]. Different levels of CP have also been used [2], [3], [5], [13] with their associated limitations. However, the major disadvantage that has been attributed to the effects of CP on fatigue crack growth in steels is hydrogen embrittlement. The degree of the hydrogen embrittlement may depend on the material, CP levels and CP design. The CP mechanism has been described by two notable reactions which are oxygen

reduction and reduction of water [13]–[16]. These reactions can be described as follows [13]:



However, reduction of water (Equation 1-5) was mentioned as the most significant during cathodic reactions due to the accompanied production of hydrogen [14]. Further explanations on the mechanism associated with the CP process can be found in [13] and [14].

1.3 Fracture mechanics approach

The advantage of the fracture mechanics approach over the S-N approach is its ability to assess the integrity of cracked bodies. In other words, the approach is used to study the propagation of cracks in components and structures. The energy criterion and the stress intensity approaches have been identified as the two methods used to analyse fracture in materials [17]. The energy based criterion was proposed by Griffith [18]. The theory states that crack advancement would occur in a material when the energy available for crack growth is enough to overcome the material's resistance [17]. The Griffith criterion with respect to the rate of energy released in an infinite plate with crack length $2a$ subjected to tensile stress σ is described as

$$\frac{dU}{da} = \frac{dW}{da} \quad (1-6)$$

Where U is the energy released, W is the energy required for crack advancement. However, with respect to the stress field for an elliptical flaw [19], Griffith determined $\frac{dU}{da}$ as

$$\frac{dU}{da} = \frac{2\pi\sigma^2 a}{E^*} \quad (1-7)$$

Where $E^* = E$ for plane stress, $E^* = \frac{E}{(1-\nu^2)}$ for plane strain, E is the Young's modulus and ν is the Poisson's ratio. The left of Equation 1-7 (the energy release rate) is replaced by G which is the strain energy in the material that is sufficient to cause crack advancement, and is expressed as

$$G = \frac{\pi\sigma^2 a}{E^*} \quad (1-8)$$

Where a is the half crack length. At fracture, with respect to the required critical stress σ_c , the term G in Equation 1-8 becomes G_{Ic} and is determined as

$$G_{Ic} = \frac{\pi\sigma_c^2 a}{E^*} \quad (1-9)$$

Where G_{Ic} is the critical energy release rate and the critical stress at fracture can be determined from Equation 1-9 as

$$\sigma_c = \sqrt{\frac{E^* G_{Ic}}{\pi a}} \quad (1-10)$$

A relationship between the strain energy release rate G and K based on the energy criterion has also been expressed as [13], [20], [21]

$$G = \frac{K^2}{E^*} \quad (1-11)$$

1.3.1 Stress intensity factor

The stress intensity factor characterises the stress field near the advancing crack tip in a material. Knowledge of the stress intensity factor with respect to the stress field around a crack tip was first introduced by Irwin [22]. This led to the concept of Linear Elastic Fracture Mechanics (LEFM) which describes the rate of crack growth with respect to the stress intensity factor. In fracture mechanics, the displacement of the crack surface or crack growth can occur in three modes [17]. These are represented in Figure 1-1

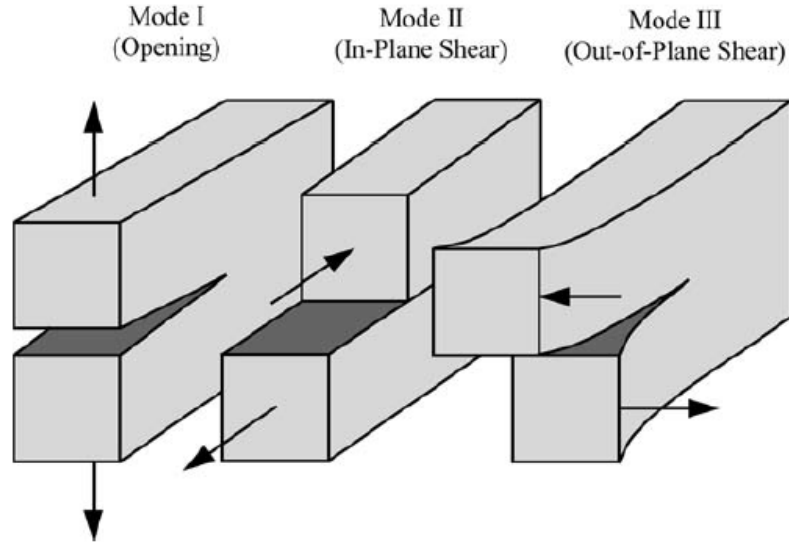


Figure 1-1 The three modes of loading experienced by crack [17]

In mode I which is referred to as the opening mode, the applied load is perpendicular to the crack plane. The opening mode has been identified in the literature as the most common loading mode. Mode II is the sliding mode or the in-plane shear loading, while Mode III is the out-of-plane shear mode. The opening mode is considered in the present work. The stress close to the crack tip varies with $\frac{1}{\sqrt{r}}$ irrespective of the configuration of the cracked material [17]. Where r is a distance from the crack tip.

$$\sigma_{yy} \propto \frac{1}{\sqrt{r}} \quad (1-12)$$

If the constant of proportionality K which is the stress intensity factor is introduced into Equation 1-12, for a mode I loading, the stress distribution in the polar coordinates of an element near the crack tip, as shown in Figure 1-2, is given as

$$\sigma_{ij} = \frac{K_I}{\sqrt{2\pi r}} f_{ij}(\theta) \quad (1-13)$$

Where K_I is the Mode I stress intensity factor, σ_{ij} are the corresponding stresses of the element ahead of the crack tip at a distance r and angle θ from the crack tip, as shown in Figure 1-2. $f_{ij}(\theta)$ is a geometry function which depends on the

geometry of the cracked body and loading mode. The solutions to the crack tip stresses can be found in fracture mechanics textbooks [17], [23].

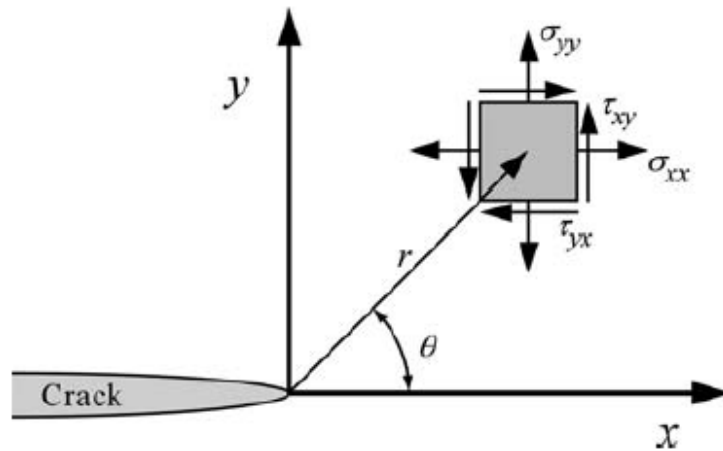


Figure 1-2 Stress field ahead of a crack tip [17]

If there is a mode I singular stress field on the plane of the crack, for $\theta = 0$ (i.e shear stress is equal to zero), the stresses in the x and y directions in Figure 1-2 are the same [17] and Equation 1-12 can be written as

$$\sigma_{yy} = \frac{K_I}{\sqrt{2\pi r}} \quad (1-14)$$

Equation 1-12 is only valid near the crack tip for small values of r . Therefore, to determine K , a modified form is required to accommodate other configurations, type of crack geometry and loading mode [14]. One of the configurations is the mode I stress intensity factor for a centre crack with length $2a$ in an infinite plate subjected to remote tensile stress σ . The stress intensity factor relationship can be expressed as

$$K_I = Y\sigma\sqrt{\pi a} \quad (1-15)$$

Where Y is a modification or geometry correction factor and a is the crack depth. Different methods of determining stress intensity factors are described in [24]. Different stress intensity factor solutions with respect to geometry and loading conditions can be found in a book on stress intensity factors by Murakami [25].

1.3.2 Elastic plastic fracture mechanics

The scope of this thesis is limited to the LEFM with analysis carried out with respect to the stress intensity factor. The results reported here are based on investigations carried out on medium strength steel. However, the elastic plastic fracture mechanics (EPFM) is briefly introduced. The LEFM is valid for the behaviour of cracked bodies with a small plastic region around the crack tip. For a time-dependent non-linear behaviour or plastic deformation, the EPFM is used [17]. The crack tip condition in elastic plastic material is described by two approaches; the crack tip opening displacement (CTOD) and the J contour integral. The CTOD was proposed by Wells [26] with the idea of determining fracture toughness through the measurement of crack tip opening [17], while the J integral was developed by Rice [27]. Both techniques are used as fracture criteria. Details of the two approaches can be found in [17].

1.3.3 Fatigue crack growth

The three regions of fatigue crack growth are represented in Figure 1-3. Region I is referred to as the threshold region below which there is no fatigue crack growth. Region II is the stable crack growth region while region III is the region of unstable fracture which is associated with accelerated crack growth. Discussions in this research are limited to region II of fatigue crack growth. The most commonly used LEFM approach for representing fatigue crack growth in region II was developed by Paris and Erdogan [28].

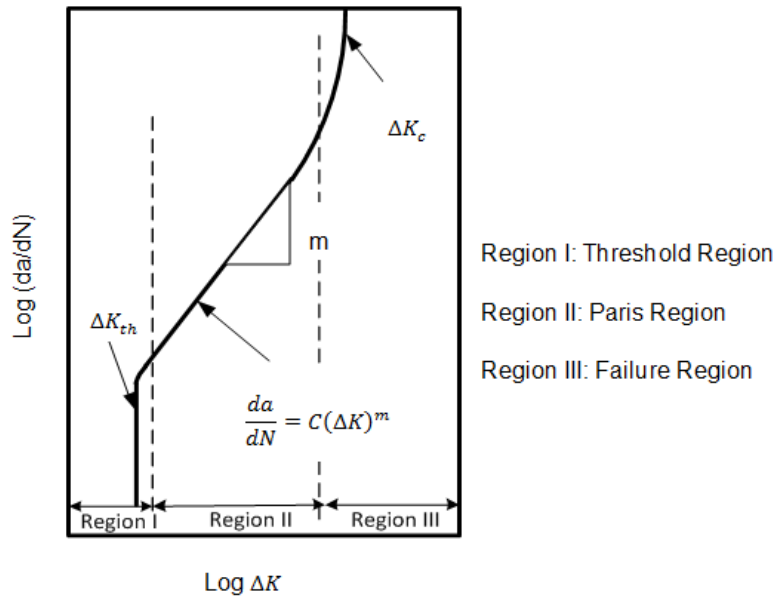


Figure 1-3 Crack growth rates versus stress intensity factor range

The Paris equation is expressed as:

$$\frac{da}{dN} = C(\Delta K)^m \quad (1-16)$$

Where $\frac{da}{dN}$ is the crack growth rate, ΔK is the stress intensity factor range while C and m are material constants which depend on the loading condition and environment. Equation 1-16 can be used to calculate the number of fatigue cycles N required to propagate the crack from an initial depth/length a_i to a final depth a_f . This can be achieved by integrating Equation 1-16 as

$$N = \int_{a_i}^{a_f} \frac{da}{C(\Delta K)^m} \quad (1-17)$$

Some models have been proposed to account for mean stress effects on fatigue crack growth as modifications to the Paris law. These are discussed in Chapter 5.

1.4 Aim and Objectives

The aim of this research is to understand the mechanism of fatigue failure of structures in marine environments using the LEFM approach, under test conditions similar to what is experienced by the structures in service.

The primary objectives of this research are outlined as follows:

1. To carry out corrosion fatigue load frequency sensitivity analysis in order to understand the effect of applied cyclic loading frequency within the range pertinent to offshore wind monopile support structures
2. To study the crack growth behaviour in parent, HAZ and weld materials in air and in laboratory simulated seawater environments, using representative materials that are used for monopile fabrications
3. To develop a model which accounts for mean stress effects on crack growth rates in offshore structures, particularly in structures for renewable energy applications.

1.5 Scope of study

This research is focused on the understanding of fatigue crack growth in monopile steel materials in air and in free corrosion conditions with respect to the loading conditions that might be experienced by the structures in service. The tests conducted in this research were carried out under constant amplitude loadings on only monopile steel materials designated S355J2+N. All the tests are limited to the stage II of fatigue crack growth (LEFM).

1.6 Thesis outline

The chapters of this thesis are outlined as follows:

In Chapter 1, the background on fatigue and corrosion fatigue crack growth mechanisms is presented coupled with discussions of corrosion challenges in offshore wind support structures. The fracture mechanics approach was introduced. The aim and objectives and scope of this research are also highlighted.

Chapter 2 presents a review of corrosion fatigue in offshore structures and highlights the difference between oil and gas structures and wind turbines support structures. State of the art in the offshore wind industry is discussed with respect to the challenges in the design of wind structures using the existing design codes and standards, as well as the need for an update to the existing

corrosion fatigue database. Some of the factors influencing crack growth behaviour in offshore structures are also discussed with reference to relevant literature.

In Chapter 3, details of the methodology used for testing are presented coupled with the new crack propagation method used in a seawater environment. The development of a Back Face Strain (BFS) regression model is also described.

Chapter 4 presents the results and discussions of the corrosion fatigue load frequency sensitivity analysis conducted. Results are also compared with literature data.

Chapter 5 presents a study of mean stress effects on crack growth rates. Relevant mean stress models are tested using experimental data. A new model that accounts for mean stress effects on crack growth rates in air and in seawater is also introduced.

In Chapter 6, crack growth behaviours in HAZ and weld materials in air and seawater are studied. The test specimen's extraction methodology is also presented. Mean stress effects on crack growth rates in HAZ materials are discussed and the results are compared with other literature data.

In Chapter 7, conclusions of this research are drawn with respect to the present findings. Recommendations for further work are also proposed.

1.7 Publications

1. Oyewole Adedipe, Feargal Brennan and Athanasios Kolios (2015), "*Corrosion Fatigue Load Frequency Sensitivity Analysis*", Marine Structures, Vol. 42. pp 115-136.
2. Oyewole Adedipe, Feargal Brennan and Athanasios Kolios "*A relative crack opening time correlation for corrosion fatigue crack growth in offshore structures*". Submitted to Fatigue and Fracture of Engineering Materials and Structures, FFEMS (**Accepted**).
3. Oyewole Adedipe, Feargal Brennan and Athanasios Kolios (2015), "*Corrosion Fatigue Crack Growth in Offshore Wind Monopile Steel HAZ*

Material’, Analysis and Design of Marine Structures V, CRC Press, Proceedings of the 5th International Conference of Marine Structures (Southampton, UK), Pp: 207-212.

4. Oyewole Adedipe and Feargal Brennan (2014), “*A Study of Fatigue Crack growth in Offshore Wind Monopile Parent Steel in Air and Seawater*”, Proceedings of the 1st International Conference on Renewable Energies Offshore (RENEW 2014) (Lisbon, Portugal).

2 Review of Corrosion Fatigue in Offshore Structures: Present Status and Challenges in the Offshore Wind Sector

2.1 Introduction

This chapter presents a review of corrosion fatigue in offshore structures with particular emphasis on the most significant factors influencing corrosion assisted fatigue damage. The discussion is primarily centred on the need for the development of new design guidance for offshore wind turbine support structures. The fracture mechanics approach to fatigue assessment crack growth was introduced in the previous chapter. Existing literature which documents results from previous campaigns is presented, including works referring to Oil and Gas structures, highlighting the significant difference in the aspects of loading and use of modern fabrication processes, with a view to illustrating the requirements for an update to the existing corrosion fatigue database that will suit offshore wind structures' design requirements. The update to the existing corrosion fatigue database will assist design engineers on how to optimise offshore structures in terms of cost and fatigue strength [29]. Some of the recent developments in the wind sector with respect to wind turbine structures are introduced in the first part of this chapter while the latter part provides a literature review on the corrosion crack growth in offshore structures.

2.2 Offshore wind turbine structures

Offshore wind is an emerging, clean and environmentally friendly renewable energy source that has developed rapidly to meet the European Union 2020 renewable energy targets [30]. This situation has significantly increased the volume of the planned wind structures that will be installed offshore. At the end of 2013, the wind producing capacity in the UK was over 50% compared to the rest of the World [31] as shown in Figure 2-1. Table 2-1 also shows the list of commissioned offshore wind farms in the UK from 2000 to 2013.

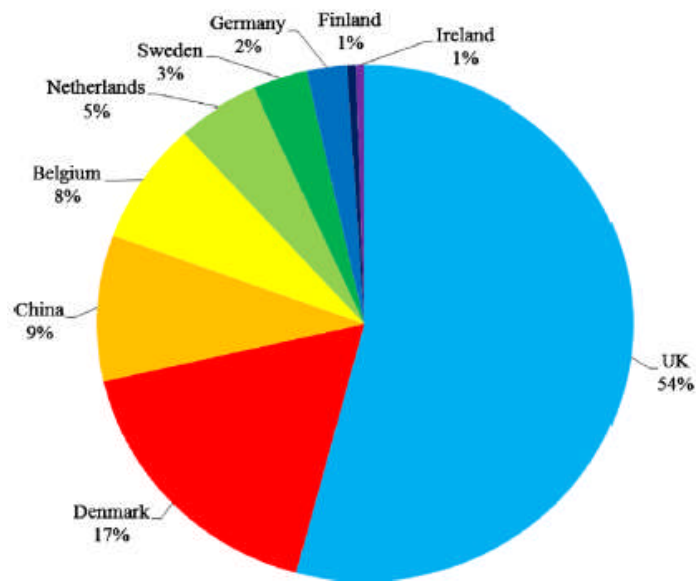


Figure 2-1 Statistical breakdown of installed offshore wind capacity [31]

Table 2-1 United Kingdom commissioned offshore wind farms [31]

Year of installation	Project	Capacity (MW)	Total capacity (MW)	Max water depth (m)	Max distance to shore (km)	Wind turbine manufacturer	Crown estate round
2000	Blyth	3.8	4	6	1	Vestas	1
2003	North Hoyle	60	64	12	7.5	Vestas	1
2004	Scroby sands	60	124	10	3	Vestas	1
2005	Kentish flats	90	214	5	8.5	Vestas	1
2006	Barrow	90	304	15	7	Vestas	1
2007	Beatrice	10	314	40	25	REpower	1
2007	Burbo Bank	90	404	10	5.2	Siemens	1
2008	Inner Dowsing	97.2	501	10	5.2	Siemens	1
2008	Lynn	97	598	10	5.2	Siemens	1
2009	Rhyl Flats	90	688	8	8	Siemens	1
2009	Robin Rigg	180	868	5	9.5	Vestas	1
2010	Gunfleet Sands	173	1041	8	7	Siemens	1
2010	Walney Phase 1	183.6	1225	23	14	Siemens	2
2011	Walney Phase 2	183.6	1408	30	14	Siemens	2
2012	Greater Gabbard	504	1912	32	36	Siemens	2
2012	Ormonde	150	2062	21	9.5	REpower	1
2012	Thanet	300	2362	23	12	Vestas	2
2012	London Array 1	630	2992	25	20	Siemens	2
2012	Sheringham Shoal	316.8	3309	23	23	Siemens	2
2013	Lincs	270	3579	15	8	Siemens	2
2013	Teeside	62.1	3641	18	2.2	Siemens	2
	Total	3641					

From projections, approximately 40,000 jobs will be provided by the offshore wind industry by 2020 if research funding, testing and demonstration facilities are fully executed by the Government [32]. From the Global Wind Energy Council (GWEC) report and statistics [33], as shown in Figure 2-2, offshore wind energy has increased by 4GW from 2011 to over 5GW at the end of 2012 globally, with the UK having the highest installed capacity of around 2GW and 3GW in 2011 and 2012 respectively.

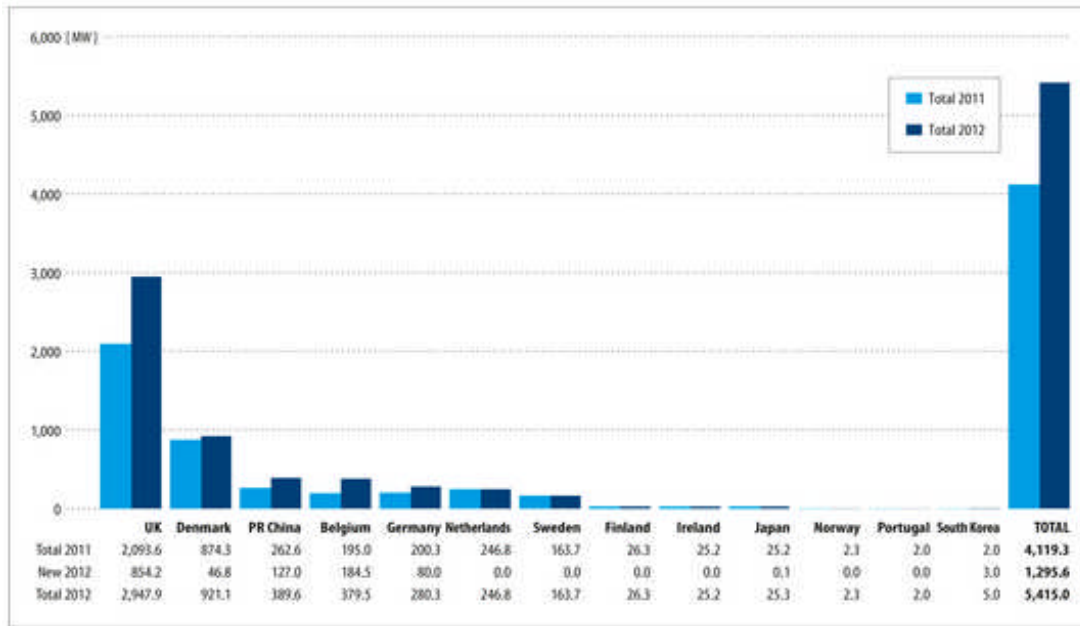


Figure 2-2 Global growth of wind sector [33]

Offshore wind turbine support structures are mainly fabricated of welded tubular members, similar to Oil & Gas structures, and are exposed to highly dynamic, harsh marine environments. However, they have significantly different structural details and design requirements due to the magnitude and frequency of operational and environmental loadings acting on the support structures. These conditions would significantly affect their structural dynamic response characteristics due to the magnitude of the applied load. This may therefore have some significant effects on the crack growth behaviour and the extent to which corrosion can be associated with damage to the support structures. However, the magnitude of the applied load might depend on a number of design factors, such as turbine size, water depth, soil conditions and type of support structures [30], [34]. It is therefore essential to design wind turbine support structures against prescribed limit states to ensure economical and safe operation.

The majority of the offshore wind farms in the UK are currently installed in shallow water depths of approximately 30m [31] with the wind turbines supported on monopile structures. Monopiles are the most commonly used wind turbine support structure due to their design simplicity and suitability for water

depths of up to 30m [35]. One of the major design requirements of these types of structures is their ability to withstand load cycles of approximately 10^9 which is equivalent to a 20 year service life [36]. However, a cost-effective design life can only be achieved if careful considerations are given to the volume of installations and the degree of operational loads envelope, which the structures are subjected to in service compared to structures used for oil and gas applications. One of the most critical factors in the installation of wind structures is the suitability of the support structures for specific sites and this may depend primarily on water depths. This implies that at increased water depth, the costs involved in the installation of the structures are likely to significantly increase. However, an advantage of the offshore wind structure over oil and gas structures, regardless of the initial capital cost, is the fact that the operating costs are lower when the structures are in operation [37].

Monopiles have a typical wall thickness of 150mm, are 6m in diameter and a weight of up to 650tonnes [35]. The wind turbine tower is supported on the monopile directly or through a transition piece. However, the major limitation of monopile supports is their flexibility in deeper waters. This is because monopiles experience some levels of deflection and vibration which are influenced by axial loads, lateral loads and bending moments. Therefore, the diameter and thickness of the monopile structures may have to be increased if they are intended for use in deeper water depths and this will significantly increase the production and installation costs.

Research is ongoing on the use of other types of support structures such as jackets structures for larger wind turbines in deeper water depths with the possibility of harnessing more wind energy at increased water depths. Jacket structures are suitable for wind turbine installation in water depths of up to 50m and they have about 50% reduction in the quantity of steel used for their manufacture compared with the monopile structure [36]. Another major challenge associated with the design of offshore wind turbine support structures is the effort involved to accurately predict the environmental and operational loads and the resulting structural dynamic responses of the wind turbine and

support structures under the synergistic effects of wave and wind loading [38]. Oil and gas structures are primarily attributed to wave loads, unlike the wind turbine structures which are under wave and wind loads. This may therefore result in complex random loading situations due to the number of parameters that may be involved [39].

Therefore, some of the currently available design concepts developed for oil and gas structures may not suit wind turbine support design requirements due to the significant differences in the design requirements. It was also mentioned that the current design guidance could be acceptable for single structures but may become costly for use in structures with significant production volumes [4] such as the wind structures. However, some of the design concepts used for oil and gas structures might still be transferred to the proposed jacket support structures for wind turbine structures in deeper water depths, but design engineers must carefully consider the effects of loading and corrosion for such structures to be optimally designed.

An approach to understanding the behaviour of wind turbine monopile support structures with respect to fatigue damage is to study their responses with respect to the type of environmental conditions encountered in service. This can only be realised through tests conducted on representative materials and structures in appropriate environments [29]. However, numerical or theoretical approaches may also be alternatives towards the understanding of the behaviour of monopile structures but experimental data are required to validate them for confidence in and reliability of the results.

Currently, about 96% of the commissioned offshore wind structures are supported on monopile structures while the remaining 4% are supported on jacket structures [31]. Due to the rapid development of the wind industry, other support structures such as Tripod, Tripile and floating structures are proposed for offshore wind farms installations depending on water depth, turbine size, soil conditions and cost of installation. Different types of support structures for offshore wind turbines with their associated water depths are shown in Figure 2-3. The figure shows that at some particular water depths, the most appropriate

support structures will be the floating types. The floating support structures include the tension leg platform (TLP), semi-submersible and spar buoy platforms with each having specific design requirements but these are not discussed here. However, it has been mentioned that the design and installation costs of the floating structures are similar to those of fixed supports structures in deeper waters and that the floating structures design are expected to be economical [40] but this prediction has not been established yet.

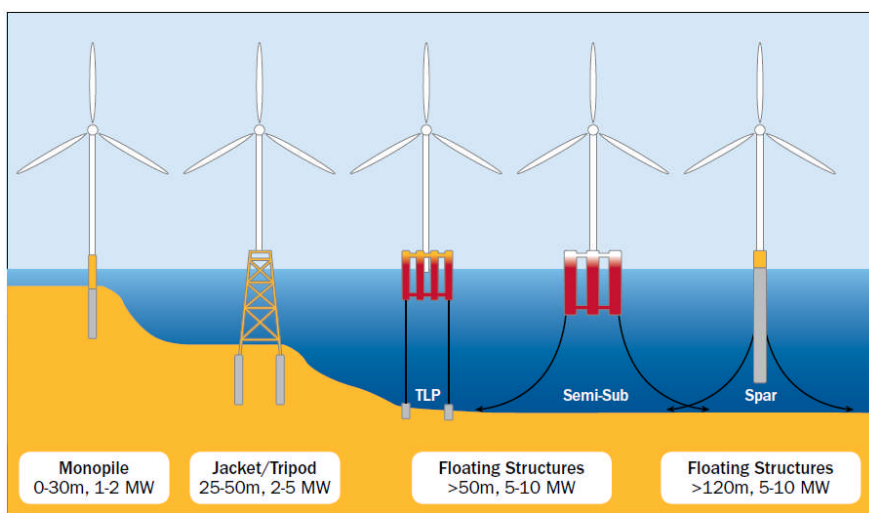


Figure 2-3 Offshore wind support structures [40]

2.3 Offshore wind energy economics

Offshore wind generation is based on experience and technology acquired from onshore wind [38], but the project cost for offshore wind structures is significantly higher than land based ones. This is due to the additional costs required of the substructure, which may also depend on the type of support structure, coupled with the effects of the harsh marine environments. Zhixin et al. [41] stated that the offshore wind system is two or three times higher than the onshore system, while Esteban et al. [42] attributed the cost of wind structures to sea operations. The operation and maintenance of wind turbines located in the Northern Baltic Sea is more challenging due to the cold climate and icing conditions [43]. This implies that the operation and installations costs of wind structures are also site dependent. At the moment, one of the major challenges for the offshore wind industry is cost reduction for wind structures

with the production and installation of the substructures covering about 20% of the capital expenditure (CAPEX) [40]. Musial et al. [38] also stated that the overall cost of the offshore systems is associated with the foundations, installation, operation and maintenance. Operation and maintenance of the foundation is around 30% of the total cost while the cost of grid connection to the shore is about 25% of the wind turbine [44]. This implies that if the production and installation costs of the substructures are reduced, there is likely to be a significant reduction in the overall cost of the wind structures. The combined cost of electrical grid connection, foundations and support structures, logistics and installations, operating and maintenance was also mentioned to be around 57% to 71% in [45]. As the wind industry is playing a key role in the UK's target of generating energy from renewables, it has been suggested that there should be collaborative efforts between the government and industry to ensure that the cost of generating power from offshore wind is reasonably reduced [37].

2.4 Challenges in design of monopile support structures against corrosion fatigue damage

Apart from the operational loads envelope encountered by monopile support structures, they are subjected to relatively harsh marine environments. A review of the structural dynamic response characteristics of offshore wind turbines is presented in Chapter 4. However, what is not known at the moment is the extent to which corrosion can be associated with damage to the monopile support structures across the relatively narrow band of frequencies reported in literature [46]–[53]. Due to rapid development in the wind sector, offshore steel manufacturers now use modern materials and fabrication techniques for the production of thicker plates for monopiles and other types of support structures. Therefore the behaviour of the newer types of materials with respect to the area of application needs to be understood. Also, fabrication techniques, such as the types of welding process employed nowadays, are likely to significantly influence crack growth behaviour in the materials in air and seawater environments. This is because of possible changes in the microstructure of the

weld materials and level of weld induced residual stresses as a result of material thickness, material type, welding input parameters, and levels of restraints employed during welding etc. Therefore, the type of crack growth behaviour, such as those reported in [2], [3], may be significantly different from those in the present steels, considering the types of fatigue testing facilities, data acquisition techniques and improved fabrication procedures that are employed currently.

It was also mentioned that the currently adopted design standards for offshore wind turbine structures are the design codes and semi-empirical correlations developed by certification authorities such as Det Norske Veritas (DNV, 2011) and American Petroleum Institute (API, 2007) for the oil and gas industry using fatigue data collected from small diameter flexible pipes [1]. Due to the significant numbers of fabrication techniques, inspection and design techniques that have evolved recently, Brennan [4] also mentioned the need for an update to the existing design standards that are used for the first generation of monopile and tubular joint steel structures. Therefore, considering the significant difference in the design requirements of wind structures compared to oil and gas structures, the currently available design standards may not accurately predict the performances of wind turbines supported on monopile structures. Given the manufacturing volumes of wind structures, it may therefore be implied that there is a requirement for new design solutions for wind structures in order to ensure their fitness for purpose.

To this end, the aforementioned challenges in the design of offshore wind turbines highlights the need for a better understanding of the fatigue and corrosion assisted fatigue crack growth behaviour in the structures with respect to their dynamic response characteristics. To bridge the gap in knowledge on the effects of corrosion on fatigue behaviour in oil and gas structures and offshore wind turbines supported on monopile structures, there is a need to carry out experimental tests on representative materials and structures in appropriate environments.

The literature search has revealed that the data available on corrosion fatigue crack growth behaviour of medium strength steels used for offshore structures are those realised from structural steels such as BS4360 50D in the 1970s and 1980s. However, it must be mentioned that although the database is without doubt a huge one, it can be considered out of date. Newer grades of steels such as S355J2+N steel are now being used for offshore wind monopile fabrication and due to better fabrication techniques, these grades of steels have improved properties in order to enhance toughness and weldability [54]. Therefore, the fatigue data realised from the old BS4360 50D steel grades may not be the same as those obtained from the current grades of steels. Some results were also obtained from 355D steel grades in air, for example in [55]–[57]. The material composition of these steels is somewhat different from that of S355J2+N steel; a typical example of the material properties can be seen in [56]. Therefore, crack growth behaviour in these steel grades is likely to be different due to variations in properties. Comparisons of crack growth behaviour of some steel grades used for offshore installations are made in Chapters 4, 5, 6 and in Appendix A. In the following section, a review of corrosion fatigue in offshore structures with respect to the effects of the environment and some other associated factors is presented.

2.5 Seawater environmental conditions

Seawater covers up to 71% of the Earth's surface with approximately 3.5% by weight of sodium chloride solution and it is challenging to replicate the natural seawater environment in the laboratory [58]. This is probably because of the significant variation in the environmental zones with respect to temperature, oxygen content, pH salinity etc. The pH of seawater ranges from 7.8 to 8.3 [58] and is considered to be mildly alkaline. It has been mentioned that fatigue behaviour can be significantly influenced by variations in temperature, pH, dissolved oxygen and salinity [59]. These variables have been studied under laboratory conditions. For example in [2], it was found that a reduction in pH from 8.5 to 6.5 and a reduction in oxygen concentration from 7 to 1mg/l had a marginal effect on crack growth rates in 50D steel, while an increase in

temperature from 5⁰C to 20⁰C increased the crack growth rates by a factor of 2. A significant number of corrosion fatigue tests have been conducted in the laboratory at a temperature between 5⁰C and 10⁰C in order to represent typical North Sea conditions [2], [3]. The results obtained using these temperature ranges are discussed in Chapters 4, 5 and 6.

However, the crack growth behaviour of steels under the above mentioned parameters may depend on the seawater composition. Most studies conducted on corrosion fatigue behaviour of marine structures have used artificial seawater prepared according to the specifications given in ASTM D1141 [60] as an alternative seawater environment, while some investigations have used either 3.5% NaCl [61], [62] or natural seawater [2]. Therefore, crack growth data obtained under these environments are likely to be different.

2.5.1 Simulating service load conditions

It is understood that most structures in service experience variable amplitude loadings with different magnitude and loading sequences which are also referred to as load interaction effects. However, the majority of fatigue data are obtained under constant amplitude loading. This is because data obtained using constant amplitude loading serve as the baseline for the understanding of the structures, are easier to analyse and are readily compared with results from other sources. Laboratory tests are studied under short duration and an attempt to simulate realistic service load conditions may not be feasible due to time constraints and cost implications. However, fatigue crack growth data realised within the laboratory simulated seawater environment might be extrapolated to predict the crack growth behaviour of real structures.

It should be mentioned that crack growth analysis under spectrum loading is far from easy and time consuming due to the load interaction effects [63] which cannot be completely accounted for. However, material data obtained under constant amplitude loading could be used to implement prediction under spectrum loading if the load interaction effects can be adequately quantified. It has been shown that the load interaction effects were negligible in the corrosion fatigue crack growth of ABS EH36 steel tested under constant amplitude and

spectrum loading [63]. The result is shown in Figure 2-4. In this type of situation it may be implied that the fatigue data realised under constant amplitude loading could be utilised for fatigue life estimations, neglecting the load interaction effects.

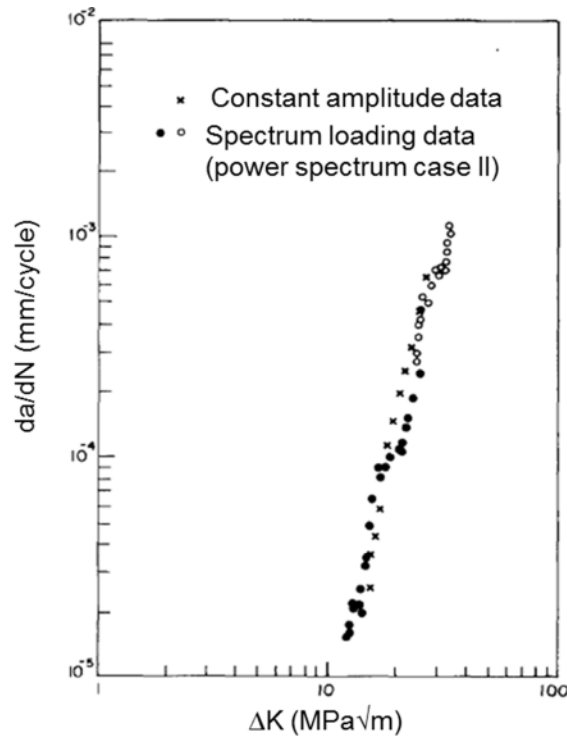


Figure 2-4 Corrosion fatigue crack growth in EH36 steel conducted under constant amplitude and spectrum loadings [63]

2.6 Factors influencing fatigue crack growth in marine environments

In wind turbine support structures, corrosion mechanisms are expected to be driven by the synergistic effects of the harsh marine environments, wind and wave loads continuously acting on the structures in service, compared to oil and gas structures where wave loads are primarily the concern. It should be mentioned that this type of study has not really been addressed in the public domain. Considering the significant quantity of steel used for monopile fabrications and in spite of the level of quality control measures applied during their fabrication, there is still the potential for defects at the intersection between the parent material and the weld region due to the significant levels of local

stress concentrations imposed by the geometry and effects of residual stresses introduced by the welding process. These defects can be significantly amplified in corrosive environments due to the synergy between fatigue loadings and harsh marine environments.

Corrosion fatigue is a complex phenomenon which may not be completely understood. This is due to the nature of the electrochemical interaction of the material involved, and the nature of the environment coupled with the significant number of the associated variables involved in the corrosion fatigue process. Each variable plays an important role in the process, thus it becomes a challenging and costly task to study them experimentally.

Some of the important factors influencing the corrosion fatigue behaviour in metals have been categorised as mechanical, metallurgical and environmental variables [64], [65]. The mechanical variables include: loading frequency, stress intensity factor, loading waveform, load interaction effects (variable amplitude loading), residual/mean stresses, material type and geometry; metallurgical variables are microstructure and material composition, mechanical properties, heat treatment etc.; the environmental variables include: temperature, pH, level of CP, coating type, oxygen concentration etc. These significant numbers of variables indicate how complex the corrosion fatigue process is and how difficult it is to justify all the variables economically. However, it is important to understand the interaction of the various factors in the corrosive environment and their effects on the material response so that the representative environment that best describes the actual service condition can be achieved with minimal experimental variations [58]. In most cases, important parameters based on the investigator's decision are varied while others are kept constant. Therefore, care must be taken when experimental data are compared with investigations from other sources during data interpretation and comparisons.

Simulating the effects of the above mentioned variables on crack growth rates using large scale specimens may not be a cost-effective approach. This is because tests using large scale specimens are expensive, laborious and also depend on the capacity of the test machine. This is why the majority of the

corrosion fatigue crack growth studies have been conducted using small scale laboratory specimens such as compact tension (CT), single edge notched specimens, or bars. These specimens can also be used to represent the through thickness direction of crack growth in welded joints as closely as possible. Another advantage of small scale specimens is that a good number of variables can be studied under laboratory conditions and the obtained crack growth data from such studies may be extrapolated to real structures. All the variables influencing corrosion fatigue crack growth are not discussed independently in this thesis but some of them, including those within the scope of this work, are discussed in later sections.

Some investigations have also examined the interaction of a number of variables influencing the corrosion fatigue behaviour of materials. For example Bhuyan et al. [66] investigated the effects of environment and mechanical loadings, such as frequency, load ratio and waveform, on corrosion fatigue crack growth in CSA G 40.21 M 350 WT steel with a yield strength of 405MPa. It was found that there was a marked influence of the environment on crack growth rates when the temperature was kept between 0⁰C and 4⁰C at a loading frequency of 0.05Hz. It was also reported that the effect of frequency in air was negligible and no significant effects of the increase in stress ratio from 0.05 to 0.3 was evident in the air environment. A similar behaviour was also reported by Johnson et al. and Vosikovsky [67], [68], as slightly higher crack growth rates were observed in seawater at an R-ratio of 0.3 relative to an R-ratio of 0.1. This may be due to the behaviour of materials with respect to increasing stress ratios, environmental conditions and the magnitude of the stress ratio used for testing. The environmental and material influences on stress ratios and crack growth rates are discussed with respect to the data presented in Chapters 4, 5 and 6. Investigations that addressed some associated mechanical and environmental factors influencing corrosion fatigue behaviour in offshore structures are discussed in the following sections.

2.6.1 Frequency effect on fatigue crack growth

Corrosion fatigue crack growth in most studies is usually referenced to the response of the material in an air environment. This can be quantified using either the S-N or the fracture mechanics approach. However, regardless of the approach used, it should be noted that the frequency content of the loading cycle is one of the important parameters that control corrosion fatigue crack growth in offshore structures. In this work, the fracture mechanics approach is employed. Lower cyclic frequencies have been shown to be more damaging in corrosive environments compared to the response in air [2], [3]. This is due to the longer time a crack tip is exposed to the electrochemical elements per cycle [34]. This implies that, using a higher frequency for crack propagation in seawater will significantly reduce the environmental influence of the corrosive media on crack growth rates. Crack growth rates in BS4360 50D steel in seawater at higher frequencies have also been reported to be similar to those obtained in an air environment [2], which implies that fatigue crack growth is more frequency dependent in seawater than in air. The use of a higher frequency for fatigue tests conducted in an air environment also depends on the capacity of the test machine. A higher cyclic load frequency may introduce vibrations in the fatigue test machine and this may significantly influence the results. Another possible explanation with respect to crack growth rates is that, at a higher loading frequency; the applied test load may not be adequately delivered at the crack tip.

It is worth mentioning that the fatigue and fracture mechanics tests conducted in the 1970s and 1980s on medium strength steel grades were realised at the wave excitation frequency of 0.1Hz to 0.2Hz [2], [3], [69]–[71], with most of them reported at a cyclic load frequency of 0.1Hz. More recently, Griffiths and Turnbull [72] used a loading frequency of 0.167Hz to compare the effect of soaking or exposure time on fatigue crack growth rates in CT specimens extracted from AISI 4340 and BS4360 50D steels respectively. Havn and Osvoll [73] also investigated the effect of CP on crack growth rates in BS4360 50D steel at a loading frequency of 0.2Hz. As mentioned in section 2.6, because wind turbine structures encounter wind and wave loadings during operation, the

cyclic load frequency which is relevant for testing monopile structures' representative materials is expected to be different from those used for oil and gas structures. An extensive search of the literature has shown that the corrosion fatigue crack growth behaviour of offshore structural steels using the cyclic loading frequency that might be experienced by wind turbine monopile support structures has rarely been reported. Therefore, for a better understanding of the corrosion crack growth behaviour in the structures, there is a need for material testing under the cyclic loading frequency and conditions that might be experienced by wind structures in service.

As mentioned earlier, it has been established that the influence of seawater on crack growth rates is not significant at higher cyclic load frequencies [2]. Vosikovsky [74] also studied crack growth rates in X65 pipeline steel at various loading frequencies, as shown in Figure 2-5. It was found that crack growth rates were increased as the loading frequency was decreased from 10Hz to 0.01Hz particularly at lower ΔK . But at higher ΔK , the crack growth curves deviated to the reference air curve. However, it was mentioned that Figure 2-5 is valid under a constant load ratio [75]. It can also be observed that the crack growth data obtained at a loading frequency of 10Hz in seawater nearly converged with the reference air curve, regardless of the level of CP. This implies that increasing loading frequency for corrosion fatigue tests is not a compromise to arrive at a reduced testing time.

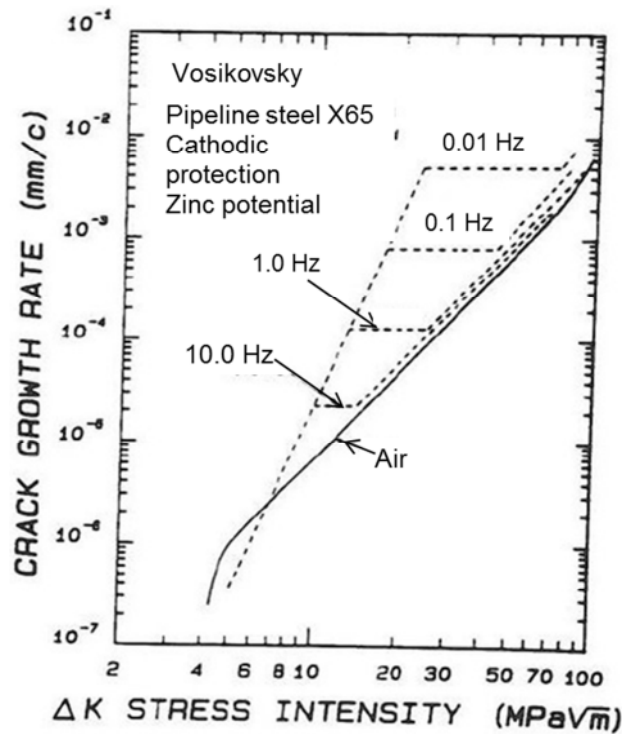


Figure 2-5 Frequency effects on fatigue crack growth in X65 pipeline steel [74]

Therefore, care must be taken when selecting the cyclic loading frequency value for corrosion fatigue tests due to the associated crack opening time. For example, in Thompson's work [76], a frequency of 0.5Hz was used for testing in order to minimize the experimental time in contrast to the approximate wave loading frequency of 0.1Hz as reported in various test programmes. It should be mentioned that at a loading frequency of 0.1Hz, the crack tip is exposed to the corrosive environment for a longer time compared to a frequency of 0.5Hz. This implies that the damaging effect of seawater on crack growth rates would be higher at a lower cyclic load frequency. An alternative to arrive at a realistic testing time would be to increase the stress level. However, care must also be taken when selecting applied stress in order to avoid plasticity at the crack tip. Comparisons made between the results of the present work and those presented in Thompson's work are discussed further in Chapter 6.

It was mentioned in Vosikovsky's work [74] that the tests were conducted at room temperature and that a hydrogen embrittlement mechanism was likely to be responsible for the observed crack growth rates under CP and free corrosion potentials. This implies that the manner of crack growth in seawater at higher

ΔK as shown in Figure 2-5 may also be both material and environment dependent. However, the type of crack growth curves shown in Figure 2-5 was not evident in the Thorpe et al. and Scott et al. works [2], [3] for tests conducted on BS4360 50D steel. In their studies, tests were conducted under a simulated North Sea wave load of 0.1Hz. Crack growth rates were found to be higher in seawater than in air across the ΔK ranges tested. This can also be supported, as shown in Figure 2-6, for tests conducted under constant stress intensity factor ranges ΔK . It can be seen that crack growth rates increased with decreasing cyclic load frequencies.

In an air environment, the effect of frequency has been shown to be insignificant [73], [74] and it was also mentioned that frequency effects on fatigue crack growth in air are, in most cases, assumed to be negligible [75]. This suggests that frequency can be increased to an appropriate level for an air test in order to save testing time. In a study of fatigue crack behaviour in TStE 355 and EStE 690 VA steels [77], a marginal effect of frequency was also seen in air over a frequency range of 0.02 to 40Hz but in free corrosion conditions and under CP, increasing the loading frequency to 10Hz exhibited nearly the same crack growth rates as in air.

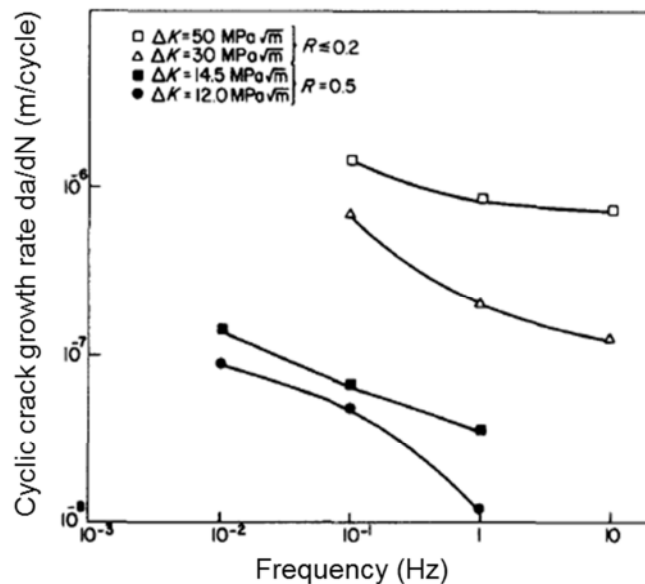


Figure 2-6 Frequency effects on corrosion fatigue crack growth [2]

The major drawback in the Thorpe et al. and Scott et al. investigations is that weld materials were not considered as test data were obtained from parent materials. The weld area is a potential spot for crack initiation due to the significant levels of local stress concentrations imposed by weld geometry and the magnitude of residual stresses introduced during welding. Fatigue cracks are initiated at the weld heat affected zones (HAZ) and propagate into the unaffected parent materials [67]. This is because the HAZ contains a heterogeneous microstructure with varying mechanical properties. However, the extent of crack propagation in the HAZ may depend on the member thickness and the HAZ dimension. Considering the microstructure variations in the HAZ, the crack growth behaviour may be significantly different from the associated base material; however, this depends on the type of weld induced residual stresses [78]. Therefore, fatigue crack growth behaviour of parent materials may not be sufficient to fully understand the damage mechanisms in offshore structures such as monopiles.

However, it must be mentioned that the HAZ is a region where the fatigue crack growth behaviour cannot be fully understood due to microstructure variation. Microstructure variation can influence fatigue crack growth rates thus leading to roughness induced crack closure, change in crack path and delayed crack growth [79], [80]. The magnitude of these factors may depend on the type of weld induced residual stresses – either tensile or compressive. Although, in a previous study [81], the tests conducted under the North Sea wave frequency of about 0.13Hz on base and materials extracted from C-Mn-V steel conforming to BS4360 50D steel, revealed that there is no marked difference between the crack growth rates obtained from parent material and HAZ ones in a seawater environment. The results were explained by a fair difference in hardness values measured in both materials. A similar behaviour was also reported from tests conducted on the HAZ of HSS in the region of 400MPa to 600MPa [54]. However, this needs to be addressed further under a cyclic load frequency similar to what is experienced in offshore wind monopile support structures in order to fully substantiate this claim. However, it is anticipated that a carefully controlled welding process using a filler material with a similar composition to

the base metal is likely to result in the same crack growth behaviour of the HAZ and base material. This is discussed further in Chapter 6.

2.6.2 Mean stress effects on fatigue crack growth

Mean stress effects on crack growth rates are generally described with respect to the cyclic stress ratios used for testing. Mean stress, or stress ratio, is a variable that plays an important role in the fatigue crack behaviour of materials in air and seawater but its effect depends on material type, specimen geometry and loading state [82]. An increase in mean stress will result in an increase in crack growth rates but this depends on the crack growth region, material and environment [83]. At a lower stress intensity factor range in a seawater environment, crack growth rates may be higher, lower or similar to those measured in an air environment. This also depends on the level of closure imposed at the crack tip with respect to the loading ratio [84]. At an increased stress ratio, the influence of seawater on crack growth rates may be significantly higher than in an air environment. This is probably due to a larger crack tip exposure area or crack opening displacement which occurs at a higher stress ratio.

The effects of mean stress have been studied in different seawater environmental conditions and materials [2], [15], [68]. These investigations have revealed different crack growth responses with increasing R-ratios. For example, in Thorpe et al.'s work [2], tests were conducted in natural seawater. At free corrosion potential, increasing mean stress resulted in an increase in crack growth rates across all the ranges of ΔK tested and at an R-ratio of 0.5 to 0.7, the effect of stress ratio gave an upper bound of approximately six times the crack growth rates observed in air. These results are shown in the right of Figure 2-7.

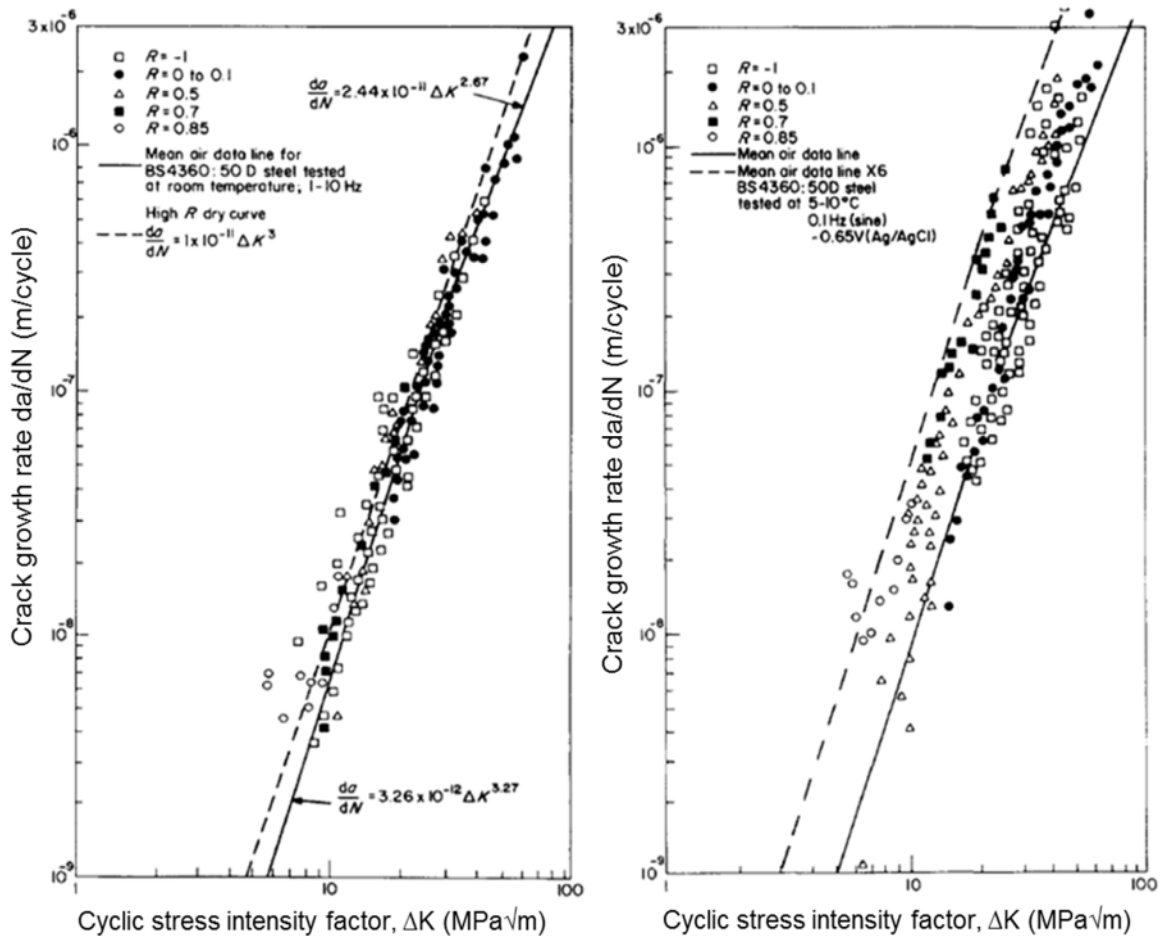


Figure 2-7 Crack growth rates of BS4360 50D steel in air and seawater [2]

However, a significant amount of scatter was obtained from the results as shown in the figure. In the left of Figure 2-7, tests conducted at stress ratios of -1 to 0.85 in air are compared. It can be seen that the data points are clustered around the mean air data regardless of the increase in stress ratio. In other words, there was no marked effect of the stress ratio in air. In the seawater tests, as shown on the right of Figure 2-7, it is possible that crack growth rates at higher stress ratios were also significantly influenced by the interaction of the environment and loading frequency with respect to crack opening time.

In Vosikovskiy's work [68], it was found that at a lower cyclic frequency, crack growth rates in X70 pipeline steel tested in a 3.5% sodium chloride solution were enhanced in a similar manner to those reported for X65 steel (Figure 2-5). The influence of the stress ratio was also found to have appreciable effects on crack growth rates both at threshold and near threshold stress intensity factor

ranges. At increased ΔK ranges, the effect of the stress ratio diminished both in air and the 3.5% sodium chloride solution.

However, significantly different crack growth behaviour was observed by Appleton [15] on tests conducted on BS4360 50D steel. It can be observed that there was no marked effect of mean stress on crack growth rates as shown in Figure 2-8. However, at lower ΔK , the observed crack growth rates as shown in the figure may be related to the marginal effects of mean stress but at higher ΔK , the crack growth curves converged and deviated from the linear segment of the da/dN vs. ΔK plot. In Appleton's work, tests were conducted at an ambient temperature of 23°C using a 3% NaCl solution; Vosikovsky's data were also obtained at a room temperature of 24°C ± 2°C while Thorpe et al.'s tests were conducted at temperatures of 5°C-10°C. Therefore, it is possible that crack growth data presented from the above studies were also significantly influenced by changes in temperature and variations in the environmental media.

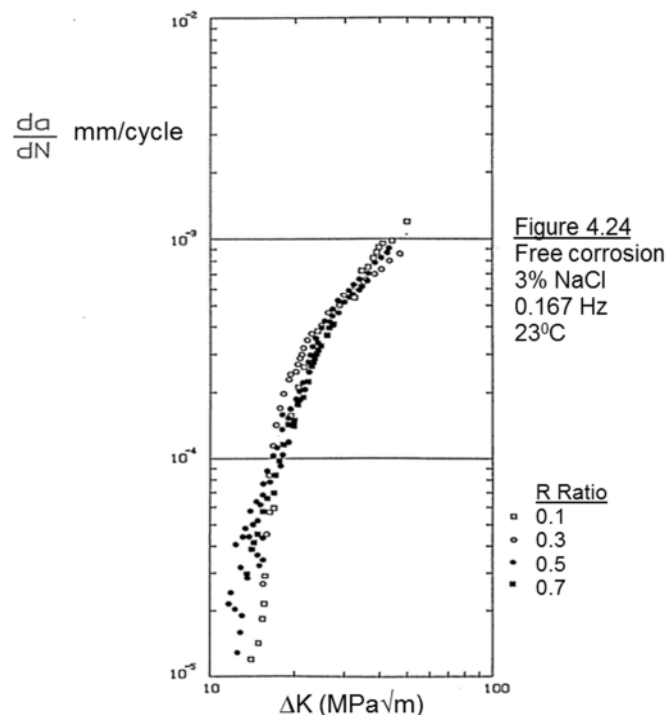


Figure 2-8 R-ratio effect on crack growth rates in BS4360 50D steel [15]

However, in Appleton's work, some tests were also conducted using ASTM artificial seawater at a temperature of 9°C to 14°C, as shown in Figure 2-9. It

can be observed that an increase in the test temperature increased crack growth rates, particularly at higher ΔK . From some previous studies, tests have also been conducted at a temperature range of 5°C-10°C [2], [3], [67] with the aim of simulating the average temperature of the North Sea. Therefore, it is expected that the range of temperatures reported in those studies compared to Appleton's work are likely to have significant effects on crack growth rates. These comparisons are discussed further in Chapter 5.

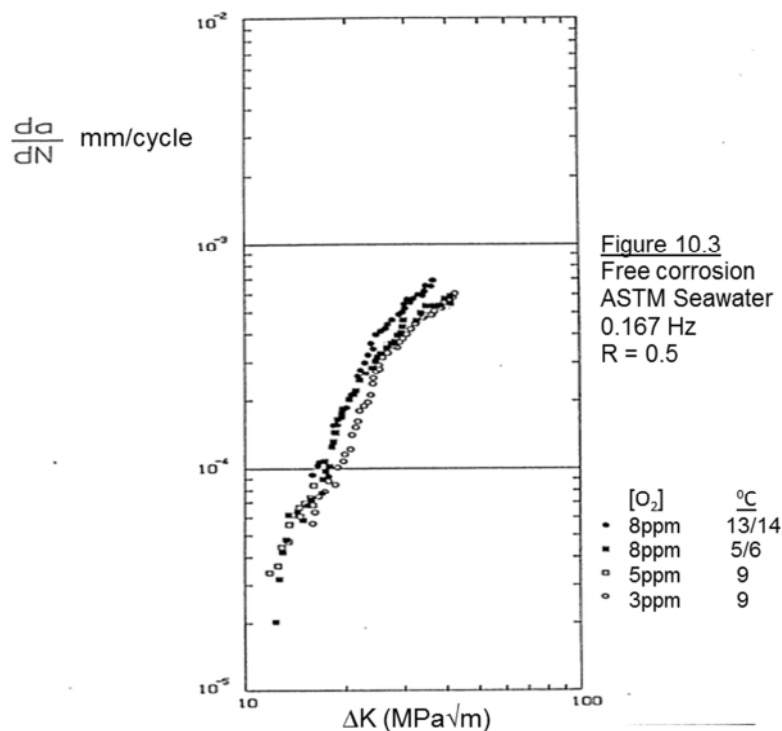


Figure 2-9 R-ratio effects on BS4360 50D steel at different temperatures [15]

To account for the effect of tensile residual stresses in welds, a higher mean stress or R-ratio of about 0.5 or 0.6 is usually used for testing, while an R-ratio of 0 is used for base materials [73]. However, the magnitude of the tensile residual stress may be limited to the near surface residual stress distribution. For relatively thick materials, such as those used for monopile fabrications, both tensile and compressive residual stress types are likely to be present. In that case, the overall magnitudes of the through thickness residual stress distribution would be required to quantify the effect of mean stress on crack growth rates. Different sources of mean stresses in structures have been categorised as stresses due to dead weight loading, weld induced residual

stresses and locked up stresses introduced during fabrication [13]. This implies that residual stresses present in welds may also be considered as mean stresses. Under constant amplitude loadings, several models have been developed to account for mean stress effects on crack growth rates [85]–[89]. These models, coupled with a new theoretical model that accounts for mean stress effects on crack growth rates in air and in seawater, are discussed in Chapter 5. However, considering the levels of uncertainty associated with residual stresses in welds, it may be difficult to completely account for the effects on crack growth rates.

If residual stresses are considered as mean stresses, crack growth behaviour may be related to either acceleration or delay mechanisms. In the presence of compressive residual stresses, crack closure or delay in crack growth may occur and this is beneficial to fatigue crack growth [90], [91]. Generally, the presence of residual stress would have an effect on the applied ΔK , depending on whether the residual stress type is tensile or compressive [92]. Tensile residual stresses keep the crack open while compressive or beneficial residual stresses induce crack closure and increase the resistance to crack growth [93]. If the fatigue crack is propagating through a compressive residual stress field, this will introduce a compressive stress cycle even if the nominally applied stress cycle is tensile. As such, the applied ΔK may not be affected but the effective R is, depending on the magnitude of the residual stress distribution. This implies that the residual stress distribution will be superimposed on the applied stress cycle. For instance, if tensile residual stress exists ahead of a crack under a compressive stress cycle, the crack might actually be experiencing a tensile cyclic stress. This can also be explained, as shown in Figure 2-10, for the case of a tensile residual stress up to the magnitude of yield stress. This is probably why higher R-ratio fatigue data are suggested as the appropriate results for estimating fatigue lives of welded joints [67].

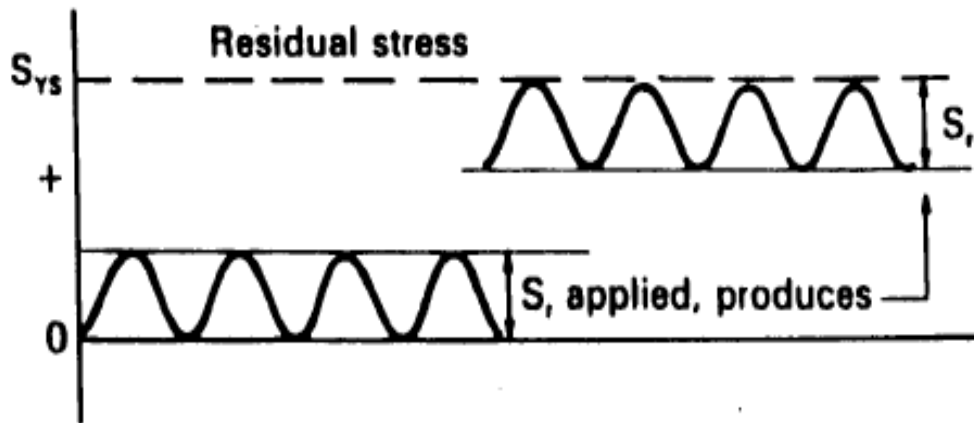


Figure 2-10 Superimposed pattern of applied and residual stress [94]

Stress relief techniques such as post weld heat treatment (PWHT) are applied on welded joints in order to remove residual stresses but it should be noted that the effect of residual stresses may not be completely removed. This is due to the levels of uncertainty associated with residual stresses [13], [94]. However, some situations may arise that require an understanding of crack growth behaviour in the presence of residual stresses, in as weld materials. Some weld improvement techniques may also reduce local stress concentration or introduce beneficial compressive residual stresses into weldments, so that fatigue lives can be significantly increased. It was mentioned that a stress relief process using heat treatment was beneficial in C-Mn steel resulting in improved fracture toughness of the HAZ [95], but this may be material dependent. It was also mentioned that residual stress with a magnitude of about 20% to 30% of material yield strength would still be present in welded joints after the application of PWHT [94]. A review of weld improvement techniques coupled with their associated advantages and limitations can be found in [94].

During crack propagation, residual stresses are released gradually or redistributed and may eventually disappear as the crack grows. However, the redistribution of residual stresses ahead of the crack tip may be directly related to the magnitude of the externally applied load. Therefore, the effects on fatigue crack growth are expected to occur in the early stages of crack propagation [13]. It was mentioned by Austin [13] that, in weld plates, the tensile or damaging part of the residual stress field extends to about a quarter of the plate

thickness, such that the stress field is compressive in the middle of the plate owing to the self-equilibrating manner of residual stresses. An example is shown in Figure 2-11 for a finite element study of residual stress distributions in 76mm thick 316L stainless steel pipes that were joined by an automated narrow gap welding process. It was found that the tensile portion of the residual stress distribution existed close to the surface of the weld plate, while compressive residual stress occurred in the middle [96]. It can also be seen from Figure 2-11 that the tensile segment of the residual stress distribution is nearly a quarter of the plate thickness. However, residual stresses and their effects on crack growth rates may be material dependent but the manner of residual stress distribution shown in Figure 2-11 is in agreement with what was reported by Austin [13].

For tests conducted at higher stress ratios, the crack faces are fully open compared to a lower R-ratio test. This suggests that at higher levels of externally applied load, possible effects of crack closure imposed by residual stresses are likely to disappear as the crack propagates.

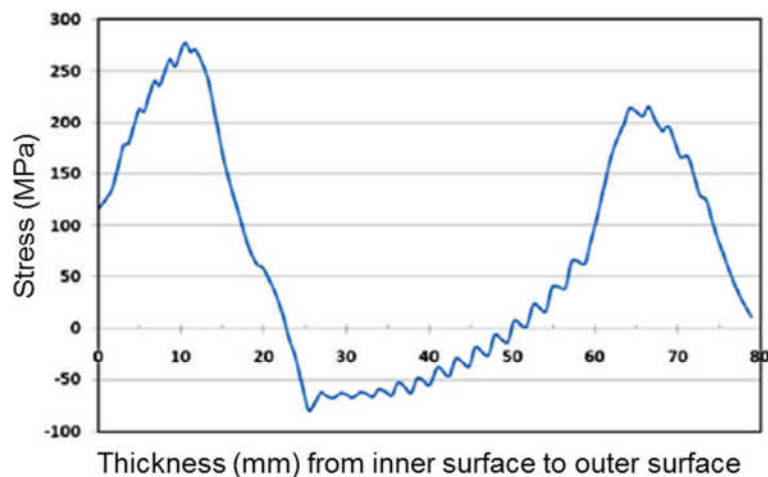


Figure 2-11 Residual stress distribution in 316L stainless steel [96]

If the residual stress distribution shown in Figure 2-11 for weld material is considered as the mean stress for an externally applied stress ratio of 0.1, it implies that the magnitude of the residual stress distribution changes the stress ratio from 0.1 to a negative value. In such a situation, negative stress ratio data may be utilised to correct for mean stress effects on crack growth behaviour in

the material. This approach is presented in Chapter 5, using a new model that accounts for mean stress effects on fatigue crack growth in offshore structures.

2.6.3 Effect of cathodic protection

The effect of CP on fatigue crack growth is not one of the variables studied in this work. However, the brief review presented in this section is to summarise some of studies conducted on the behaviour of offshore structures with respect to CP. The effects of the corrosive environment were found to enhance fatigue crack growth rates by a factor of 2/4 relative to in air, depending on the stress intensity factor range and applied levels of CP [62], [97]. This was observed from tests conducted on BS4360 50D steel in 3.5% NaCl solution which may be different from the data obtained in laboratory simulated seawater prepared according to ASTM D1141 [60].

The two primary processes that have been identified with corrosion in marine structures are the anodic, oxidation reaction and cathodic, reduction reaction [58], as discussed in Chapter 1. It was mentioned that the former process is the major environmental influence of free corrosion condition while the latter is associated with CP [58], [13]. Corrosion fatigue crack growth is primarily controlled by dissolution of metal at the crack tip and hydrogen embrittlement [98]. At high dissolution rates, it was mentioned that the mechanism of crack blunting is likely to occur, particularly at higher stress intensity factor ranges accompanied by a larger plastic zone size [16]. As mentioned in Chapter 1, the reactions occurring under CP are oxygen reduction and reduction of water leading to hydrogen production [13]. The reduction of oxygen is a cathodic reaction while hydrogen reduction might occur due to a low level of dissolved oxygen and cathodic over protection, either by impressed current or sacrificial anode CP systems [58]. Both the S-N and the fracture mechanics have been used in various test programmes to study the effect of CP on the behaviour of steels in marine environments. However, corrosion fatigue damage is associated with both crack initiation and propagation, which can only be addressed by the fracture mechanics approach. Therefore, the approach can be used for the design of structures through monitoring their behaviours with

respect to inspection intervals [99]. Also, if fatigue cracks are discovered in structures, fracture mechanics can be employed as a useful tool to quantify the severity of the cracks and to plan for remedial actions against possible failure [100].

Coatings are also alternative corrosion protections to CP particularly in monopile support structures. However, coatings are applied on the outside of the monopile structures but the inside should also be considered as a potential crack initiation site. The fact that a free corrosion condition is not designed for in offshore structures does not guarantee it from occurring and also corrosion protection (coatings) may be damaged during transportation, installation and operation. Therefore, there is a need for a better understanding of the actual effects of corrosion in marine structures. However, in situations where crack initiation or damage occurs inside the monopile structure, it would be a challenging task to carry out an inspection, especially when there are multiple crack initiation sites. It is therefore important to also consider the effect of corrosion inside the monopile structures when estimating their expected operation lives. This is because the inside of currently installed monopile structures are not protected either by coating or CP and contain a significant amount of seawater and oxygen access [101]. Over time, corrosion may be induced and hence fatigue damage, leaving the structures to operate under a free corrosion condition. The only alternative for internal protection of future monopile structures might be to employ a protective coating during the design and fabrication stage.

Installation of CP systems inside the monopile structures may not be an appropriate approach for corrosion protection due to the hydrogen production and change in water chemistry. Efforts have been made to investigate the possibility of installing internal CP systems in monopile support structures [7]. This study is at an early stage and further experimental studies on the application of the selected types of galvanic anodes on representative materials, operating under similar loading conditions experienced by monopile structures, may reveal a better understanding of the performances of the

corrosion protection systems. However, the installation costs of internal corrosion protection systems based on manufacturing volumes of monopile structures need to be carefully considered. In other words, there may be a significant increase in the capital expenditure, considering the additional costs that might be incurred at the project setting up stage concerning corrosion control measures. However, the original design life of the structures can be extended if proper inspection and monitoring facilities are deployed. The use of better inspection techniques coupled with a good understanding of crack propagation behaviour will inform the frequency of inspection so that a fitness for purpose can be achieved [62].

Due to the significant volumes of anticipated wind structures offshore, compared to oil and gas structures, there is a need to operate the wind structures with lower costs and close to the actual design capacity [29]. However, at the moment, there is still a deficit of information concerning free corrosion conditions in representative monopile steels.

Most of the previous research studies regarding offshore oil and gas structures were conducted under free corrosion potentials and with CP. The free corrosion potential of -0.65V or -0.7V with respect to Ag/AgCl electrodes have been used in steels [2], [67]. A value of -800mV has also been referred to as the effective corrosion protection in steel structures [102]. Some studies, for example [2], have investigated the effects of CP at potentials between -0.6V and -1.3V with respect to Ag/AgCl electrodes on crack growth rates in BS4360 50D steel. Crack growth rates were found to be higher at higher levels of CP than at free corrosion potential [2].

Lindley and Rudd [102], also reported the effects of CP on the corrosion fatigue behaviour of welded RQT501 steel by varying the levels of potential between -900mV and -1050mV with respect to Ag/AgCl electrodes. The results when compared with those obtained from BS4360 50D revealed that crack growth rates in both steels were significantly higher in seawater than in air regardless of the levels of CP. These results are shown in Figures 2-12 and 2-13. It was

found that the effectiveness of CP was more appreciable at near threshold stress intensity factor ranges than in the Paris region.

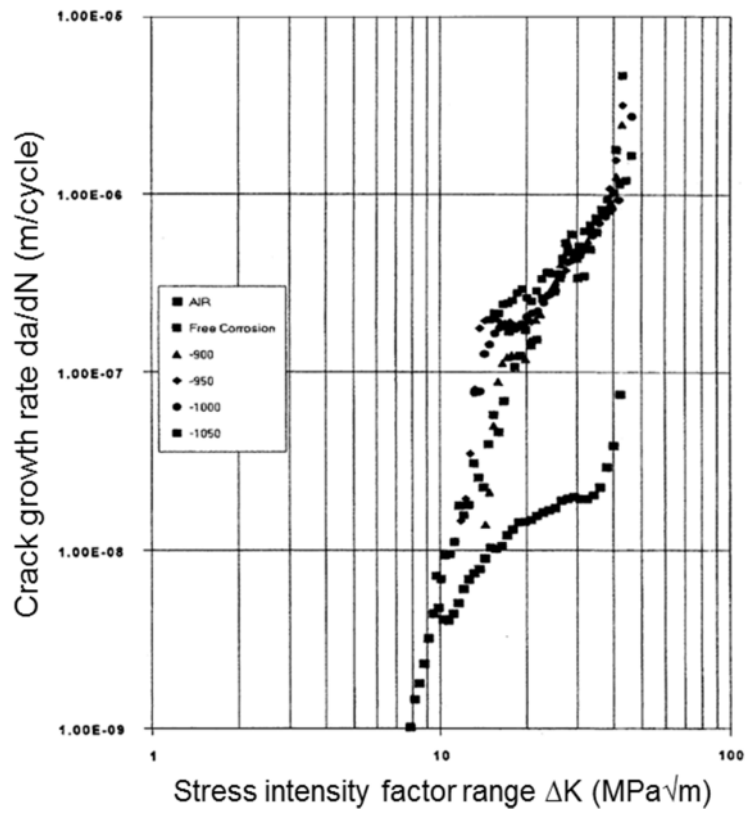


Figure 2-12 Fatigue crack growth rate for RQT501 steel [102]

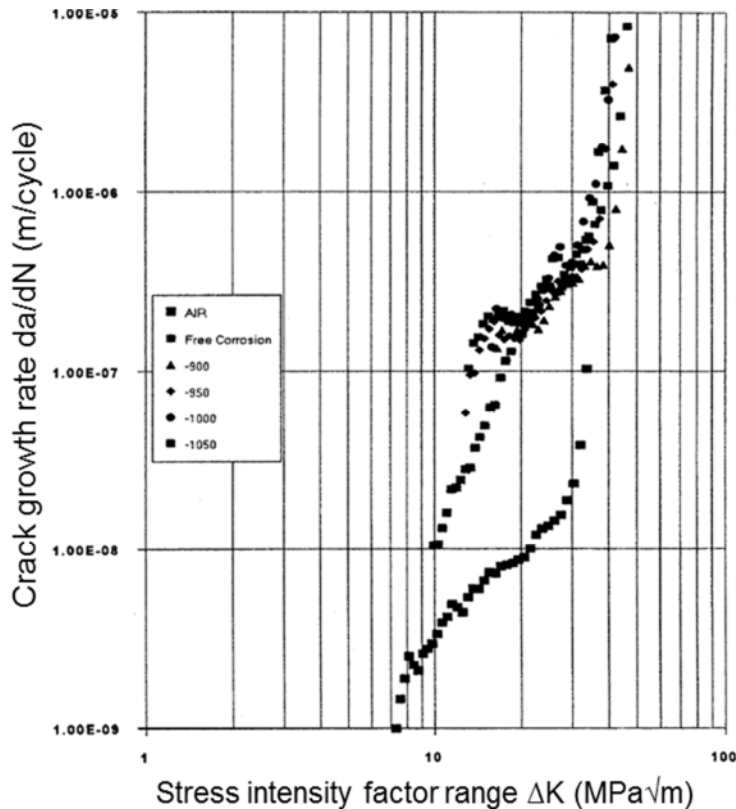


Figure 2-13 Fatigue crack growth rate of normalized steel [102]

It should be mentioned that crack growth data obtained under a free corrosion potential in seawater are likely to be different from those obtained under free corrosion conditions without any protection. This is because a free corrosion potential in a CP system may still be associated with hydrogen production as a result of cathodic reaction, especially when the CP system is not well designed. This may result in some levels of hydrogen embrittlement at the crack tip leading to an increase in crack growth rates. Crack growth rates in BS4360 50D steel have also been attributed to hydrogen embrittlement at all the applied potentials, including free corrosion potential [3]. Hydrogen production from CP systems would result in an increase in fatigue crack growth rates [69]. In HSS such as SE702, the effect of hydrogen produced by CP in 3.5% NaCl increased at lower stress intensity factor ranges and decreased at increased crack growth rates [75]. The influence of CP on hydrogen embrittlement was also found to be more significant in HSS such as SE702 than in BS4360 50D steel [69]. This implies that higher strength steels may be more susceptible to hydrogen embrittlement than lower strength steels. In X65 pipeline steel, Vosikovsky [74],

found that in seawater, below the plateau region where there was an increase in crack growth rates at increased ΔK , the effect of hydrogen embrittlement near the crack tip was more significant.

Corrosion fatigue behaviour of super duplex stainless steel was also investigated to examine its applicability in the offshore wind sector [103]. Tests were conducted on Zeron 100 weld metal in synthetic seawater at a temperature of 20°C under potentials of +600mV and +1034mV with respect to saturated calomel electrodes. Crack growth rates were higher in seawater than in air environment. The crack growth behaviour of the weld material in seawater was found to be similar to those measured in the equivalent base materials. However, it was mentioned that the measured crack growth rates in seawater were significantly influenced by the test temperature.

As mentioned earlier, due to the significant volumes of offshore wind structures, a CP system may not be a cost-effective approach for the steel monopile structures. However, crack growth data obtained under a free corrosion condition using representative parent and weld/HAZ steel materials may be useful for a conservative estimation of the service performance of monopile structures. These types of studies have rarely been reported in the literature and hence remain inadequately understood. As such, one of the objectives of this work, as set out in Chapter 1, is to address this current gap in knowledge with respect to the types of medium strength steels used for monopile fabrications. However, a considerable effort has been made on studying the corrosion fatigue behaviour of HSS weldments. These are briefly discussed in the following section.

2.6.4 Corrosion fatigue behaviour of high strength steels

Steels used for the fabrication of marine structures have been classified into conventional steels (yield strength 350MPa), HSS with yield strength in the range of 400MPa – 600MPa and extra HSS with yield strength of 700MPa – 900MPa [54]. Other types of steels above 900MPa yield strength are also available from steel manufacturers but these are not discussed here. The intention of the review presented in this section is to introduce the crack growth

behaviour of the commonly used HSS for offshore applications. The data obtained from these steels are compared with those used in this work in Chapters 4, 5 and 6. Significant efforts have been made towards understanding the behaviour of medium strength steels such as BS4360 50D. There has also been considerable interest in the use of HSS for the design and construction of offshore structures in the past. HSS with yield strength between 450MPa and 700MPa are normally used for fabrication of the leg members of jack-ups [69]. One of the drawbacks in using HSS for offshore structures is that they are not easily weldable due to their high carbon equivalent values [104] coupled with the addition of other alloying elements. However, offshore steel manufacturers have now employed modern fabrication techniques with the intention of improving steel performances. Another disadvantage in using HSS compared to medium strength types, is their susceptibility to hydrogen embrittlement [105], which also occurs due to CP [106]. A review of the performance of HSS has been conducted in [107], where it was also mentioned that HSS are susceptible to hydrogen embrittlement.

Therefore the behaviour of some HSS in air and seawater are likely to be different from medium strength steel grades. For example in the work of Zhang and Brook [82], fatigue crack growth tests were conducted on RQTuf 501 with yield strength of 462MPa in air and in seawater at stress ratios of 0.1 to 0.7. It was found that there was little effect of stress ratio within the range of ΔK tested. The RQTuf 501 steel exhibited similar fatigue crack growth behaviour under variable amplitude and constant amplitude loadings with crack growth retardation playing a primary role in the variable amplitude loading.

Corrosion fatigue crack growth in SE702 steel with yield strength of 780MPa was also found to be slightly better than those measured in BS4360 50D steel regardless of CP, but in air crack growth behaviour in the two steels were similar [108]. It was also found that the HAZ material exhibited a slightly better fatigue crack growth behaviour than parent material in air, but there was a reduction in the observed difference in seawater. In an air environment, it has also been reported that crack growth rates in S355 steel were lower than those

measured in S690 steels [56]. It is anticipated that newer types of medium strength steels used for offshore installations are likely to be more resistant to crack growth than HSS due to the susceptibility of the latter to hydrogen embrittlement. It would therefore be useful to compare the crack growth behaviour in both medium and HSS for an adequate understanding of their behaviours in marine environments. These comparisons are established in Chapters 4 and 6.

2.6.5 Fatigue crack growth in weldments

Most offshore structures are fabricated from welded joints which are potential spots for fatigue crack initiation. The weld heat affected zones are associated with different microstructures and mechanical properties depending on the type of welding process used. Crack growth behaviour in HAZ materials may depend on the crack initiation site – either close to the weld or parent materials. The types and properties of the filler material used in welding are also important factors that can influence the properties of weldments and the crack growth rates. The HAZ are generally known, with tensile residual stresses which may be up to the magnitude of the yield stress. These stresses can be reduced under cyclic loading, under a stress amplitude higher than the material endurance limit [109]. The implication of this is that tests conducted under a high mean stress may be sufficient enough to cancel out the effect of residual stress as the fatigue crack propagates, as discussed in section 2.6.2.

The HAZ regions are less tough and are associated with less fatigue resistance when compared to the base material [110]. However, this may depend on the particular region of the HAZ with respect to the different microstructure, mechanical properties and type of welding process. Another factor that may influence the HAZ microstructure and hence crack growth behaviour is the number of welding passes. The microstructure of the coarse grain HAZ region may be refined by tempering through the subsequent welding deposits during multi-pass welding [111]. Hence, some of the weld induced residual stresses may be relaxed in the process. However, this may depend on the cooling rates, the composition of both the steel and the filler material. At this juncture, it must

be mentioned that the behaviour of an HAZ to fatigue crack growth may be material dependent, due a number of associated factors influencing the HAZ properties, as mentioned above. In Chapter 6, various data taken from literature relating to steels used for offshore structures are compared with the results obtained from the present investigation. The discussion presented in this section is to provide an understanding of the behaviour of weldments regardless of material types.

Fukuda et al. [81] investigated the crack growth behaviour in stress relieved HAZ and base material of C-Mn-V steel having a similar composition to the BS4360 50D steel in air and in synthetic seawater. The tests were carried out at a loading frequency of 5Hz in air and 0.1333Hz in seawater with the temperature maintained at 15⁰C. Crack growth rates in the HAZ material were found to be similar to those measured in the parent material regardless of the difference in test conditions. The crack growth behaviour was explained with the slight difference in the hardness values of the two materials. However, this may also be related to the influence of the welding conditions accompanied by the heat treatment employed after fabrication. The HAZ is associated with varying microstructures; therefore it is likely that crack growth rates in an HAZ will be enhanced in seawater due to the rates of metal removal.

Crack growth rates in parent, HAZ and weld specimens fabricated from BS 4360 50D steel were also investigated by Thompson [76]. The HAZ and weld specimens were extracted with the notches located 1mm from the fusion zone and at the weld centre line. Crack growth rates were found to be lower in the weld than in the HAZ and parent materials for tests conducted in air at ΔK less than 37MPa \sqrt{m} . The direction of crack growth in the HAZ materials was also found to be towards the parent materials. The preferred crack path of the HAZ material was attributed to the decrease in hardness values across the HAZ. Healy et al. [112] also found that microstructure variation ahead of the crack tip was responsible for a preferred crack path in weld CSN3:82 cast steel, as the crack deviated from the tougher regions of the HAZ. A similar phenomenon was also reported by Trudel et al. [78] in CA6NM stainless steel weld. Therefore,

due to the heterogeneous nature of HAZ, crack path deviation from the HAZ region towards the parent material is likely to be experienced during propagation. Crack propagation can be influenced by several factors including crack closure induced by residual stresses, as previously mentioned. For example, in Tsay et al.'s study [111], crack growth behaviour in EH36 TMCP (Thermo-mechanical controlled process) steel was investigated. The HAZ specimen notch was located about 1mm from the fusion zone. It was found that, due to residual stress induced crack closure at lower ΔK below $22\text{MPa}\sqrt{m}$, crack growth rates were lower in HAZ specimens than in base materials. In some cases, crack path deviation accompanied by a saw tooth like pattern might also occur during propagation leading to a da/dN vs. ΔK relationship as shown in Figure 2-14. This was observed in Q345 steel with a yield strength of 370MPa [79]. The crack growth rates in the weld materials were found to be lower than in the parent materials at a lower stress ratio, but at a higher stress ratio the resistance to crack growth was nearly the same in both materials. The effect was explained by residual stress induced crack closure in the HAZ.

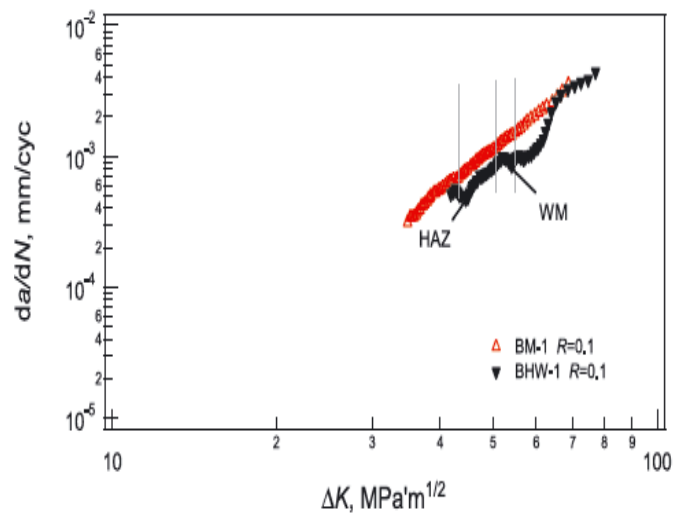


Figure 2-14 Crack growth rates comparison in HAZ and base materials [79]

At a higher R-ratio ($R \geq 0.5$), the crack surfaces are fully open, therefore the manner of crack growth shown in Figure 2-14 may not be observed for tests conducted at higher stress ratios; these are discussed further in Chapter 6.

In a situation when a specimen's notch tip is located near the compressive segment of the residual stress distribution, delayed crack growth is likely to occur due to crack closure phenomenon. However, for a tensile residual stress type, accelerated crack growth might occur. The effect of residual stresses in C-Mn weldments with yield strength of 490MPa was investigated in air and in seawater by Bertini and Beghini & Bertini using CT specimens [113], [114]. For the three materials tested, i.e. parent, HAZ and fusion zones, crack growth rates were found to be higher in the base material than in HAZ and fusion zones in both air and seawater environments. Crack closure induced by residual stresses was suggested to be the reason for the crack growth behaviour particularly at lower ΔK . This was described by a change in slope of BFS versus the applied load, as shown in Figure 2-15. The only drawback in the Bertini [112] investigation was that no data were obtained under a free corrosion condition as all the seawater tests were conducted under CP.

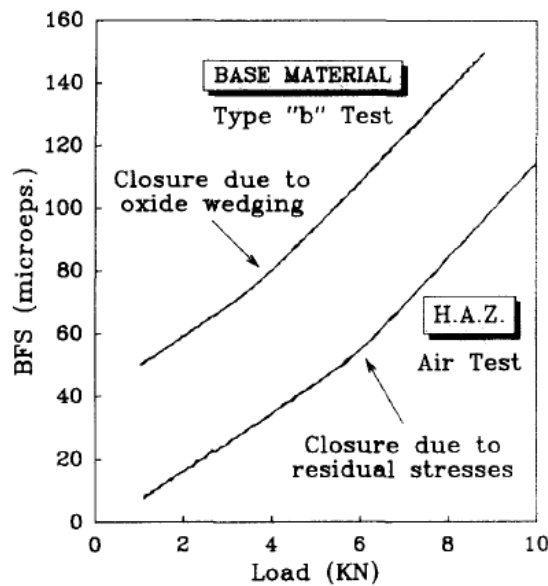


Figure 2-15 Crack closure effects on fatigue crack growth [113]

As mentioned in section 2.6.3, despite the existing database concerning medium strength steels used for offshore installations, very limited data are available on HAZ and weld materials, particularly for tests conducted at higher stress ratios. It should also be mentioned that the data obtained from these studies may not be truly representative of those obtained from modern steels

such as S355J2+N steel. This is due to the fact that modern steels now have improved properties which are achieved by the addition of other alloying elements which may significantly influence the microstructure of the material and hence the crack growth behaviour. Therefore, experimental tests conducted in appropriate environments are needed in order to understand the crack growth behaviour of the newer grades of medium strength steels used for offshore structures such as monopile support structures.

2.7 Summary

The need for an understanding of the behaviour of offshore wind monopile support structures has been highlighted with respect to the state of art and challenges in the offshore wind sector. Crack growth behaviour in different steels has been reviewed and particular attention given to the steels used for offshore installations. The following conclusions can be drawn from this chapter

- Currently available fatigue design guidance needs to be updated to suit the design requirements of offshore wind structures.
- There is need for an understanding of the behaviour of parent, HAZ and weld materials similar to those used for monopile fabrications in an environment that simulates what the structures experience in service as closely as possible.
- A review of literature has shown that corrosion fatigue crack growth behaviour of steels in marine environments can be influenced by a number of variables. Significant differences in environmental test conditions may also result in appreciable variations in crack growth behaviour of the materials subject to dominating parameter used in testing.
- Mean stress effects on fatigue crack growth may depend on materials and test environments. The effect may not be significant in an air environment, but in seawater, an increase in stress ratio can influence crack growth rates with respect to the interaction of the environment and loading frequency.

- Fatigue crack growth behaviour in weldments is not only material dependent but may also be significantly influenced by the environment, loading conditions, microstructure, welding procedure and residual stresses.

3 Experimental Procedure and Data Acquisition

3.1 Introduction

This chapter describes the methodology used for conducting the fatigue crack growth tests in this research. The need for fatigue crack growths tests relevant to offshore wind monopile steel materials in appropriate environments was highlighted in Chapter 2. The fatigue crack propagation method described in this chapter is not just a well-established method, but is also a cost-effective approach. This methodology was developed as part of the Structural Lifecycle Industry Collaboration (SLIC) project managed by Centrica Energy (UK) Ltd. The experimental programme was carried out using the Structural Integrity Laboratory test facilities available at Cranfield University.

A new methodology for fatigue crack propagation tests named the 'Loop type waveform method' has been written using the wave matrix software developed by Instron. This method has proved useful for tests conducted using sensitive non-destructive crack monitoring techniques such as the alternating current potential drop (ACPD), the direct current potential drop (DCPD) and strain gauges.

3.2 Fatigue test machine

The fatigue pre-cracking and propagation tests were carried out on two 100kN capacity Instron 8801 machines equipped with control towers and data acquisition systems. The machines have an actuator stroke of $\pm 75\text{mm}$ and the set-up was carried out in position control while the fatigue tests were carried out in load control to ensure constant load characteristics through the tests. The experimental set-up is shown in Figure 3-1. Prior to the commencement of the tests, the machines were checked for alignment through a purpose designed alignment tie.

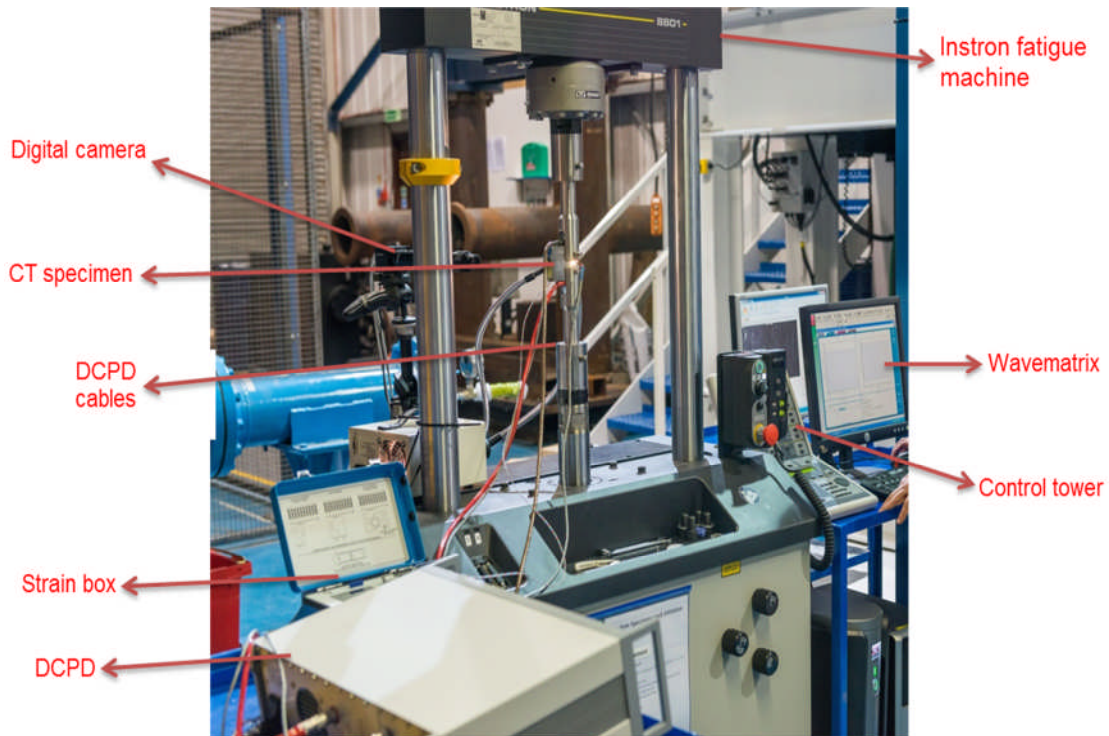


Figure 3-1 Instron 8801 100kN fatigue test machine

3.3 Alignment and loading fixtures

One of the primary objectives of this study is to conduct fatigue crack propagation tests in a seawater environment. Therefore, the choice of an appropriate material for the loading fixture is an important factor that requires careful consideration in order to avoid possible interaction of the materials with the corrosive environment. The loading pins and clevis were manufactured from 2205 duplex stainless steel while the end fixtures were made from EN24T steel. The clevis, loading pins and end fixtures are depicted in Figure 3-2. The design of the loading fixtures is set out in Appendix B.

To establish the reliability of the alignment procedure that was devised using the purpose designed alignment tie, a small tensile test specimen of a known cross section was utilized for the alignment. The importance of this procedure was to ensure that the applied tests loads are actually delivered by the machine load cell. The diameter of the specimen's tests section was 4mm and the elastic modulus was 197 GPa. A linear strain gauge was installed on the specimen as shown in Figure 3-3 and the strain values were monitored using a Vishay P3

strain indicator and recorder. A range of loads were carefully applied to the specimen and the strain values recorded accordingly.



Figure 3-2 Loading fixtures



Figure 3-3 Load and alignment check

The test was repeated three times and the theoretical forces were determined using the average strain values and the dimensions of the gauge section of the specimen. A plot was then derived to compare the experimental forces with the theoretical calculations, as shown in Figure 3-4. It can be seen from the figure

that the experimental data agree well with the theoretical calculations. However, the difference between the results was within an error of 4%.

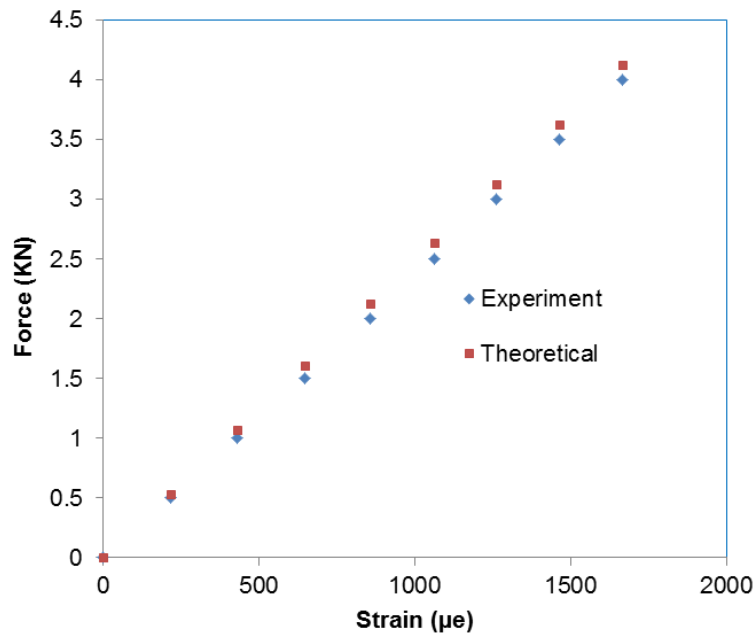


Figure 3-4 Results of load and alignment check

3.4 Material and specimen preparation

The material used for this research was designated EN10025-2:2004 S355J2+N steel. The material certificate is given in Appendix C. The rolling direction of the material was examined to ensure that the notch direction of the Compact Tension (CT) test specimens used for investigation were aligned perpendicular to it, in order to reproduce the direction of crack growth in real monopiles. Samples were cut from the base plate and were examined using metallographic observations of the grain directions at both the longitudinal and transverse sections of the plate.

The thickness of the CT specimens was determined at 16 mm with the notch machined using spark erosion perpendicular to the rolling direction of the base metal plate. CT specimen dimensions were chosen based on preliminary calculations, considering the capacity of the available loading machine, the choice of the appropriate test load to cause crack initiation and specification according to ASTM E647 [115] and BS EN ISO 11782-2:2008 [116] standards.

The CT specimen design is shown in Figure 3-5. Prior to testing, the specimens' surfaces were polished with 120, 600 and 800 grits emery papers in ascending order to allow an adequate visual observation of the crack front.

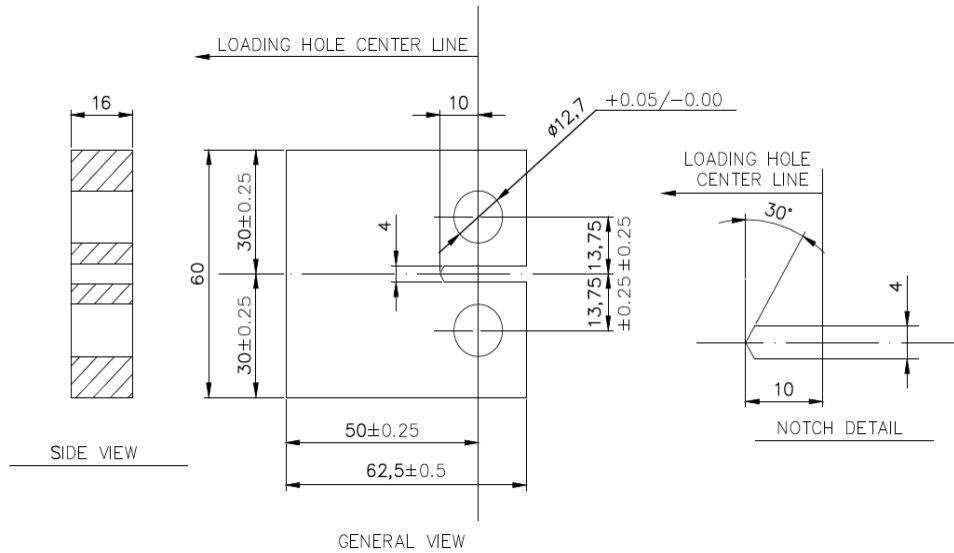


Figure 3-5 Compact Tension specimen design

3.5 Test procedure

Fatigue crack propagation tests were carried out in accordance with ASTM E647 [115] under load control on two 100kN capacity servo-hydraulic machines with digital controllers. The specimens were pre-cracked in air with the load gradually reduced as recommended in ASTM E647 until a pre-cracked length of 4mm was achieved. This was to ensure that both air and corrosion tests were carried out over a valid crack length that would minimize the effect of the plastic zone size associated with the notch. For the corrosion fatigue tests, the pre-cracked specimens were soaked for 48 hours in the seawater before the commencement of the test in order to enhance crack growth in seawater. 'Air tests' refers to tests carried out at room temperature. Tests were conducted in air and in free corrosion conditions using constant amplitude sinusoidal waveform at load ratios of 0.1, 0.5 and 0.7, and loading frequencies of 2Hz to 5Hz in air and at 0.3Hz in artificial seawater. The justification for choice of test frequencies for corrosion fatigue tests is described in Chapter 4.

Crack lengths were monitored by at least one or more of the four methods; ACPD, DCPD, optical measurements through the StreamPix5 digital camera and travelling microscope, and Back Face Strain (BFS). The crack monitoring methods were validated with each other in an air environment. The technique found particularly efficient here is the determination of crack length by BFS method in simulated seawater environment. Details of this will be given in a later section. Crack lengths were recorded with respect to the number of cycles and crack growth rates were determined from the plots of crack lengths a and number of cycles N using a seven point incremental polynomial method [115]. This method is preferred over the secant method due to its ability to numerically smooth experimental data. Cyclic crack tip stress intensity factor range ΔK was determined by the function of the form [115], [116]:

$$\Delta K = \frac{\Delta P Y}{B\sqrt{W}} \quad (3-1)$$

Where:

ΔK is the stress intensity factor range ($\text{MPa}\sqrt{\text{m}}$), ΔP is the applied cyclic load range (MN), B is the specimen thickness (m) and W is the width of the specimen (m). Y is a dimensionless stress intensity correction factor which is given by:

$$Y = \frac{(2 + \alpha)(0.886 + 4.64\alpha - 13.32\alpha^2 + 14.72\alpha^3 - 5.6\alpha^4)}{(1 - \alpha)^{1.5}} \quad (3-2)$$

Where: $\alpha = \frac{a}{W}$ and a is the crack length (m).

3.5.1 Pre-cracking

As mentioned earlier, pre-cracking is usually performed on fracture mechanics test specimens to minimize the effect of the notch on fatigue crack growth results. The pre-cracking was performed in air at room temperature and measurements of the laboratory and specimens temperatures were monitored by the wall and hand-held infrared thermometers respectively. The applied

loads were gradually reduced to achieve reduction in ΔK with respect to change in crack lengths. The loading pins were lubricated with a slight amount of WD40 lubricant to reduce friction at the loading surface specimens when installed within the loading pins and clevis arrangement. It is also important to align the specimens perpendicular to the loading axis in order to establish a straight crack path. This was performed with the aid of a magnetic base alignment level that was positioned on the back face of each specimen before testing. A suitable pre load of about 0.5 kN was applied to avoid movement of the pins before the test commenced. Both position and load limits were chosen based on actuator position and load range. The limits were armed before the commencement of each test to keep the machine and specimen in safe mode through the test.

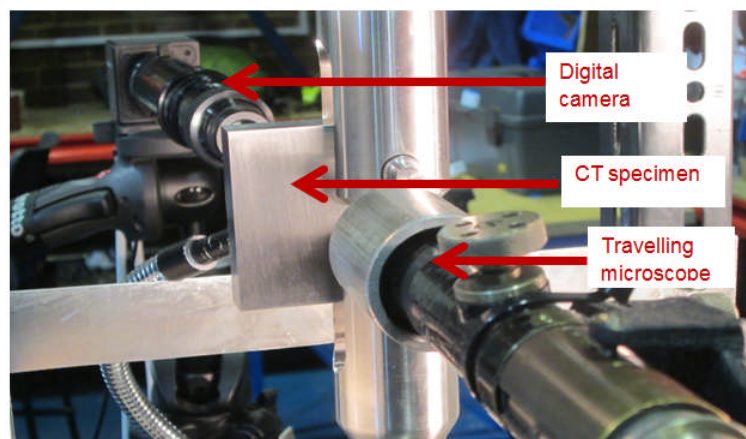


Figure 3-6 Crack length monitoring by digital camera and travelling microscope

It is also important that the maximum fatigue pre-cracking force does not exceed the force that will cause excessive plasticity at the crack tip and subsequent crack retardation during the propagation stage. This was controlled by making sure that the stress intensity factor K applied to the specimen did not exceed $20\text{MPa}\sqrt{m}$, which was sufficient for crack initiation. It was also ensured that crack initiation was monitored on both faces of the specimen, as shown in Figure 3-6. To achieve a valid pre-cracked length, a test was usually terminated when crack initiation occurred on only one side of the specimen. In such situations, the specimen and loading fixtures were carefully checked for alignment before the tests recommenced.

A constant amplitude loading waveform was programmed with the Instron wave matrix software to accommodate an envelope of 15 seconds to reach the maximum pre-cracking load as shown in Figure 3-7. An envelope of 15 seconds was also programmed before the test ends, when a change in load was required for subsequent pre-cracking.

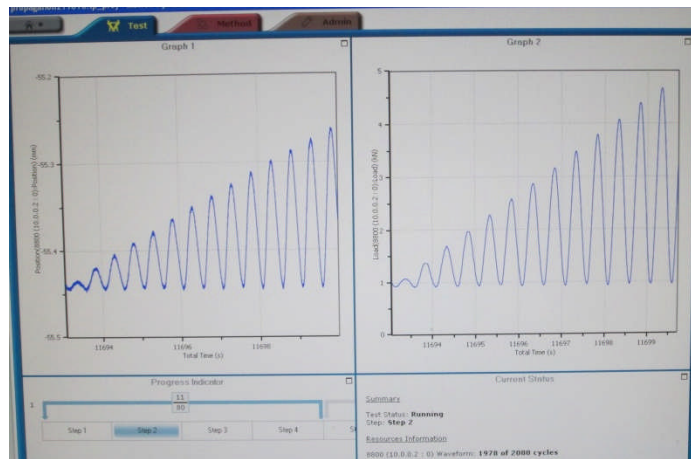


Figure 3-7 Wave matrix with envelopes

The pre-cracking procedure comprises three steps:

In step 1, the machine was programmed to ramp from the preload to the minimum pre-cracking set point of 1.7kN with a ramp rate of (0.2kN/s). This corresponds to the test minimum load. In step 2, a sinusoidal waveform with a set point of 270⁰ was applied to the specimen to achieve the test amplitude of 7.65kN. The set point was used to allow a tension-tension loading case that is relevant for testing CT specimens.

This load was gradually reduced, as mentioned earlier, until a crack length of 4mm was achieved as the initial crack length for crack propagation.

3.5.2 A new crack propagation methodology

A novel methodology for fatigue crack propagation was written using the wave matrix software developed by Instron. This methodology is named the 'loop type' wave matrix in this thesis and is an extension of the commonly used sinusoidal waveform. The loop type method was developed to reduce the significant deviations from the ACPD and strain gauge outputs, and to allow the

determination of reliable crack growth rates from the crack length measurements. The commonly used sinusoidal waveform, tagged 'single wave matrix' in this thesis, is shown in Figure 3-8. The loop type waveform method was developed based on the anticipated total number of cycles for the tests. Each loop comprises four steps, as shown in Figure 3-9, and these are repeated a number of times based on the user's judgement.

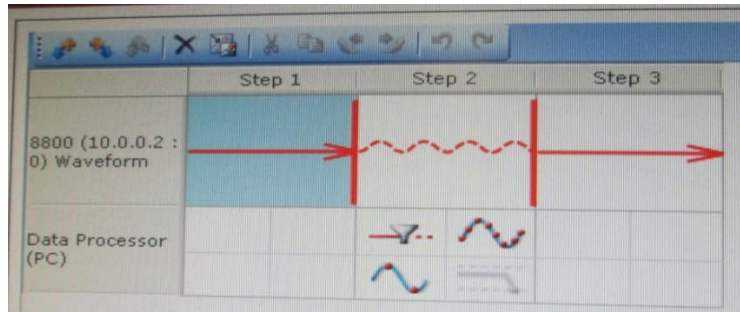


Figure 3-8 Single wave matrix

Each of the waveforms has a start and end envelope of 20 seconds. The choice of the number of cycles for each loop is attributed to the number of the desired data points and the total number of cycles for the entire test. This was decided based on a trial test for a load range of 9kN and R-ratio of 0.1. The steps in each loop are described as follows:

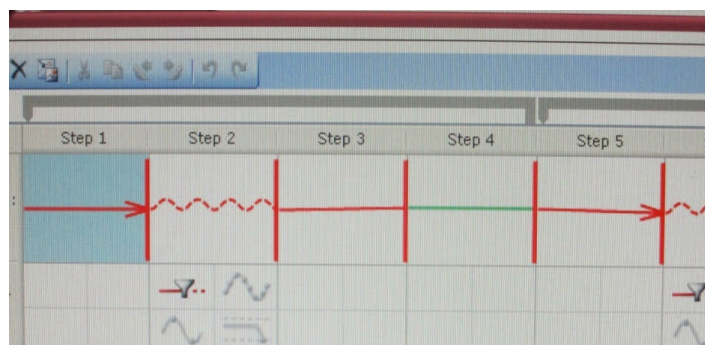


Figure 3-9 Loop type wave matrix

In step 1: The wave matrix is ramped from the preload to the set point (minimum test load) at a ramp duration of 20 seconds.

In step 2: The sinusoidal waveform is applied to the specimen at the desired number of cycles using the defined start and end envelopes respectively.

In step 3: The wave matrix was defined to ramp to the mean load such that the crack is fully opened to allow reasonable measurements from the ACPD, DCPD and strain gauge.

In step 4: The wave matrix was defined to hold at the set mean load for 20 seconds to allow ample time for the measurements. On completion of step 4, the counter is returned to step 1 to commence a new loop.

3.6 Determination of crack length by back face strain (BFS) method

The BFS method was also employed as an alternative means of correlating crack lengths with optical measurements. The advantage of the BFS method is its simplicity and relatively low cost compared to other crack length measurement methods. Optical measurements of crack lengths were performed in air to allow for calibration data for the BFS measurements that were employed for the corrosion fatigue tests. The next section describes the strain gauges installation procedure coupled with some of the precautions that were taken during the procedure.

3.6.1 Strain gauge installation and strain measurements

Linear strain gauges designated FLA-6-11, with gauge lengths of 6mm, gauge factor 2.12 and gauge resistance 120 ± 0.3 were installed on the back face of each specimen, as shown in Figure 3-10. The specimen's gauging areas were degreased using a CMS-2 degreaser to remove any contaminants that may have significant effect on the strain readings. Dry abrading was performed on the surfaces using 220 and 320 grits abrasive papers. The process was repeated with wet abrading using the M-prep conditioner 5A and the surfaces were cleaned in one direction using a gauze swab. A few drops of M-Prep Neutralizer 5A were then applied on the surfaces to ensure their suitability for strain gauge installation.

The desired locations of the strain gauges were carefully marked on the specimens using a ballpoint pen to obtain a good alignment between the strain gauge orientation and where the strain was to be measured. It was ensured that

the arrows on the strain gauges coincided with the centre line on the specimens' back faces in a direction perpendicular to the notch tip. Thin layers of cyanoacrylate adhesive were then applied on the gauge areas to facilitate the strain gauge bonding. The bonded strain gauges were thumb pressed for about 1 min to give an optimum bond performance and to achieve a suitable curing time. The installed strain gauges were left for about 15 minutes prior to further procedure. After the installation procedure, the lead wires were soldered to the strain gauges through the connecting terminals and the other ends of the wires were connected to a Vishay P3 strain indicator and recorder (see the right hand side of Figure 3-10).

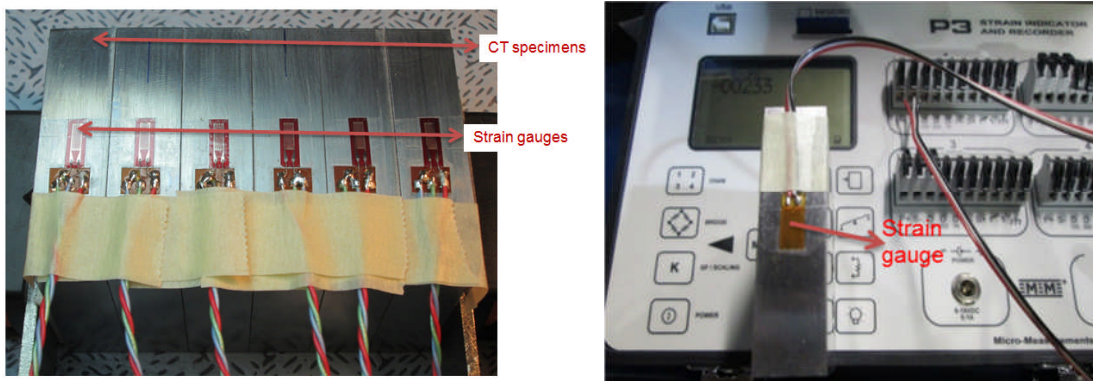


Figure 3-10 Left – Installed strain gauges, right – connection to P3 box

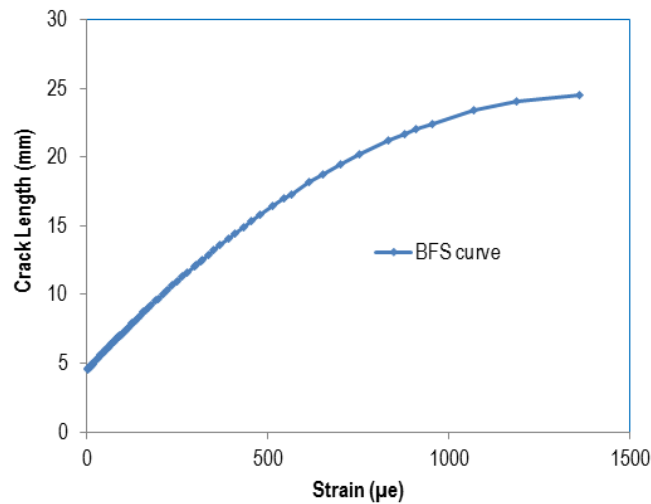


Figure 3-11 Crack length versus back face strain (BFS)

The strain values were then recorded with respect to crack lengths taken from optical measurements to derive the plot shown in Figure 3-11. A regression

model that was later developed from the strain measurements is described in Chapter 4 and was compared with other BFS relations in the literature.

3.6.2 Strain gauge coating

The loading pattern of the strain gauged specimen within the loading grips of the machine is illustrated in Figure 3-12. An important issue to consider in using a strain gauge for crack length measurements in seawater is the protection against the corrosive environment. This was achieved by coating the surfaces with an N-1 coating material. The coating material is a Neoprene rubber material with an operating temperature of -30°C to 80°C and is suitable for protection against moisture and water. Four different layers of the coating material were applied over the strain gauges and under the lead wire until a thickness of about 2mm was achieved. This is shown in Figure 3-13.

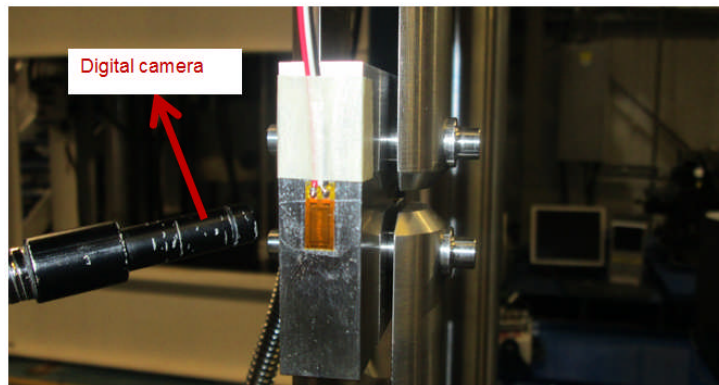


Figure 3-12 Strain gauge calibration procedure

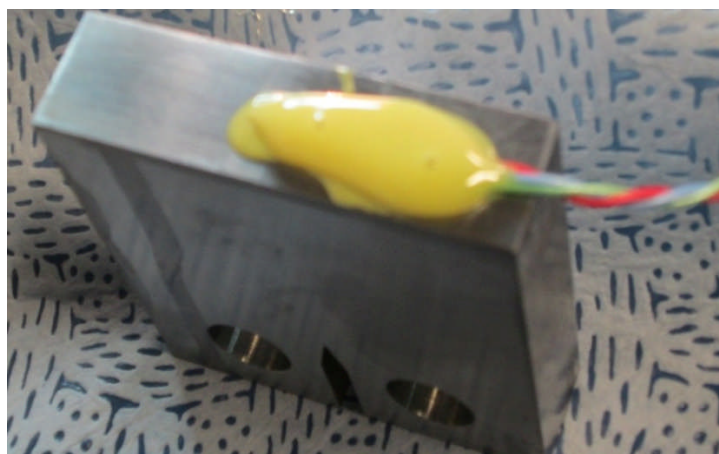


Figure 3-13 Strain gauge protection

3.7 Procedures for crack length measurement using ACPD and DCPD methods

The alternating and direct current potential drop methods have been employed in this work to measure crack lengths and to establish comparisons with strain gauges and optical measurements. These methods are briefly described.

3.7.1 The alternating current potential drop (ACPD) method

The TSC (Technical Software Consultants) ACPD equipment embedded with Long-term Inspection and Monitoring of Structures (LIMOS) software was used for measurements. The crack length monitoring using the ACPD set-up is usually carried out through movable or fixed probes. To avoid deviations in the measurements due to cyclic loads, it is important to minimize the movement of the probes during testing. This was achieved by spot welding a total of six fixed probes on the measurement areas of the CT specimens. Two probes were welded to the sides of the specimen to inject the current, two probes were placed across the notch 10mm away from each other and lastly two probes were placed reference to the uncracked surface of the material, as shown in Figure 3-14.

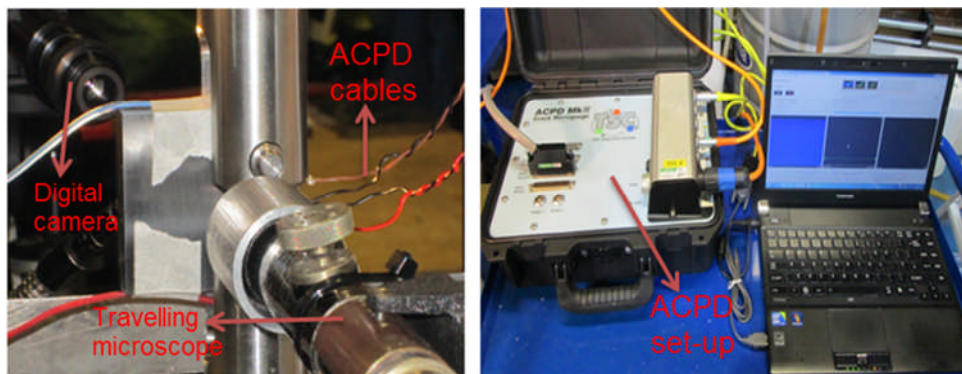


Figure 3-14 ACPD set-up

The ACPD technique relies on the alternating current flowing through the metallic material with the current flow concentrated in a thin skin close to the surface of the material [117]. The voltage taken across the crack and reference to it with respect to the current path along the crack faces is used to obtain the crack lengths, which are read directly onto the computer. Details of the process

can be found in [117]. However, observation after several trials revealed that the ACPD technique was highly sensitive to the movement of the probes and it was difficult to obtain a suitable injected field in such small-scale laboratory specimens. The crack length measurements taken from the ACPD equipment are given in Chapter 4.

3.7.2 The direct current potential drop (DCPD) method

In order to complement the deviations in result of the ACPD technique, the DCPD technique was also used as an alternative crack length measurement technique. The DCPD set-up is shown in Figure 3-15 and the calibration was performed with respect to optical measurements. This method appears more reliable than the ACPD technique. In the DCPD technique, current is injected into the test specimen and the voltages due to a change in crack lengths are accumulated.

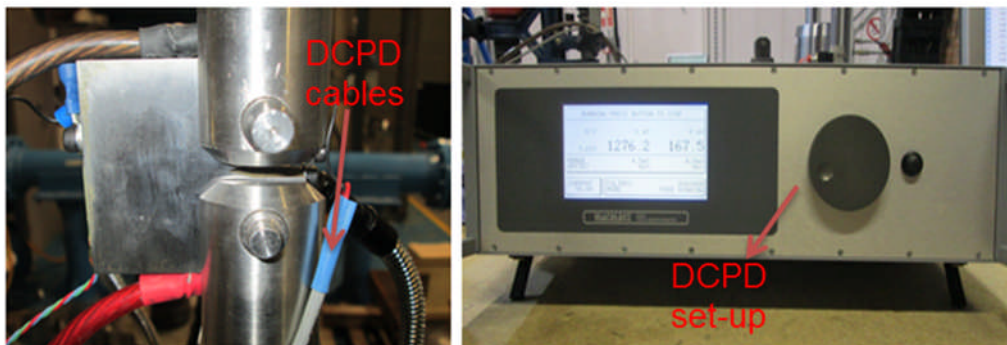


Figure 3-15 Crack length monitoring by DCPD method

Six probes were also attached to each specimen: two at the sides of the specimen to inject the current, two were placed across the notch to measure the active voltages, while two were placed at the back face to measure the reference voltages and complement a likely change in readings due to variations in temperature. It was ensured that the connected terminals were tightly fixed to the specimen to avoid variation in the injected current and voltage. Temperature difference between the test environment and the specimen may also be a source of error. However, the results from this finding indicate that lower temperatures such as those experienced in a seawater

environment did not have any significant effect on the response of the DCPD technique. The active and reference voltages were recorded with respect to a change in crack length. Active voltages were plotted as a function of crack lengths, as shown in Figure 3-16.

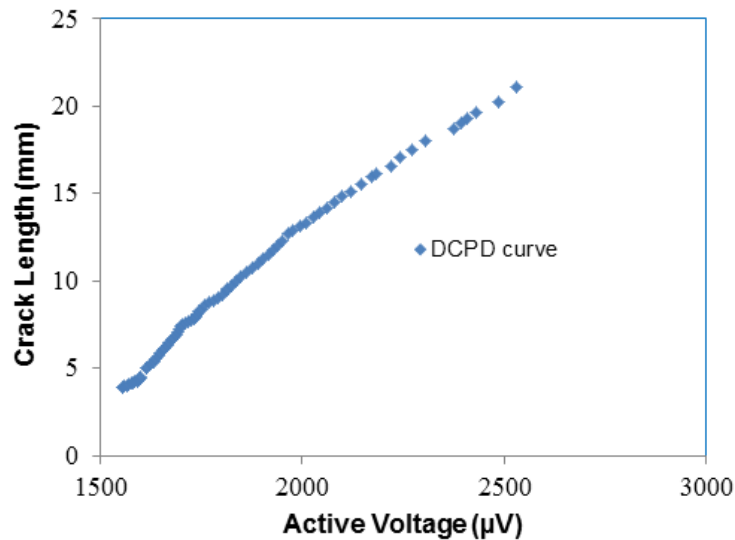


Figure 3-16 DCPD calibration curve

3.8 Laboratory simulated seawater environment

In order to simulate the condition of the North Sea, laboratory simulated seawater was used for all the corrosion fatigue tests conducted in this research. After careful consideration of previous studies reported in the literature, for example in [2], [3], artificial seawater was selected for the corrosion fatigue crack growth tests. The artificial seawater was prepared according to the specifications in ASTM D1141 [60] and was circulated past the fully immersed specimens through a purpose designed and built Perspex environmental chamber at the rate of 3 litres per minute, at a temperature of 8⁰C -10⁰C and at a pH of 7.78 to 8.2. The seawater temperature was controlled by a refrigeration unit and was monitored at the reservoir through an RS206-3738 digital thermometer. The temperature was monitored at the corrosion chamber using a hand-held infrared thermometer with the probe positioned close to the notch tip, in order to achieve the required water temperature at the crack tip. The entire corrosion system – the chamber, fittings, flow lines, reservoirs and pumps – are made of plastic to avoid the introduction of other metallic ions into the water. A

stainless steel sieve of an appropriate size was also installed on the return flow line to avoid metal debris from entering into the reservoir. The enclosed CT specimen is shown in Figure 3-17.

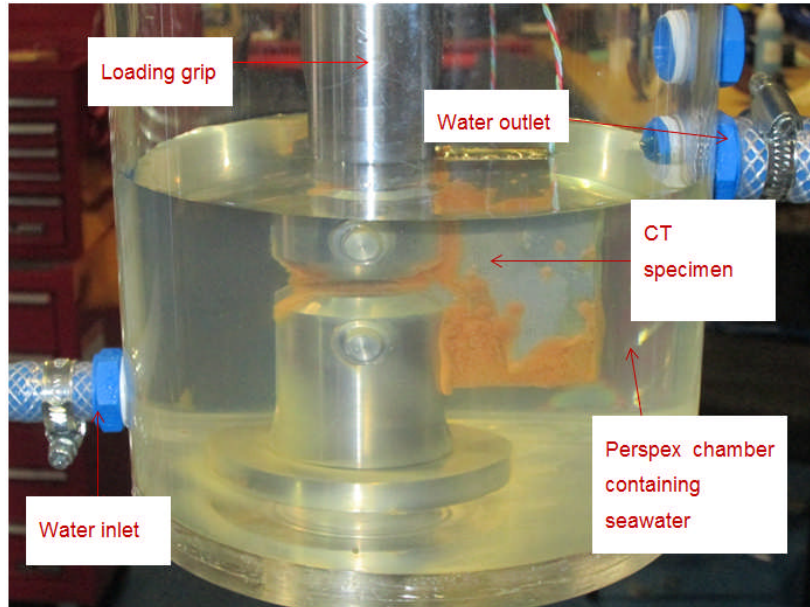


Figure 3-17 CT specimen in laboratory simulated seawater

Other specifications of the apparatus used are defined as follows:

1. A 100 litres capacity Polytank reservoir;
2. Hailer HC -100A refrigeration unit;
3. Two Alphacool VPP 655, 12 Volts pumps;
4. HANNA – HI 9828 pH meter.

The corrosion fatigue test rig is schematically shown in Figure 3-18 with the following descriptions:

1. 100kN fatigue testing machine;
2. CT specimen;
3. Perspex chamber;
4. Infrared thermometer;
5. Digital thermometer;
6. Reservoir;
7. Pumps;
8. Refrigeration unit;

The experimental procedure for the tests conducted is summarised in Figure 3-19.

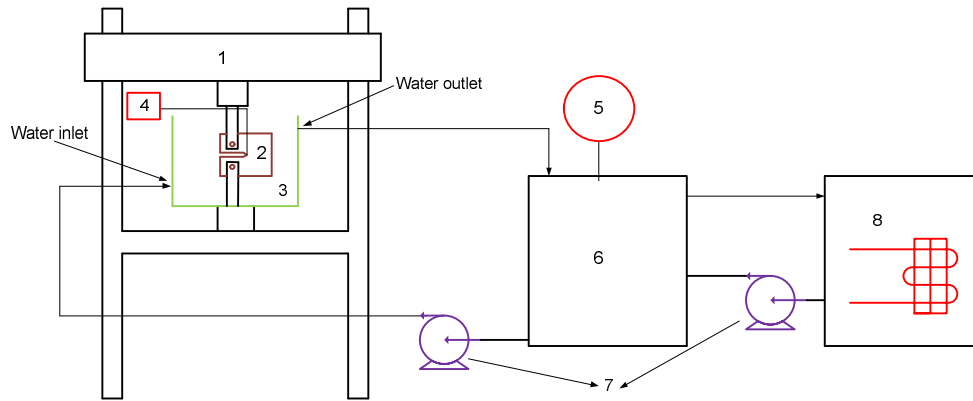


Figure 3-18 Corrosion fatigue test rig

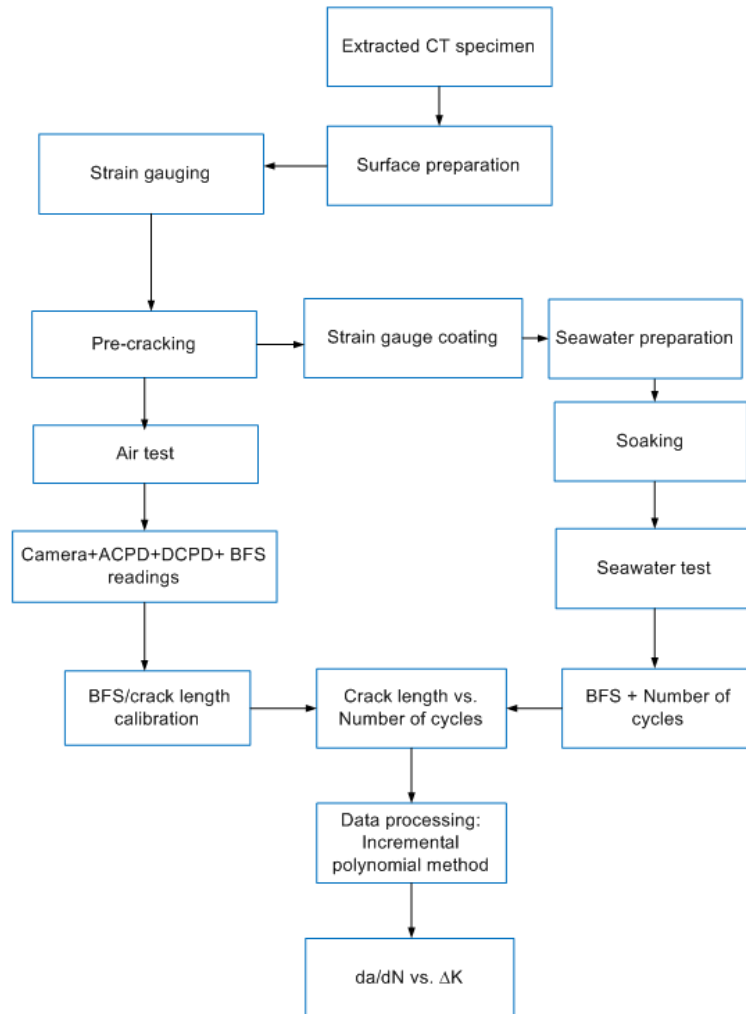


Figure 3-19 Flow chart of experimental procedure

3.9 Summary

The experimental procedure used for the fatigue crack propagations tests in air and seawater was described with respect to the associated standards. The fatigue test machine, loading fixtures and specimen preparation have been described. The procedure for the development of the new methodology that was employed for crack propagation in air and in a free corrosion seawater environment using the wave matrix software was explained. Several non-destructive crack monitoring techniques were also described with their possible source(s) of error and how to mitigate these.

4 Corrosion Fatigue Load Frequency Sensitivity Analysis

4.1 Introduction

Corrosion is a time dependent mechanism and therefore corrosion fatigue tests need to be conducted at cyclic load frequencies representative of those experienced in service. However, an understanding of dominant cyclic frequency is important when designing offshore wind structures against corrosion assisted fatigue failure.

This chapter provides a study of the dominant cyclic frequency that is relevant for testing offshore wind monopile representative materials and structures. A review of the cyclic load frequencies in offshore wind turbines is provided and this informs the choice of the appropriate load frequencies used for the corrosion fatigue tests.

The methodology used for testing has been described in Chapter 3 and the results of fatigue crack propagation tests conducted on parent materials in air and in free corrosion seawater environment are presented here for comparison. The BFS calibration described in Chapter 3 was used to derive a regression model which was also compared with other BFS relationships in the literature. Comparisons were also made with existing literature data that were obtained from different classes of steels used for offshore installations.

4.2 Review of cyclic load frequency in offshore wind turbines

Offshore wind turbines' monopile structures are slender structures with a more complex dynamic behaviour than the offshore platforms used in the oil and gas industry due to the operational loads envelope compared to what is obtainable in oil and gas platforms. The first natural frequency of offshore wind turbines is considered dominant between wave and rotor load frequencies [46]. The DNV 2013 guidelines on the design of offshore wind turbine structures [49], stipulated that the natural frequency of wind turbines lies in a narrow band between the 1P and 3P frequencies which are specifically at least $\pm 10\%$ away from the 1P and

2P/3P frequencies. 1P and 3P are referred to as the rotor frequency and the blade passing frequency for a three-bladed wind turbine.

A considerable number of researches have been conducted on the structural dynamic response characteristics of offshore wind turbine structures with the outcomes of their natural frequencies [47], [48], [118]. These studies have revealed that the support structure first-order structural dynamic response lies in the range of 0.3Hz-0.4Hz. However, this depends on a number of design factors such as water depth, monopile diameter and thickness, turbine size and soil conditions. With the rapid development of the wind sector, there are possibilities for using larger wind turbines and different types of support structures in deeper water depths with a view to increasing their generating capacities. Therefore, such wind turbines are likely to have different dynamic response characteristics. As mentioned in Chapter 2, what is not known at the moment is the extent to which corrosion fatigue crack growth rates in offshore wind farm monopile structures are influenced by cyclic load frequencies across the relatively narrow band of frequencies reported in the literature. Some of the investigations that were conducted on the structural dynamic response characteristics are discussed in this section and these outcomes informed the range of cyclic load frequencies used for testing in this work.

In Arshad and O'Kelly's work [1], it was mentioned that the first excitation frequency (1P) of the rotor with a speed of 10-20rpm lies in the range between 0.17Hz and 0.33Hz while in Andersen et al.'s [118] paper, a value of 0.12Hz-0.20Hz was mentioned for a rotor with a speed of 7-12rpm. Three design approaches that have been characterised based on soil structure interaction [118], with respect to wind turbine designs are soft-soft, soft-stiff and stiff-stiff designs. These design approaches are represented in Figure 4-1.

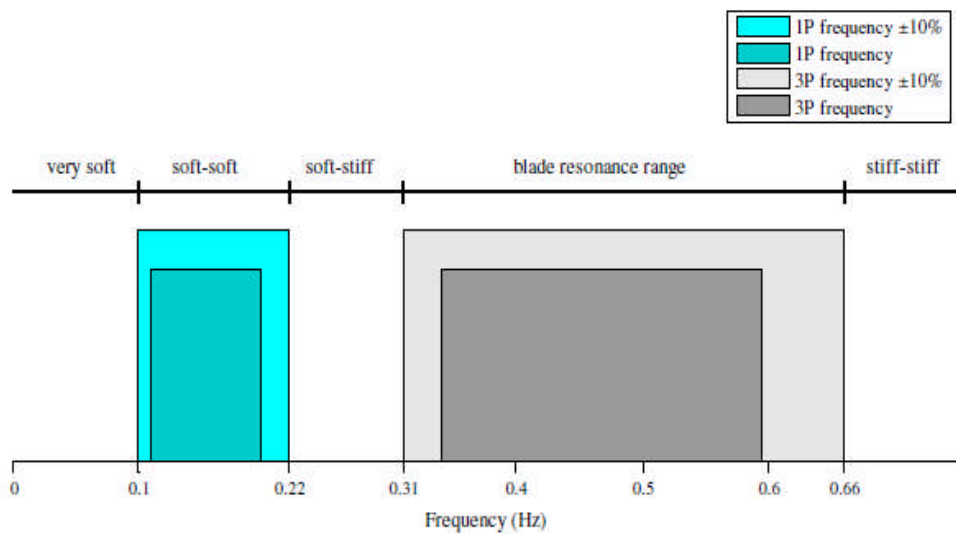


Figure 4-1 Design approaches for wind turbines [118]

For soft-soft designs, the wind and wave excitation frequency falls within this zone while for the stiff-stiff zone, the natural frequency of the tower is more than the blade passing frequency [118]. It was therefore concluded that the aforementioned regions are not suitable for the design of the structures due to the structural flexibility and rigidity associated with these regions [1]. Also, the soft-soft design approach may cause a significant reduction in fatigue life while the stiff-stiff design, which requires a more rigid support structure, may be costly. Therefore, for optimum design against resonance effect, the soft-stiff design where the natural frequency of the structure falls between frequencies 1P and 3P is generally adopted for monopile support structures in order to avoid resonance [118].

Bhattacharya et al. [48] reported that the 1P and 3P values lie in the range 0.115Hz-0.2Hz and 0.345Hz-0.6Hz respectively. In their study, it was concluded that for a 'soft-stiff' system, the global fundamental frequency of a monopile was chosen to lie between 1P and 3P values in the range of 0.22Hz and 0.31Hz. Details of this are given in [48]. Figure 4-2 describes the excitation loads acting on three different wind turbines and their responses; it can be seen that the monopile support structure response frequency is between 0.2Hz and about 0.4Hz with a peak of around 0.3Hz.

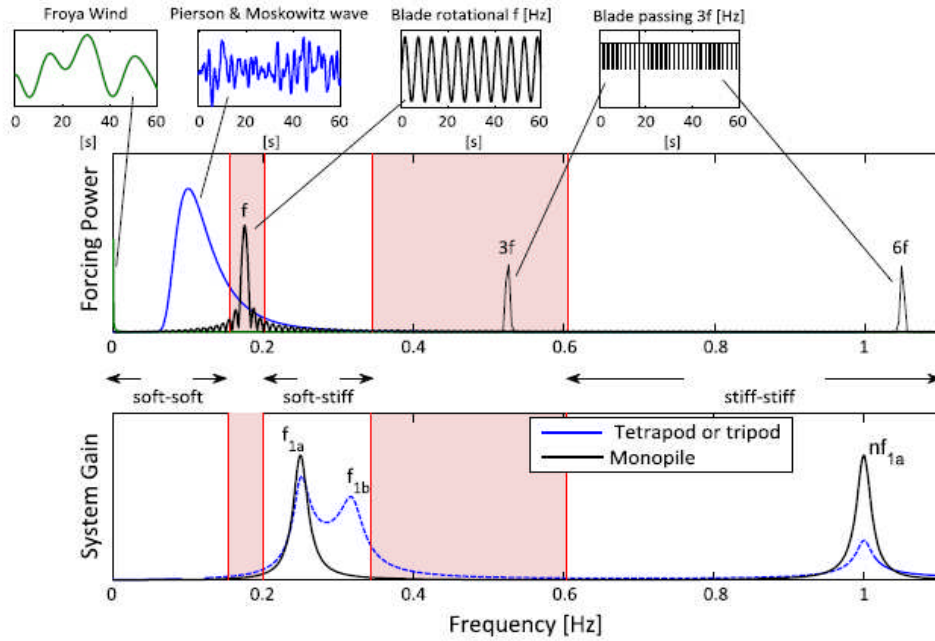


Figure 4-2 Description of natural frequency against applied load [48]

The first natural frequency of offshore wind farm monopiles was also reported to lie within the range of the rotor speed and blade passing frequency [50]. Using Horns Rev 1 Offshore Wind Farm as a reference case study, it was found that the first natural frequencies were in the range of 0.279Hz to 0.293Hz. Damgaard et al. [119], also estimated the dominant cyclic frequency of an offshore wind turbine with a tower height of 60m, in average water depth of 6/8m and supported on a monopile of about 4.3m in diameter to be 0.35Hz. The result of the investigation is shown in Figure 4-3 and it can be observed that the dominant frequency of the turbine occurs at about 0.35Hz.

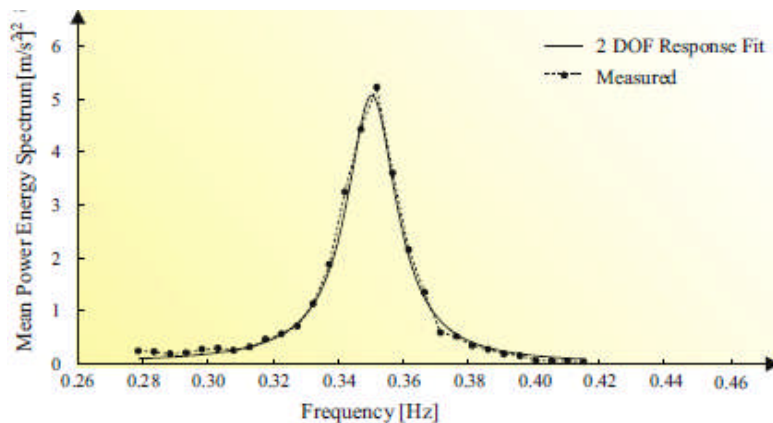


Figure 4-3 Spectral analysis on response during power generation [119]

In the Offshore Wind Turbines at Exposed Sites (OWTES) project, a frequency sensitivity study of the response of offshore wind turbine supports based on data collected at the Lely and Irene Vorrink offshore wind farms was discussed [51]. The reported dominant first natural frequencies of the wind turbines were between 0.546Hz and 0.560Hz from the measurements, while predicted values from finite element analysis were between 0.517Hz and 0.541Hz respectively. The dynamic response of offshore wind turbine monopiles based on the results of three different wind turbine model packages was studied in [52]. It was found that the dominant frequency of the system occurred at a peak of approximately 0.3Hz. This value is in good agreement with some of the earlier reported findings in this section.

Camp et al. [51] estimated the natural frequency of the Blyth (UK) Vestas V66 2 MW turbine to be 0.41Hz while Carter [120] also predicted the natural frequency of North Hoyle (UK) Vestas V80 2 MW turbine to be 0.35Hz. The soft-stiff system design approach was adopted in both cases and it can be observed that these values are reasonably close. Andersen et al. [118] also considered a simple model wind turbine supported on a monopile to estimate the natural frequency at 0.285Hz. The response of the monopile structure with respect to wind and wave forces was not accounted for in their study, as this could reveal the difference in the estimated natural frequency compared to values earlier reported in this section.

Considering the number of studies which have been reviewed in this section on the dynamic response characteristics of offshore wind turbines, it can therefore be implied that the cyclic frequency of offshore wind farm monopile support structures based on measurements and analytical investigations are averagely within the range of 0.3Hz to 0.4Hz and are dominant at 0.3Hz. In order to investigate if there is any appreciable difference in the effect of corrosion fatigue damage within the relatively narrow band of frequencies reported above, tests have been conducted in this study under free corrosion conditions using representative compact tension (CT) laboratory specimens. Air tests were also conducted at laboratory room temperature to allow for comparison with the free

corrosion tests. The results that are discussed in this chapter were obtained from crack propagation tests conducted on S355J2+N steel parent materials. Another importance of the study conducted in this chapter is to provide a point of reference in evaluating the real effect of corrosion fatigue damage in newer types of offshore structures, operating under the influence of combined wave and wind loads.

4.3 Methodology

The general methodology used for testing was described in Chapter 3 with details of the test machines and the description of various crack length measurement techniques. The methodology used for testing in air and in seawater was in accordance with ASTM E647 [115]. The description of the purpose designed and built corrosion rig has also been given in Chapter 3. The free corrosion tests were conducted at cyclic load frequencies of 0.3Hz, 0.35Hz and 0.4Hz respectively, while the air tests were conducted at 2Hz-5Hz. The load ratio used for testing was 0.1 and in order to study the effect of mean stress on fatigue crack growth, some tests were also conducted in air and in free corrosion conditions at an R-ratio of 0.5. The test matrix is given in Appendix H.

The types of waveform used for pre-cracking and propagation were described in Chapter 3. Due to the significant fluctuation that is associated with the estimation of crack lengths using the ACPD, it was anticipated that the method would not be a valid approach for the determination of crack lengths in the corrosion fatigue tests. As mentioned earlier, a novel method used for crack propagation was developed in order to overcome this difficulty and to allow the reasonable determination of crack lengths with minimal fluctuations in the output of the crack length measurement techniques. The method was also planned in a manner that permits the desired number of data points to be recorded without interrupting the tests throughout their entire duration. The performance of this new crack propagation method was checked by comparing the crack growth response with the data obtained using the most commonly used sinusoidal waveform. This method has proved reliable considering the excellent correlation which exists between the new method and the commonly

used fatigue crack propagation method. Crack growth rates were obtained from the plots of crack lengths versus the number of cycles using the seven point incremental polynomial method [115], while the stress intensity factor ranges were computed using Equations 3-1 and 3-2 respectively.

4.3.1 Development of a new regression model for the prediction of crack lengths in corrosive environment

The BFS compliance relationship was used in the study to measure crack length as a function of elapsed cycles in simulated seawater at a temperature between 8^oC and 10^oC. BFS represents the compressive strain measured at the back face of specimens along which the notch is machined, as shown in Figure 4-4. The purpose of the strain gauge is to detect the strain values as the fatigue crack propagates through the specimen. The most commonly used compliance relation to crack lengths is the crack mouth opening displacement (CMOD) technique [115]. The method involves the monitoring of crack lengths by measuring the displacement at the front face of the specimen through an inserted CMOD gauge. The standardized procedure is outlined in ASTM E647 [115] but a BFS relation to optical measurements is not included yet and has not been reported. The CMOD/BFS have been extensively used for the prediction of crack lengths in small laboratory specimens such as CT and four-point bend specimens. Deans and Richards [121] developed a BFS crack length compliance equation for CT specimens using the CMOD technique. Their proposed relationship was valid for $0.1 \leq a/W \leq 0.7$. A finite element code (FRANC2D) was employed by Riddell and Piascik [122] to develop a compliance relation for CT specimens within the range of $0.1 \leq a/W \leq 0.9$. However, their compliance equation was expressed in logarithmic form compared to other linear relations that will be mentioned shortly in this section.

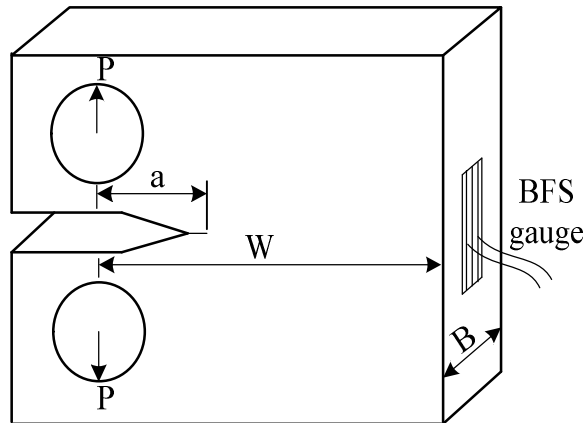


Figure 4-4 Compact tension specimen with BFS gauge

A BFS crack length calibration equation in the range $0.2 \leq a/W \leq 0.7$ was also developed by Shaw and Zhao [123] using CT specimens that were manufactured from an aluminium alloy. Huh and Song [124] reported the BFS relation for a four-point bend specimen obtained from finite element analysis and experimental studies. The validity of their calibration equation was $0.15 \leq a/W \leq 0.6$ and reasonable agreement was achieved between the two methods. Recently, Newman et al. [125] determined a BFS crack length compliance relationship for CT specimens using the FRANC2DL, a finite element code and FADD2D, a boundary element code which is valid over crack length to a width ratio of 0.1-0.95. Their results are similar to those published by Riddell and Piascik [122].

In this study, a mathematical expression has been developed for monitoring crack lengths based on optical measurement on a $W = 50\text{mm}$ specimen. The reliability of the compliance relationship here has been demonstrated for the prediction of crack lengths in a corrosive environment.

Using the approach described in ASTM E 647 [115], the relationship between the force versus displacement slope normalised for modulus of elasticity, specimen thickness and crack length for several standard specimens, has been expressed as a relationship of $E\nu B/P$ and the normalised crack length a/W [115], [125], where V is the Crack Mouth Opening Displacement (CMOD). The relationship in this work is formulated by replacing V with the absolute strain

multiplied by the specimen width and by correlating the optically measured crack lengths with BFS. The mathematical expression is represented by the polynomial equation of the form:

$$a/W = C_0 + C_1U + C_2U^2 + C_3U^3 + C_4U^4 + C_5U^5 \quad (4-1)$$

Where a/W is the crack length to width ratio and C_0 to C_5 are the regression coefficients which depend on crack length to width ratio.

$$U = \left[(|EB\varepsilon W|/P)^{1/2} + 1 \right]^{-1} \quad (4-2)$$

Where $|EB\varepsilon W|/P$ is a dimensionless BFS parameter which is represented in the literature [122]. E is Young's modulus, B is thickness, ε is strain and P is applied load. The regression coefficients for $0.2 < a/W < 0.65$ which is considered in this study based on $W = 50\text{mm}$ specimen are:

$$C_0 = 0.4427 \quad C_1 = -3.4995 \quad C_2 = 15.925$$

$$C_3 = -37.93 \quad C_4 = 39.313 \quad C_5 = -12.9123$$

Within the range of validity of the present mathematical relation, the polynomial expression fits the data point obtaining a correlation coefficient of approximately 1. The result of the strain normalising parameter is displayed in Table 4-1 as a comparison with other published compliance relations.

Table 4-1 Back face strain parameter versus a/W

a/W	$ EB\varepsilon W /P$				
	Riddell & Piascik (1998)	Deans & Richards (1979)	Shaw & Zhao (1994)	Newman et al. (2011)	Present study
0.1	1.803	-	-	1.783	-
0.15	-	-	-	2.162	-
0.2	2.71	-	3.002	2.704	2.707
0.25	-	-	3.405	3.449	3.453
0.3	4.436	4.26	4.492	4.443	3.995
0.35	-	5.56	5.999	5.742	5.227
0.4	7.422	7.17	7.868	7.437	7.093
0.45	-	9.31	10.24	9.66	9.296
0.5	12.581	12	13.461	12.62	12.376
0.55	-	15.6	18.076	16.66	16.501
0.6	22.197	20.6	24.834	22.35	23.008
0.65	-	27.8	34.687	30.74	28.840
0.7	43.003	38.3	48.787	43.83	-
0.75	-	-	-	65.93	-
0.8	100.076	-	-	107.3	-
0.85	-	-	-	198	-
0.9	420.5	-	-	460.1	-
0.95	-	-	-	1809	-

Figure 4-5 also compares this study with other reported BFS relations considering results that fall within the range of validity of the present expression. Variations in presented results may be attributed to specimen dimensions,

applied load and the properties of the material. The range of validity of the BFS relation in this work is a function of the specimen width ($W=50\text{mm}$) and the remaining uncracked ligament which has to be carefully monitored without fracturing the specimen. Deans and Richards' results agree well with the present result except at a/W ratios of 0.55 to 0.65. Riddell and Piascik's results are also similar to the present results but it could be noted that some intermediate results were not given within the range of the validity of their proposed equation.

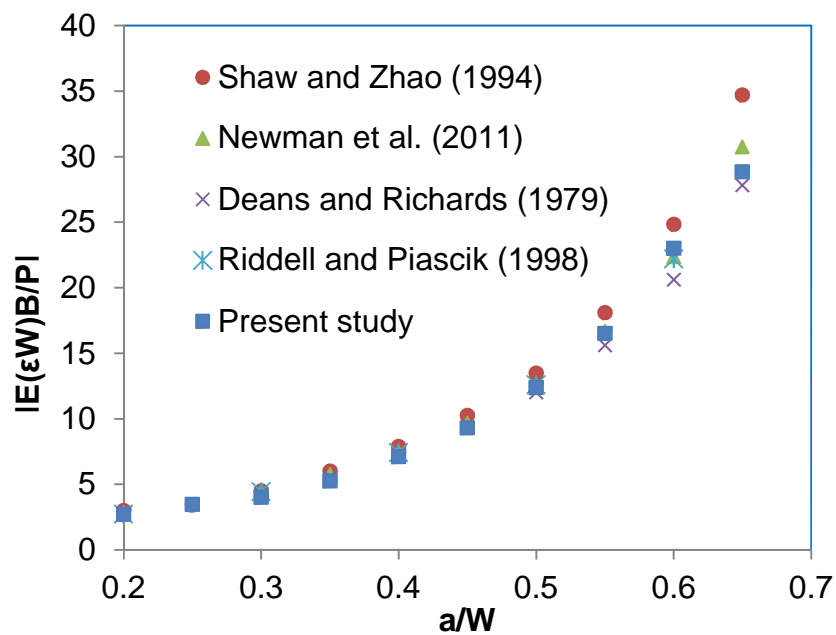


Figure 4-5 Calibration curve for crack length and back face strain

The Newman et al. [125] relation gave a better agreement based on the considered a/W ratio in the present equation. The relation here has been compared with other CMODs and numerically derived relations to verify the accuracy of the present method (Figure 4-5). The prediction of crack lengths through protected strain gauges have also been demonstrated in a corrosive environment at low temperatures using the present BFS relation to obtain good agreement with other crack length measurement methods.

In order to verify the accuracy of the BFS further, a calibration curve was produced for the estimation of crack lengths by DCPD method. The data points were fitted by a polynomial equation of the form:

$$a = -7 \times 10^{-6}v^2 + 0.0474v - 52.276 \quad (4-3)$$

Where a is the crack length and v is the active voltage. The BFS and DCPD calibration curves were developed using the previously reported test parameters in air.

4.4 Fatigue crack growth results in air and discussion

All the results that are discussed in this work were analysed using the seven point incremental polynomial method, due to its ability to numerically smooth experimental data as mentioned in chapter 3. However, the secant method was used to calculate crack growth rates for the first and last three data points of the a vs. N curves. These data points are included in the plots that are presented in Appendix G.

The results of fatigue crack growth behaviour of the S355J2+N steel in air in relation to crack monitoring methods and loading pattern of CT test specimens are shown in Figures 4-6 to 4-15. Figure 4-6 compares the ACPD technique with the optical methods for crack length measurements. The ACPD procedure was described in Chapter 3. Measurement probes were spot welded within the notch and the sides of the specimens to provide the suitable current field terminals and to permit the estimation of crack lengths across the crack front. Crack growth rates obtained with the aid of three independent crack measurement methods under the same loading conditions are shown together in Figure 4-6. It can be seen that there is good agreement between the digital camera and the travelling microscope, particularly at the start of crack growth. However, some disparities were observed between the two optical methods. This can be attributed to an error in the accuracy of the travelling microscope. Some discrepancies of up to an error of 31% were observed between the optical measurements and the ACPD method. It can also be seen that the ACPD underestimated and in some cases overestimated the optical

measurements over the entire crack lengths taken. This error could be attributed to the sensitivity of the equipment to movement of the probes and the difficulty in obtaining a suitably injected field in such small-scale laboratory specimens.

From the crack growth curves plotted in Figure 4-6, it appears that the crack length measurements obtained using the digital camera are most consistent. Therefore, the data were processed to derive the plot of crack growth rates versus the cyclic stress intensity factor range, as shown in Figure 4-7. Crack growth rates were obtained at cyclic stress intensity factor range (ΔK) of greater than $25\text{MPa}\sqrt{m}$. Since only region II of the crack propagation test was considered in the present study, the experimental outcome of the crack growth data correlates well with the Paris law. This is described by a relationship of the form $\frac{da}{dN} = 4.1 \times 10^{-12} \Delta K^{3.20}$.

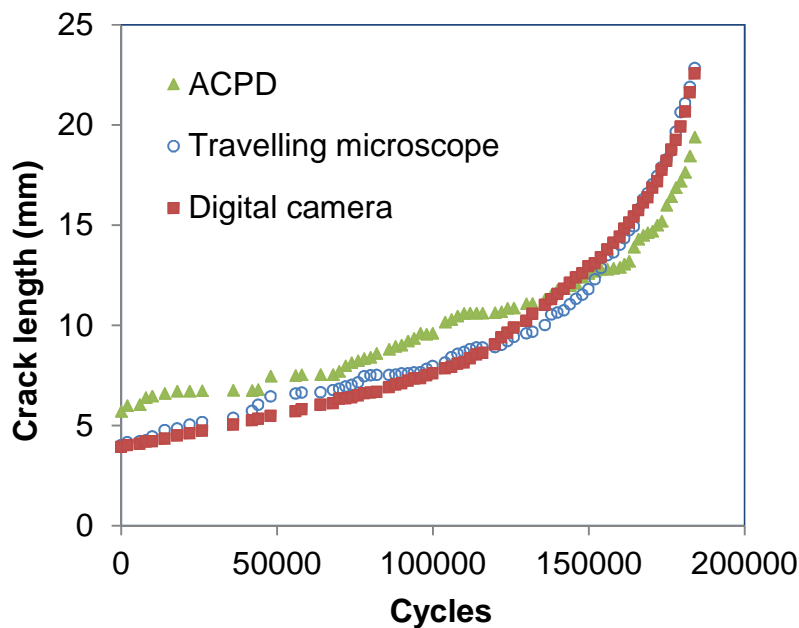


Figure 4-6 Fatigue crack growth in CT specimens ($\Delta P = 10.8\text{kN}$)

However, prior to data analysis using the LEFM approach, the plastic zone sizes (r_p) corresponding to the final crack lengths of no more than 22.5mm from the notches of the specimens were determined for both plane strain and plane stress conditions using the relationships given in [17]. The data plotted in Figure

4-7 were obtained using a load range of 10.8kN and the determined plastic zone sizes, corresponding to the final crack length were 2.2mm and 6mm for plain strain and plane stress conditions. These values are far less than the final crack length, which implies that the LEFM was still valid.

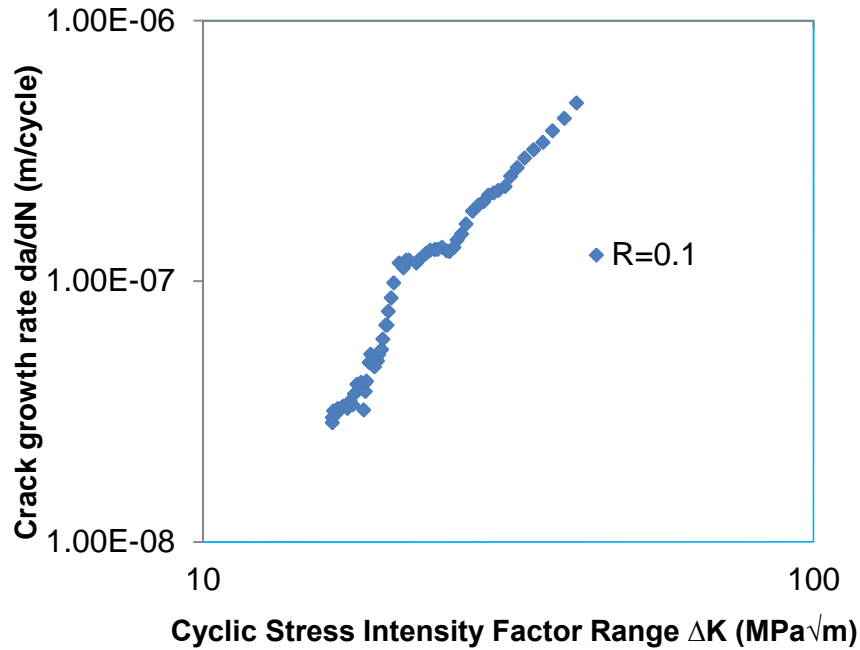


Figure 4-7 Crack growth rate in CT specimens ($\Delta P = 10.8\text{ kN}$)

The crack propagation results of the specimens tested at a load range of 9kN using the two types of waveforms described in Chapter 3; the loop method and the single wave matrix method are presented in Figures 4-8 to 4-11. The difference between the two waveforms is the accumulated holding time in the loop method when the waveform is at the mean load, a stage when the fatigue crack is fully open to allow a stable strain and ACPD measurements. As described in Chapter 3, the single wave matrix method is the commonly used uninterrupted sinusoidal waveform for fatigue crack propagation. In the loop method, a loop was created to repeat several times based on the total number of cycles for the test. In each loop, the wave matrix was programmed to hold for a few seconds at the test mean load after the desired number of cycles had been applied through the sinusoidal waveform.

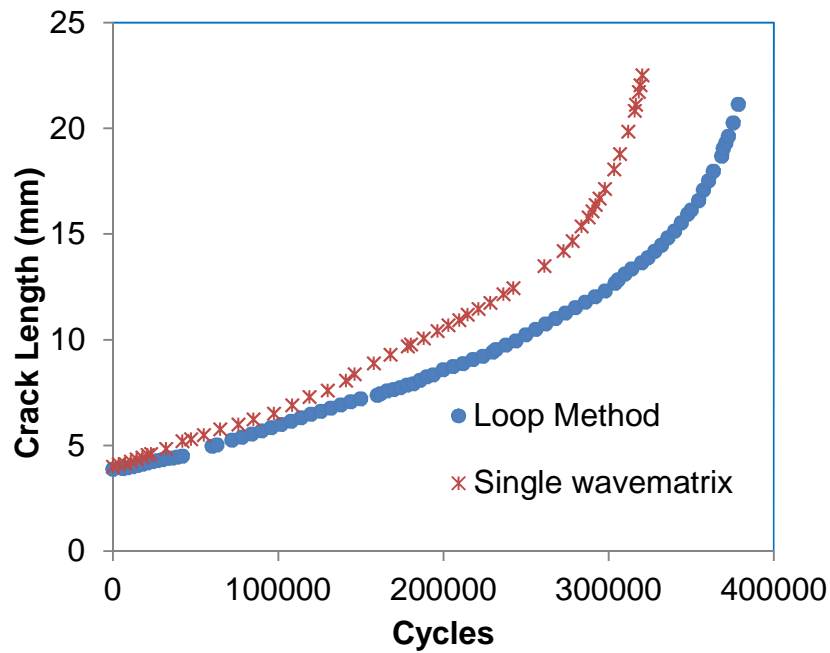


Figure 4-8 Fatigue crack growth for CT specimens ($\Delta P = 9\text{kN}$)

Crack propagation data were recorded for over 330,000 cycles for the single wave matrix method, while the specimen tested by loop control waveform extended to over 374,000 cycles, despite the similarity in loading conditions for both specimens. The disparity in the number of cycles experienced in the specimens could be attributed to the effect of accumulated waveform interruption in the loop control method, as mentioned earlier. Crack growth rates for the specimens were obtained at ΔK of $19\text{MPa}\sqrt{m}$ and $23\text{MPa}\sqrt{m}$ respectively. It can be seen, as shown in Figure 4-9, that the loading pattern of the specimens did not have a major effect on the crack propagation results. Consequently, the crack growth data for a load range of 9kN in the specimens were represented by $\frac{da}{dN} = 1.0 \times 10^{-11} \Delta K^{2.8}$ for loop control waveform and by $\frac{da}{dN} = 1.1 \times 10^{-11} \Delta K^{2.8}$ for single wave matrix. The plastic zone sizes for plane strain and plane stress conditions were determined to be 1.2mm and 3.5mm for a final crack length of 21mm. For plane strain, the above value is less than one-tenth of the final crack length. In this work, it must be mentioned that for tests conducted at a load range of 9kN and loading ratio of 0.1, the determined r_p values for a maximum crack length of 22.5mm, for both plane strain and plane

stress conditions did not exceed 1.5mm and 4.5mm. This implies that the LEFM approach was still valid considering the difference between these values and the final crack length.

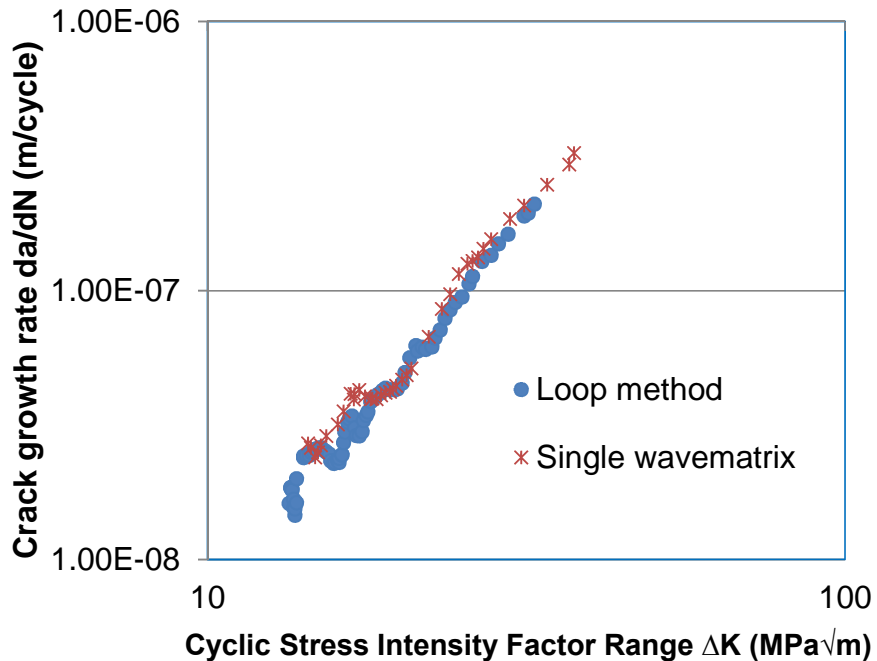


Figure 4-9 Crack growth rate for CT specimens ($\Delta P = 9\text{kN}$)

A change in load range was adopted during the crack propagation test on one of the specimens tested in air in order to study the effect of load range. The results are compared in Figures 4-10 and 4-11. An increase in crack propagation rates can be seen in these figures due to an increase in applied load range within all the applied ΔK range. This is also evident in the test data plotted in Figure 4-10; the significant effect of load range was shown by a reduction in the number of loading cycles with a factor of approximately 2 in the higher ΔP test relative to the lower ΔP . It was also observed from the experimental data that higher ΔK values were obtained at a higher load range than the lower one as should be expected. The result of the present investigation compared well with those obtained using a 37.5mm CT specimen from similar material [2], [3]. The comparison of the air tests with other steels used for offshore installations will be provided in a later section.

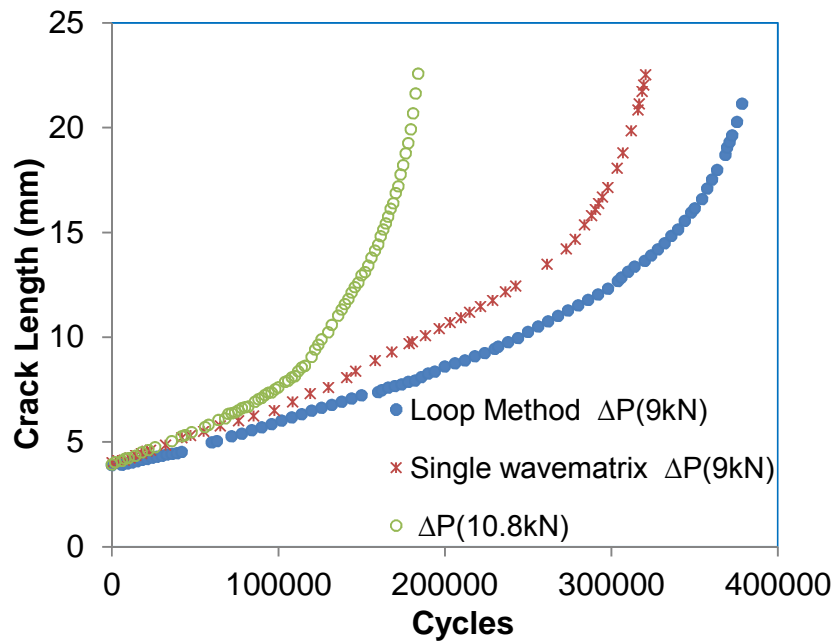


Figure 4-10 Comparison of fatigue crack growth in air at different loads

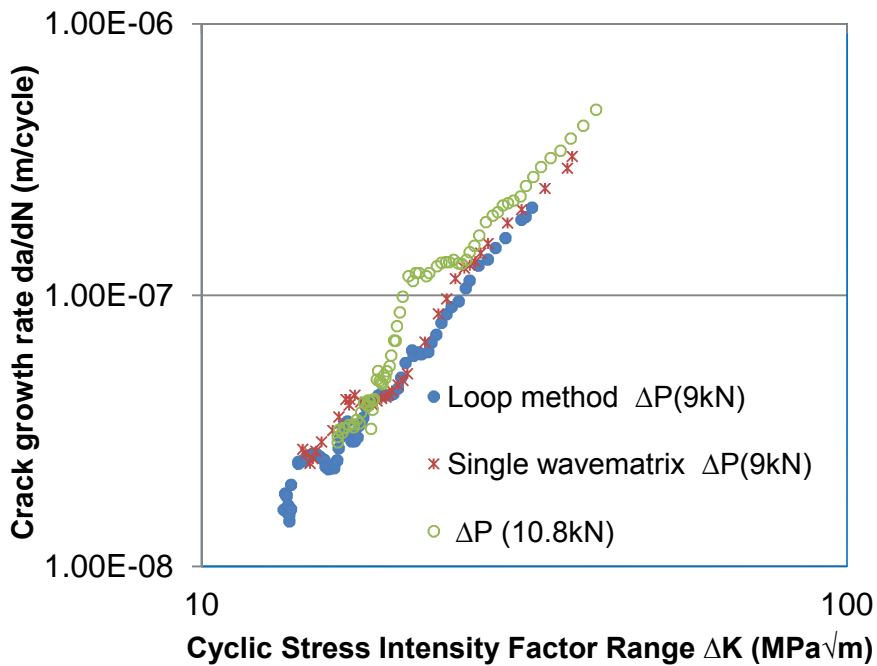


Figure 4-11 Crack growth rate in air at different load ranges

Table 4-2 summarises the loading parameters of the specimens and the material constants. The results of the tests carried out on CT specimens from the same plate and subjected to different loads and loading patterns are

presented for comparison. The notable test variable here is the applied load range (ΔP). Also included in Table 4-2 are values of the multiple correlation coefficients resulting from the line of best fit through the $\frac{da}{dN}$ vs. ΔK plots. The fitting is satisfactory, considering that all the determined coefficients correspond to R^2 values of above 95%, which represents a good fit.

Table 4-2 Loading Scenarios and material constants for S355J2+N steel in air

ΔP (KN)	R	C	m	R^2
10.8	0.1	4.1×10^{-12}	3.2	0.95
9 (Loop)	0.1	1.0×10^{-11}	2.8	0.98
9 (Single)	0.1	1.1×10^{-11}	2.8	0.97

4.4.1 Frequency effects on crack growth rates in air

It is generally believed that frequency has a significant effect on fatigue crack growth in air [73], [75]. From the results plotted in Figures 4-12 and 4-13, it can be seen that the conclusions on the frequency effect in air may be acceptable. The tests were conducted at loading frequencies of 2Hz to 5Hz and the graphs clearly show that the crack growth behaviours are parallel over the range of tested ΔK . The implication of this is that a higher cyclic load frequency can be used for crack propagation tests in air in order to save experimental time. However, as mentioned in Chapter 2, at a much higher loading frequency, the applied load may not be fully delivered on the specimen. Therefore, care must be taken in using the optimum frequency due to the interaction between applied load, frequency and the available capacity of the test machine.

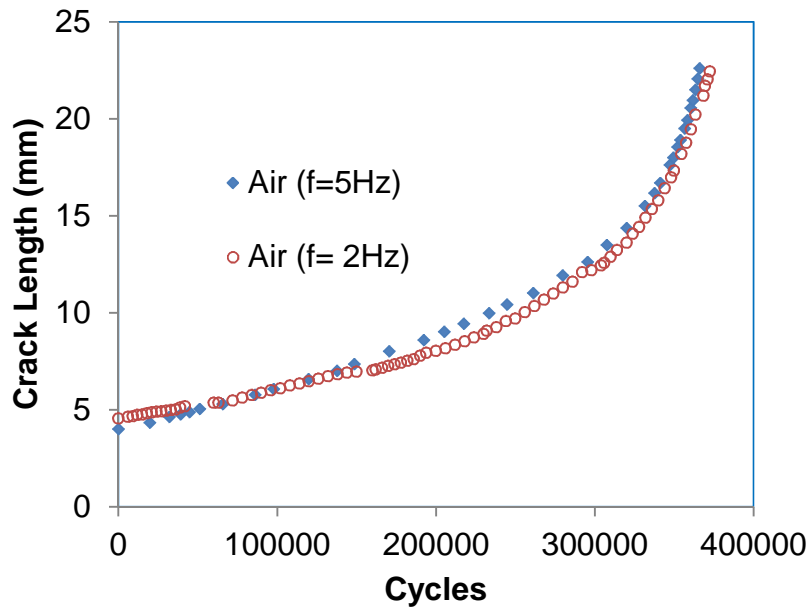


Figure 4-12 Frequency effect on fatigue crack growth in air

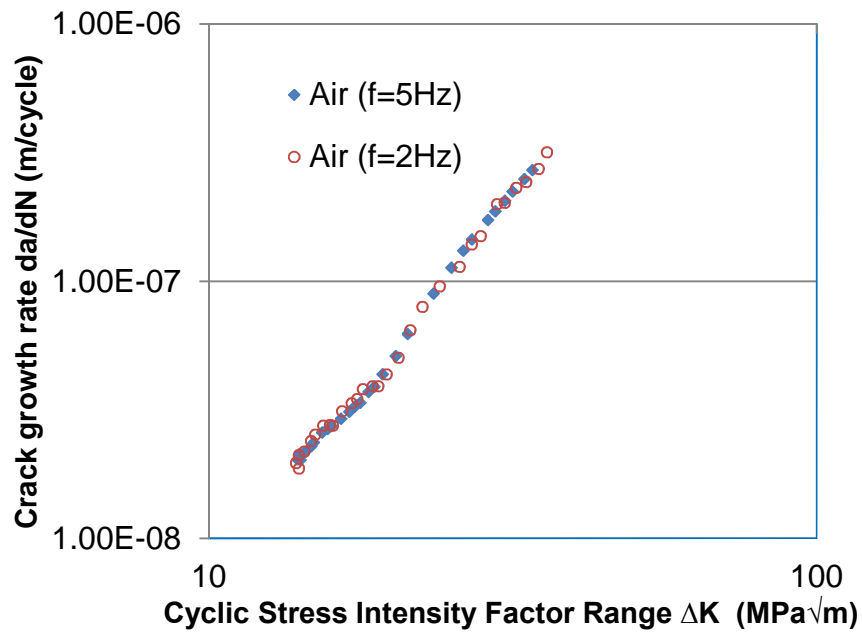


Figure 4-13 Frequency effect on crack growth rates in air

4.4.2 Stress ratio effect on crack growth rates in air

Figure 4-14 compares the load ratio effects on fatigue crack growth in air. The intention of this was to study if there is any appreciable effect of load ratio in an air environment. It is anticipated that the crack growth rates will be higher at a

higher stress ratio ($R \geq 0.5$) than at a lower one due to the associated stress level and a crack closure free effect which occurs at higher stress ratios. The effect of the stress ratio was not dominant until the stress intensity factor range approached nearly $15\text{MPa}\sqrt{m}$. At this level, the crack growth rates did not increase by more than a factor of 2 over the ranges of ΔK . However, at a stress ratio of 0.5, a relatively lower initial ΔK values were observed compared with those obtained at a stress ratio of 0.1. A negligible effect of stress ratio on fatigue crack growth in BS4360 50D steel in air was reported in Reference [13] and a slight effect of stress ratio was also observed in Reference [2] in a study of fatigue crack growth rate of BS4360 50D steel in air. Judging by the crack growth response of the material, as shown in Figure 4-14, coupled with the derived material constants at both stress ratios, the effect of stress ratio in air can be considered marginal. The plastic zone sizes determined for the tests conducted at an R-ratio of 0.5 were 0.8mm and 2.6mm for a final crack length of 22.35mm.

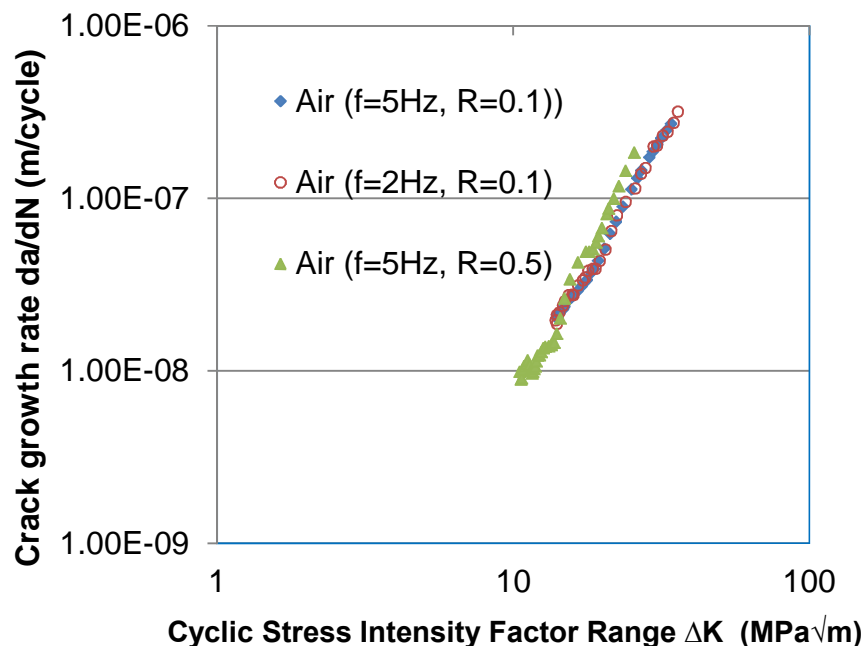


Figure 4-14 R-ratio effect on crack growth rates in air

Figure 4-15 shows the plot of the mean air data. It can be seen that there is consistent crack growth behaviour over the stress intensity factor ranges. The

crack growth rates increased in a monotonic manner and the closely matched nature of the data points indicates the test results are consistent and repeatable. The mean data is represented by $\frac{da}{dN} = 9.1 \times 10^{-12} \Delta K^{2.9}$.

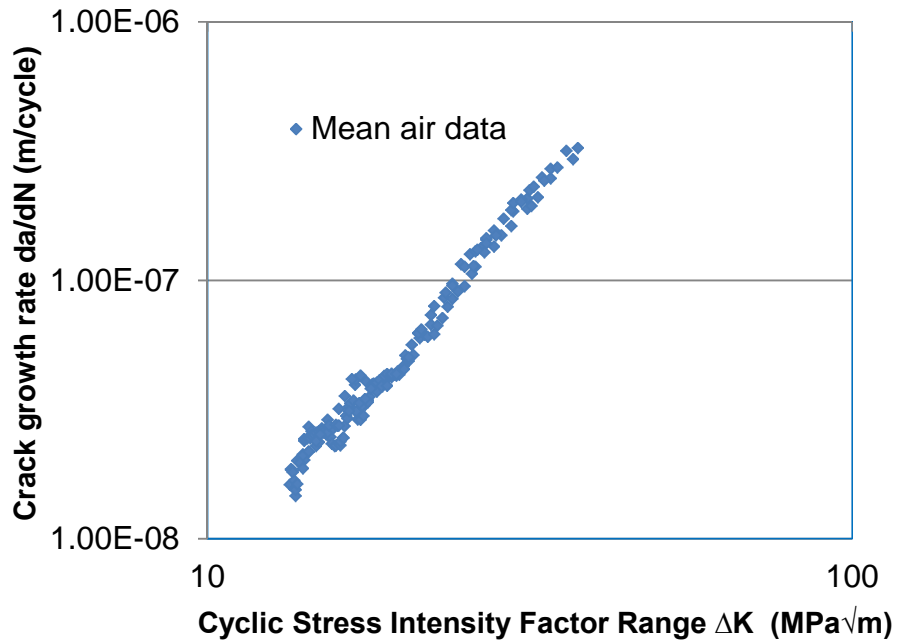


Figure 4-15 Mean crack growth rates in air

4.5 Fatigue crack growth results in seawater and discussions

Corrosion fatigue crack propagation tests were conducted on parent materials under free corrosion conditions at a load range of 9kN and 12kN, loading frequencies of 0.3, 0.35 and 0.4Hz and loading ratios of 0.1 and 0.5 respectively. The primary reason for the choice of these loading frequencies was to study their sensitivities to fatigue crack growth rates and to establish the most appropriate test frequency for subsequent corrosion fatigue tests. The selected range of test frequencies was also based on the review that was provided in section 4.2 on the structural dynamic response characteristics of offshore wind turbines. Tests under a free corrosion condition using the representative loading frequency may provide a better understanding of the real effect of corrosion on monopile structures so that the structures can be operated close to the actual design life. Representative free corrosion condition tests results are discussed in this section.

To establish the accuracy of the crack monitoring methods used in this work further, the BFS and DCPD crack growth curves are compared with optical measurements in air, as shown in Figure 4-16. It can be seen that the response of the three crack monitoring methods agree well with each other.

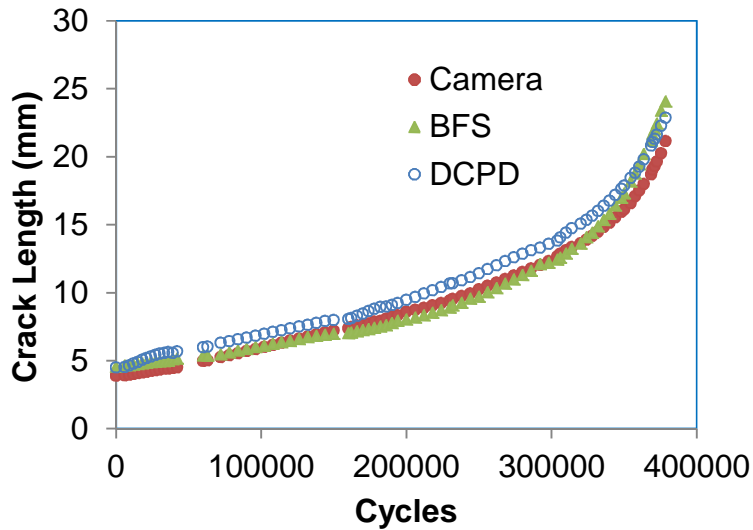


Figure 4-16 Comparisons of crack measurement methods in air

Crack growth data obtained from one of the tests conducted using the DCPD and BFS are compared, as shown in Figure 4-17. It can be seen that there is an excellent agreement between the two curves over all the ranges of loading cycles.

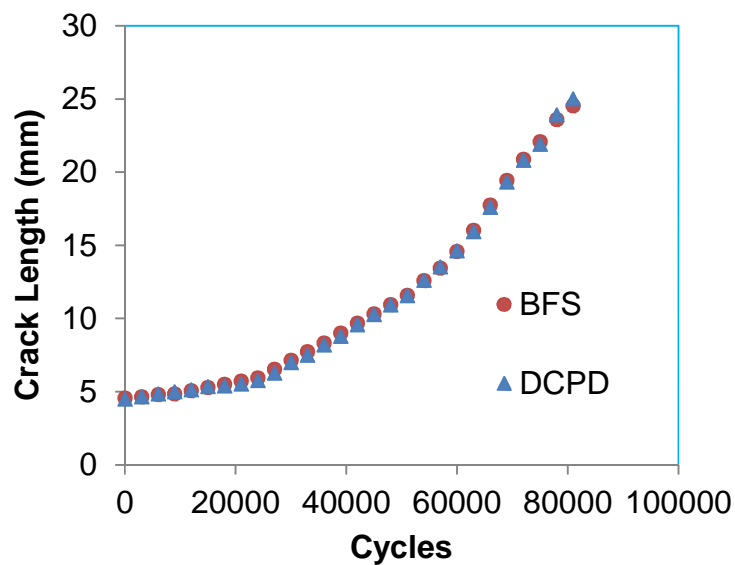


Figure 4-17 Comparisons of DCPD and BFS responses

Seawater tests conducted at loading frequencies of 0.3Hz, 0.35Hz and 0.4Hz are plotted together and presented in Figures 4-18 and 4-19 as plots of crack lengths versus number of cycles, and crack growth rates versus the cyclic stress intensity factor ranges. The effect of different load frequencies and load ranges are compared on the measured crack growth rates in order to establish the sensitivity of the crack growth rates to the test load frequencies. Similar crack growth behaviour is demonstrated from the three load frequencies especially at lower load cycles, as shown in Figure 4-18. It can be seen that the crack propagation data generated from the test frequencies are parallel over a substantial range of load cycles but this was obvious between the tests conducted using load ranges of 9kN.

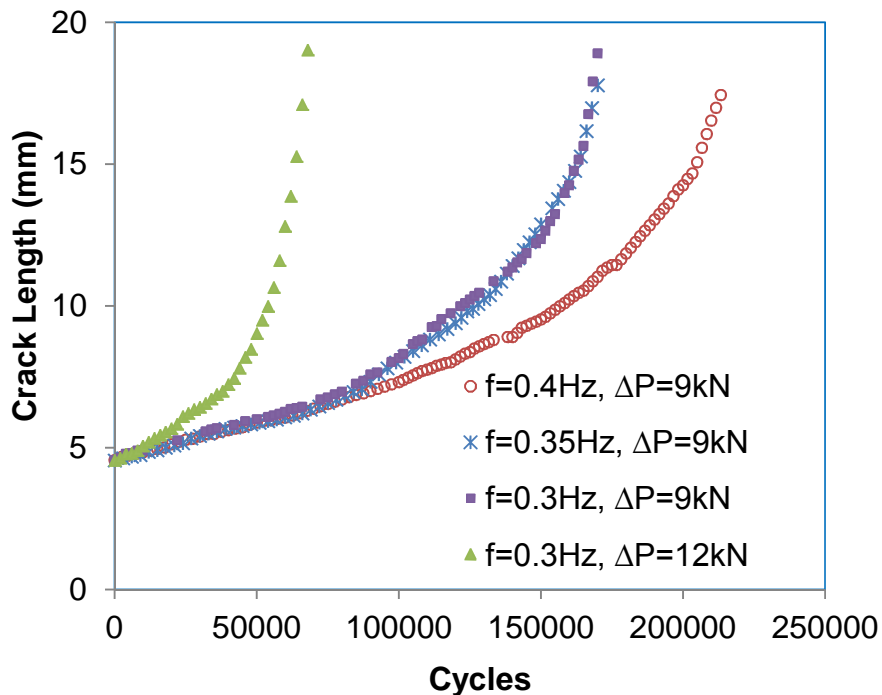


Figure 4-18 Fatigue crack growth in seawater under different loading conditions

The tests conducted using the frequency of 0.3Hz and 0.35Hz also exhibited similar crack growth behaviour with a marginal difference over the range of loading cycles. The profound effect of the seawater environment and test frequency was not dominant at 0.35Hz and 0.3Hz for tests conducted at a load range of 9kN until nearly 30% of the total number of cycles was expended compared to what was observed at 0.4Hz. Since corrosion is a time dependent

phenomenon, its effect on crack advancement depends on the time and rate at which the crack tip is exposed to the electrochemical elements. Therefore, such behaviour could be attributed to the effect of seawater which progressively manifests at an increased crack opening displacement and subsequent increase in ΔK at each fatigue cycle. At a load range of 9kN and load frequency of 0.4Hz, the number of cycles required to complete the test was higher than at a frequency of 0.3Hz as shown in Figure 4-18. However, the time required to complete the test at a load frequency of 0.3Hz was approximately half a day longer than at a load frequency of 0.4Hz.

However, at a frequency of 0.3Hz using a load range of 12kN, the testing time was much reduced compared to the test duration using the lower load range, as would be expected. The results generally revealed that there was a considerable reduction in fatigue propagation life, up to a factor of 3 in specimens tested at a higher ΔP , at a frequency of 0.3Hz, than the ones tested at a lower ΔP at the same loading frequency. This implies that the only approach to accelerating corrosion fatigue tests may be to increase the stress level. A higher loading frequency would likely result in similar crack growth rates as those measured in air, as mentioned in Chapter 2. A previous study [2] also mentioned that crack growth rates in BS4360 50D steel at a higher load frequency in seawater were similar to those measured in air. This behaviour was due to the lesser time available for the corrosion mechanism to occur at the crack tip at a higher loading frequency.

In Figure 4-19, the crack growth rates for the examined four cases are plotted together as comparisons. At lower ΔK , the crack growth rates are similar but at higher ΔK , the crack growth rate at a frequency of 0.3Hz and 0.35Hz were not up to twice that of 0.4Hz. At an intermediate ΔK of $18\text{MPa}\sqrt{\text{m}}$, the crack growth rates were also found to be similar regardless of the difference in test conditions. The overall comparison suggests that there is no marked difference in crack growth rates within the tested range of frequencies irrespective of the load ranges used, as shown in Figure 4-19. This was probably due to the relatively narrow range of the cyclic load frequencies used for testing.

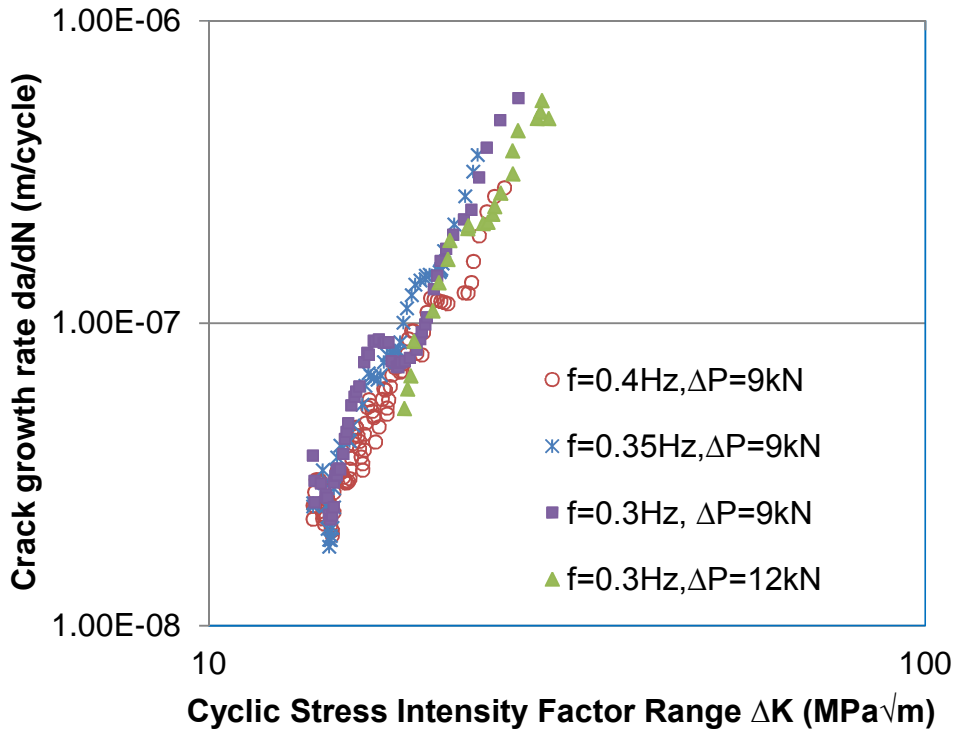


Figure 4-19 Crack growth rates in seawater under different loading conditions

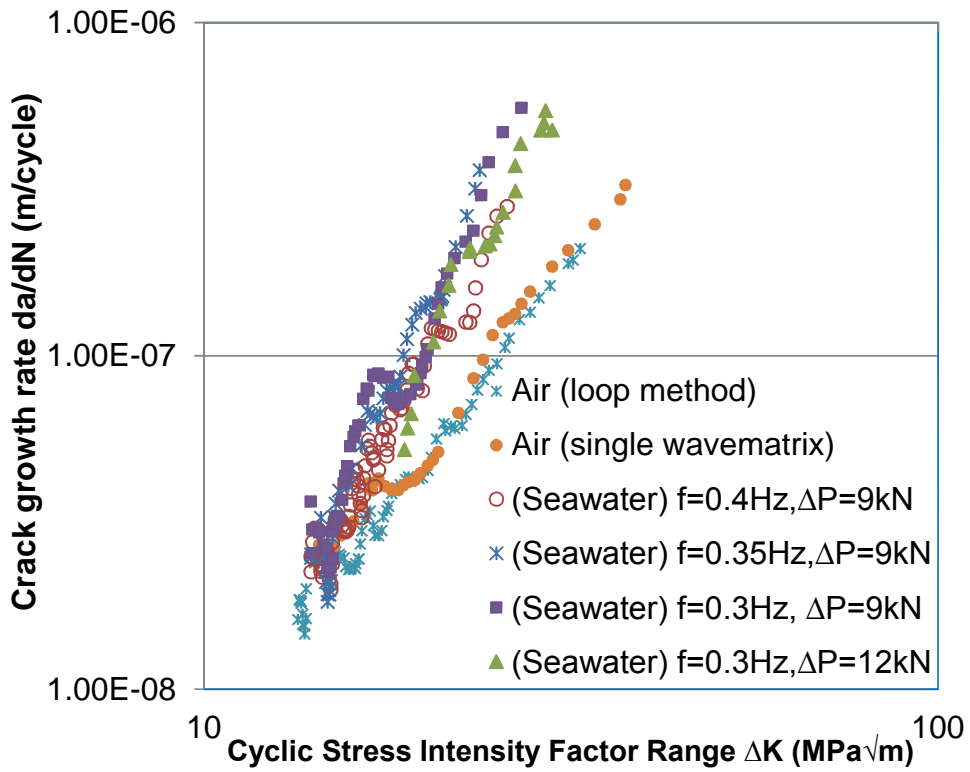


Figure 4-20 Comparison of crack growth rates in air and seawater

The air and seawater test results are compared in Figure 4-20. The results generally revealed that crack growth rates are faster in seawater than in air across all the stress intensity factor ranges tested. This is also evident in the overall number of cycles consumed in the seawater tests which were approximately half of the time consumed in air. From the data comparison, it was found that at higher ΔK , crack growth rates in seawater were higher than in air but at lower ΔK , the difference was not significant. The underlying reason for this could be attributed to the time dependent phenomenon of corrosion fatigue damage which increases as the crack propagates through the specimen.

At ΔK $13\text{MPa}\sqrt{\text{m}}$, the $\frac{da}{dN}$ in seawater was approximately twice that of air. The results show the crack growth plateau in the range of $13\text{MPa}\sqrt{\text{m}}$ - $25\text{MPa}\sqrt{\text{m}}$. At higher ΔK , the crack growth rate increased by a factor of approximately 4 in seawater than in air. This was observed at ΔK of $24\text{MPa}\sqrt{\text{m}}$ in both cases. It can also be observed that the specimen tested in seawater exhibited a higher crack growth rate at the start of the experiment at approximately the same ΔK as in air. The explanation for this may be due to the effect of the pre-exposure period of 48 hours to the corrosive environment prior to testing. In other words, the time dependent accumulation of the simulated salt water was expected to have some effect on the crack tip of the specimens prior to the start of the experiments. Generally, from the seawater data, it was observed that better crack growth response was achieved due to the reduction in experimental scatter, compared to results from the similar material [2], [3].

Higher initial ΔK values were also found in the seawater tests compared to those obtained in air. In BS4360 50D steel, a higher ΔK_{th} was also reported for at R-ratio of 0.1 in seawater [126]–[128]. This effect was attributed to crack closure effects at lower R-ratios and particularly at an R-ratio of 0.1 but at an R-ratio of 0.7, the effect disappeared and produced the same ΔK_{th} as in air. This may be due to the fact that for tests conducted at a higher R-ratio, the crack surfaces do not touch during the unloading part of the stress cycle.

4.5.1 Stress ratio effect on fatigue crack growth in seawater

The effect of stress ratio was also studied in free corrosion conditions, as shown in Figure 4-21. It can be seen that the stress ratio of 0.5 has significantly lower ΔK values and this resulted in higher crack growth rates than tests conducted at an R-ratio of 0.1 across the tested stress intensity factor ranges. It can be seen that the curves are parallel to each other. The mean data in seawater for tests conducted at a stress ratio of 0.1 can be represented by $\frac{da}{dN} = 4.1 \times 10^{-13} \Delta K^{4.2}$, while the data obtained at a stress ratio of 0.5 can be represented by $\frac{da}{dN} = 3.1 \times 10^{-14} \Delta K^{5.6}$. This implies that the effect of stress ratio is more dominant in seawater than in air due to the interaction between the stress ratio, loading frequency and the environment. From a design perspective and considering the role of the corrosion fatigue crack growth mechanism in the presence of tensile residual stress or higher mean stress, the material data determined at a higher stress ratio may be most conservative data for estimating lifetime to be expected for offshore installations.

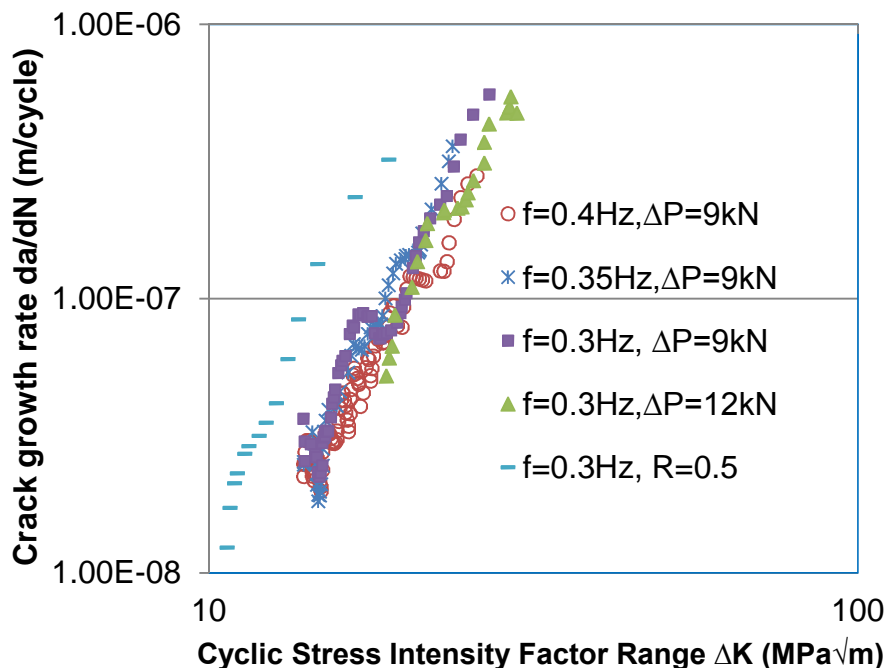


Figure 4-21 R-ratio effect on crack growth rates in seawater

In Figure 4-21, the calculated plastic zone sizes at an R-ratio of 0.5 for a final crack length of 22.5 were 0.9mm and 2.7mm for plane strain and plane stress conditions. These values are similar to those determined in air at an R-ratio of 0.5 as discussed in section 4.4.2; and are quite lower than those obtained for tests conducted at an R-ratio 0.1.

In Figure 4-22, the mean air data line is compared with the crack growth rates in seawater. Included in the figure is the upper bound line which is six times the mean crack growth rates in air. It can be seen that the majority of the data points are encompassed by the upper bound curve. This is in agreement with a previous study on the effect of mean stress on fatigue crack growth [2]. It was found that the effect of seawater on crack growth rates in BS4360 50D steel was dominant at the higher R-ratio ($R = 0.5$ to 0.7) to give an upper bound of approximately six times the average growth rates in air, as shown on the right of Figure 2-7.

Figure 4-23 compares the crack growth rates in air and seawater at an R-ratio of 0.5. It can be seen that the crack growth rates are higher in seawater than in air across all stress intensity factor ranges tested. At a lower ΔK , below $12\text{MPa}\sqrt{m}$, crack growth rates in seawater were nearly three times higher than in air, while at a higher ΔK , crack growth rates were six times higher in seawater than in air. This implies that the presence of high mean stress increased the crack growth rates in seawater over those in air at an R-ratio of 0.1 by nearly a factor of 2. The underlying reason for this is probably due to the associated crack closure free situation at a higher R-ratio. Also, with the interaction of the loading frequency, corrosive environment and the larger crack tip exposure area at a higher mean stress, it is therefore expected that the crack growth rates will be significantly influenced in seawater, more than in air.

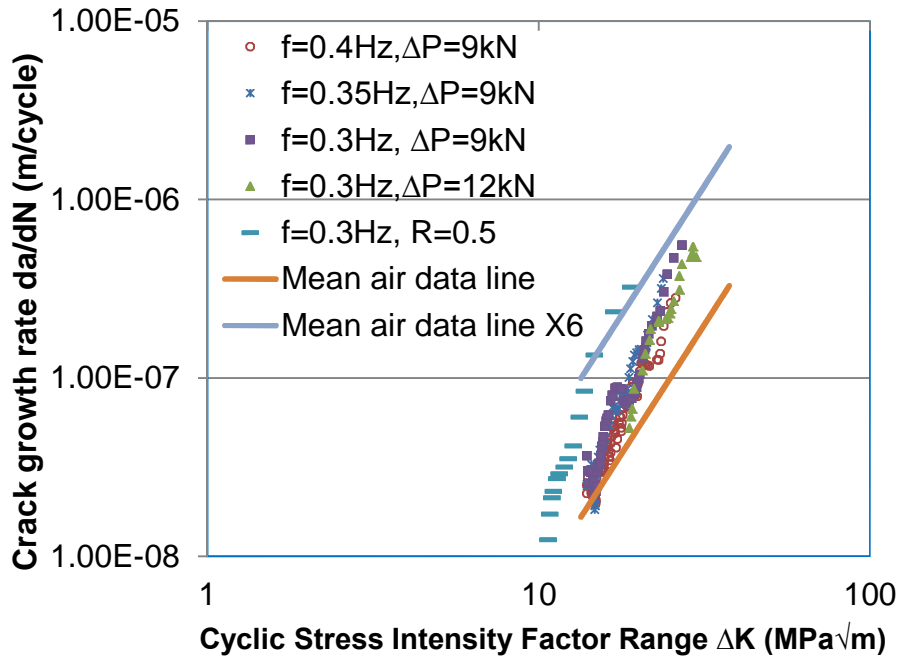


Figure 4-22 Crack growth rates in air at R-ratio of 0.1 to 0.5

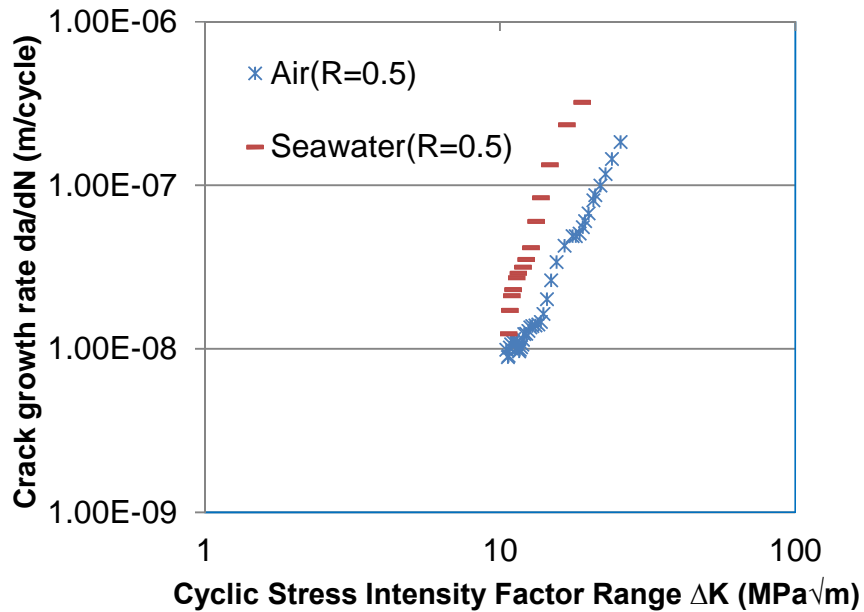


Figure 4-23 Crack growth rates in air and seawater at an R-ratio of 0.5

4.6 Comparison of test results with literature data

Fatigue crack growth data have rarely been obtained in free corrosion conditions under representative wind and wave load frequencies such as those

reported in this work and it should be mentioned that the environmental condition under a free corrosion potential is likely to be different from a free corrosion condition. This is because a free corrosion potential is likely to be associated with hydrogen production due to cathodic reactions. This may result in some levels of hydrogen embrittlement at the crack tip, a proportion of which depends on the level of protection and the type of material. It has been mentioned that the mechanism associated with crack growth rates in a free corrosion condition can be explained by anodic dissolution [11], [13], [129]. However, the fact that a free corrosion condition is primarily associated with the anodic dissolution of steels by corrosion does not imply that the same process will occur under a free corrosion potential. This requires careful consideration when results are being interpreted. Also, previously published data, for example in [2] and [3] have categorised different levels of applied CP of -0.6V, -0.85V and -1.3V potentials with reference to Ag/AgCl electrodes as free corrosion, normal protection and over protection potentials respectively. Crack growth rates at all the levels of potentials, including free corrosion potential were associated with hydrogen embrittlement [3]. As mentioned in Chapter 2, modern steels such as S355J2+N now have improved properties such as toughness and weldability compared with the BS4360 50D steel, due to the reduced levels of carbon and the additions of other elements. This is an important factor that should be noted when results are compared with data from other sources.

However, data taken from the literature, a number of which have been discussed in Chapter 2, are compared with the results of the present investigation in this section. Comparisons are also made with the BS7910 recommendations [130]. The results comparison is discussed with respect to data obtained from offshore structural steels with yield stresses in the region of 350MPa-900MPa. These steels have been categorised into conventional steels (yield strength of about 350MPa), HSS (yield strength of 400MPa-600MPa) and extra HSS used in ships and jack-up platforms (yield strength of 700MPa-900MPa) [54]. Data obtained in air, under free corrosion conditions/potential and those obtained under CP will be presented for comparison.

4.6.1 Discussion of medium strength steels data

Figure 4-24 compares the results fatigue crack response of the steels used in this work with other similar medium strength steels such as BS4360 50D and C-Mn-V steels [2], [3], [62], [73], [81]. The data plotted in the left of the figure are the mean air data obtained from this work at an R-ratio of 0.1. The air data are plotted on the left of Figure 4-24 while the seawater results are compared on the right. It can be seen that the crack growth trend of the S355J2+N steel in air is similar to the other data plotted over the stress intensity factor ranges. However, the results of Fukuda et al. [81] and Havn and Osvoll [73] deviate from the present results particularly at lower ΔK and resulted in bi-linear trends, with the Havn and Osvoll data having approximately twice the crack growth rates obtained in S355J2+N steel at $\Delta K > 27 \text{MPa}\sqrt{\text{m}}$. The response from S355J2+N steel also shows a significantly reduced scatter compared to Thorpe et al.'s [2] data. The use of the better fatigue data acquisition techniques of today compared to those used in the 1970s and 1980s may be responsible for the reduction in experimental scatter.

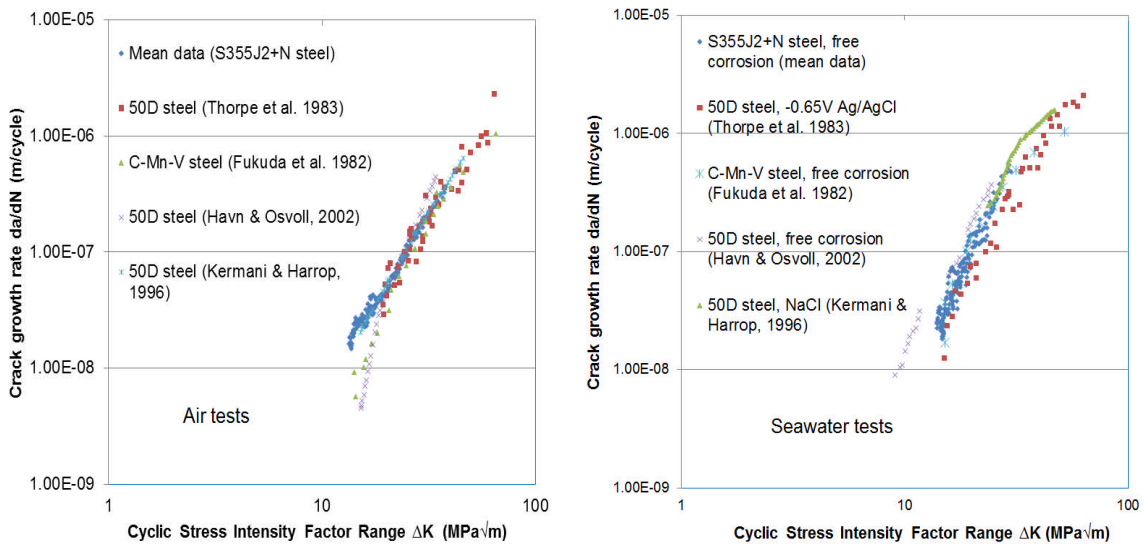


Figure 4-24 Comparison of crack growth rates in air and seawater with medium strength steels

The crack growth rates in seawater plotted on the right of Figure 4-24 are the mean data obtained at the three cyclic load frequencies used for testing in seawater. It can be seen that the present data are reasonably closely

matched compared to the significant scatter derived from the Thorpe et al. data [2]. Thorpe et al.'s results were obtained at a test frequency of 0.1Hz under free corrosion potential while those of C-Mn-V steel were obtained at 0.133Hz. Therefore, it is expected that the crack growth rates will be higher than those obtained in the present work due to the longer time the crack tip is exposed to the corrosion elements per cycle but this is not evident in their results. It is possible that the crack growth rates were influenced by a difference in load range, material properties, the level of potential used in the case of Thorpe et al., and specimen dimensions in terms of thickness and dimension W. Also, natural seawater was used in Thorpe et al.'s [2] investigation, Kermani and Harrop [62] used NaCl solution in their study with higher crack growth rates as shown in the figure, while the present results and those reported by Havn and Osvoll [73] were obtained in laboratory simulated seawater prepared according to ASTM D1141. Therefore, it is possible that the differences in environmental conditions of the seawater used for each test had a significant influence on the crack growth rates. This can also be argued by the crack growth behaviour in the Havn and Osvoll study which was obtained at a cyclic load frequency of 0.2Hz. It can be seen from Figure 4-24 that the curve shifted to the left of the present results which revealed the effect of a lower frequency as expected.

However, the difference in crack propagation behaviour in Havn and Osvoll studies, particularly at lower ΔK compared to the others curves, may also be due to the effect of the test load range. It should be mentioned that crack growth behaviour may not be only load or cyclic frequency dependent, but may also be material dependent. However, the overall comparison in seawater, as shown in the right of Figure 4-24, generally reveals that the crack growth trend in the present investigation agrees well with the other curves plotted in the figure.

4.6.2 Discussion of high strength steels data

In Figure 4-25, crack growth rates in S355J2+N steel in air and in seawater are compared with those in HSS, such as pipelines and offshore platforms steels (C-Mn, API X70, API X65 and RQTuf 501) with yield stresses of 400MPa to 600MPa [68], [74], [82], [113]. It can be seen in the left of the figure that the

crack growth trends of S355J2+N steel are similar to those of HSS, but crack growth rates are higher in the other three steels than those reported by Bertini [113] for a C-Mn steel. The crack growth data of S355J2+N steel also fall within the growth rates in API X70 [68], API X65 [74] and RQTuf 501 [82] steels. It can also be seen that the crack growth rates in API X70 are higher than in API X65 particularly at higher ΔK . The S355J2+N steel has a lower yield strength than the API X65, API X70 and RQTuf 501 steels but an effect of this was not evident in their responses, as shown in the air comparison plots.

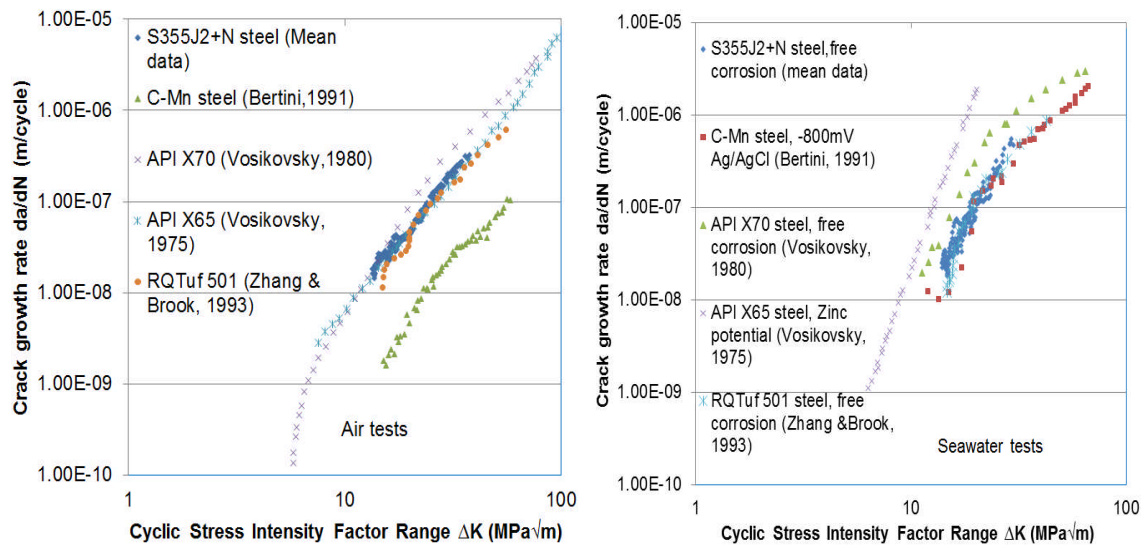


Figure 4-25 Comparison of crack growth rates in air and seawater with high strength steels

However, in the seawater tests comparison, as shown on the right of Figure 4-25, the crack growth rates in the steels are similar except for those reported by Vosikovsky [74] for an API X65 steel under zinc potential. It is possible that the difference in environmental test conditions was contributing to the observed crack growth rates. There is also a noticeable effect of the corrosive environment in the crack growth rates of C-Mn compared to the behaviour in air due to the associated mechanisms promoting crack growth rates in seawater. Despite the optimum protection of -800mV that was offered to C-Mn steel, it can be seen that there is no marked difference in the crack growth rates compared with the responses from S355J2+N and RQTuf 501 steels respectively. This implies that the crack growth behaviour of S355J2+N in a seawater

environment is adequate. It can also be observed from Figure 4-25 that crack growth rates are higher in API X65 and API X70 steels than in the other steels compared. The difference in crack growth rates in API X65 and API X70 are higher in the seawater environment compared to their responses in air, probably due to the differences in corrosion potential offered to both steels.

4.6.3 Discussion of extra high strength steels data

Figure 4-26 compares the crack growth rates in S355J2+N steel with those in HY 130 [61] and SE702 [108] steels in air and in seawater. HY 130 steel is used for ship design and fabrication while SE702 steel is a jack-up steel. Their yield stresses are in the range of extra HSS as classified in [54]. The S355J2+N steel appears to have a better resistance to fatigue crack growth compared to HY 130 and SE702 steels in air, as shown in the left of the figure. The crack growth behaviour of HY 130 steel shows a bump shape particularly at intermediate levels of ΔK , while at higher ΔK , the curve almost converged with that of S355J2+N steel. At lower ΔK in air, crack growth rates in S355J2+N steel are similar to in SE702 steel but at higher ΔK , crack growth rates are twice higher than those measured in S355J2+N steel.

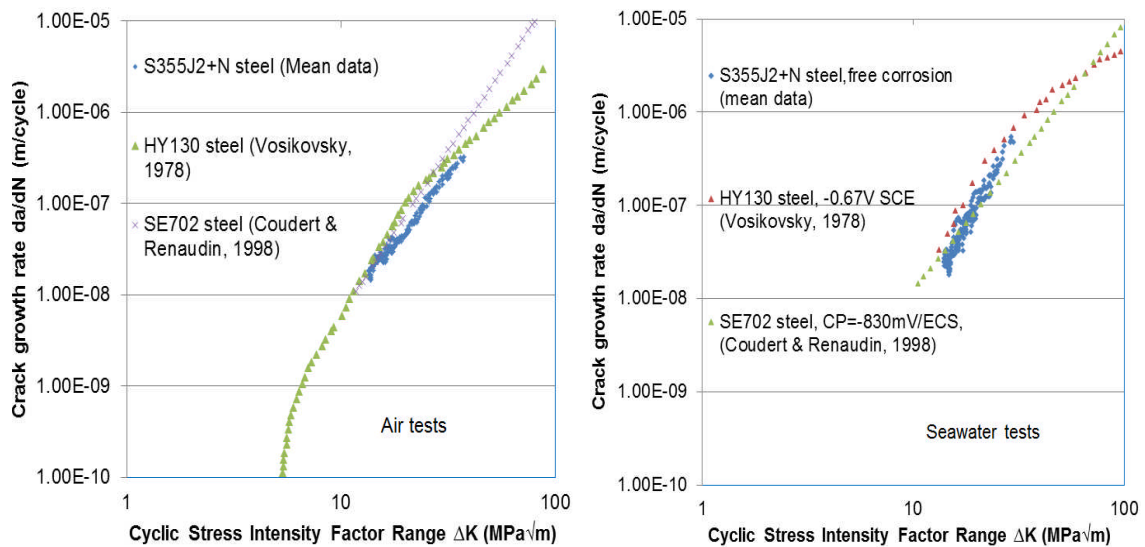


Figure 4-26 Comparison of crack growth rates in air and seawater with extra high strength steels

The seawater comparison is plotted on the right of Figure 4-26. It can be seen that the crack growth behaviour of the steels are similar at lower ΔK . However, at higher ΔK , crack growth rates in HY 130 steel are slightly higher than in the other two steels and the curve converged with that of SE702 steel. Regardless of the levels of CP applied to the SE702 and HY 130 steels, it can be observed that their behaviours are similar to that of S355J2+N steel tested in a free corrosion condition, particularly at lower ΔK . In some lower values of ΔK , crack growth rates in S355J2+N steel were slightly lower than in SE702 and HY 130 steels, but at higher ΔK , the majority of the data points fall between the SE702 and HY 130 curves. Overall comparison of the fatigue crack of S355J2+N shows a similar and in some cases better behaviour than the crack growth rates in the different grades of steels compared in this section. In a review provided in [131], it was also found that the behaviour of high strength steels were similar to medium strength steels used for offshore installations. Therefore, it appears that the resistance of S355J2+N steel to crack growth is satisfactory.

4.6.4 Mean stress and cathodic protection

The free corrosion tests results are compared with those obtained under a free corrosion potential, normal protection and cathodic over protection as shown in Figures 4-27 to 4-30. Mean stress effects on corrosion fatigue crack growth in BS4360 50D steel have been investigated under a range of CP [2].

Figure 4-27 compares crack growth rates in S355J2+N steel in free corrosion conditions with those obtained by Thorpe et al. under a free corrosion potential. Included in the figure are the data obtained from single edge notch specimens at an R-ratio of -1 [2]. The crack growth trends of the data plotted in the figure are similar but it can be observed that the response of S355J2+N steel in seawater appears better when considering the increasing crack growth rates in a monotonic manner compared to the significant scatter obtained from the BS4360 50D steel. As previously mentioned, the currently used improved data acquisition techniques for fatigue tests compared to those used in the 1970s and 1980s may be a contributing factor in the reduction of experimental scatter in the present material. It can also be seen from Figure 4-27 that crack growth

rates increased with an increase in stress ratio at all the ΔK ranges. This is also evident in the S355J2+N steel crack growth data at an R-ratio of 0.5 as shown in the figure. The experimental test conditions of the present study in terms of loading frequency and possible difference in the free corrosion condition and free corrosion potential used in Thorpe et al.'s study, are also likely to influence the crack growth behaviour in the materials, as mentioned earlier.

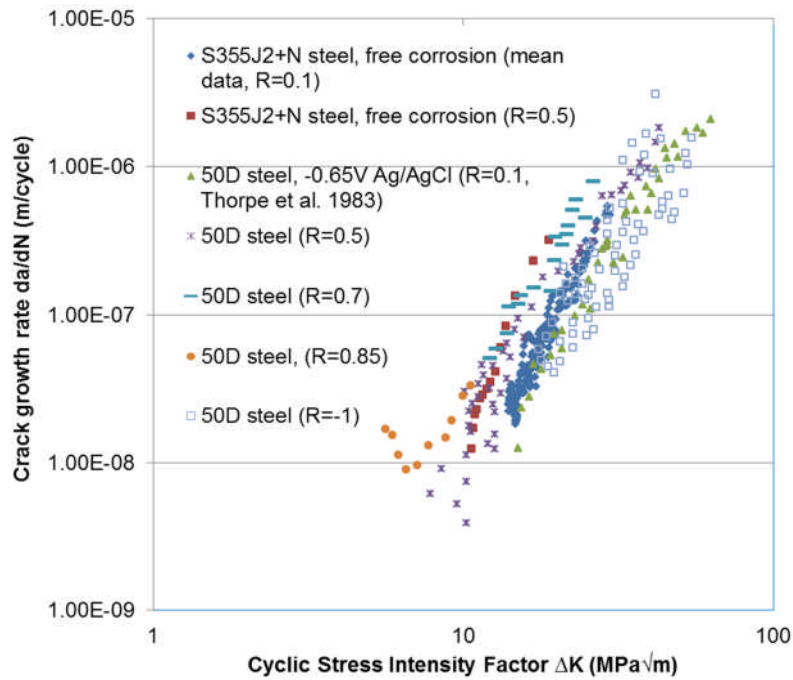


Figure 4-27 Result comparison with Thorpe et al. data (-0.65V free corrosion potential)

Crack growth data obtained in BS4360 50D steel at optimum CP of -0.85V are compared with those in S355J2+N steel, as shown in Figure 4-28. It was expected that lower crack growth rates will be obtained under an optimum protection compared to in a free corrosion condition, but this is not observed at an R-ratio of 0.1 as shown in the figure. At higher stress ratios ($R > 0.5$), the interaction between stress ratio and the applied CP was only dominant in 50D steel at lower ΔK but at higher ΔK , the crack growth curve nearly converged with the data obtained at a lower stress ratio. This implies that the effect of CP may not be effective at a higher ΔK . An understanding of the behaviour of the structures in a free corrosion condition may provide information on how to optimise the design of the structures on occasions when loss of corrosion

protections occurs. From Thorpe et al.'s crack growth trend, it is possible that the crack advancement was delayed by excessive corrosion debris deposited within the crack as it propagates, particularly at higher ΔK . This was reported in their study as an effect of calcareous deposits at the crack tip due to CP, but a discussion of the effect of calcareous deposits on crack growth rates is not relevant in this study as the crack growth data were obtained under free corrosion conditions.

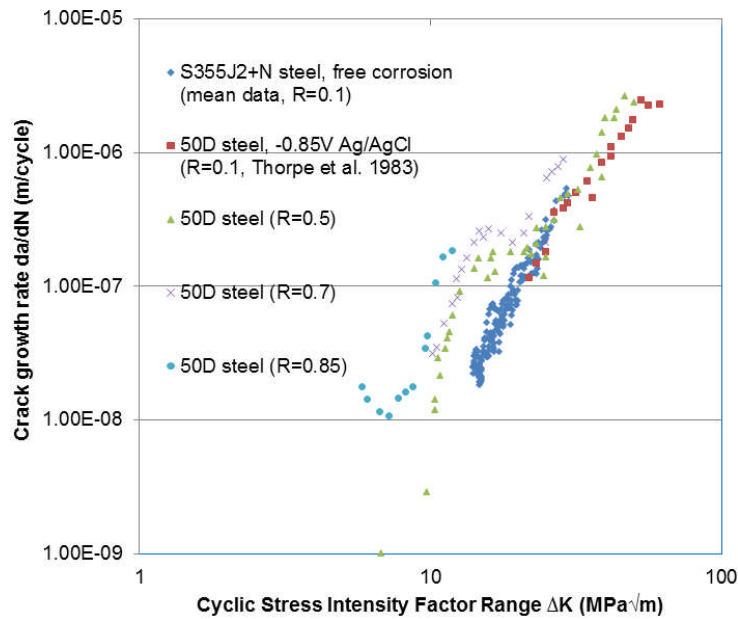


Figure 4-28 Result comparison with Thorpe et al. data (-0.85V cathodic protection)

Figure 4-29 compares the crack growth rates under CP of -1.1V with the results of S355J2+N steel. Included in the figure are the data obtained by Kermani and Harrop [62]. Crack growth rates were generally higher at more negative potential than in free corrosion condition and were found to increase with increasing R-ratio. The effect of CP became pronounced at a potential of -1.3V as shown in Figure 4-30. Hydrogen embrittlement was used as an explanation for the enhanced crack growth rates, particularly at higher levels of CP (-1.1 and -1.3V). Since cathodic over protection has shown to be more damaging at higher stress ratios, it implies that for structures operating in the presence of high tensile residual stress, corrosion protection by CP may not be a good alternative. Crack growth rates at a higher R-ratio, above 0.5 were not studied

in parent materials in seawater during this investigation but an approach for modelling mean stress effects on crack growth rates at a particular R-ratio of interest was developed and described in Chapter 5. The intention of the modelling is to reduce the cost and time involved in obtaining crack growth rates at all possible stress ratios.

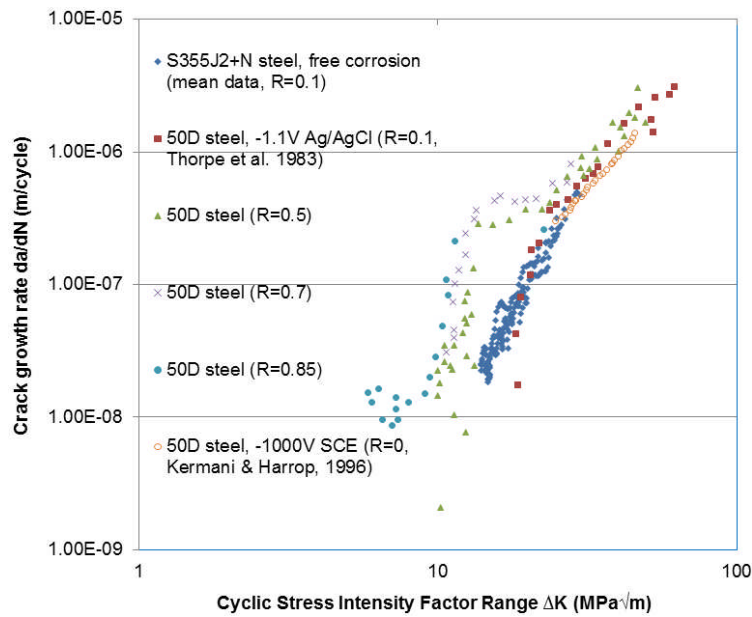


Figure 4-29 Result comparison with Thorpe et al. data (-1.1V cathodic protection)

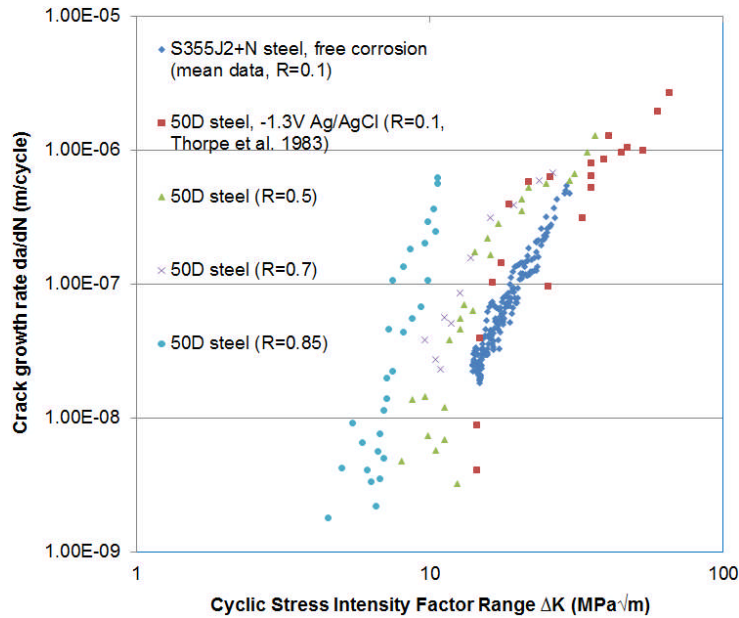


Figure 4-30 Result comparison with Thorpe et al. data (-1.3V cathodic protection)

4.6.5 Results comparison with the BS7910 recommendations

The crack growth rates in S355J2+N steel in air and seawater are compared with the BS7910 recommendations [130], as shown in Figure 4-31. The mean air and seawater data lines are plotted in the figure. The data lines are in accordance with the recommendations, as shown in the figure, as they generally lie within the acceptable region of the recommended air and free corrosion design curve for base materials.

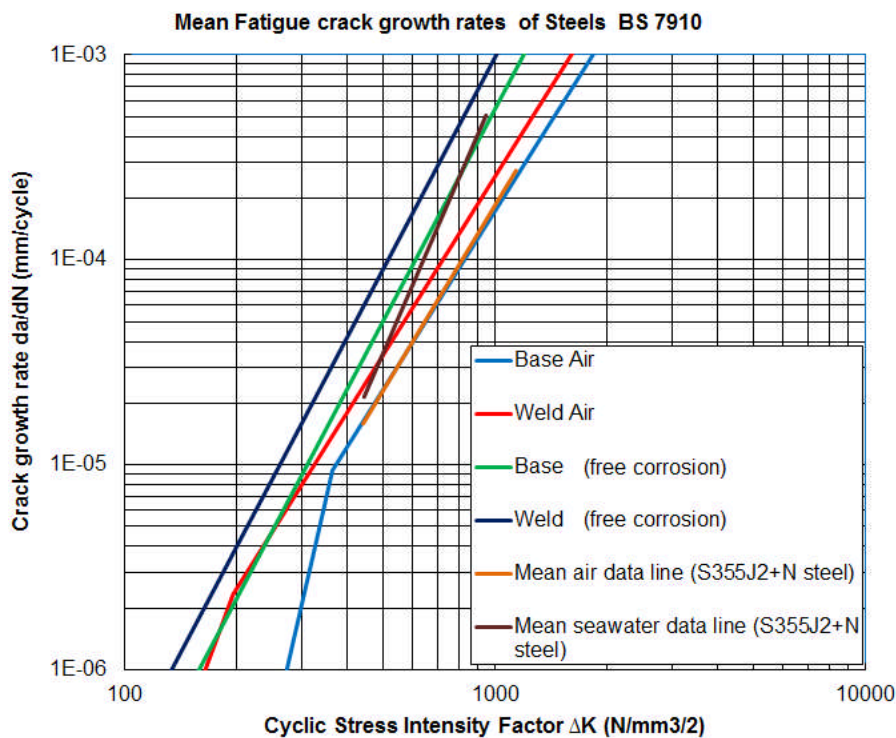


Figure 4-31 Comparison of crack growth rates in air and seawater with BS7910 recommendations

4.7 Summary

The crack growth behaviour of S355J2+N steel was investigated in a corrosion fatigue environment similar to that experienced by offshore wind farm monopiles under various cyclic load frequencies, in order to assess the effect of the cyclic frequency of the applied loading within a frequency range pertinent to the structure. The intention of this study with respect to the literature survey was to investigate if any appreciable difference was apparent between cycling at 0.3Hz and 0.4Hz. The following conclusions can be drawn:

- The existing corrosion fatigue database is almost 30 years old and therefore requires an update coupled with new design solutions that will suit newer types of offshore structure requirements due to their volume of manufacturing.
- Crack growth data obtained in free corrosion conditions can assist operations and design engineers on how to operate offshore structures at reduced cost and closer to the true design lives.
- Crack growth rates when compared with the equivalent air tests revealed an environmental reduction factor (ERF) of 2 and 4 at lower and higher stress intensity factor ranges respectively.
- There was no consistent trend observed indicating a more severe situation at a slower cyclic frequency of 0.3Hz compared to cyclic load frequencies of 0.35Hz and 0.4Hz. The seawater tests showed similar crack growth rates using the three test frequencies regardless of load range, and this implies that the results are consistent and repeatable. The frequency of 0.3Hz may therefore be recommended for subsequent corrosion fatigue tests in order to increase the damaging effect of seawater and to comply with the most dominant cyclic frequency relevant to offshore wind support structures.
- The use of the novel crack propagation methodology has proved useful and allowed crack growth rates to be reliably determined in corrosive environments. It must be mentioned that crack lengths were estimated in seawater based on BFS calibrations produced in air. Therefore, possible source of error such as fluctuations in the strain measurements cannot be completely neglected in seawater. However, this effect can be considered insignificant due to the trend of the data.
- ACPD was shown to be unsuitable for crack growth monitoring in CT test specimens.
- DCPD and BFS measurements were seen to be reliable and cost-effective methods for crack growth measurement in a corrosion environment where optical measurements are not applicable.

- A new BFS regression model has been developed and its effectiveness was particularly demonstrated in the simulated marine environment.
- The fatigue crack growth behaviour of S355J2+N steel was shown to be similar and in some cases better than different grades of steel used for offshore installations. The behaviour in air and seawater was also in accordance with the BS7910 recommendations.

5 Modelling Mean Stress Effects on Fatigue Crack Growth

5.1 Introduction

Fatigue cracks in components and structures are undesirable and could propagate to failure or collapse when the load carrying capacity of the structural member is unable to withstand the externally applied cyclic loads. Cracks or defects can be introduced into structural members during fabrication, transportation and installation. Mean stresses may also be introduced into structural members during fabrication due to residual stresses. Offshore support structures are fabricated from rolled steel through longitudinal and circumferential welding processes and these structures experience significant levels of both cyclic loads and the harsh marine environment during service.

The degree to which corrosion can amplify fatigue crack growth in offshore structures depends on the magnitude of the applied cyclic loads and the degree of stress concentration induced by existing defects. Therefore, to avoid economic losses, it can be advantageous to employ suitable monitoring tools that can detect fatigue cracks and the extent of damage so that reliable life predictions can be made. The accuracy of such predictions is important for cost-effective and optimal design of offshore structures. Experimental data relating to fatigue crack growth in S355J2+N steel under free corrosion conditions have been provided in Chapter 4. These data are used in this chapter to establish a methodology for predicting mean stress effects on fatigue crack growth in air and seawater.

A considerable amount of research has been carried out on the prediction of mean stress effects on fatigue crack growth in structures using fracture mechanics based models. Newer types of structures are now being developed for use in highly dynamic, harsh marine environments as compared to the existing oil and gas structures. Therefore, the extent to which mean stresses can enhance corrosion assisted fatigue damage in these structures needs to be better understood. Corrosion fatigue is a complex phenomenon due to the

nature of the electrochemical interaction of material and the corrosive environment. At a lower loading frequency, more time is spent in exposing the crack tip to the corrosion effects and this accelerates the crack growth rates. However, corrosion fatigue is not only frequency dependent but the process is also driven by a number of variables which cannot be completely studied by a single model. This is because each variable plays an important role in the corrosion fatigue process making it a challenging and costly task to study experimentally.

The degree to which corrosion fatigue crack growth can occur in offshore support structures also depends on various load interactions which are either applied locally or induced by residual stress at different parts of the structures with likely different behaviour at the weld areas. This implies that the stress level plays a significant role in the corrosion fatigue mechanism.

In welded joints, tensile residual stresses of up to the magnitude of material yield strength are present in the HAZ. These stresses are caused by thermal transients and phase transformation which occur during welding processes but their influence on fatigue crack growth should disappear when the applied stress range at the weld toe reaches the material yield stress [132].

In this chapter, various fracture mechanics based fatigue crack prediction models are discussed with respect to a number of curve fitting parameters. As mentioned in Chapter 2, the intention of these models is to reduce the number of experimental tests required to obtain the required material constants for a particular stress ratio. This approach is considered to be a useful engineering concept due to the time constraints, associated cost and difficulty in obtaining experimental data at different stress ratios. A new theoretical model which accounts for mean stress effects on corrosion fatigue crack growth in offshore structures is also proposed. The model is compared with some of the experimental data obtained in Chapter 2 and with other crack propagation models. The following section provides a review of some of the fatigue crack propagation models.

5.2 Fatigue crack propagation models

The majority of the test results discussed in this work and those reported in Chapter 2 are obtained under constant amplitude loading. Although most offshore structures are subjected to variable amplitude loading with associated load interaction or sequence effects which may significantly affect crack growth behaviour, constant amplitude models do not account for these effects. Fatigue analysis and accurate life prediction under variable amplitude loading is far from easy, if not impossible, because the load interaction effects cannot be fully accounted for. This is also due to the difficulty in correctly modelling the associated variable amplitude loading parameters such as stress ratio, amplitude and frequency. Also, a unique loading sequence is experienced by each structure in service, and it may be impossible to obtain the fatigue behaviour of a number of structures with respect to the load sequence experienced by a specific structure. This is why most of the fatigue crack growth analyses are usually performed using data obtained under constant amplitude loading. However, a simpler approach to the prediction of fatigue lives under variable amplitude loading is to neglect the load interaction effects and determine the crack growth rates on a cycle by cycle approach with respect to a constant amplitude crack growth law. This implies that constant amplitude material response data can also be used for predictions under variable amplitude loading if the sequence effects are not considered, but this procedure is outside the scope of this work. The models described in the next section are of constant amplitude crack growth which will be discussed with respect to their range of validities. As previously mentioned, conducting experiments at all possible R-ratios in order to investigate their effects on fatigue crack growth may be laborious and costly. Therefore, modelling the material response as a function of the R-ratio may be a useful concept. Some of the commonly used models for crack growth predictions are reviewed in this section.

5.2.1 Paris model

The most widely used method for predicting fatigue crack growth is the LEFM concept, which was first introduced by Paris and Erdogan [28] as a relationship

between crack growth rates and cyclic Stress Intensity Factor ranges ΔK . The Stress Intensity Factor is a variable which characterises the stress field in the vicinity of the crack. The Stress Intensity Factor (ΔK) is also recognised as the crack driving parameter, as a fatigue crack extends through the thickness of the material at a corresponding crack growth rate. The Paris equation was defined in Equation 1-16. The Paris relationship is limited to only region II of fatigue crack growth but below the threshold (region I) and during unstable crack growth (region III), the Paris Law is not applicable. Another limitation of the Paris model is its inability to predict the effect of mean stress or stress ratio on fatigue crack growth.

Mean stress effects are associated with stress ratio or R-ratio which can be expressed as a ratio of applied minimum stress to applied maximum stress in a fatigue cycle.

$$R = \frac{\sigma_{min}}{\sigma_{max}} = \frac{K_{min}}{K_{max}} \quad (5-1)$$

For most steels subjected to different stress ratios, a number of parallel straight lines are produced on a da/dN vs. ΔK plot and result in similar m values but specific C values [21]. Mean stress effects can be schematically represented by Figure 5-1 for a particular material under increasing or reducing R-ratio. As mentioned earlier, several models have been proposed to account for mean stress effects on fatigue crack growth as modifications to the Paris law, due to its limitation to account for R-ratios effects. Such models are capable of representing fatigue crack growth data with different curve fitting parameters.

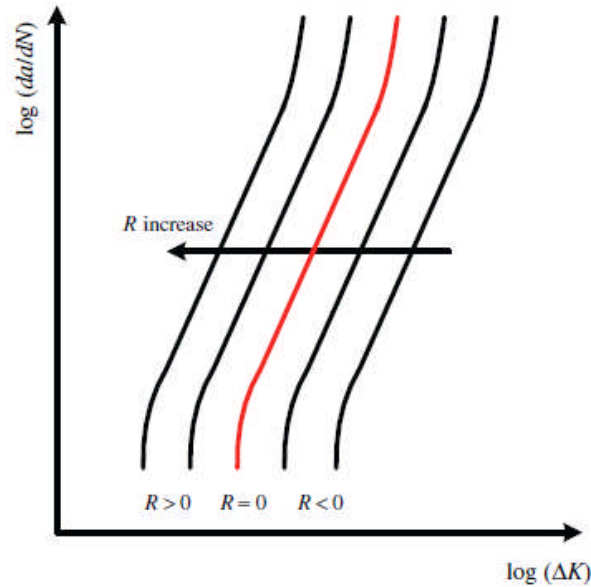


Figure 5-1 R-ratio effect on fatigue crack growth [89]

5.2.2 Elber's model

The well-known crack closure concept was proposed by Elber [133] by using the effective stress intensity factor range as the crack driving parameter responsible for crack growth. The concept of crack closure is based on the fact that fatigue crack closes during compressive loads and opens under tensile loads. Because of this, Elber expressed crack growth rates as a function of the effective stress intensity factor range ΔK_{eff} such that the Paris equation (Equation 1-16) was modified to be

$$\frac{da}{dN} = C(\Delta K_{eff})^m \quad (5-2)$$

$$\Delta K_{eff} = K_{max} - K_{op} \quad (5-3)$$

Where K_{op} is the corresponding stress intensity factor at the crack opening stress. Equation 5-2 is valid within the R-ratio of -0.1 to 0.7. Various effective stress intensity factor correlations have been proposed in the literature [134]–[136] but these are not discussed here. At threshold, the determined ΔK_{eff} at a lower R-ratio is usually lower than that determined at a higher stress ratio where

crack closure free mechanisms occur [137]. However, studies suggest that the crack closure concept was overestimated in the past coupled with the difficulty in obtaining appropriate K_{op} during experimental tests [138]–[140] and due to its relationship to R-ratios [89]. It was also mentioned that the crack closure concept depends on the material type and the environment [141]. K_{op} is usually derived at the crack opening load corresponding to 2% deviation from the load versus displacement relationship, as recommended in ASTM E647 [115]. McClung [142] also suggested that the crack closure theory should be attributed to the three regions of fatigue crack growth while Dinda and Kujawski [143] mentioned that Elber's crack closure concept is not the only method that can be applied to predict fatigue crack growth accurately.

5.2.3 Walker's model

To further address the inability of the Paris model to account for the effect of stress ratio, Walker [86] improved the Paris model to incorporate the mean stress effect on crack growth rates. A third curve fitting parameter was introduced to the Walker's model, which adjusts the stress intensity factor (ΔK) to produce similar crack growth as K_{max} at an R-ratio of 0. Walker's model can be expressed as

$$\frac{da}{dN} = C \left(\frac{\Delta K}{(1-R)^{(1-\gamma)}} \right)^m \quad (5-4)$$

Where γ is the Walker's exponent. The values of γ for metals range from 0.3 to approximately 1 with an average value of 0.5. Lower values of γ indicate a stronger influence of R on fatigue crack growth and vice versa. Walker's model is valid for $R \geq 0$. If $\gamma = 1$, it implies that the denominator of Equation 5-4 cancels out and this implies that there is no effect of stress ratio on fatigue crack growth. The implication of Equation 5-4 is that it produces crack growth curves that are parallel to each other irrespective of the stress ratio used.

5.2.4 Forman's model

Another commonly used model which depicts the mean stress effect by including region III of fatigue crack growth was developed by Forman [85]. The

form of failure at this region can be described by the critical stress intensity factor or fracture toughness K_c . The Forman model was developed to account for the associated unstable crack growth rates in region III. Forman's equation can therefore be considered as a modification of both the Paris and Walker models and is capable of representing data for various stress ratios at both regions II and III. The Forman equation is expressed as

$$\frac{da}{dN} = \frac{C(\Delta K)^m}{(1-R)K_c - \Delta K} = \frac{C(\Delta K)^m}{(1-R)(K_c - K_{max})} \quad (5-5)$$

Where K_c is the critical stress intensity factor or the fracture toughness of the material under consideration. As K_{max} approaches K_c the denominator of Equation 5-5 approaches zero and the crack growth tends towards infinity. This describes the accelerated crack growth rate in region III. It was mentioned that mean stress, microstructure and thickness effects have a large influence on fatigue crack growth at this region compared to what is obtainable at region II [21]. However, in this work, the Forman's model was not considered as part of the models that are compared in later sections due to the challenge in obtaining the exact K_c value for the material tested.

5.2.5 Kujawski's model

A two parameter driving force for fatigue crack growth in aluminium alloys was introduced by Kujawski [87] without considering the crack closure effects. The model is expressed as

$$\Delta K^* = (K_{max}\Delta K^+)^{0.5} \quad (5-6)$$

Equation 5-6 was developed on the premise that for negative R-ratio, the compressive part of the fatigue cycle does not contribute to crack growth. Equation 5-6 was later modified [137] to

$$\Delta K^* = (K_{max})^\alpha (\Delta K^+)^{1-\alpha} \quad (5-7)$$

Where ΔK^+ is the positive or damaging part of stress intensity factor range, K_{max} is the corresponding maximum value of the applied stress intensity factor while α is an empirical curve fitting parameter that was determined from the

average of slopes of the logarithmic plots of K_{max} vs. K^+ for a given constant crack growth rate. $\Delta K^+ = \Delta K$ when $R \geq 0$ and $\Delta K^+ = K_{max}$ for $R < 0$. It was specified that Equation 5-7 yields a good correlation for most aluminium alloys and some other metallic materials [87], [137], [143]. However, it was also mentioned that Kujawski's model was better for correlating data at positive R-ratios compared with negative values [88], [144]. Kujawski's model is valid within the stress ratio of -1 to 1.

5.2.6 Huang and Moan model

Huang and Moan [88] introduced an improved crack growth model which is capable of collapsing all crack growth curves obtained at different R-ratios to that corresponding to an R-ratio of 0. The validity of the model is within the R-ratio of -5 to 1. Huang and Moan's model can be used to predict crack growth rates at different stress ratios using the material response data derived at an R-ratio of 0. The Huang and Moan model is expressed as:

$$\frac{da}{dN} = C_0(M\Delta K)^{m_0} \quad (5-8)$$

$$M = \begin{cases} (1 - R)^{-\beta_1} & -5 \leq R < 0 \\ (1 - R)^{-\beta} & 0 \leq R < 0.5 \\ (1.05 - 1.4R + 0.6R^2)^{-\beta}, & 0.5 \leq R < 1 \end{cases} \quad (5-9)$$

Where $\beta_1 = 1.2\beta$, β , β_1 are material parameters but how they were derived was not described in Huang and Moan's paper [88]. However, they did mention that the stated values of the parameters were for illustration purposes only, as more investigation was needed to determine them absolutely. The constant β was assigned a value 0.7 for aluminium and steels if there is insufficient experimental data [88], [145]. The Huang and Moan model has been applied to predict crack growth curves at various R-ratios for some steel materials. The results are shown in Figures 5-2 to 5-4. Experimental results are given on the left of the figures while on the right are the condensed crack growth curves obtained by applying the Huang and Moan model using the value of β that best

consolidates the data. It can be seen that all the plotted data condensed to the R-ratio of 0 including the data obtained at an R-ratio of -1.

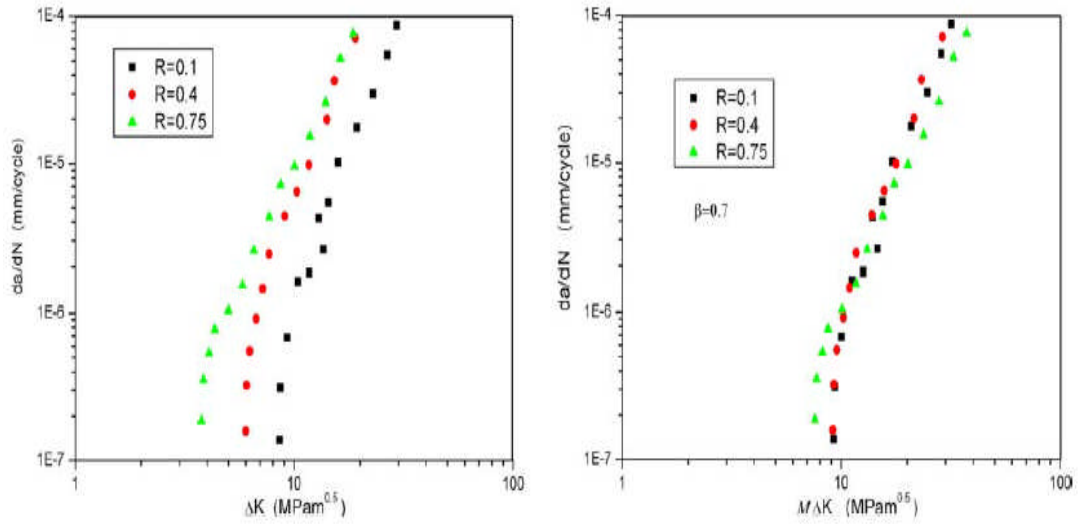


Figure 5-2 Fatigue crack growth in CrMoV steel at R-ratios of $0.1 \leq R \leq 0.75$ [88]

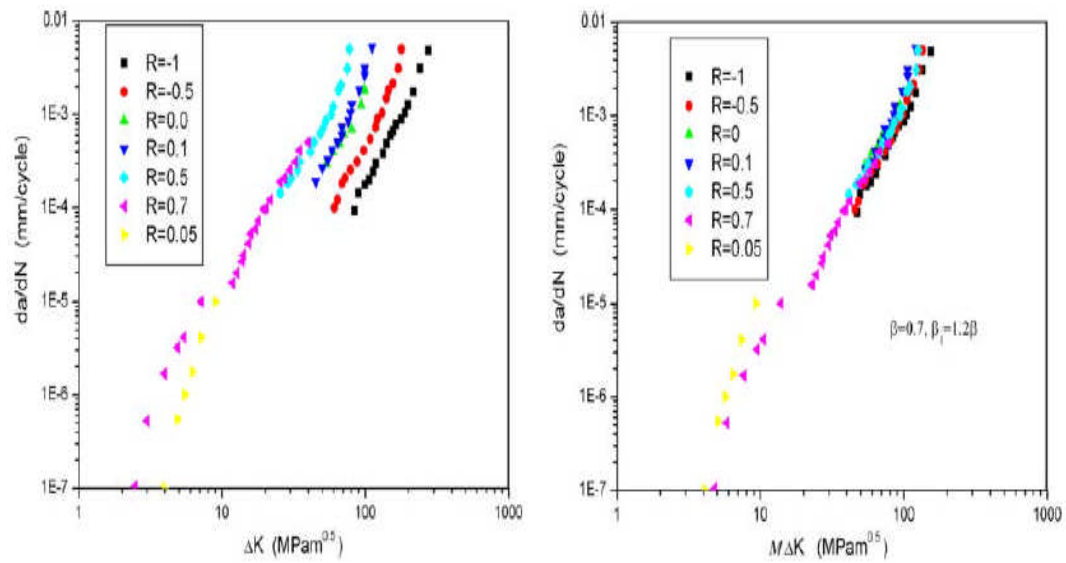


Figure 5-3 Fatigue crack growth curves for 4340 steel at stress ratios $-1 \leq R \leq 0.7$ [88]

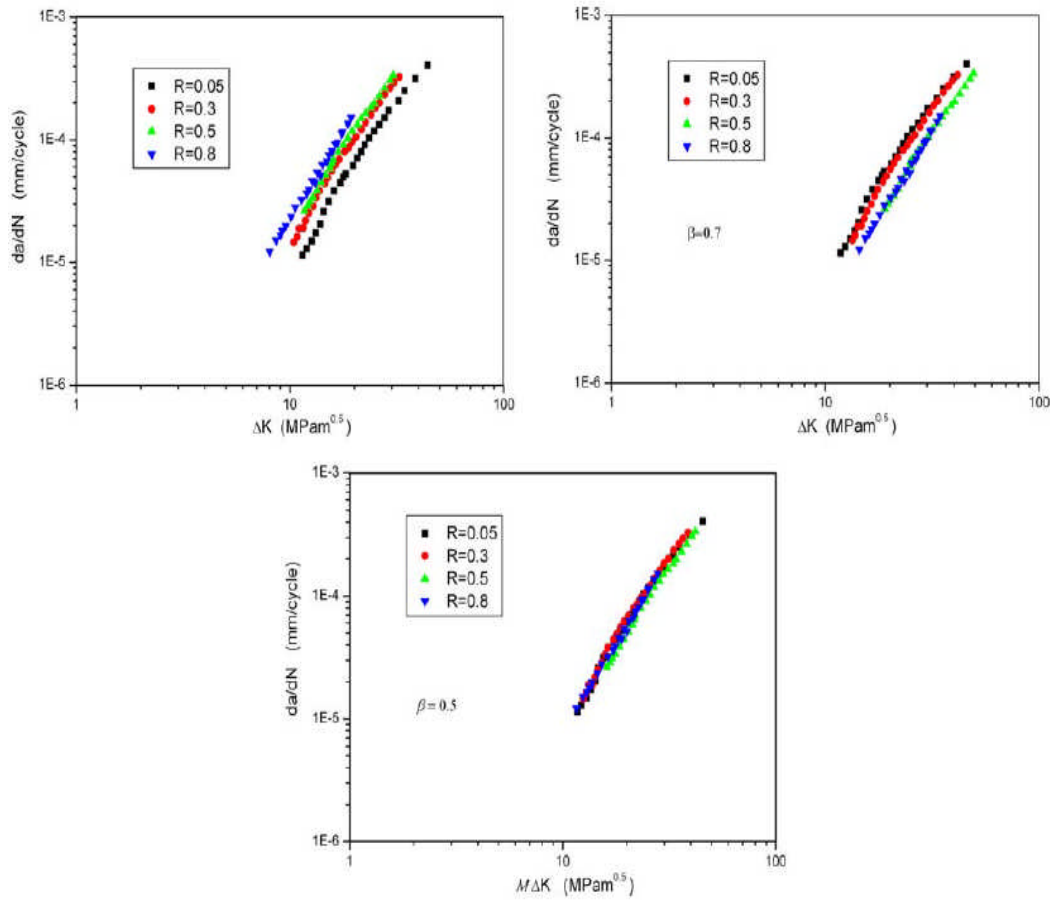


Figure 5-4 Fatigue crack growth curves for 300M steel $0.05 \leq R \leq 0.8$ [88]

5.2.7 Zhan et al.'s model

An approximate model similar to that developed by Huang and Moan was recently proposed by Zhan et al. [89] to account for the effect of stress ratios on fatigue crack growth. The model was developed using aluminium alloys and medium carbon steel data taken from literature at various stress ratios. The model is valid for stress ratios in the range $-1 \leq R \leq 1$ and can be used to predict crack growth rate at various stress ratios when only the data at $R=0$ are obtained experimentally. The model is expressed as

$$\frac{da}{dN} = C_0(\phi\Delta K)^{m_0} \quad (5-10)$$

Where ϕ is a correction factor which depends on the R-ratio. The material constants in Equation 5-10 are the same as those given by Huang and Moan in Equation 5-8. The correction factor can be defined as

$$\Phi = \exp(\alpha R) \quad (5-11)$$

From an extensive analysis using experimental data taken from the literature, the value of $\alpha = 0.65$ was assigned to low strength metallic materials, $\alpha = 0.75$ for high strength metallic materials such as Ti- alloys, while a value of $\alpha = 0.65$ was set for all other metallic materials.

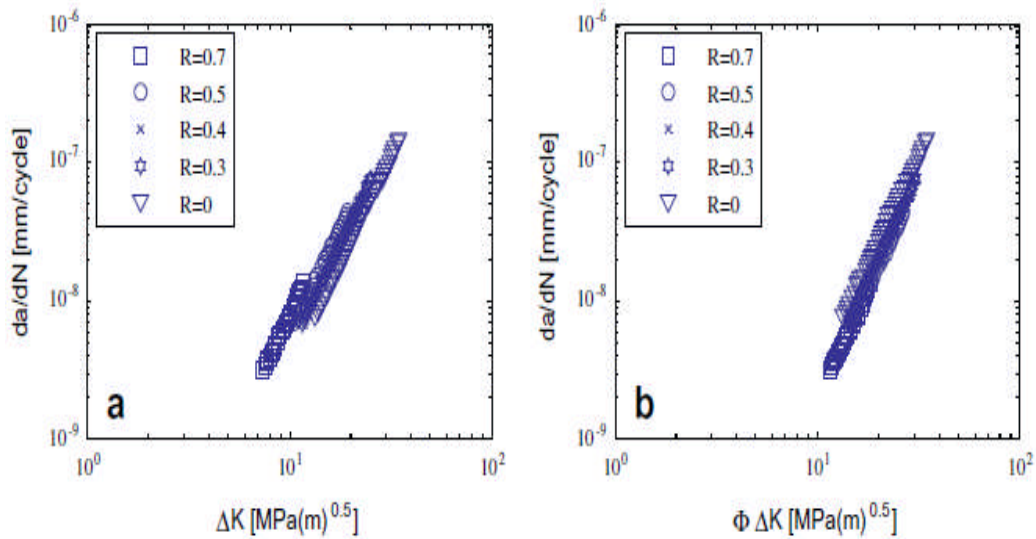


Figure 5-5 Fatigue crack growth of medium carbon structural steel [89]

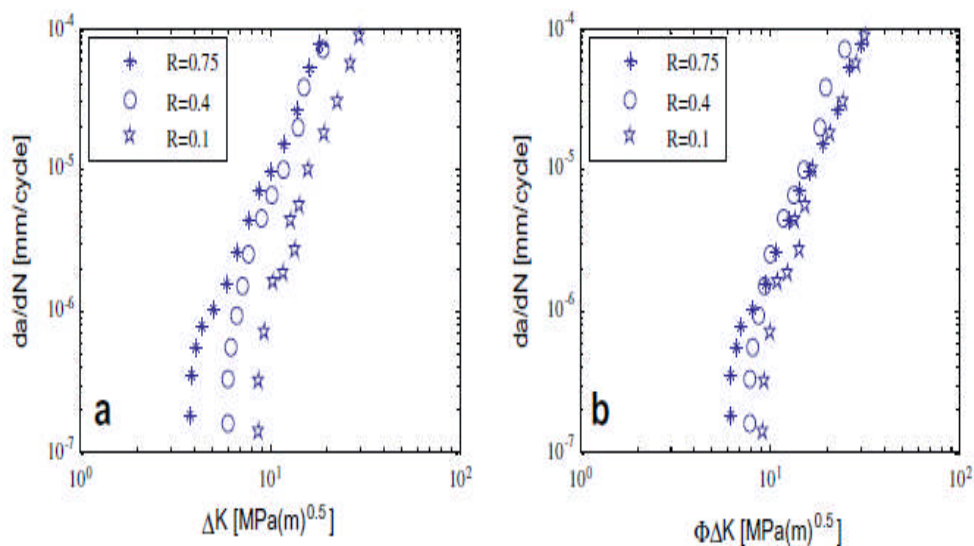


Figure 5-6 Fatigue crack growth of CrMoV steel [89]

Figures 5-5 and 5-6 describe the application of Zhan et al.'s model to the experimental data taken from the literature. Experimental data are plotted on the left of the figures while the predicted crack growth curves are plotted on the right. It can be seen that the model condensed the curves towards the data obtained at R-ratios of 0 and 0.1 respectively. The same experimental data plotted in Figure 5-6 was also shown in Figure 5-2. The condensed crack growth curves using both figures are similar, which indicates a good agreement between the Huang and Moan, and Zhan et al. models.

5.3 Comparison of mean stress effects on fatigue crack growth in air

One of the main intentions of this study is to develop a fracture mechanics based model for predictions of mean stress effects on corrosion fatigue damage. Prior to this, preliminary predictions using the models described in the previous section were made. The purpose of this preliminary modelling exercise is to establish comparisons among the models at lower and higher stress ratios using the experimental data obtained from this study at an R-ratio of 0.1 as the baseline data.

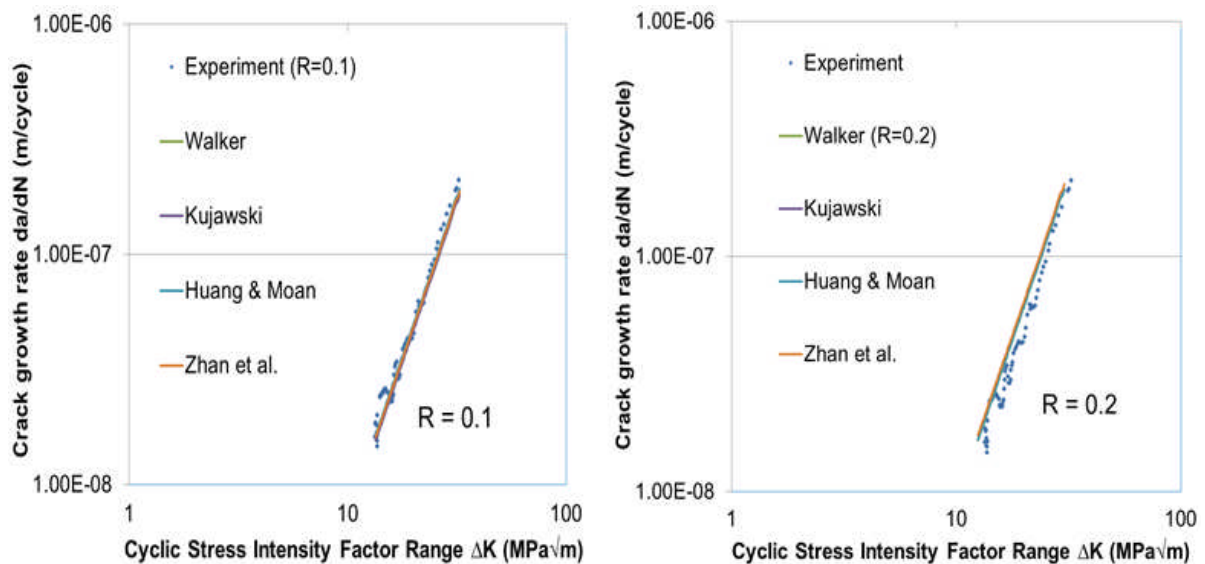


Figure 5-7 Predicted crack growth rates in air at R-ratios of 0.1 and 0.2

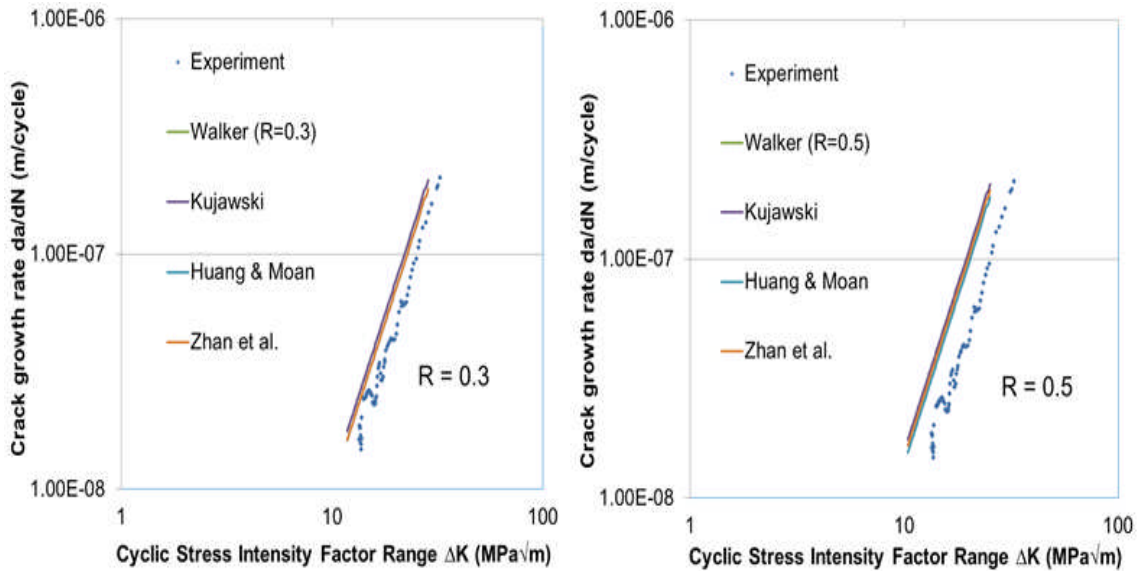


Figure 5-8 Predicted crack growth rates in air at R-ratios of 0.3 and 0.5

The predicted crack growth rates in air at R-ratios of -1 to 0.7 using the models described from Equation 5-4 and Equations 5-6 to 5-11 are shown in Figures 5-7 to 5-9. In the left of Figure 5-7, it can be observed that the predicted curves at an R-ratio of 0.1 are parallel to the experimental data over the entire range of ΔK . The curves also move to the left of the baseline ($R=0.1$) for R increasing cases, while for an R-ratio of -1, the predicted curves shift to the right of the baseline (Figure 5-9). Crack growth rates were found to be higher at higher stress ratios and vice versa. It can also be seen that the difference in deviation between the predicted curves and the baseline data is significantly higher at higher stress ratios ($R \geq 5$) than at lower stress ratios. This may be attributed to the crack closure free surface at higher stress ratios, a situation where the crack surfaces do not touch during the unloading portion of the stress cycle. The models agree well with each other up to an R-ratio of 0.5. However, at an R-ratio of 0.7, Kujawski's model agrees with Walker's model, while the predicted curve using Huang and Moan's model also agrees with that of Zhan et al.'s model.

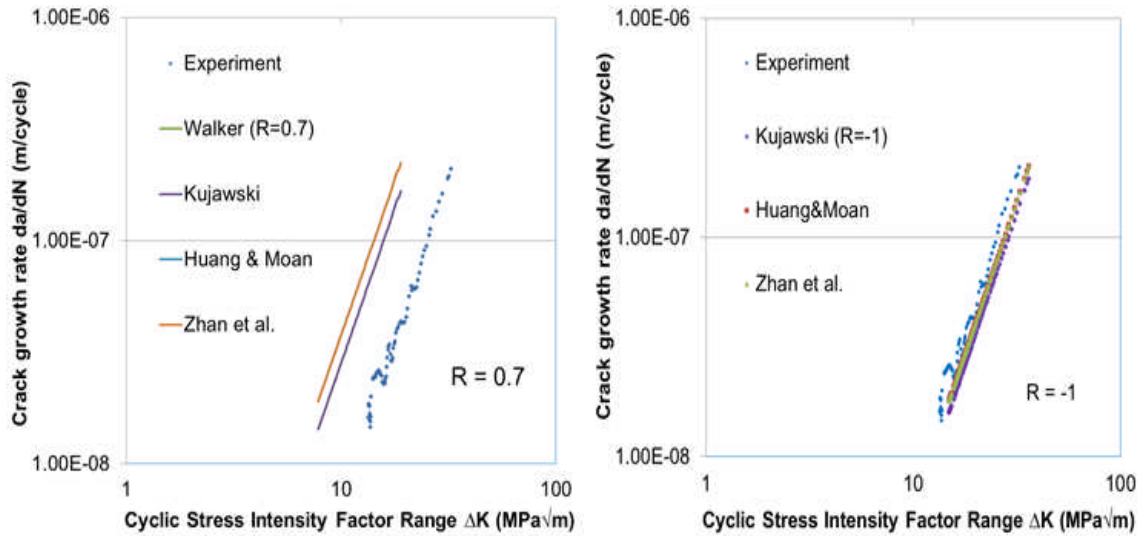


Figure 5-9 Predicted crack growth rates in air at R-ratios of 0.7 and -1

At an R-ratio of -1, Kujawski's, Huang and Moan's and Zhan et al.'s models are the only valid correlations that are applicable. The predicted results using the models are shown in the right of Figure 5-9. It can be seen that the predicted curves shifted to the right of the baseline data as expected. In this situation only the tensile portion of the load cycle is effective in propagating the crack and is controlled by K_{max} , therefore lower crack growth rates compared to those at an R-ratio of 0.1 should be expected. Also, at $R=0$, $\Delta K=K_{max}$ but at $R=-1$, only the tensile portion of the load cycle is effective and is controlled by K_{max} . Analytically, common practice is to exclude the compression segment of the loading cycles since there is no crack propagation during the compression portion; and on the assumption that the crack closes during compression.

5.4 Comparison of the mean stress effects on fatigue crack growth in seawater

Figures 5-10 to 5-12 present the predicted crack growth rates in seawater at R-ratios of -1 to 0.7 using the crack growth data obtained under free corrosion at an R-ratio of 0.1 as the baseline. At an R-ratio of 0.1, the predicted curves are parallel to the experimental data, as shown in the left of Figure 5-10. Crack growth rates were also higher in seawater for R increasing cases as expected. At an R-ratio of 0.2, Huang and Moan's model slightly overestimated the crack growth rates compared to the other models but this difference was marginal

compared to what was observed at R-ratios of 0.3 and 0.5 respectively. At an R-ratio of 0.5, it can also be observed that the predicted curves of the other three models fall below Huang and Moan's predicted curve.

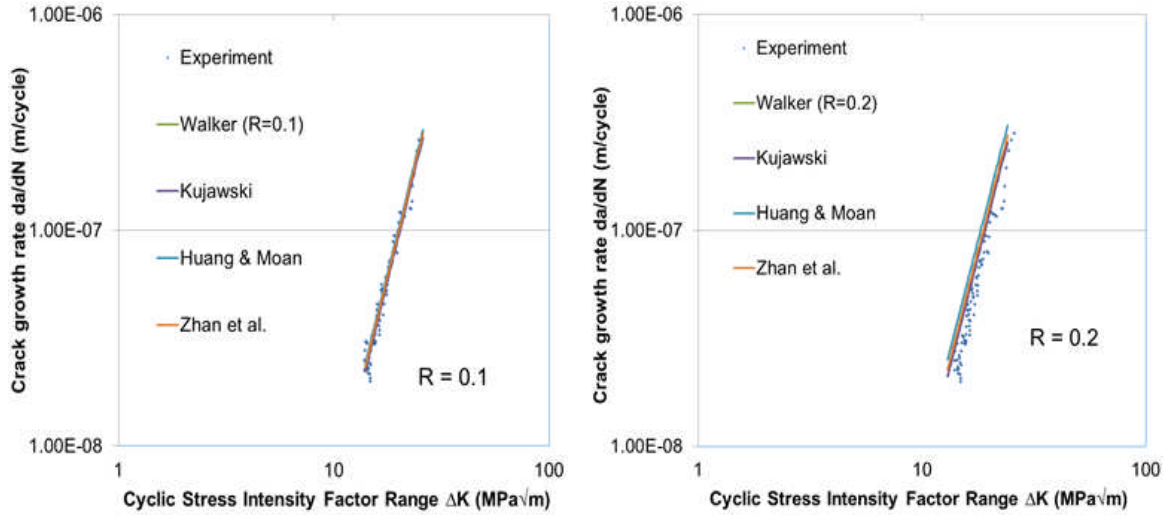


Figure 5-10 Predicted crack growth rates in seawater at R-ratios of 0.1 and 0.2

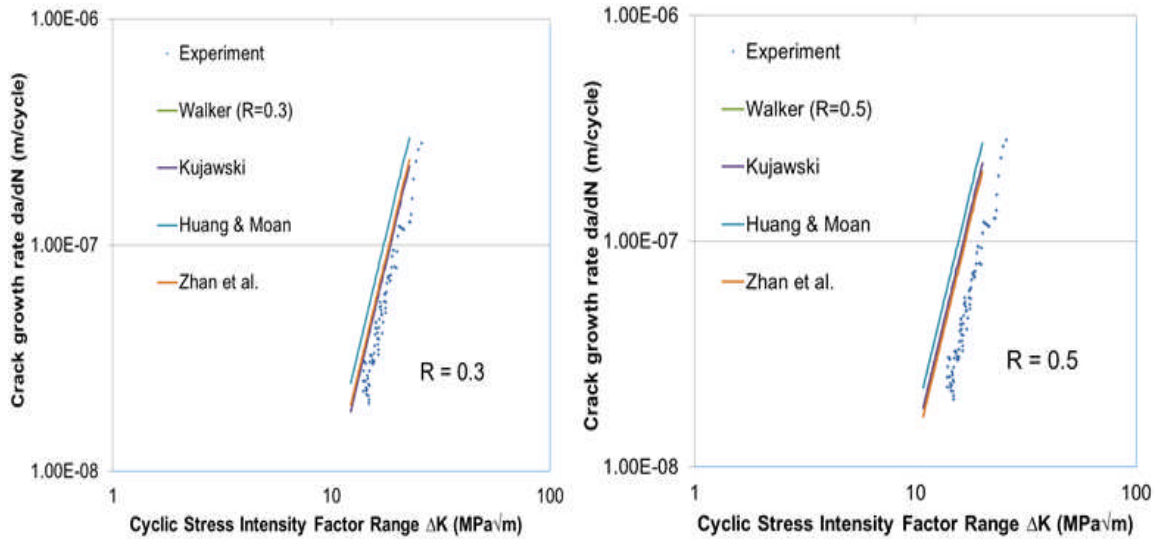


Figure 5-11 Predicted crack growth rates in seawater at R-ratios of 0.3 and 0.5

At an R-ratio of 0.7, the predicted crack growth curves agree well with each other as shown on the left of Figure 5-12. It is worth mentioning that the models used in this work are more consistent in air than in seawater for the ranges of R-ratios examined. It is possible that the environmental interaction may be

contributing to the crack growth rates compared to in air. The predicted crack growth rates in seawater at an R-ratio of -1 are shown on the right of Figure 5-12 with lower crack growth rates compared to the baseline data (R=0.1). The methodology employed for the predictions at negative R-ratio is the same as that used previously except that the material parameter used here is different. It can be seen that Kujawski's predicted crack growth rates at an R-ratio of -1 agree well with Huang and Moan's model, while Zhan et al.'s predicted curve shifted above the two other models. Comparing the responses derived from the applied models in air and seawater with respect to that of the baseline, it is worth mentioning that Kujawski's predictions are conservative and appear to be more precise for the positive and negative stress ratios examined in the comparisons made in this section.

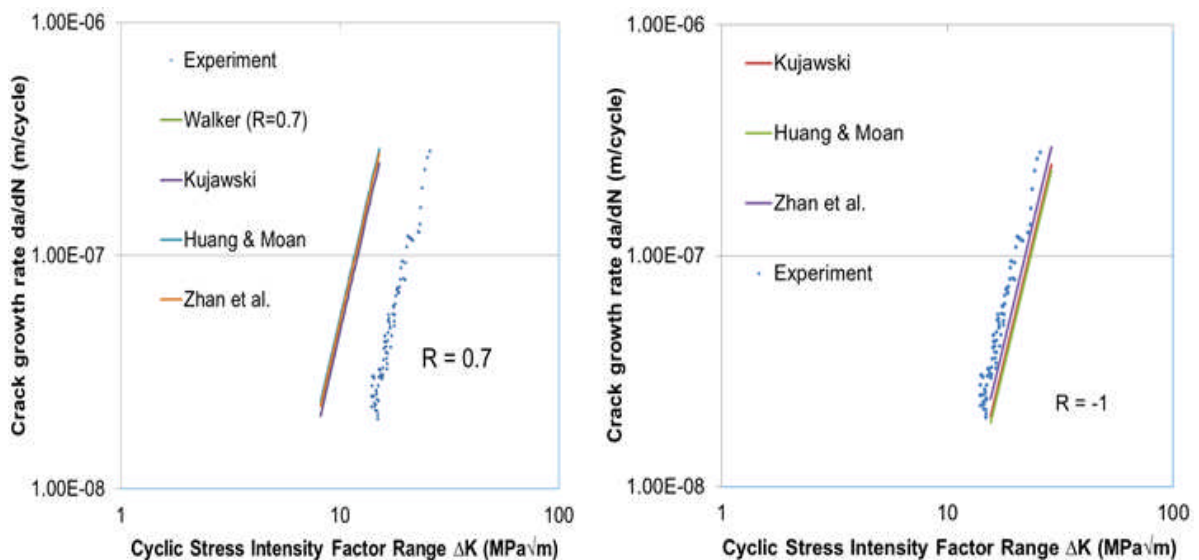


Figure 5-12 Predicted crack growth rates in seawater at R-ratios of 0.7 and -1

5.5 Prediction of low, medium and high cycle fatigue

As mentioned in Chapter 2, monopile support structures experience some levels of deflection and vibration which are influenced by axial loads, lateral loads and bending moments. It is anticipated that significant levels of tensile mean stresses might be present in some parts of the structures but on the overall scale, the structures may be experiencing tension-compression loadings, unlike the usual tension-tension loading type used for testing CT

specimens in the laboratory. Therefore the stresses imposed by the combination of the aforementioned loads can influence fatigue damage in a manner similar to that experienced under a negative R-ratio. The material response data obtained at such stress ratios will be useful for prediction. In reference to the prediction made in the previous section, Kujawski's model was selected in this section as the baseline for the negative R-ratio case due to its consistency. Therefore the predictions are made using the material response data derived from the three applied models in seawater at an R-ratio of -1. This is to provide an estimate of the response of the material under reduced operating stress conditions similar to those experienced in offshore structures and to establish the most conservative fatigue result for design in the case considered here. The predicted low, medium and high cycle fatigue curves are shown in Figures 5-13 to 5-15.

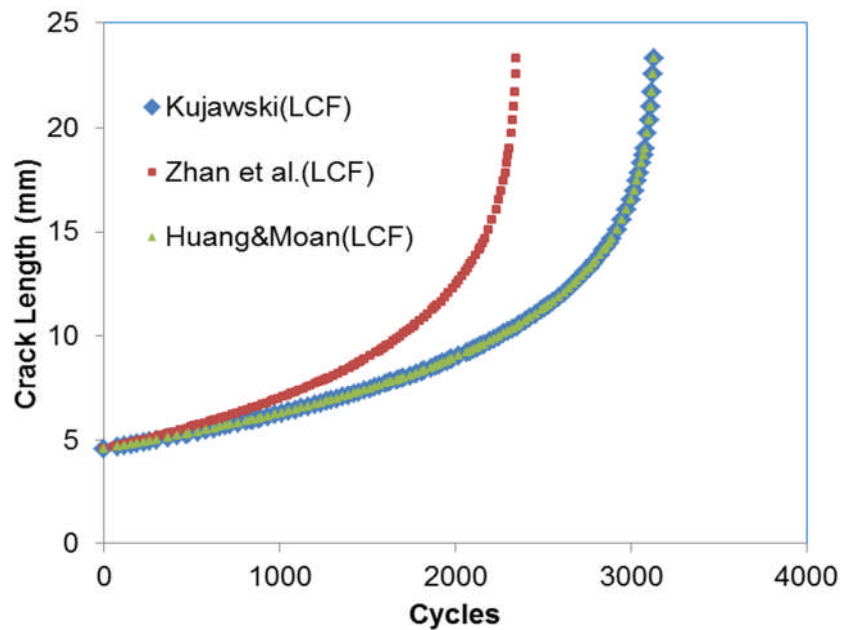


Figure 5-13 Prediction of low cycle fatigue (LCF)

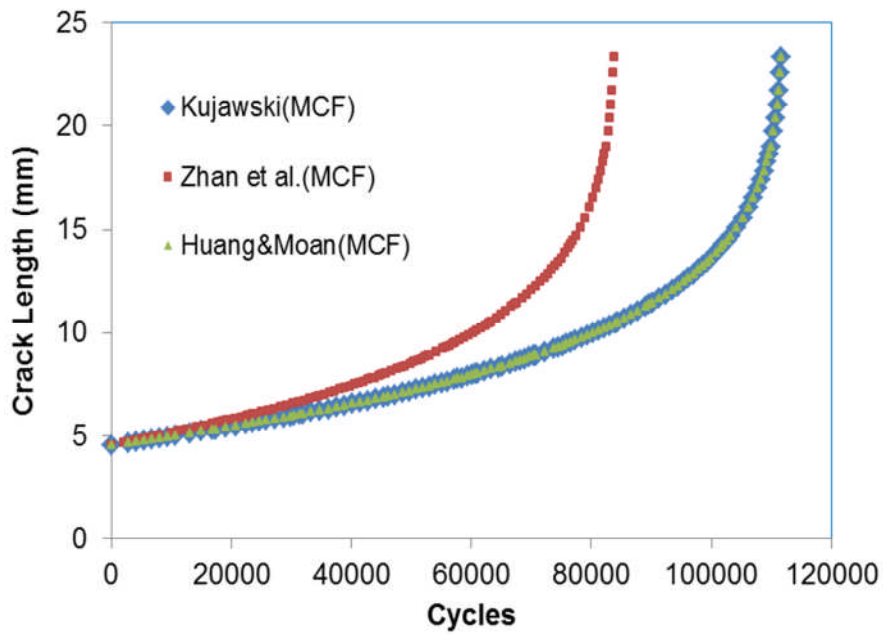


Figure 5-14 Prediction of medium cycle fatigue (MCF)

As previously mentioned, Kujawski’s predicted curve was used as the baseline relative to the Huang and Moan and Zhan et al. models. It can be seen from Figures 5-13 to 5-15 that Kujawski’s and Huang and Moan’s predicted curves are parallel to each other for all three load scenarios. This shows a reasonable agreement between the two models at an R-ratio of -1. The amount of deviation in the number of loading cycles in the LCF region between the baseline and the other two curves was less than 1,000 cycles. This could be attributed to the effects of the applied stress.

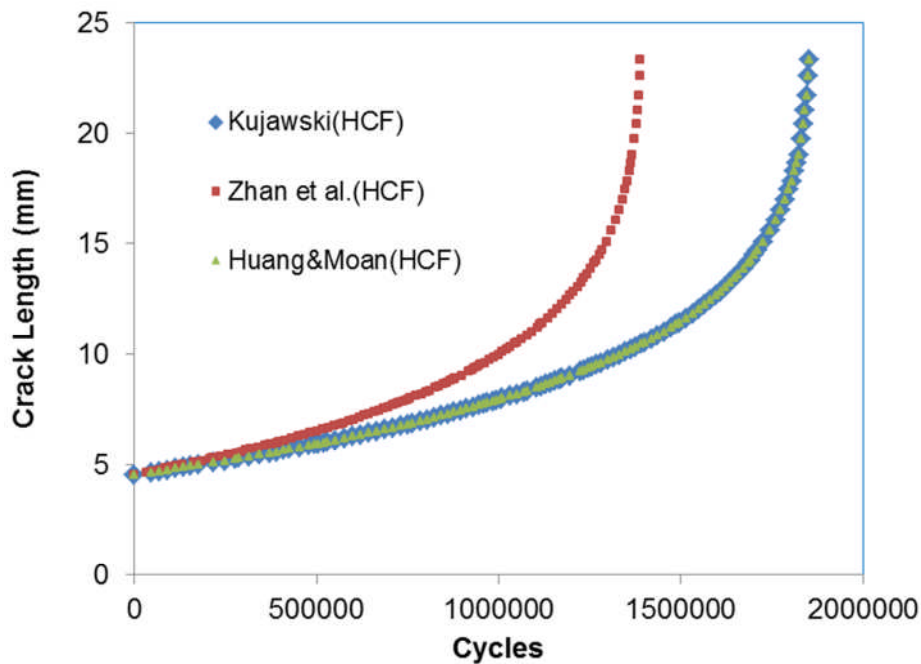


Figure 5-15 Prediction of high cycle fatigue (HCF)

In MCF, a difference of ten times greater than what was obtained in the LCF region was observed. The highest deviation in the number of stress cycles was experienced in the HCF region with more than half a million cycle differences between the baseline and those predicted by Zhan et al.'s model. This implies that the effect of applied stress to fatigue crack growth is significantly higher in LCF life compared to what occurs in the MCF and HCF lives respectively. This appears practical considering the behaviour of offshore structures in service.

From a design perspective, a conservative life prediction of these structures is more convincing in fatigue assessment with respect to design life under low load and long life situations (i.e. HCF). From the procedure described above, the predicted life by using Zhan et al.'s model appears conservative for design, and could represent safely the response of the structures in service considering the predicted number of stress cycle which was significantly lower than that predicted by the Kujawski and Huang and Moan models respectively.

5.6 A relative crack opening time correlation for corrosion fatigue crack growth in offshore structures

This section describes a new model that accounts for mean stress effects on fatigue crack growth both in air and in a free corrosion condition. The new theoretical model is proposed based on the two fatigue crack growth driving parameters ΔK and K_{max} . The model is valid for stress ratios in the range $-1 \leq R \leq 0.9$ and is proposed using the constant amplitude loading material response data derived at an R-ratio of 0.1 in air and seawater as the baseline. The major assumption of the correlation is that corrosion fatigue damage is equivalent to the proportion of time that the fatigue crack is open over a range of loading cycles. This is based on the rationale that the compressive portion of the loading cycle does not contribute to corrosion fatigue damage, i.e. only half the time of the loading cycle is spent in the damaging or crack opening situation for a fully reversed cycle.

The physical basis for the model development is shown in Figure 5-16. The figure describes the increasing and reducing R-ratio cases coupled with the representation of tensile and compressive portions of loading cycles at an R-ratio of -1. It is assumed in this work that the area of the damaging part of the fully reversed loading is related to the area under the applied stress cycle at an R-ratio of 0.1. As the mean stress or R-ratio is increased, for example from 0.1 to 0.2, the applied stress cycle shifts above the corresponding stress cycle of an R-ratio of 0.1, as shown in the figure. The degree of the shift above the R-ratio of 0.1 stress cycle is a function of the level of the imposed mean stress or R-ratio. The hypothesis here is that the area under the applied stress cycle of a specific positive R-ratio, with reference to an R-ratio of 0.1 can be used as a correction to obtain the crack growth rates corresponding to that particular R-ratio. A description of the areas under the sine curve corresponding to the applied stress cycles at R-ratios of 0.2 and -1 with respect to an R-ratio of 0.1 is shown in Figure 5-17.

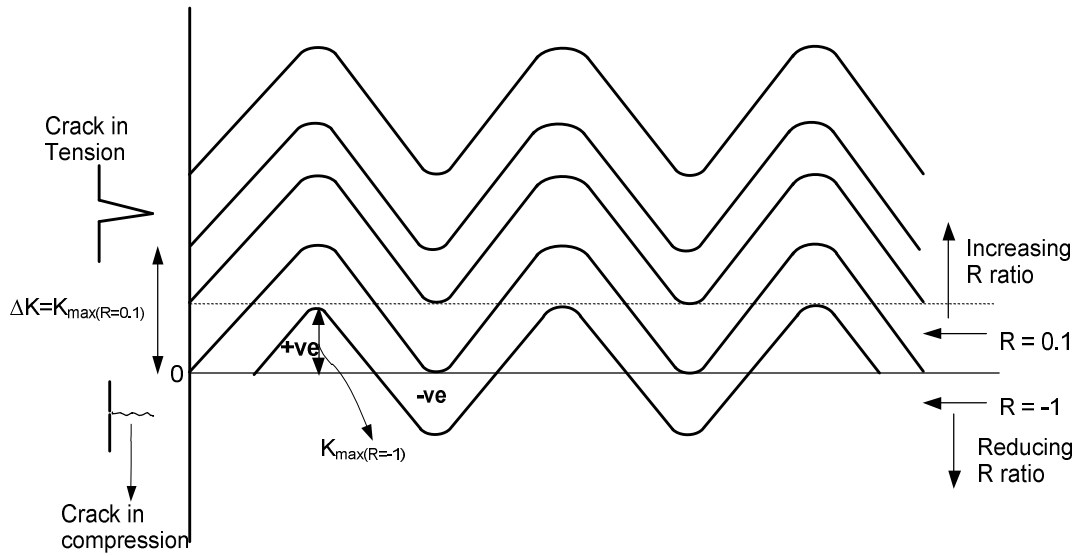


Figure 5-16 Superimposed stress patterns of positive and negative R-ratios

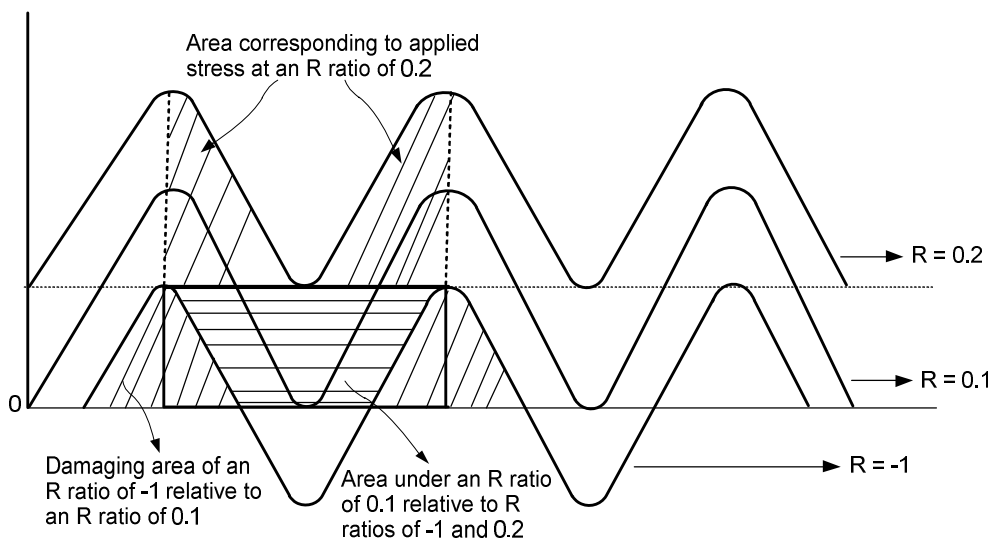


Figure 5-17 Schematic diagram of area ratio correlation

Ideally in an air environment, the fatigue crack closure occurs when the crack is under a compressive stress field and opens when a tensile stress field is applied. This effect results in some changes in the externally applied load and subsequent changes in the applied stress intensity factor range. Therefore, the effects of the residual stresses, which can also be described as crack opening and closing situations, can also be accounted for in crack growth rates by considering the residual stresses as mean stresses. This concept is employed

in this study. The methodology for the model development which considers positive and negative stress ratios is described further in the following sections.

5.6.1 Model development methodology for positive R-ratios

For positive R-ratios, the model is schematically shown in Figure 5-18 for a constant amplitude loading case. The left and right sides of the figure are equivalent to each other over a loading cycle and the figure represents the R-ratios of 0.1 and 0.2 loading cycles. For other increasing R-ratios, the loading pattern will be similar to Figure 5-16 and the area under an R-ratio of 0.1 will increase with respect to an increase in R-ratio. For the corresponding full corrosion effects at a positive R-ratio, the assumption made in the model development here is that only the tensile segment or the positive part of the loading cycle contributes to fatigue crack growth (tension-tension loading case).

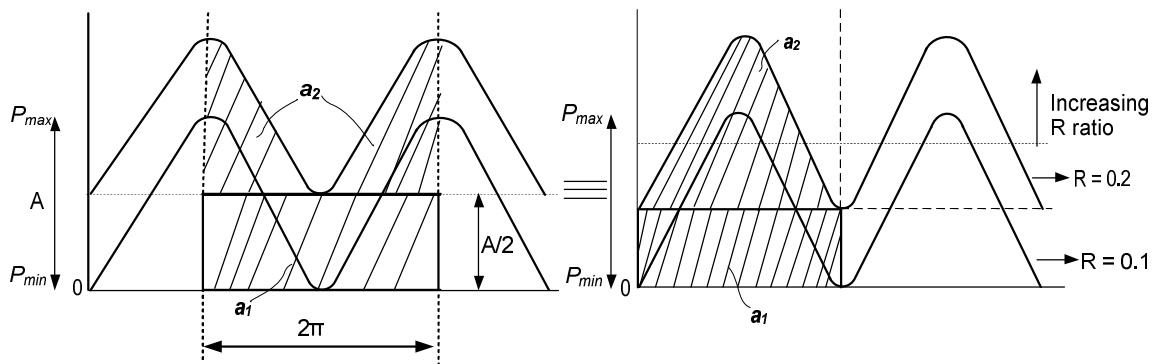


Figure 5-18 Representation of crack opening area at positive R-ratios

The crack opening at a positive R-ratio with reference to an R-ratio of 0.1 is highlighted by the shaded portion of Figure 5-18. This implies that R-ratio effects on fatigue crack growth can be modelled using the crack growth response corresponding to an R-ratio of 0.1. The parameters in the figure are defined as follows:

Area 1 (a_1) is the area of the rectangular segment of the shaded portion, Area 2 (a_2) is the area under the curve above a_1 , P_{min} and P_{max} are the minimum and maximum applied loads in a cycle. It can also be seen that a_2 encompasses some portion of the sinusoidal curve in a_1 , which is the area representing an R-

ratio of 0.1 in the figure. This means that the damage cycle at a positive R-ratio of interest relative to that at an R-ratio of 0.1 with respect to the opening area situation can be given as

$$\frac{a_1 + a_2}{a_1} \quad (5-12)$$

Where for a loading cycle

$$a_1 = \pi A \quad (5-13)$$

$$a_2 = 2 \left(\int_0^{P_{max}} \int_0^{\pi} A \sin \omega d\omega dA \right) \quad (5-14)$$

Where A is amplitude and ω is angular frequency. Equation 5-12 is the area ratio theory multiplier for positive R-ratios in corrosion fatigue and is applied to modify the Paris law (Equation 1-16) as

$$\frac{da}{dN_{corr(+veR)}} = C_{corr} \left(\frac{a_1 + a_2}{a_1} \right) \Delta K^{m_{corr} \left(\frac{a_1 + a_2}{a_1} \right)} \quad (5-15)$$

Where $\frac{da}{dN_{corr(+veR)}}$ is the crack growth rate for the positive R-ratio of interest, while C_{corr} and m_{corr} are the material constants corresponding to an R-ratio of 0.1. In order to obtain crack growth rates in air, Equation 5-15 can be applied by replacing C_{corr} and m_{corr} with C_{air} and m_{air} .

5.6.2 Model development methodology for negative R-ratios

For an R-ratio of 0, $\Delta K = K_{max}$, but for an R-ratio of -1, only the tensile or damaging portion of the loading cycle is effective in crack propagation. Hence, the compression portion of the loading cycle is neglected analytically on the premise that a crack closes during compression. This means that the fatigue crack growth in this situation is controlled by K_{max} (the positive part of ΔK). This also implies that for a specific load/stress range, only half of the time of the fatigue cycle is spent in the damaging or crack opening situation at an R-ratio of -1. The model description is schematically shown in Figures 5-19 and 5-20. If

the two figures are superimposed for the crack opening period at $R = -1$ relative to $R = 0.1$, a_1 is equivalent to the area of the shaded portion under the sine curve for $R = 0.1$ (Figure 5-19), while a_2 is the area of the (shaded) positive part of the sine curve for $R < 0$ (Figure 5-20). The combination of Figures 5-19 and 5-20 is shown in Figure 5-21. Included in the figures are corresponding tensile and compressive segments of the stress cycles.

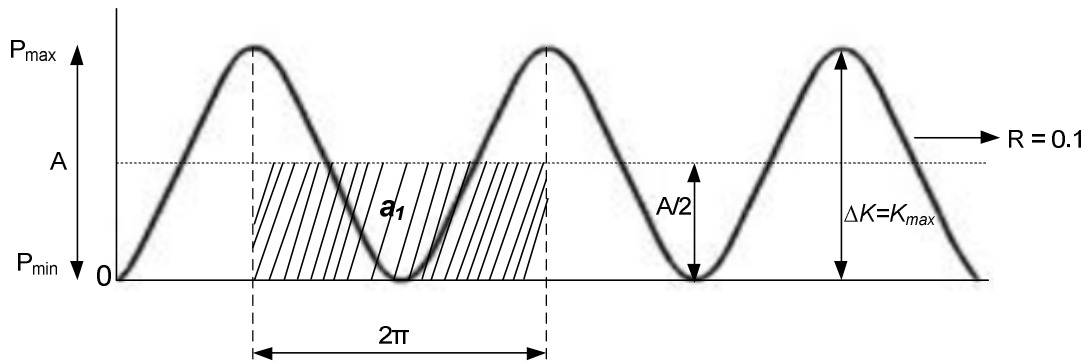


Figure 5-19 Area of loading cycle corresponding to R-ratio of 0.1

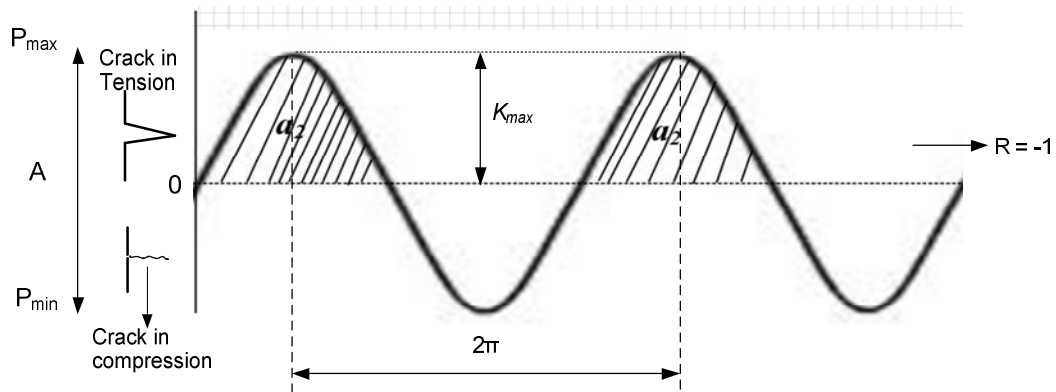


Figure 5-20 Damaging portion of the loading cycle corresponding to R-ratio of -1

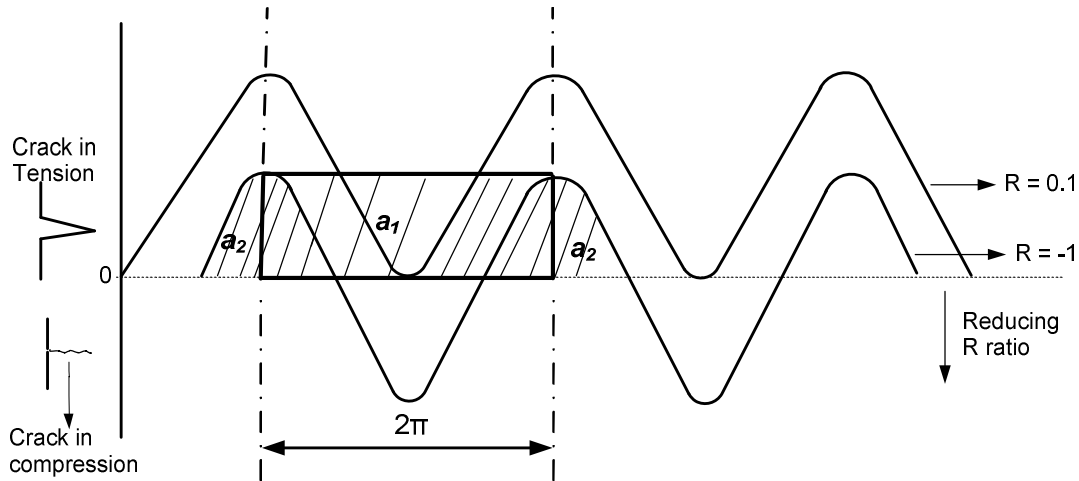


Figure 5-21 Representation of crack opening area at negative R-ratios

Therefore the corrosion fatigue damage cycle at $R = -1$ relative to $R = 0.1$ for an opening area situation is defined as

$$\frac{a_2}{a_1} = \frac{2 \left(\int_0^{P_{max}} \int_0^{\pi} A \sin w d w d A \right)}{\pi A} \quad (5-16)$$

Equation 5-16 is the area ratio multiplier which is applied to predict corrosion damage at $R = -1$ with respect to the unified air and seawater crack growth response. The crack growth rates at $R = -1$ in seawater should lie between the air crack growth data and the crack growth rates obtained at the baseline full corrosion effect ($R = 0.1$). Also, considering only the positive part of the loading cycle, the stress intensity factor range ΔK in Equation 1-16 is replaced by K_{max} and the crack growth rate in air is corrected as

$$\frac{da}{dN_{air R=-1}} = C_{air} (K_{max})^{m_{air}} \quad (5-17)$$

Based on the methodology described above and combined with Equation 5-17, the model for predicting crack growth rate in seawater at $R = -1$, is proposed as follows:

$$\frac{da}{dN_{corr(R=-1)}} = \left[C_{corr} + \frac{a_2}{a_1} (C_{air} - C_{corr}) \right] K_{max}^{\left(m_{corr} + \frac{a_2}{a_1} (m_{air} - m_{corr}) \right)} \quad (5-18)$$

Where $\frac{da}{dN_{air\ R=-1}}$ and $\frac{da}{dN_{corr(R=-1)}}$ are the crack growth rate in air and seawater environments respectively at an R-ratio of -1, while C_{air} and m_{air} are material constants in air at an R-ratio of -1, and C_{corr} and m_{corr} , are material constants in seawater corresponding to an R-ratio of -1.

5.6.3 Experimental studies

The methodology used for testing was described in Chapter 3 but a summary will be given in this section. The material data used for the modelling were obtained from tests that were conducted in accordance with ASTM E647 standard [115]. These data were obtained from the constant amplitude tests conducted on a 16mm thick CT specimen in a laboratory simulated seawater environment at a temperature of 8⁰C-10⁰C, pH of 7.8 to 8.2, loading frequency of 0.3Hz and at loading ratios of 0.1 and 0.5 respectively. The simulated seawater was prepared in accordance with ASTM D1141 [60] and was continuously circulated past the fully immersed specimen at the rate of 3 litres per minute. The data obtained at an R-ratio of 0.1 was used as a baseline in the modelling exercise as previously mentioned.

5.7 Results and discussion of corrosion fatigue crack growth modelling

The predicted crack growth curves in seawater at positive R-ratios are shown, together with experimental data obtained at an R-ratio of 0.1 in Figure 5-22 as plots of da/dN vs. stress intensity factor range ΔK . Stress ratio effects on fatigue crack growth were modelled at R-ratios of 0.2 to 0.7 relative to the baseline data (R-ratio of 0.1) using Equation 5-15. It can be seen that the predicted crack growth curves move to the left of the baseline with increasing R and are parallel to each other with respect to the stress intensity factor range ΔK . It was observed that the crack growth rates increased in a similar manner with respect to ΔK for all R-ratios. Crack growth rates were found to increase with an increase in R-ratio. At R-ratios of 0.1 to 0.4, similar m values were observed from the crack growth response but the C values were different with respect to a

particular R-ratio. However, at the other higher stress ratios ($R \geq 0.5$), slightly higher slopes were obtained.

The effect of higher mean stress can be seen in Figure 5-22 by the noticeable deviations between the crack growth curves at higher R-ratios compared to the lower values. This implies that at higher stress ratios, the crack faces are fully open. Therefore, a crack closure free condition occurs, such that the crack face does not come in contact during the unloading portion of the stress cycle. Another explanation of this is that at a higher stress ratio in seawater, the magnitude of the corrosive elements entering the crack tip are relatively greater than at a lower stress ratio due to the mechanisms of crack tip opening displacement or opening area and the associated stress levels in promoting rapid crack growth. As such, this synergistic interaction between the applied high stress ratio and the corrosive environment is therefore expected to enhance the corrosive activity in the crack tip.

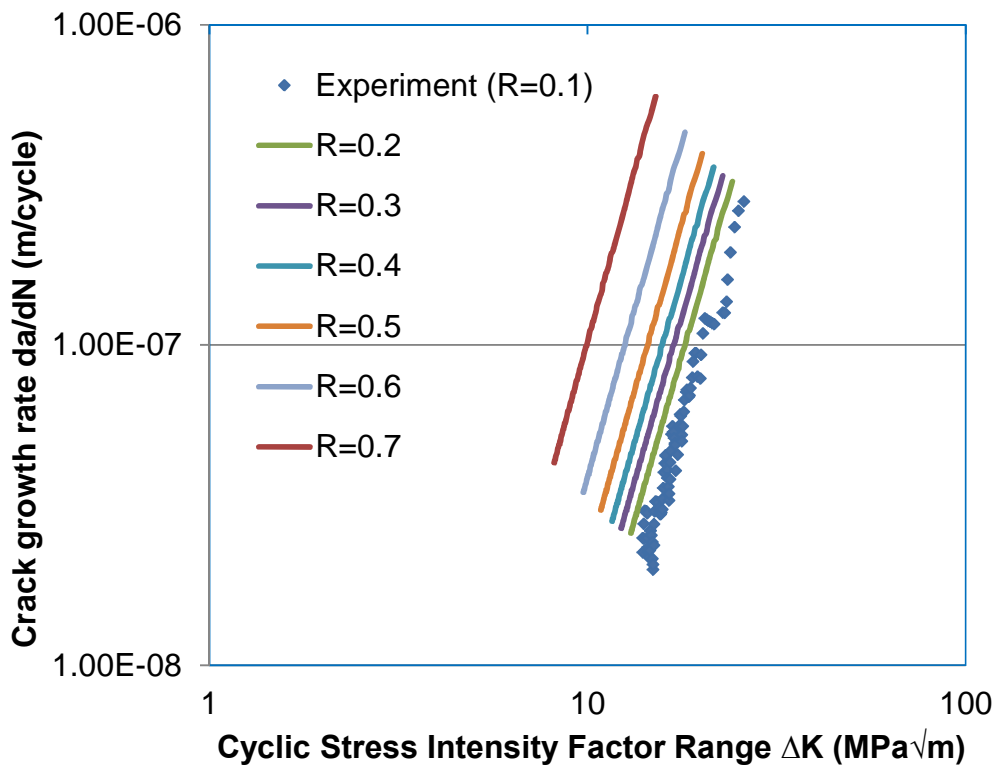


Figure 5-22 Predicted crack growth rates at positive R-ratios

5.7.1 Model validation at positive R-ratios in seawater

The validation of the present model is demonstrated in Figure 5-23. The figure compares experimental data obtained at R-ratios of 0.1 and 0.5 in seawater with modelled crack growth curves at an R-ratio of 0.5. It can be seen from Figure 5-23 that the predicted crack growth curve using Equation 5-15 gave a fairly good agreement with the experimental data, as shown by the similarity in crack growth trends, and with a mean percentage absolute error of 0.3. The present model can be utilized to predict crack growth rates at a particular R-ratio when experimental data for such loading conditions are not available, provided the R-ratio of interest is within the range of validity of the present model.

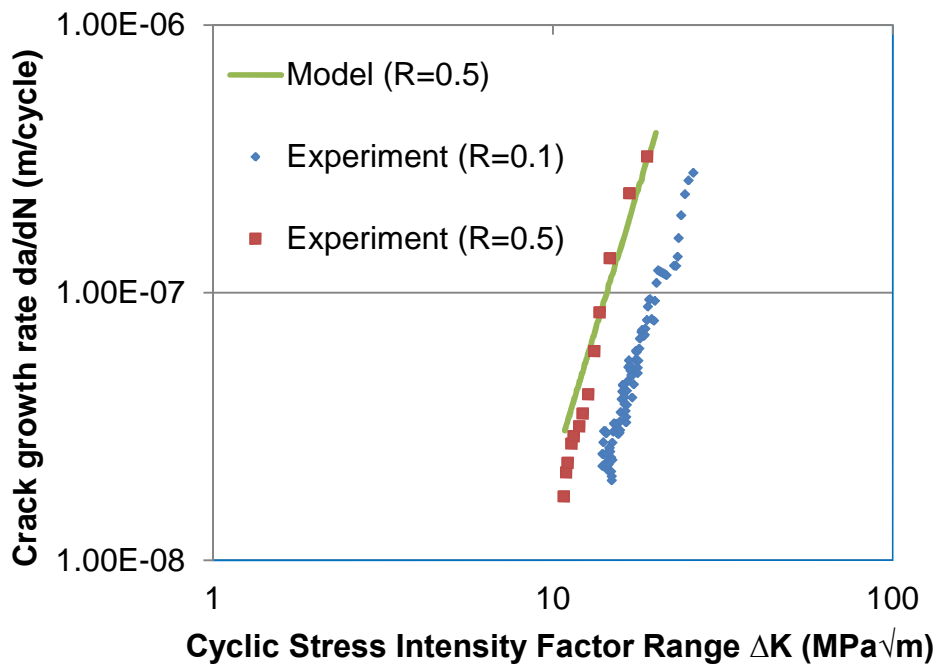


Figure 5-23 Comparison of predicted crack growth rates with experimental data in seawater

The predictions of Equation 5-15 are compared with the observed crack growth rates in seawater at an R-ratio of 0.1, as shown in Figure 5-24. It was observed that nearly 70% of the data points were within $\pm 20\%$ with a mean percentage absolute error of 0.18. The data points that fell outside $\pm 20\%$ are those that were obtained particularly at lower ΔK . This may be as a result of the significant

number of data points recorded during testing. It should be mentioned that the comparison made for an R-ratio of 0.1 was based on back substitution of the C and m values into the crack growth model. However, this would be useful for discussion for the comparison made at an R-ratio of 0.5.

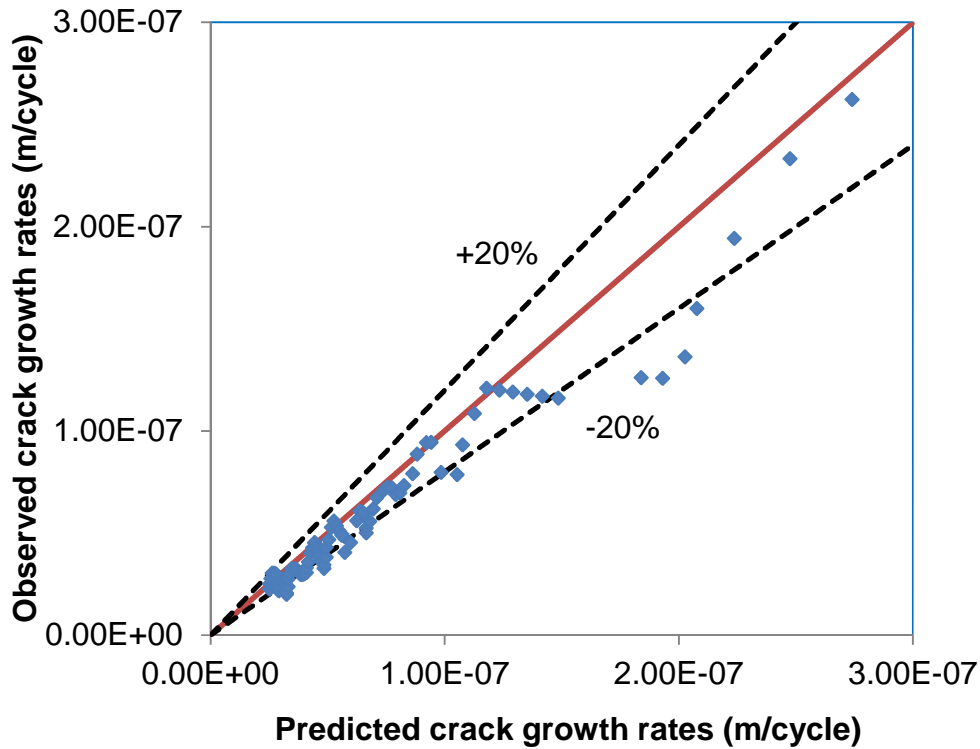


Figure 5-24 Observed versus predicted crack growth rates in seawater at an R-ratio of 0.1

The predicted crack growth rates using Equation 5-15 are compared with those measured experimentally at an R-ratio of 0.5 in seawater, as shown in Figure 5-25. It can be observed from the figure that there was a fairly good correlation with the experimental data and the majority of the data points are predicted to within $\pm 30\%$ with a mean percentage absolute error of approximately 0.3.

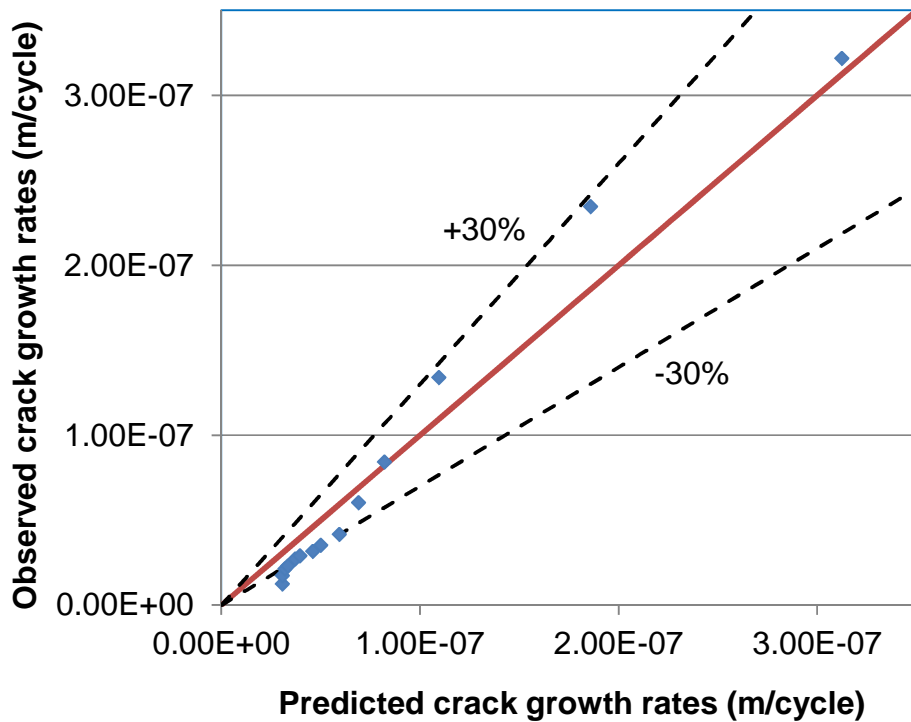


Figure 5-25 Observed versus predicted crack growth rates in seawater at an R-ratio of 0.5

The model developed for the positive R-ratio case was compared with the seawater baseline data and with data corresponding to R-ratios of 0.1 in [2], [15], [68], [74], as shown in Figure 5-26. It can be seen that the present model agrees well with the experimental data. There is also a reasonable agreement between the present experimental data and those obtained by Appleton [15] and Thorpe et al. [2] particularly at lower ΔK , but at higher ΔK the present model and experimental data fall between Appleton and Thorpe et al.'s data respectively. As mentioned in Chapter 2, the environmental test conditions of the results plotted in Figure 5-26 are different from each other with respect to the composition of the seawater and it is anticipated that the effect of the corrosive environment will be dominant at higher ΔK . Therefore the crack growth trends in the figure at higher ΔK may be expected. It can also be seen that the present data increased in a monotonic manner over the entire ΔK while the crack growth trends of Appleton's study are not consistent and converged with Thorpe et al.'s data at higher ΔK . Coupled with a difference in cyclic load

frequency, it is also possible that the difference in chemical composition and mechanical properties of the C-Mn steel used in Appleton's study was related both to the crack growth trend and the closely matched crack growth data obtained at various R-ratios, as mentioned in Chapter 2. It is expected that crack growth rates would increase with an increase in R-ratio, as demonstrated by the present study and as reported by Thorpe et al., despite the amount of scatter in their results, but no effect of R-ratio was seen in Appleton's study at either free corrosion potential or under CP. This implies that mean stress effects on crack growth rates may be material dependent. Included in Figure 5-26 are data obtained from API X65 and API X70 [68], [74] at R-ratios of 0.05 and 0.2 respectively. It can be seen that the API X65 steel crack growth data shifted to the left of the model as expected.

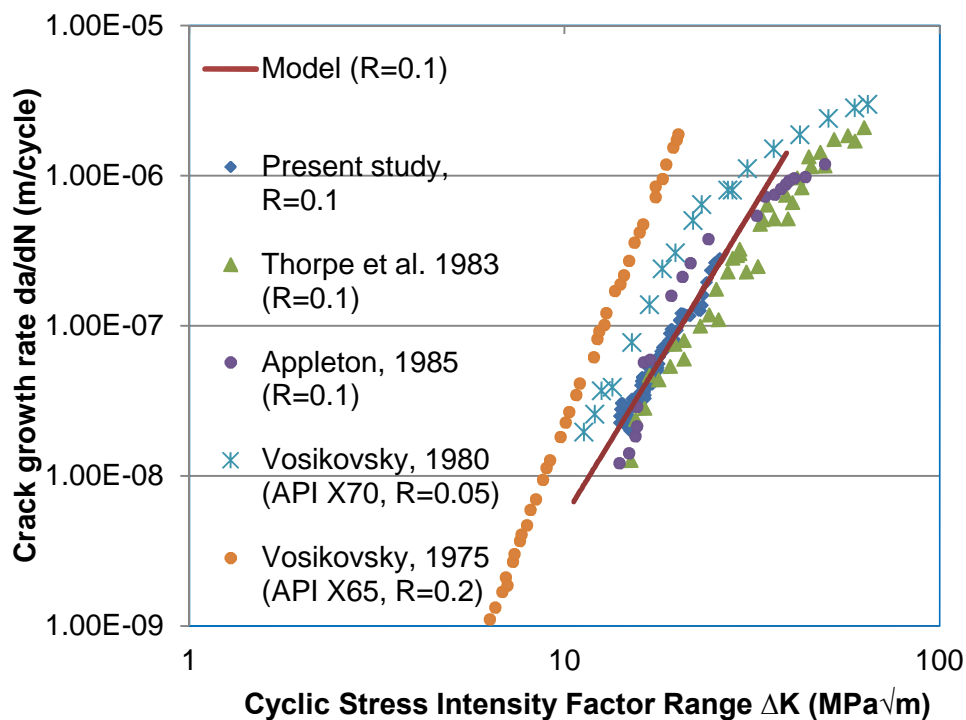


Figure 5-26 Model comparison with experimental data at an R-ratio of 0.1 and 0.2 in seawater

The model was further compared with experimental data collected at an R-ratio of 0.5 from [2] and [15], as shown in Figure 5-27. Included in the figure are the same experimental data plotted in Figure 5-23. It can be observed from Figure

5-27 that the present experimental data appear better when compared with both Appleton's data [15] and the significant scatter observed in Thorpe et al.'s data [2]. However, the predicted curve yields a good agreement with the experimental data and it can also be seen that Thorpe et al.'s data agrees with those obtained in this study, particularly at lower ΔK . However, it is worth mentioning that the effects of CP, applied load and load frequency used in Thorpe et al.'s investigations, and temperatures used for testing in Appleton's study could have a significant effect on the crack growth rates compared to the present study. Therefore, it is important to understand the interaction of these parameters and most importantly the frequency content of the stress cycle for fatigue assessment and results comparison.

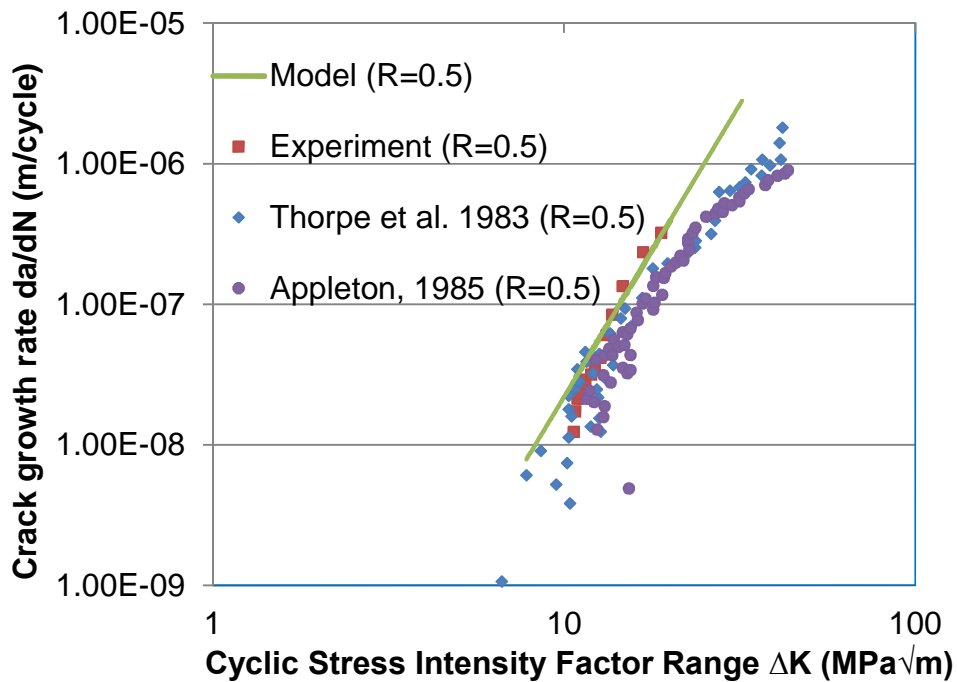


Figure 5-27 Model comparison with experimental data at R-ratio of 0.5 in seawater

Figure 5-28 compares the present model with data obtained using ASTM artificial seawater at various temperatures [15]. It can be seen that there is a little effect of temperature on crack growth rates. It can also be seen that the present model overestimated Appleton's data and shifted to the left of the data points. From the data analysis, the minimum ΔK in the R-ratio of 0.5 test was 10

MPa \sqrt{m} while in Appleton's study for the three cases plotted in Figure 5-28, the minimum ΔK was in the range of 13MPa \sqrt{m} to nearly 16MPa \sqrt{m} . Therefore the shift in the present modelled curve relative to experimental data, as shown in Figure 5-28, could be attributed to the effects of applied load range. However, it can be seen the crack growth trends of the three cases plotted in the figure are quite similar to the modelled curve between ΔK ranges of 10MPa \sqrt{m} to 20MPa \sqrt{m} , above which the crack growth trends deviate towards the right, resulting in a bi-linear relationship.

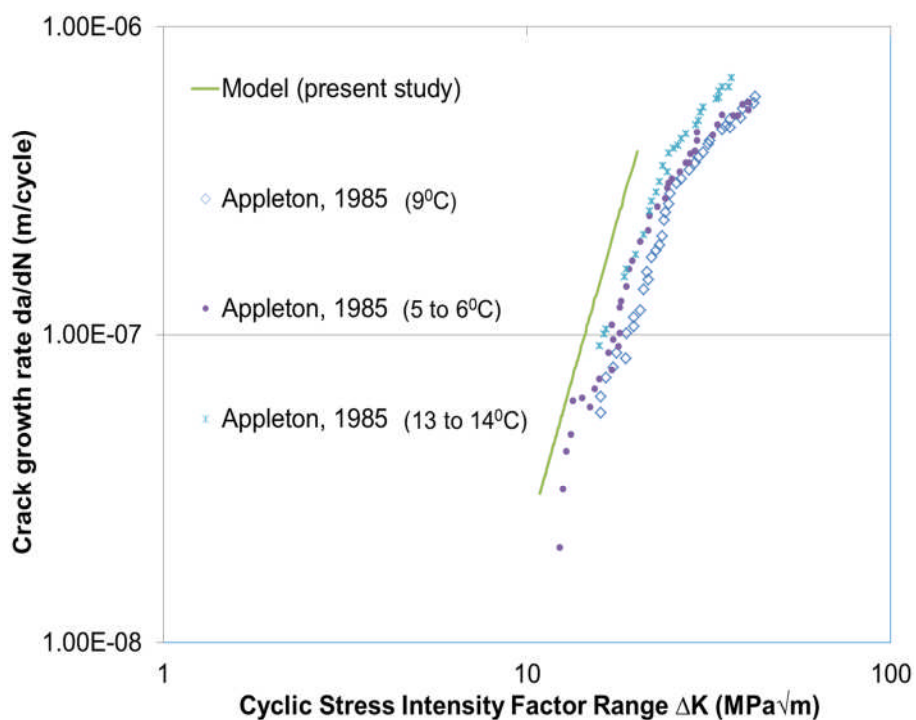


Figure 5-28 Model comparison with Appleton data at an R-ratio of 0.5

The predicted crack growth curves using Equation 5-15, coupled with the material parameters derived at R-ratios of 0.1 and 0.5, are shown in Figures 5-29 and 5-30 as comparisons with the experimental data. The modelled curves showed similar crack growth trends with the experimental data across the range of loading cycles. In the R = 0.5 test, a higher crack growth was measured compared to the predicted one, as shown in Figure 5-30. It should be noted that these are not entirely independent predictions, particularly at an R-ratio of 0.1, as the C and m values from the same tests were back substituted into the crack growth model.

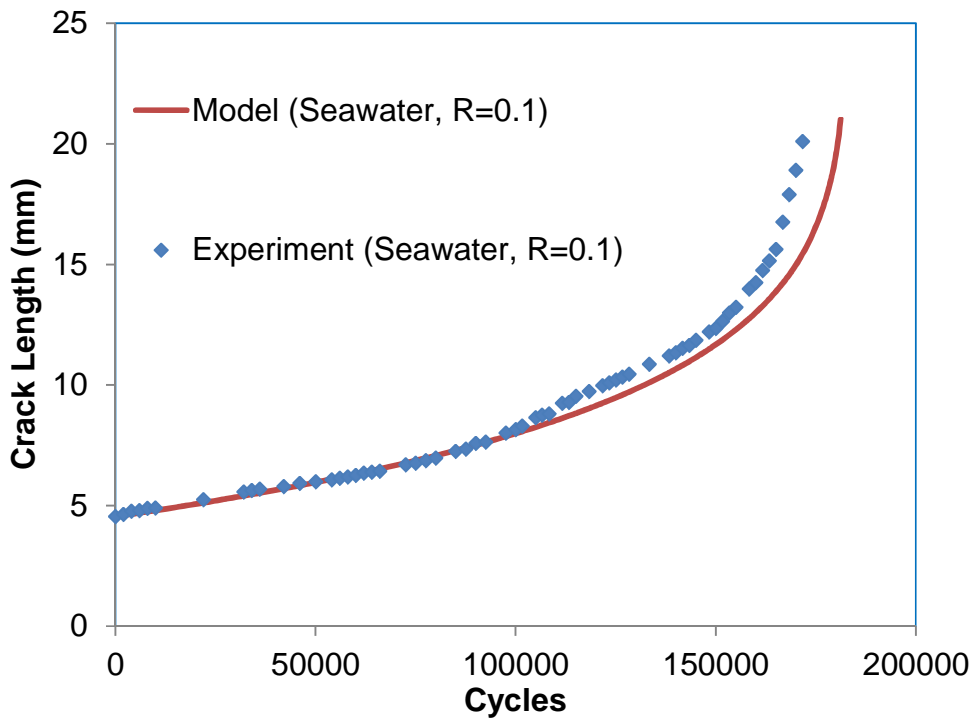


Figure 5-29 Comparison of predicted crack growth in seawater with experimental data at R-ratio of 0.1

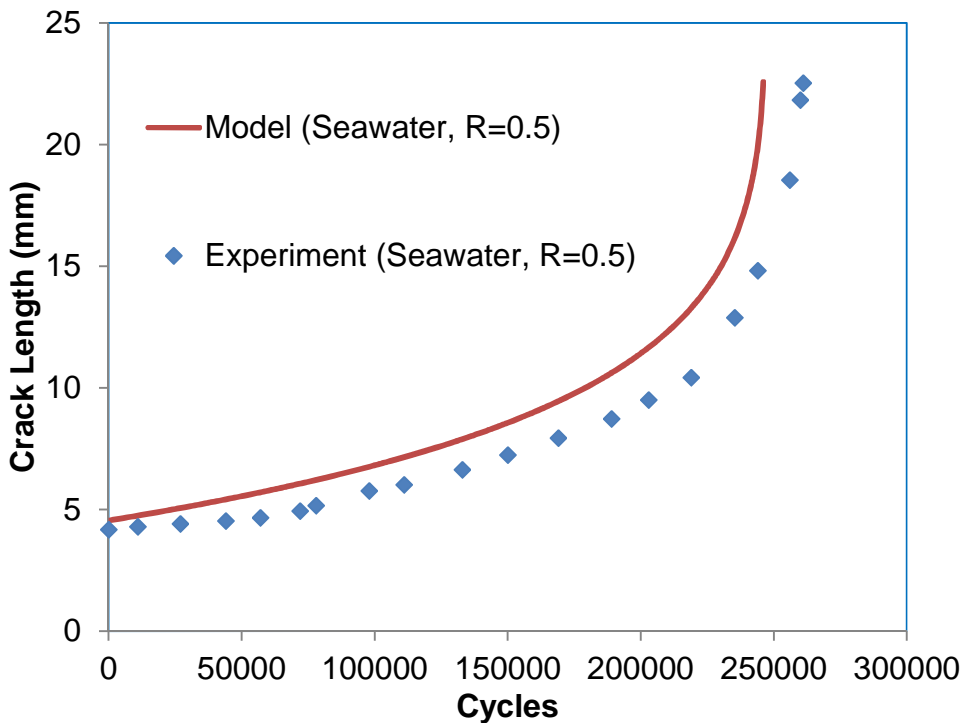


Figure 5-30 Comparison of predicted crack growth in seawater with experimental data at R-ratio of 0.5

This approach can also be extended to predict the lifetime of a welded joint considering a near surface residual stress distribution, on the assumption that the life of a welded joint is consumed under a high stress ratio, as mentioned previously, due to the significant levels of weld induced residual stresses present. However, for a through thickness residual stress distribution that can be found in relatively thick welded steel materials with a similar thickness to that used in newer types of offshore structures, the magnitude of the residual stress distribution may be compressive compared to the near surface tensile residual stress. Therefore, Equation 5-15 cannot accurately predict crack growth rates and Equation 5-18 can be recommended for predictions in such situations.

5.7.2 Model validation at positive R-ratio in air

The predictions of Equation 5-15 are compared with the experimental data obtained at R-ratios of 0.1 and 0.5 in air, as shown in Figure 5-31. It can be observed that the two predicted curves are parallel to each other resulting in similar m values but different C values as expected. The predicted crack growth rates agree well with the experimental data, particularly at an R-ratio of 0.1. However, at an R-ratio of 0.5, the predicted crack growth curve deviated from the experimental data at lower ΔK , but at higher ΔK the predicted curve agrees well with the experimental data. The observed difference between the predicted and measured crack growth rates might be due to the response of the material to mean stress effects at lower ΔK with respect to the material properties and environment.

Also, the trend of the air and seawater data (Figures 5-23 and 5-31) implies that crack growth rate is more sensitive to mean stress effects at higher ΔK ranges than at lower ones. The model comparison with experimental results appears better in seawater (Figure 5-23) than in air. This is probably due to the fact that at a particular stress ratio, the synergistic effects of the corrosive environment and cyclic frequency would enhance the fatigue damage process. Therefore, dissimilar crack growth behaviour may be expected in the air environment where the crack driving force ΔK and crack growth rates were only influenced

by the applied stress ratio. This suggests that the influence of R-ratio on crack growth rates is significantly higher in seawater than in air.

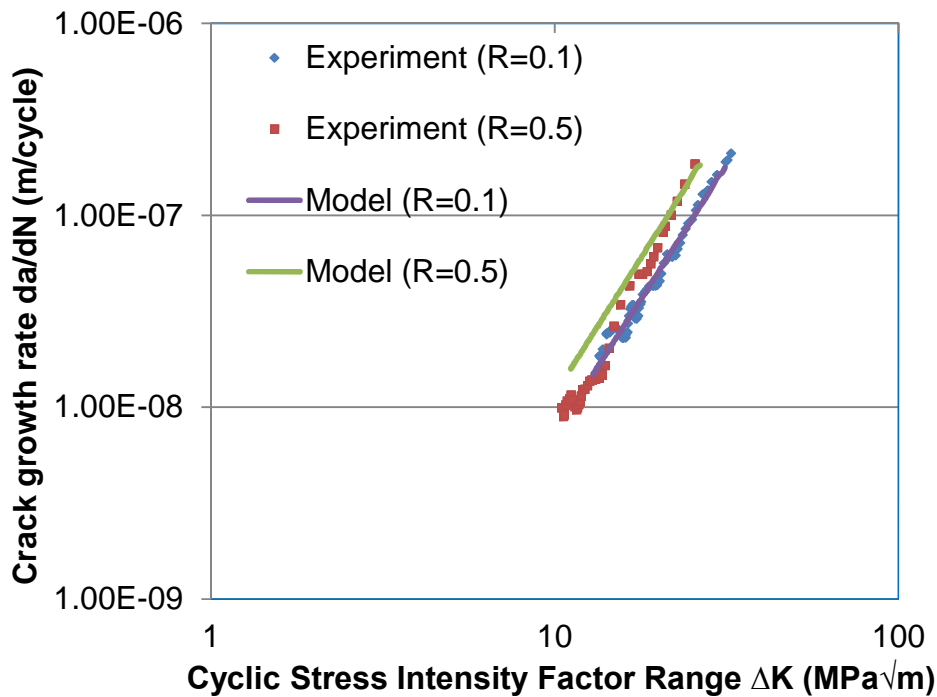


Figure 5-31 Comparison of the predicted crack growth rates in air with experimental data

The predicted crack growth rates in air at an R-ratio of 0.1 using Equation 5-15 are compared with the experimental ones, as shown in Figure 5-32. The data points are predicted to within $\pm 20\%$. It was found that nearly 90% of the data points were within $\pm 20\%$ with a mean absolute percentage error of 0.11. In Figure 5-33, the measured crack growth rates in air at an R-ratio of 0.5 are compared with those predicted using Equation 5-15. The data points were predicted to within $\pm 30\%$ with a mean absolute percentage error of 0.4. The calculated mean absolute percentage error and the corresponding number of data points that fell outside $\pm 30\%$ in the parity plots, as shown in Figure 5-33, also suggest that the new correlation represents the experimental data fairly well.

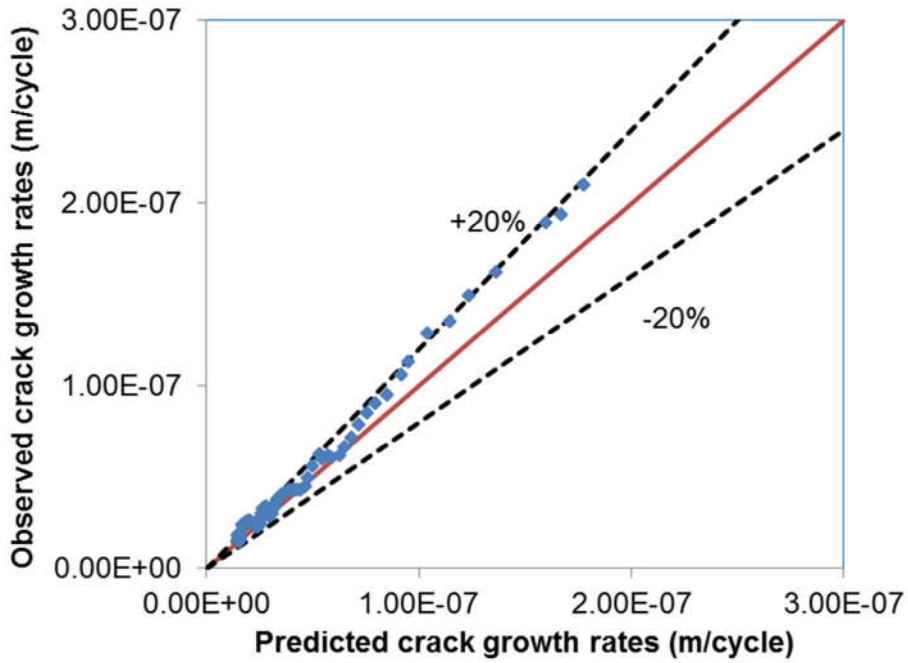


Figure 5-32 Observed versus predicted crack growth rates in seawater at an R-ratio of 0.1

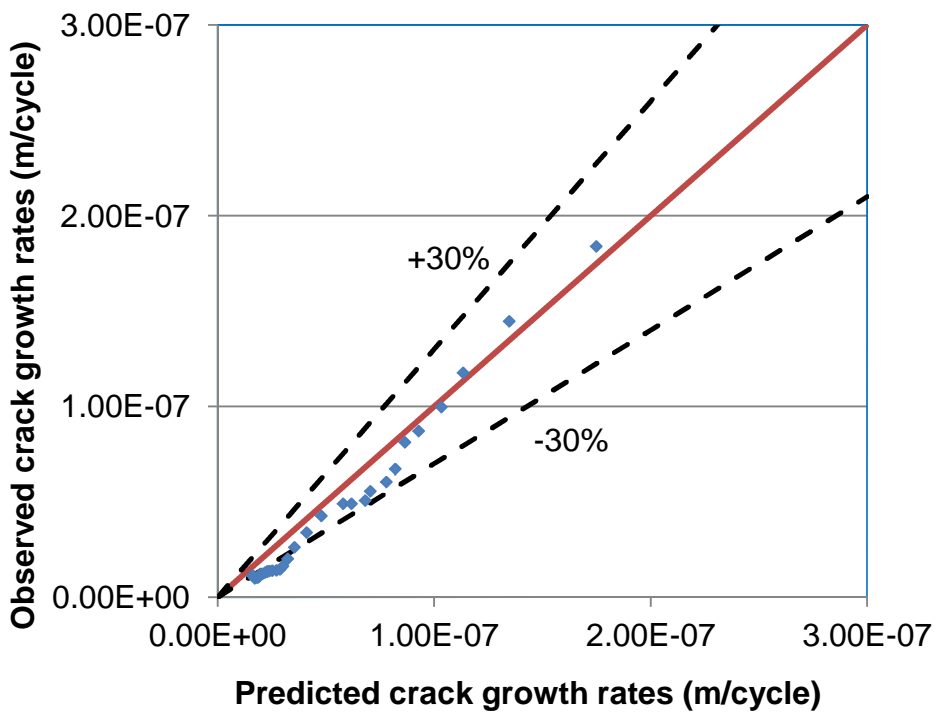


Figure 5-33 Observed versus predicted crack growth rates in air at an R-ratio of 0.5

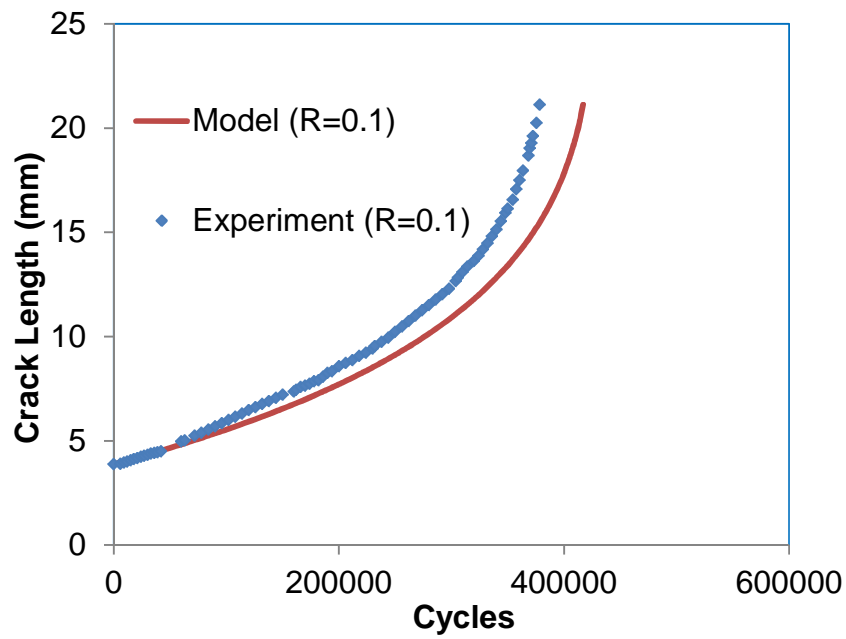


Figure 5-34 Comparison of predicted crack growth in air with experimental data at R-ratio of 0.1

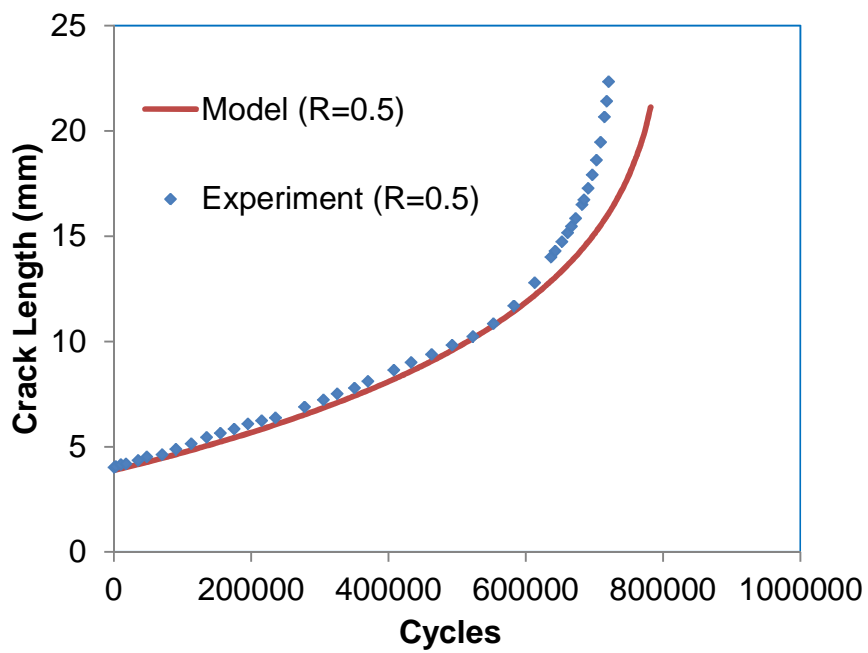


Figure 5-35 Comparison of predicted crack growth in air with experimental data at R-ratio of 0.5

Figures 5-34 and 5-35 compare the predicted crack growth curves in air with experimental data. The modelled curves advanced in a similar manner to the experimental results over the entire test duration, as shown in the figures, but the model slightly over-predicted the experimental data; however, this difference can be considered marginal considering the similarity in the shape of the curves. Further comparisons are made between the predicted and experimental lives in air and in seawater, as shown in Table 5-1.

The ratios of the predicted to the measured life range from 0.94 to 1.01. Correlations of predictions with experimental data have been considered as accurate if the ratio of the predicted to the experimental life is 1 [21]. The ratios depicted in Table 5-1 are nearly 1 which implies that the present model might therefore be considered suitable for fatigue life calculations following more validation against experimental tests.

Table 5-1 Comparison of experimental and predicted lives in air and seawater

Stress Ratio (R)	Experimental life, N_{exp} (Cycles)	Predicted life, N_{pred} (Cycles)	N_{pred}/N_{exp}
Air			
0.1	378500	417000	1.10
0.5	720500	781600	1.08
Seawater			
0.1	171650	181200	1.05
0.5	261000	246000	0.94

5.7.3 Discussion of negative R-ratio data

For the negative R-ratio case, the crack growth rates obtained at an R-ratio of 0.1 in air were corrected by replacing ΔK by K_{max} in Equation 1-16 to obtain Equation 5-17 in terms of the crack driving parameter (K_{max}). This implies that

only the tensile segment of the stress cycle is considered to be the effective region responsible for crack growth. This result is plotted in Figure 5-36 and included in the figure are the experimental data obtained at an R-ratio of 0.1. As mentioned earlier, it is assumed that the predicted crack growth rates at an R-ratio of -1 in seawater would lie between the air and seawater data obtained at an R-ratio of 0.1. The derived crack growth data in air using Equation 5-17 was utilized to achieve this procedure. The result is shown in Figure 5-36 where it can be seen that the crack growth curve for an R-ratio of -1 shifted to the right of the baseline data (R=0.1). Crack growth rates were also found to be higher at an R-ratio of 0.1 than at an R-ratio of -1 as expected.

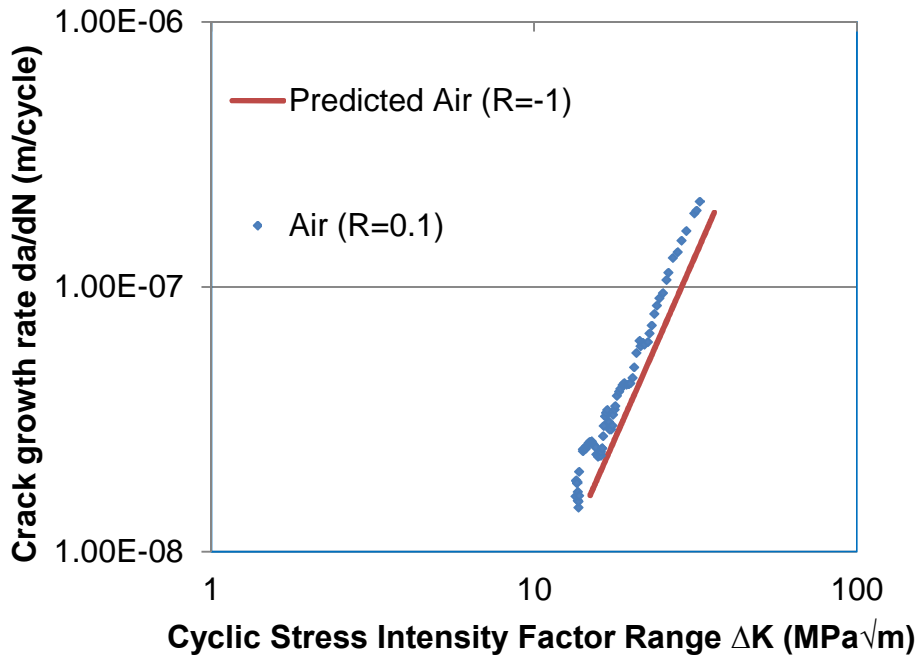


Figure 5-36 Crack growth rates in air

Figure 5-37 also shows a comparison between the prediction of Equation 5-17 and the experimental result obtained at an R-ratio of 0.1 as a plot of crack length versus number of cycles. A noticeable difference of approximately one third of the number of cycles consumed at an R-ratio of 0.1 was observed between the two curves.

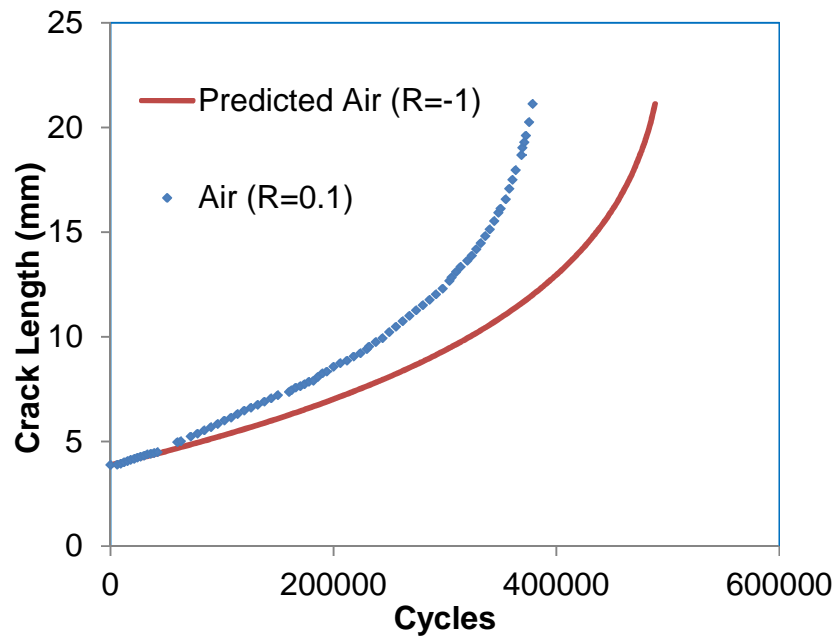


Figure 5-37 Fatigue crack growth in air

Figure 5-38 shows the predictions of fatigue crack growth in seawater for a negative R-ratio using Equation 5-18. The predicted curve is compared with experimental data obtained in air and in seawater at R-ratios of 0.1 respectively. It can be seen that the predicted curve lies between the seawater and the air data and moves to the right of the seawater curve which implies the mean stress effect at R-ratio of -1 is clearly demonstrated. Crack growth rates were also shown to be higher at an R-ratio of 0.1 than at an R-ratio of -1. This appears practical because only half of the stress cycle was spent in the damaging portion at an R-ratio of -1, compared to wholly tensile loading at an R-ratio of 0.1.

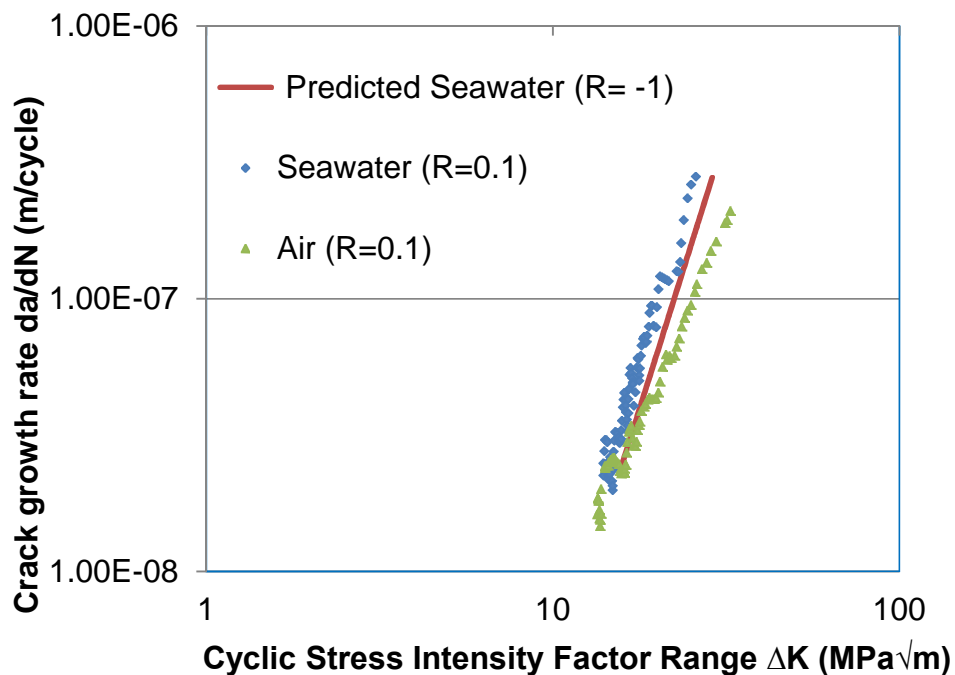


Figure 5-38 Comparison of the predicted crack growth rates in seawater with experimental data

Therefore, it is expected that the degree of damage caused in the R-ratio of 0.1 test will be relatively higher than at an R-ratio of -1 where the crack propagation with respect to environmental damage would be limited to the tensile segment or half the stress cycle. The significance of the model (Equation 5-18) for negative R-ratios is its ability to predict the material behaviour under the action of tension-compression loading in seawater using the material response data obtained in air and seawater under the tension-tension loading case. The novel modelling procedure developed and discussed in this section may be adequate for generating data for a positive and negative R-ratio without testing.

5.7.4 Model application to service life prediction

It is anticipated that in service, the loading scenario experienced by the structures will be similar to the nature of stress range which occurs at an R-ratio of -1 due to a combination of bending moments that might be experienced from lateral loads. Therefore it will be preferable to relate the crack growth results obtained here to the expected life of the structure or a particular section with a

pre-existing defect under a low stress and high cycle regime. This extrapolation procedure can provide useful information in planning inspection and repair scheduling so that fitness for purpose can be successfully realised. Typical offshore structures such as those used for offshore wind and oil and gas applications are designed for a 20-year service life. Therefore, the procedure described here was conducted for a 20-year design life under reduced operating stresses by applying the predicted response data obtained at an R-ratio of -1 in seawater. It should be noted that the predictions made in this section were based on CT specimen geometry which does not represent the geometry of the real offshore structures. Therefore, the K_{max} values substituted in Equation 5-18 to obtain the number of cycles are those derived using CT specimen geometry. However, the approach described here might be useful if extended for the prediction of crack growth in real structures using the exact geometry and K solutions. The number of years at a particular crack depth was estimated using Equation 5-19, for a structure experiencing a cyclic loading frequency of 0.3Hz. While the applied load used for predicting a 20-year design life corresponds to 10^8 cycles.

$$number\ of\ years = \frac{number\ of\ cycles}{days \times time \times frequency} \quad (5-19)$$

Due to the low stress encountered in service, it is assumed that the fatigue crack will advance gradually relative to the design life such that an existing crack of known dimension can be planned for inspection in the future. Similar crack growth behaviour of offshore structures describing the number of cycles to failure for a service life of 20 years is shown in Figure 5-39. The data plotted in the figure were scaled up to predict the crack growth behaviour in a 150mm thick plate in order to represent a similar damage scenario in real offshore structures. The initial data with a minimum crack depth of 4mm were also offset to zero. The result of this prediction is depicted in Figure 5-40.

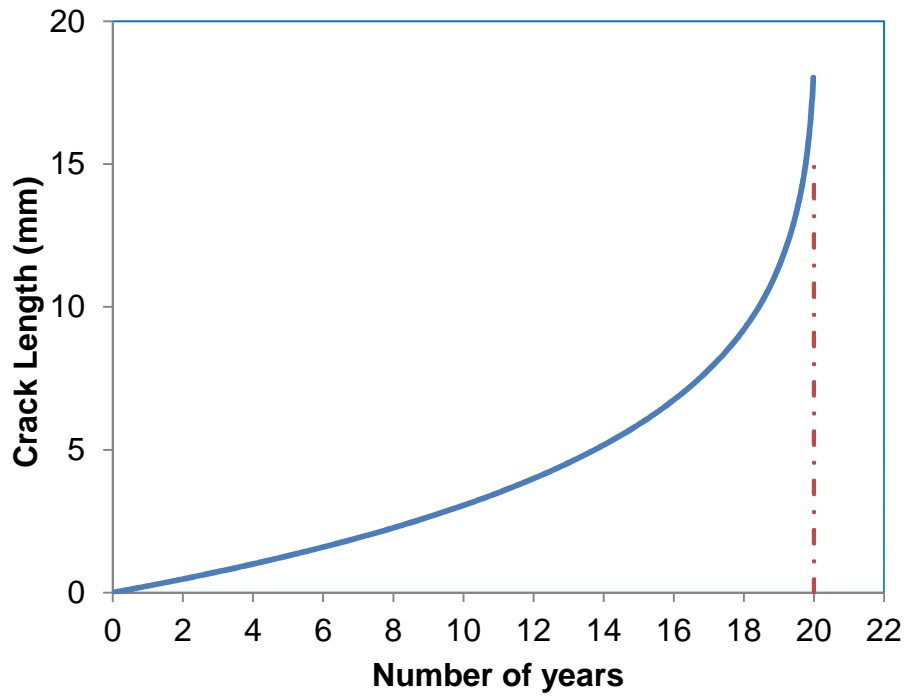


Figure 5-39 Prediction of crack growth behaviour in service

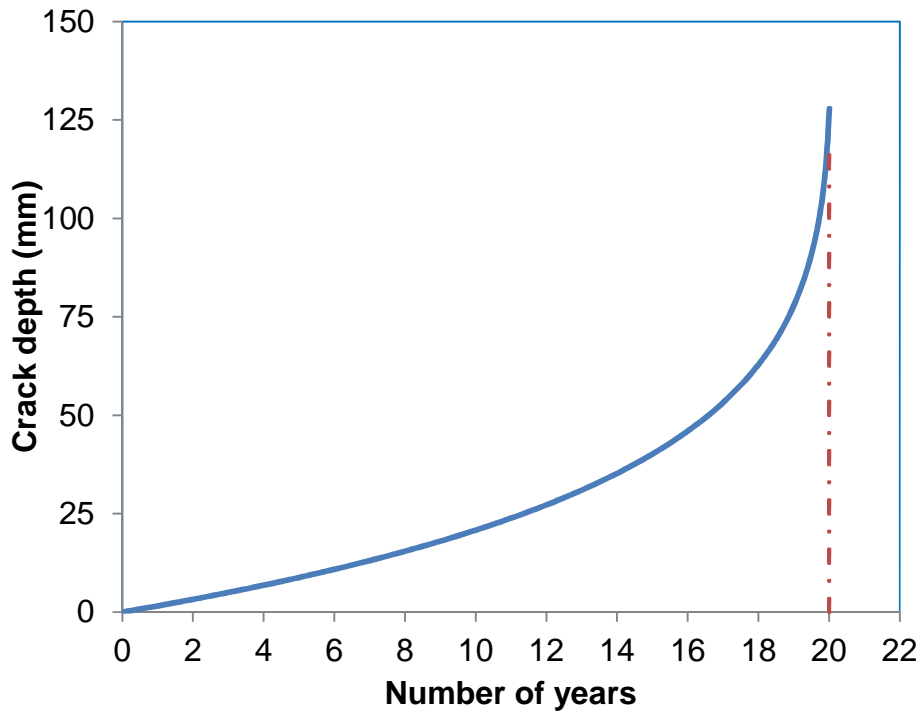


Figure 5-40 Crack growth prediction for a 150mm thick structural member

It is understood that offshore tubular section varies in thickness but the approach described here may be applied in studying the crack growth

behaviour of a particular section with respect to the thickness. In accessing the through thickness cracks in a joint with an assumed initial cracked depth, Figure 5-40 implies that in 4 years the crack would have grown to a depth of approximately 7mm if the thickness effect is assumed to be negligible. For example, if a 4 yearly inspection procedure was set out as the initial plan, it means that in 8 years, the crack would have reached a depth of nearly 16mm. If a repair procedure had been recommended at the first inspection, it is possible that the crack would not have attained that depth in 8 years. In such situations, the cost of repair will significantly increase, coupled with the frequency of inspection. In 18 years, Figure 5-40 shows that the fatigue crack would have attained nearly half the thickness of the member such that the load carrying capacity of the remaining uncracked ligament would have significantly reduced. In this situation a repair attempt may not be realistic. Therefore, the procedure described above implies that the behaviour of the structures under laboratory conditions using representative materials can provide useful information towards understanding how to schedule the frequency of inspection and repair procedures. The application of the present model to weldments will be described further in Chapter 6.

5.8 Model comparison with other fatigue crack propagation models

The present model was also verified by comparing the response with some of the previously described fracture mechanics based models given in Equations 5-4 to 5-11. Crack growth curves in air are compared in Figure 5-41. In Figure 5-41a, the present model and all the other applied models are parallel with the experimental data obtained at R-ratio of 0.1 in air. As the R-ratio was increased (Figure 5-41b to 5-41e), the predicted curves shifted to the left of the baseline as expected.

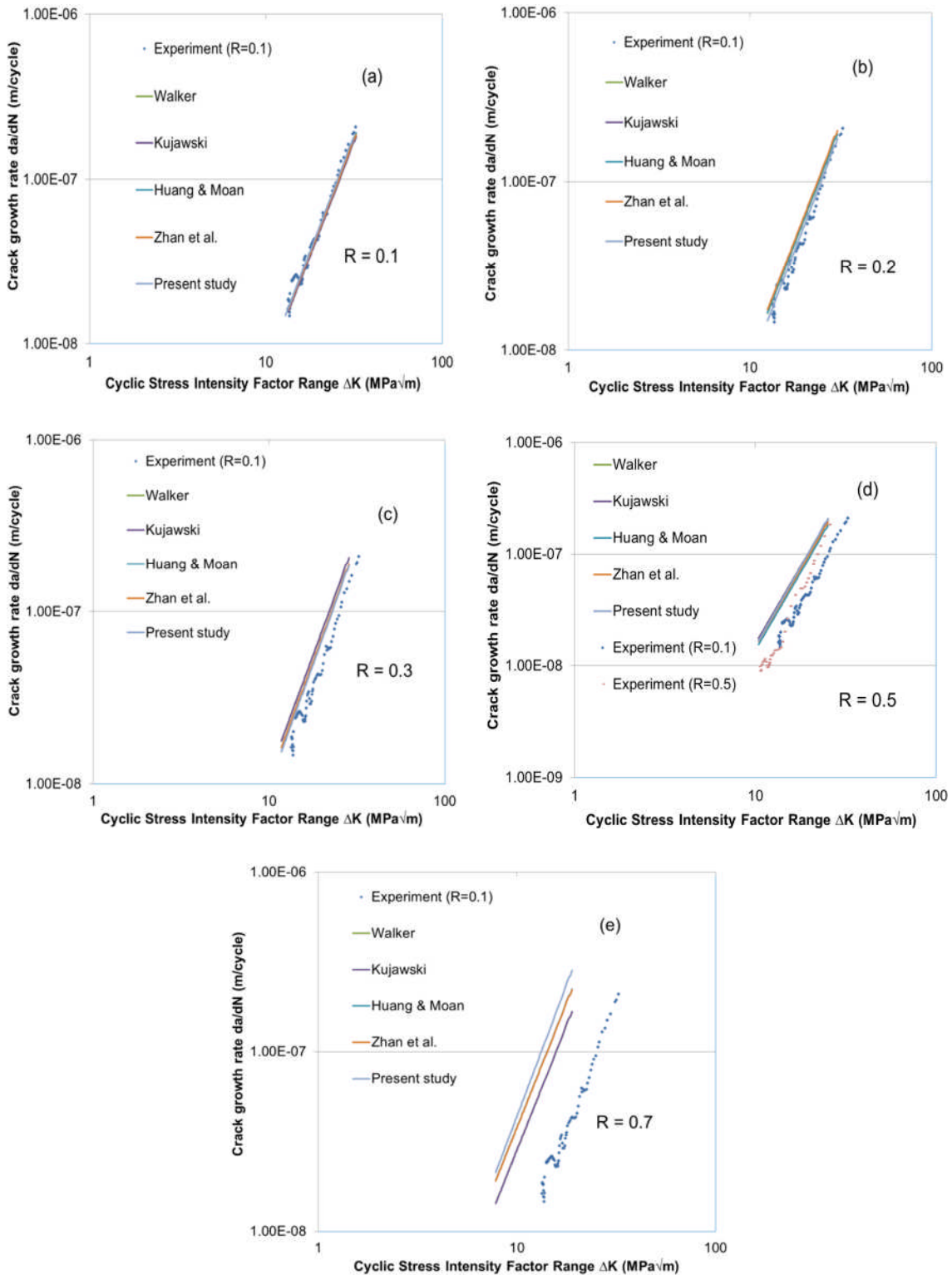


Figure 5-41 Model comparison with other crack propagation models in air

The present model agrees well with the other models examined in air from R-ratios of 0.1 to 0.5, as shown in Figure 5-41. At an R-ratio of 0.7, Kujawski's and

Walker's predicted curves are parallel and resulted in lower growth rates compared with the present model and Zhan et al.'s predictions. It can also be observed from Figure 5-41e that the Zhan et al. predicted curve is closer to the present model compared to the remaining models tested. The inconsistent responses from the models, particularly at an R-ratio of 0.7, may be due to the difference in correction factors associated with the models, which is likely to have appreciable effects on crack growth rates at higher stress ratios.

The predicted crack growth curves in seawater are compared in Figure 5-42 and it can be seen that the present model agrees well with the other models at R-ratios of 0.1 and 0.2. These results are shown in Figures 5-42a and 5-42b. At an R-ratio of 0.3, only Huang and Moan's model agrees with the proposed model while Kujawski's and Walker's predicted curves deviate from the other predictions. At an R-ratio of 0.5 and 0.7, the present model overestimated the crack growth rates compared with the other models. It should be noted that crack propagation mechanism in seawater is different from in air due to the various factors contributing to the process. Therefore it is expected that mean stress effect will be more significant in seawater than in air. Comparing the general behaviour of the models used for prediction against the current model, for the cases considered in the present investigation, much better agreement was observed at all the positive R-ratios considered in air and at lower R-ratios in a seawater environment.

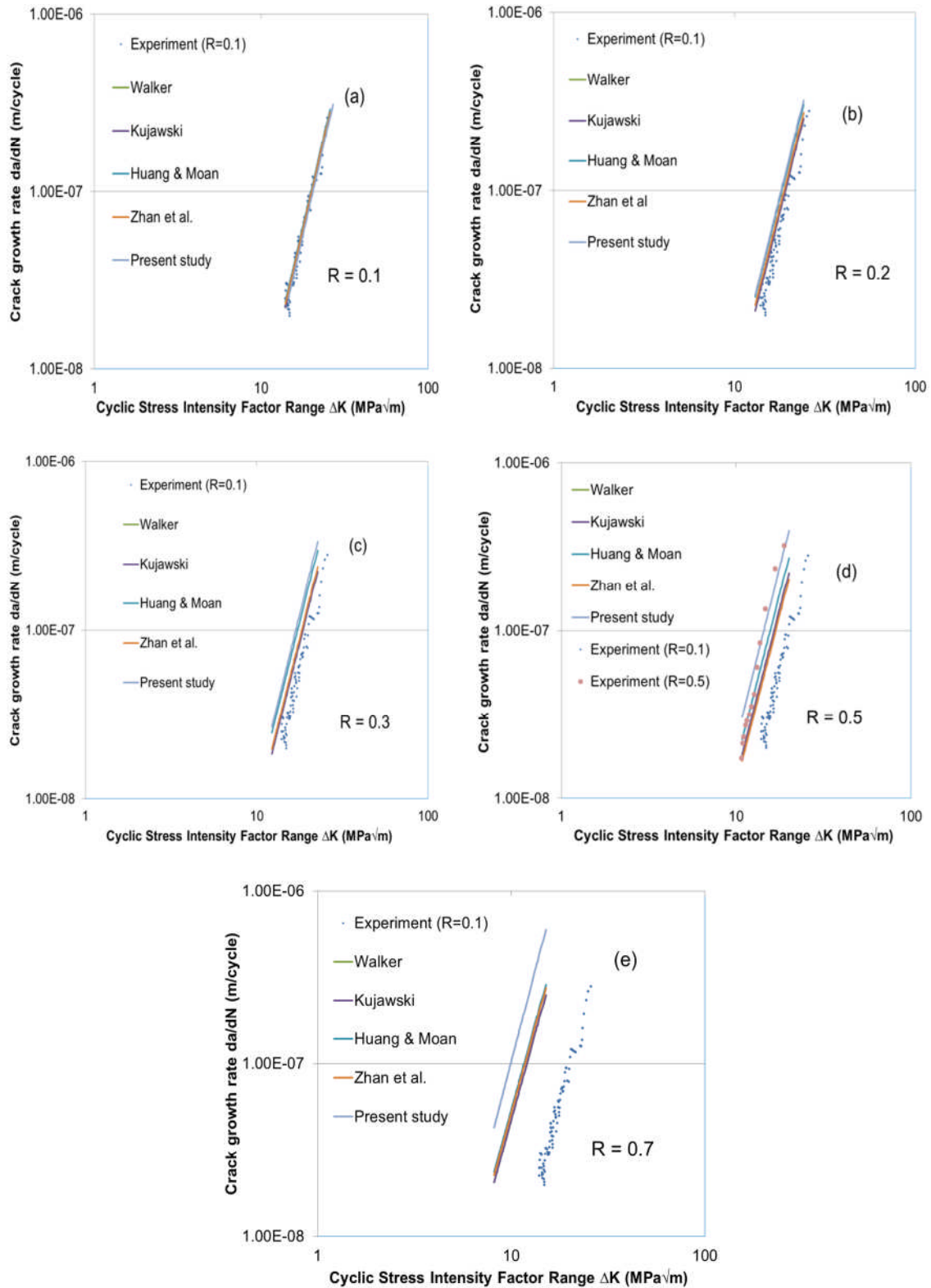


Figure 5-42 Model comparison with other crack propagation models in seawater

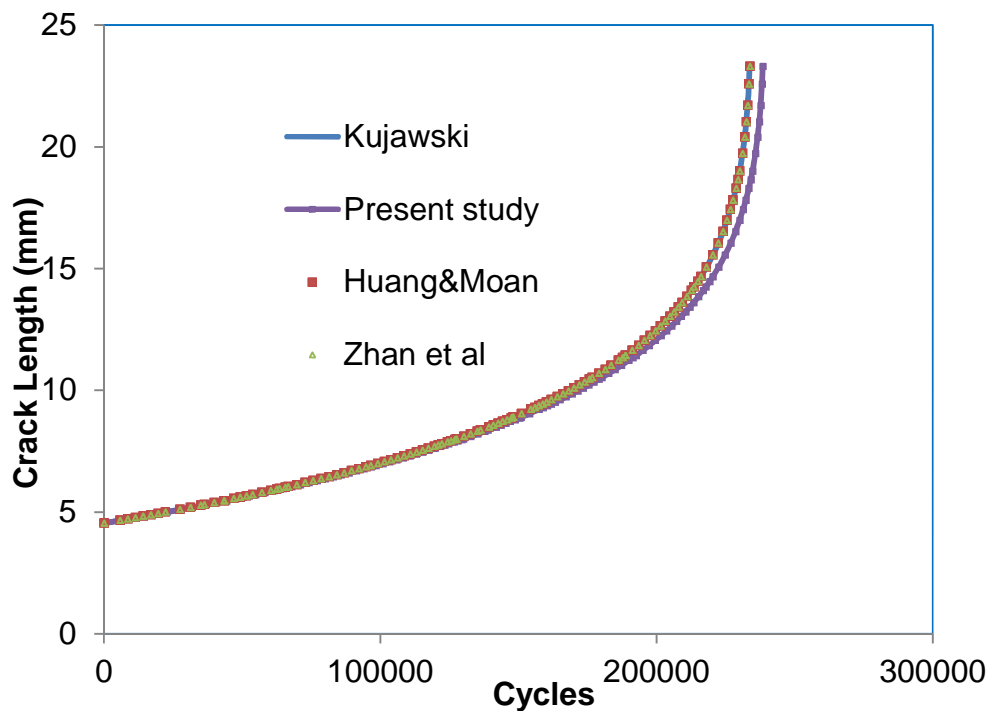


Figure 5-43 Comparison of predicted fatigue crack growth in seawater at an R-ratio of -1

To verify the accuracy of the present model for the negative R-ratio case in seawater, the predicted curve using Equation 5-18 is compared with the other examined models, as shown in Figure 5-43. The comparison was made considering only the models that are valid for a negative R-ratio, as previously described. The model yields a good agreement with the other tested models as shown in the figure. This is evident from the similarity in the curves over all the range of loading cycles. From the results and analysis carried out in this chapter, it should be mentioned that the present model appears better for negative R-ratio cases than the positive cases in air and seawater respectively. The analyses made in this chapter may represent both tensile and compressive mean stress/residual stresses depending on their locations within the structure. However, experimental data obtained under similar conditions as those used in the present work are needed to further validate the model developed for the negative R-ratio case.

5.9 Summary

Various fracture mechanics based fatigue crack propagation models have been discussed in this chapter. The accuracies of the models have been demonstrated by comparing them with the experimental test results reported in Chapter 4 and with those from the literature. A new methodology has been developed to estimate corrosion fatigue crack growth considering the crack opening area corresponding to only the damaging part of a fatigue cycle. This methodology is unique and not considered by the current fracture mechanics based models. The following conclusions can be drawn:

- Prediction of lifetime in service can be reliably achieved if an appropriate model is used that takes into account the effects of mean or residual stress similar to what is experienced in service.
- Due to the time and cost involved in conducting experimental tests at all possible stress ratios, modelling R-ratio effects on crack growth rates may be a valid and cost-effective approach for generating data for fatigue life calculations.
- A new methodology that accounts for mean stress effects on fatigue crack growth rates using the crack opening period per fatigue cycle has been presented. This methodology was developed using constant amplitude crack growth data and may be applied for predictions under random loading if the associated load interaction effects can be quantified.
- The model developed has been used to explain a preliminary extrapolation approach to represent similar crack growth behaviour in typical offshore structures with a service life of 20 years. It would be useful to extend this procedure for prediction using the geometry and stress conditions experienced by real structures so that decisions regarding inspection and repair of the structures in service can be made.
- The present model, when compared with experimental data, gave fairly good agreement. The verification of the new model was also achieved by comparison with other fracture mechanics based crack propagation

models to obtain a reasonable agreement. However, more tests are needed, especially at higher R-ratios ($R > 0.5$) in air and in seawater in order to validate the model further and also to verify the applicability of the model within the reported range of validity.

6 A Study of Fatigue Crack Growth in Offshore Wind Monopile Steel Weldments

6.1 Introduction

Significant data relating to crack growth behaviour in parent plates of steels used for offshore structures was presented in Chapter 4. However, a combination of the crack growth behaviour in parent materials and weldments may provide a better understanding of fatigue damage mechanisms in offshore structures. Since it has been established from the literature survey that fatigue cracks initiate at the HAZ and propagate into the unaffected parent material, the crack growth mechanism of welded joints therefore needs to be better understood. Also, in spite of the significant number of corrosion fatigue data that are available in the literature, almost none has been generated from structural steel grade S355J2+N steel HAZ and weld materials.

In this chapter, a study of the corrosion fatigue behaviour of HAZ and weld materials fabricated from offshore structural steel plate similar to those used for offshore wind monopile support structures is presented. The specimen characterisation and extraction procedure is described. Comparisons are made between the data generated in this chapter and those obtained from parent materials. The results of the findings are compared with the literature data and are also discussed with respect to fractography and metallography examination of crack surfaces and crack paths.

6.2 Material and welding procedure

In order to represent the crack growth behaviour in monopile structures as closely as possible, a 90mm thick plate was selected for investigation. The weld plate is shown on the left of Figure 6-1, while the right of the figure depicts the dimensions of the weld plate. The plate was manufactured from S355J2+N steel and welded with filler materials with a similar composition to the base material and through a standard procedure similar to those used for monopile support fabrications. The weld direction was parallel to the rolling direction of

the plate as shown on the right of Figure 6-1, in order to represent the rolling and weld directions of monopile structures.

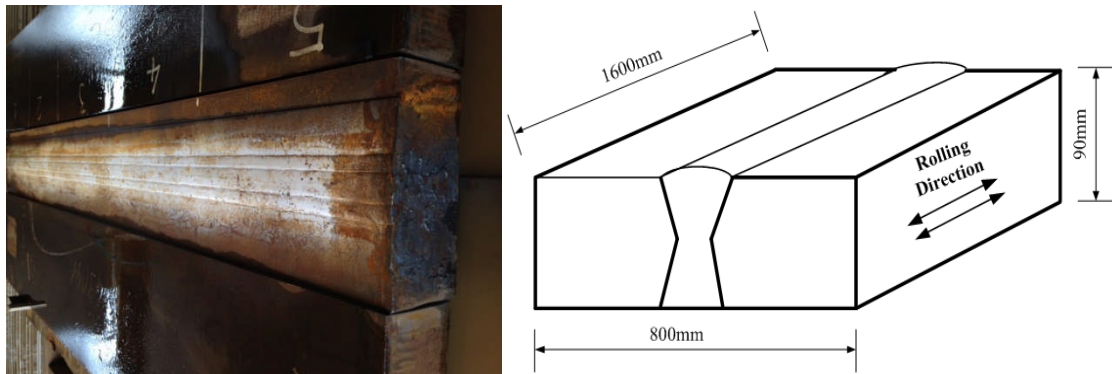


Figure 6-1 (a) 90mm thick weld plate (b) weld plate dimensions

The welding was conducted by EEW and the Sif group and was carried out in accordance with DNV-OS-C401 recommendations, using the submerged arc welding (SWA-Twin/Tandem-twin) process with the filler material designated as S466 FB S3Si. The filler material was 4mm in diameter and has a similar composition to the base material. The composition of the filler material was taken from [146] and is set out in Appendix D. Details of the welding procedure are also given in Appendix D.

6.3 Specimen preparation

In order to ensure that the direction of crack growth in the HAZ of circumferential welded monopile supports can be reproduced using small scale laboratory specimens, it is important to align the HAZ along the crack path. The alignment technique and the specimens' extraction methodology were developed at Cranfield University. Prior to the specimens' extraction, a 10mm thick plate with a width of 200mm which encompasses the weld area was cut through the thickness of the weld plate in order to establish a datum reference line to the weld area.

6.3.1 Cutting

It was anticipated that the HAZ is a narrow region of the parent material, as also observed from a previous investigation of a 50mm thick weld plate. In order to

ensure a successful alignment of the crack path with the HAZ zone, a datum line of 1mm depth was created at about 70mm from the weld centre line and along the length of the plate, as shown by the red arrow in Figure 6-2.

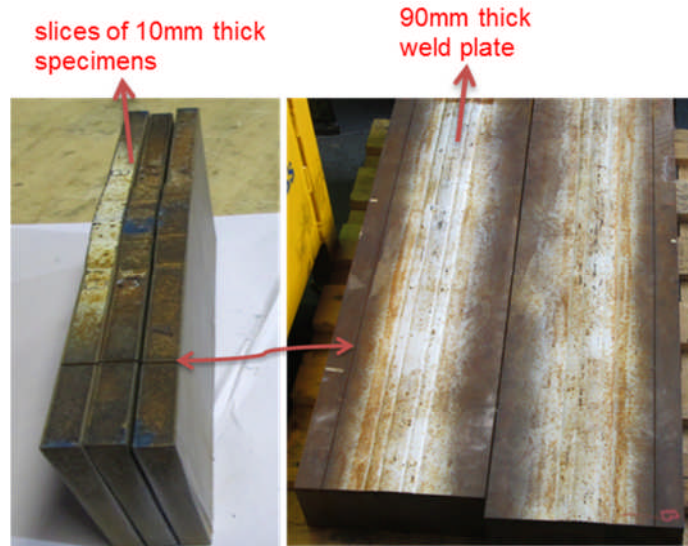


Figure 6-2 Cutting procedure

The intention of this was to assist the specimen's fabricators in locating the HAZ areas of the weld plate effortlessly. Three slices of 10mm thick specimens were machined from the edges and the middle section of the plate, as shown in the left of Figure 6-2 in order to establish uniform HAZ dimensions. 100mm length specimens were then extracted from the three slices of the specimens taken across the length of the weld plate for grinding and polishing.

6.3.2 Grinding and polishing

Grinding of the specimens' surfaces was conducted under wet abrading on a Metaserv grinding and polisher with the aid of 120, 240 and 1200 grit silicon carbide abrasive papers in ascending order. The specimens' surfaces were then sprayed with alcohol, cleaned and dried to avoid rust deposits. The specimens were polished using a polisher cloth of the appropriate size mounted on the rotating wheel of the Metaserv polishing machine. The cloth was sprayed with alcohol intermittently in order to achieve a wet surface throughout the process. The process was carried out with the application of diamond paste on the polishing cloth in order to achieve a surface finish of 6 μ m. This was

repeated with a polishing cloth corresponding to a surface finish of 1µm while a final surface finishes of 0.5µm was achieved using colloidal silica master polish. In order to avoid the introduction of pits which may have a significant effect on metallography examinations, the specimens were washed with soap and water and dried using a hand dryer.

6.4 Characterisation of the heat affected zone (HAZ)

In order to reveal the HAZ and weld areas, the characterisation procedure was conducted on the three polished specimens in a manner similar to that used for the previously characterised 50mm thick plates. This was to assist the specimen fabricators with adequate information prior to the specimens' extraction.

6.4.1 Etching

Etching was carried out by applying a 2% Nital solution (Nitric acid in Methanol) on the entire surface of the material to reveal the weld runs and the HAZ, as shown in Figure 6-3a. The surfaces were then washed with water for about 2 minutes and subsequently sprayed with alcohol and dried. When the surfaces were analysed, it was observed that the width of the HAZ was about 3.5mm from the weld toe at the top and bottom sections of the analysed plates, while in the middle sections of the plates, the HAZ had a width of about 1.5mm from the weld root. The weld and HAZ dimensions are illustrated in Figure 6-3b.

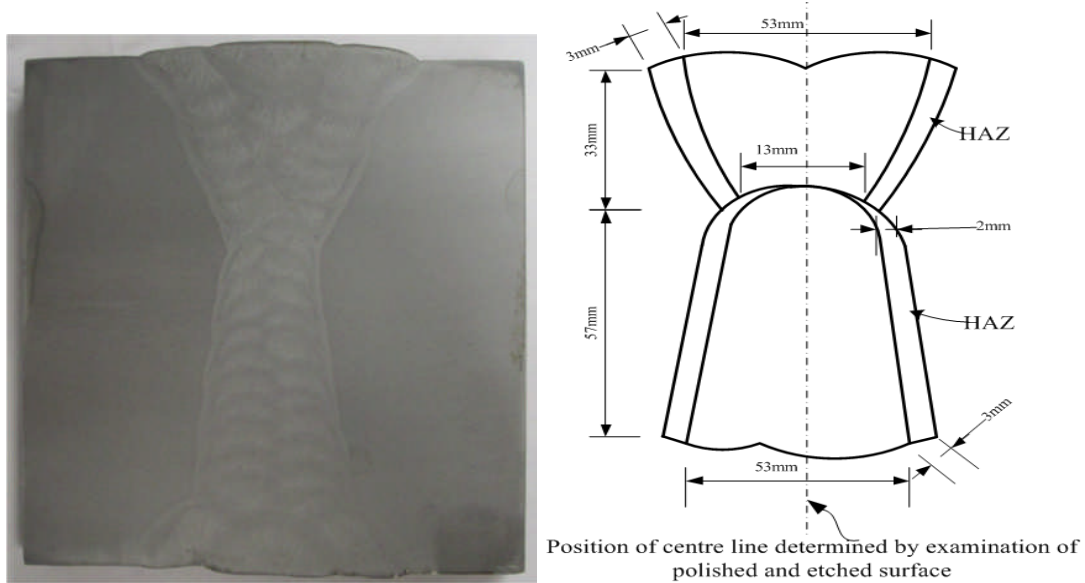


Figure 6-3 (a) Weld runs and HAZ (b) Weld and HAZ dimensions

6.4.2 Specimen extraction

A number of 16mm thick CT specimens with width $W=50\text{mm}$, designed in accordance with ASTM E647, were extracted through the thickness of the plate with the notch perpendicular to the rolling direction of the plate. The specimens' starter notches were prepared by spark erosion and positioned at the HAZ.

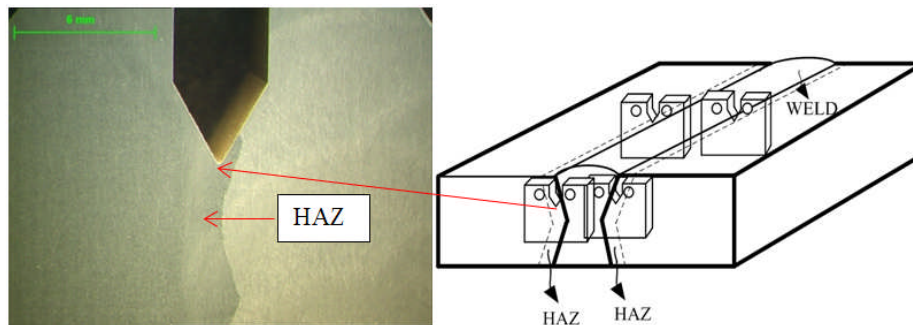


Figure 6-4 Compact tension specimens extraction

Careful precautions were taken to substantiate that the HAZ was aligned with the crack path to avoid the possibility of cracks initiating from the parent material or the weld region. The extraction description is represented in Figure 6-4 indicating the HAZ location in the direction of the machined notch. Pictures taken from some of the characterised CT specimens are given in Appendix E. In order to also understand the crack growth behaviour of weld materials and

establish the comparison of the HAZ, weld and parent materials, CT specimens were extracted with their starter notches aligned in the weld centre line. All the extracted specimens' surfaces were polished with emery papers of appropriate grits for adequate visual observation of the crack front.

6.5 Experimental procedure

The experimental procedure used for fatigue crack growth measurements have been reported in Chapter 3. The tests parameters and specimens' loading patterns are the same as those used for the tests reported in Chapter 4. The air tests were conducted at room temperature, while the seawater tests were conducted under free corrosion conditions at a load loading frequency of 0.3Hz and a temperature of 8⁰C-10⁰C, as previously mentioned. All fatigue crack propagation tests were in accordance with ASTM E647.

6.5.1 Metallurgical Examination

After the fatigue crack growth tests in parent, HAZ and weld materials, the specimens were etched using the procedure given in section 6.4.1. Macro examination of the crack paths was conducted using a Nikon SMZ745T microscope coupled with an AxioCam ERC5S camera. This was followed by micro examination of the crack surfaces. The micro examination was conducted from the notches towards the end of the crack using the Nikon eclipse ME600 optical microscope with magnifications X5 and X20 respectively. The process was also repeated on uncracked specimens in order to verify the crack initiation sites and paths. The HAZ were examined from the weld region towards the parent materials.

6.5.2 Fractography analysis

In order to carry out macro and micro analysis of the fracture surfaces, the specimens were fully immersed in liquid nitrogen with a temperature of about -196⁰C for a minimum of four hours. They were then broken into two halves by hammer while mounted on the workshop vice. The specimens were then sprayed with alcohol, dried and kept in a desiccator to protect the surfaces from contamination prior to further examinations.

6.5.3 Scanning electron microscope (SEM) analysis

Prior to the SEM analysis, the surfaces of the specimens were cleaned ultrasonically, sprayed with alcohol and dried. It was also important to remove deposits of corrosion products from the seawater test specimens before the analysis. This was achieved by cleaning the surfaces with about 20% hydrochloric acid solution, stannous chloride and distilled water. The SEM analysis was carried out using the Philips XL 30 SFEG Oxford EBSD system. The analysis was carried out from the notch to some selected areas of the cracked surfaces using magnifications X200, X1000 and X4000 in ascending order.

6.6 Fatigue crack growth of HAZ material in air and seawater

In Chapters 4 and 5, discussions of the results were based on fatigue crack growth in parent materials, but in this section, the results are presented of crack growth response of the HAZ materials tested in air and in free corrosion conditions.

6.6.1 Results and discussion of HAZ materials crack growth data in air

The crack growth results obtained from the HAZ materials are presented in Figure 6-5 as plots of crack lengths and number of cycles. The crack growth patterns in the specimens are similar over the entire range of loading cycles. However, a difference of about 190,000 cycles was recorded between test 1 and tests 2 and 3, as shown in the figure. This may be due to the difference in crack initiation sites, propagation pattern and the degree of crack branching within the specimens. The metallographic examination of the specimens revealed that the notch tips of most of the specimens used in this work were aligned in the intercritical (middle) region of the HAZ, while a few of the specimens' notch tips fell in the coarse grain region close to the weld material. In test 1, the notch tip was closer to the coarse grain, while in tests 2 and 3, the notch tips were aligned in the middle region of the HAZ. This would have influenced the difference in the number of loading cycles.

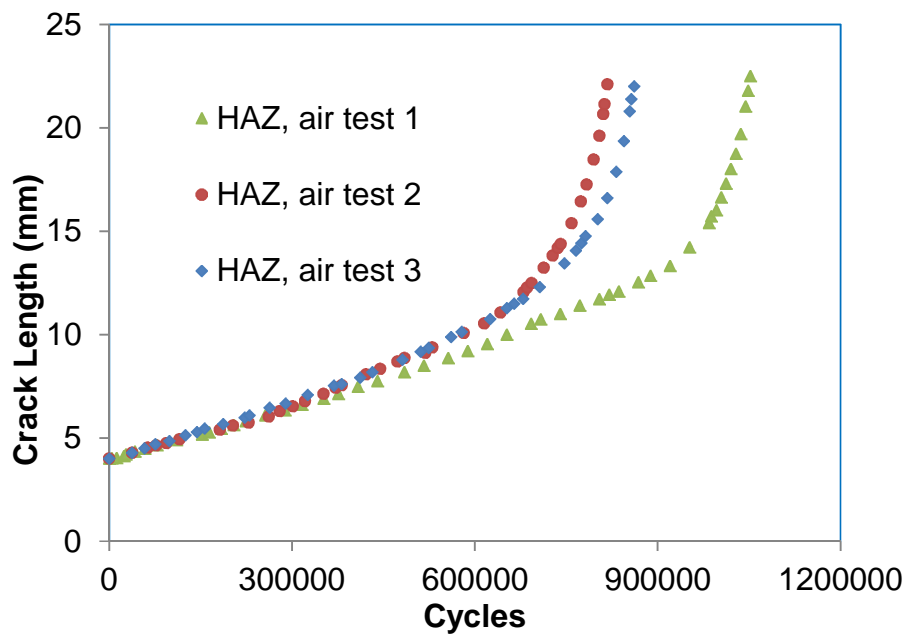


Figure 6-5 Fatigue crack growth in HAZ materials in air at an R-ratio of 0.1

As mentioned in section 6.1, cracks initiate at the HAZ of welds and propagate into the unaffected parent material. Therefore, it is expected that the degree of crack branching towards the parent material would be more if the cracks initiate near the weld compared to near the parent material; and this may result in changes in the number of loading cycles. The deviation of the crack from the coarse grain region towards the region closer to the parent material suggests that crack deviation was a factor of the region having a lower resistance to crack growth. A similar phenomenon relating to crack branching and tortuous crack path with enhanced crack closure and higher crack growth resistance was also reported in weld materials extracted from Q345 steel [79].

Also, in tests 2 and 3, the specimens were extracted close to the edge of the weld plate, while in test 1; the specimen was extracted close to the middle of the plate. Therefore, the difference in cooling rate across the weld plate would have probably influenced the crack growth behaviour of the specimens. However, on the da/dN vs. ΔK plot, the variation in the number of loading cycles did not produce any marked difference in the curves, particularly at higher ΔK , as shown in Figure 6-6 and all the crack growth curves resulted in bi-linear

relationships. However, at lower ΔK below $18\text{MPa}\sqrt{m}$, a marginal difference was observed between test 1 and the other two test data plotted in the figure. It can be seen that the agreement of the data plotted in Figure 6-6 is quite encouraging and provides an appreciable level of confidence in the experimental data due to their repeatability. At lower ΔK , prior to the change in slope of the da/dN vs. ΔK plot, it can be observed that there was delayed or retarded crack propagation behaviour. Beyond this point, a linear relationship and accelerated crack growth behaviour can be observed. It will be recalled from the literature survey that this type of mechanism, coupled with crack deviation, has been explained by crack closure effect induced by compressive residual/mean stress ahead of the crack tip [79], [113], [114].

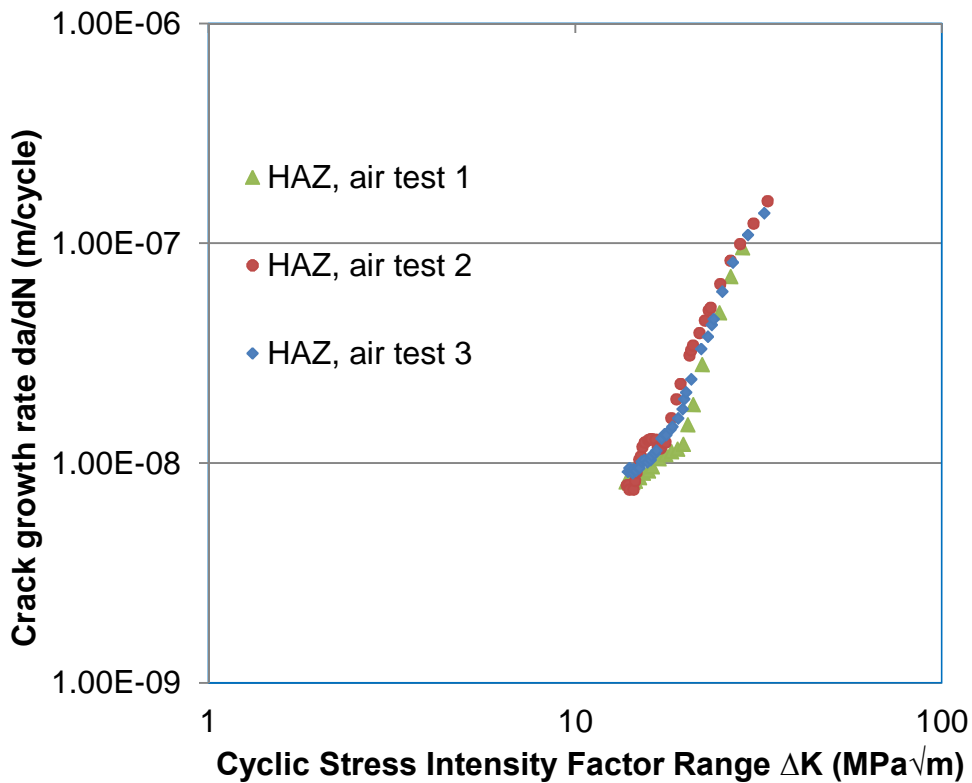


Figure 6-6 Crack growth rates in HAZ materials in air at an R-ratio of 0.1

The effect of crack closure induced by mean or residual stresses was explained by changes in the slope of the BFS and ΔK [30], as shown in Figure 6-7. A similar phenomenon was also reported in a study of crack growth rates in C-Mn

steel HAZ material with a yield strength of 400MPa [113], [114]. Details of this can be found in [113].

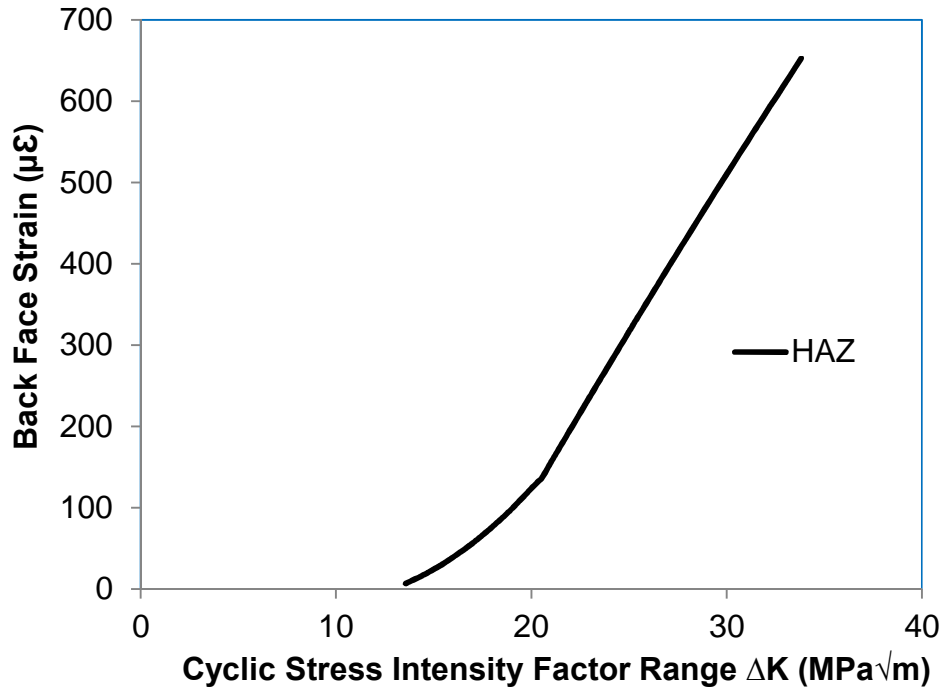


Figure 6-7 Closure effect due to residual stresses in HAZ

Lower crack growth rates due to crack closure effects may lead to a compressive stress cycle in fatigue crack propagation even if the nominal applied stress cycle is wholly tensile. In such situations, the applied ΔK is not affected but the effective R may be increased or reduced depending on the magnitude of the stress and its location within the reference structure. Also, considering the effects of the welding sequence employed in preparing the plate as shown in Figure 6-3(a), and the nature of the HAZ crack growth curve in air (Figure 6-6) at lower ΔK on the type of through-thickness crack growth that might be experienced by the circumferential weld regions of real monopiles, one can also say that the effect of the damaging portion of the residual stress distribution that might be present in the welded area will affect crack growth close to the surface regardless of the crack initiation site(s) (either from inside or outside of the weld area) relative to the beneficial effect which is likely to occur in the middle of the weld.

As mentioned in Chapter 2, in welded plate, the tensile or damaging part of the residual stress field is about a quarter of the plate thickness, such that the stress field is compressive in the middle [13]. Judging from the orientation of the specimens within the welded plate, as shown in Appendix E, it is likely that the local tensile residual stress close to the advancing crack was released during the pre-cracking stage. Also, during fatigue pre-cracking, a slightly larger crack front and large plastic zone size was observed at the early stage of crack growth through optical observations using the digital camera, but subsequently, a much smaller crack front was observed. This may be due to the effects of tensile residual stresses present in the material at a depth close to the surface of the plate. However, during propagation, the determined plastic zone sizes for plane strain and plane stress, for the data plotted in Figure 6-6 were not more than 1.5mm and 4.5mm for a final crack length of 22.5mm. The change in slope of the da/dN vs. ΔK plot in Figure 6-6 and the transition to the accelerated crack growth regime occurred at ΔK less than $19\text{MPa}\sqrt{m}$, a point where the crack length was approximately 11.25mm from the notch and about 47.5mm through the thickness of the weld plate. This depth was found to be approximately at the mid-section of the 90mm plate used for the present investigation. Therefore the crack growth response in the HAZ materials reported in this work appears to be consistent with the explanations given in [13] and may be used to interpret the data.

Another possible reason for the delayed crack growth at the earlier stages of crack growth in the HAZ materials might be due to the effect of the welding sequence employed during the fabrication. It can be seen from the welding specification depicted in Appendix D that the inside of the plate with the weld root located at about 10mm from the notch was welded first, followed by the outside. The HAZ toughness and its resistance to crack growth at this region may be improved by tempering due to subsequent welding layers and some of the residual stresses are likely to be relaxed in the process, but this may not be absolutely. The implication of this on the inspection of monopile structures is that firstly, the welding procedure should be planned in such a way that damaging portions of the residual stresses present in the weld would be

significantly reduced. Secondly, the section containing the first sets of weld sequences with possible compressive residual stress fields in some regions should be located inside the monopile, such that the remaining damaging portion of the residual stress fields are located outside. Through this, crack initiation is likely to occur at the easily accessible outside section of the monopile structure and the possibility of crack initiating from the inside may be significantly reduced, coupled with a reduction in the cost of inspection.

Table 6-1 Material constants for HAZ materials in air

Tests	R	C	m	R ²
1	0.1	1.1×10^{-12}	3.3	0.88
2	0.1	5.1×10^{-13}	3.6	0.98
3	0.1	1.0×10^{-12}	3.4	0.96

The material constants (*C* and *m*) derived from the line of best fit through the data points for the three tests plotted in Figure 6-6 are set out in Table 6-1, with the corresponding values of the load ratios and the multiple correlation coefficients (*R*²) resulting from the line of best fit through the $\frac{da}{dN}$ vs. ΔK plots. It can be seen that the values of *m* agree well with each other, while the slight variation in the values of *C* could be attributed to microstructural variation in the HAZ materials as previously mentioned.

6.6.2 Results and discussion of HAZ materials crack growth data in seawater

The crack growth data obtained at an R-ratio of 0.1 in the HAZ materials in free corrosion conditions are plotted in Figures 6-8 and 6-9. It can be seen that the data plotted in Figure 6-8 progressed in a similar manner over the range of loading cycles irrespective of the difference between the curves. The difference between the two curves may be related to microstructure variation in the HAZ zones. Therefore, it is worth mentioning that, regardless of the similar crack paths in all the HAZ specimens used in this work, there is the possibility of having different crack growth behaviours due to microstructure variations.

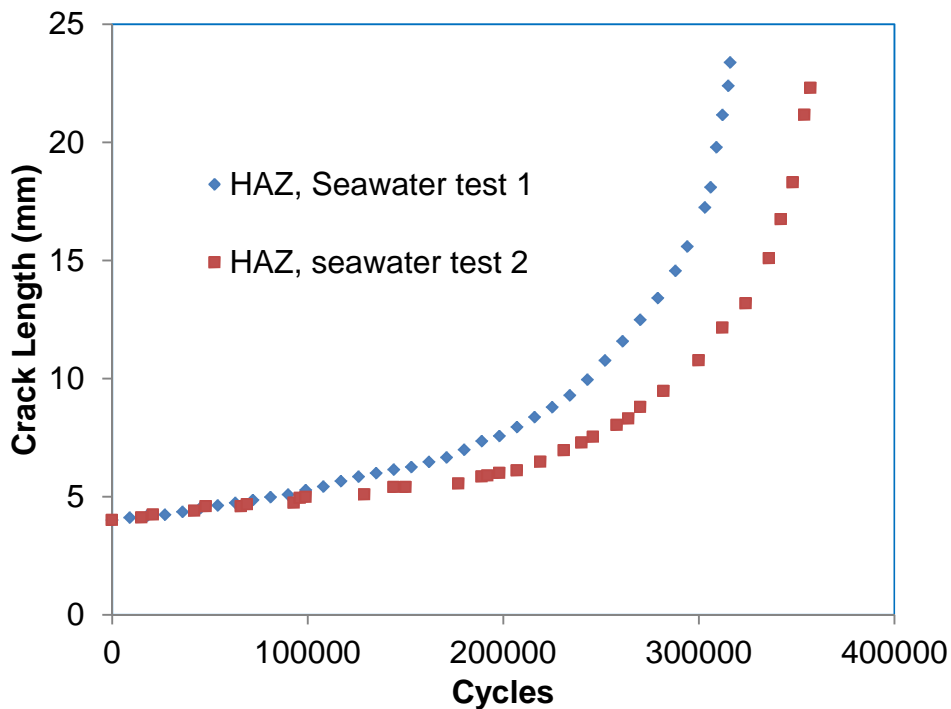


Figure 6-8 Fatigue crack growth in HAZ materials in seawater at an R-ratio of 0.1

Figure 6-9 compares the crack growth rates in the HAZ material in seawater versus cyclic stress intensity factor ranges. It can be seen that the curves have similar patterns over the ΔK ranges tested. Crack growth rates in both specimens were obtained at stress intensity factor ranges of $13\text{MPa}\sqrt{m}$ to $30\text{MPa}\sqrt{m}$. However, the plastic zone sizes were determined to be 1.5mm and 4.5mm for plane strain and plane stress, for a final crack length of 22.3mm. Crack growth rates were found to be slightly higher in test 2 than in test 1 but this difference was not significant. However, the type of crack growth trends that were observed in HAZ materials tested in air (Figure 6-6) was not evident in seawater, as shown in Figure 6-9. Corrosion fatigue damage is time dependent and in free corrosion conditions the effect can be amplified by testing at a lower cyclic frequency. Therefore, crack advancement under a longer opening time in seawater is expected to be significantly different from what is obtainable in air due to the interaction of the crack tip with the environment.

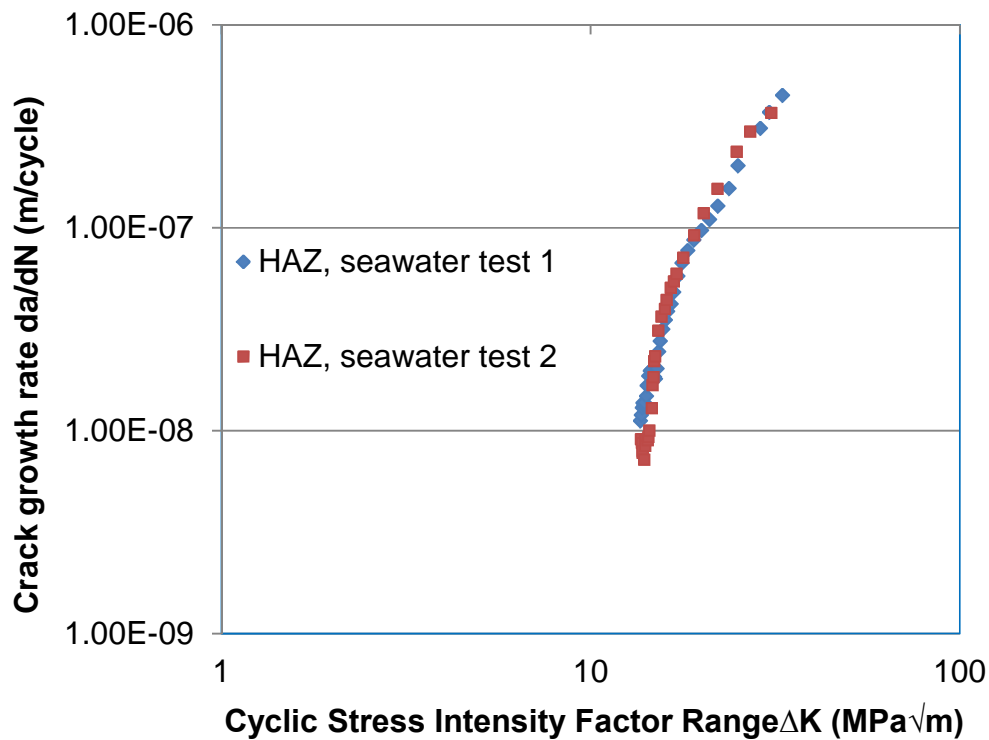


Figure 6-9 Crack growth rates in HAZ materials in seawater at an R-ratio of 0.1

Since it was established in the literature survey that residual stresses are released as fatigue crack progresses, their effect under a corrosive environment may significantly be reduced only to a marginal extent, thus leading to the environment being more dominant when compared to residual stresses. However, this proposal was only confined to the observed HAZ crack growth response in seawater. Also, due to welding process induced microstructural changes in the HAZ and weld materials, it was observed after testing that their corroded surfaces were more severe than in the parent materials tested under the same environmental and loading conditions. Therefore it may also be implied that crack growth rates in the HAZ materials are promoted by these microstructural variations, accompanied by rates of material removal.

Table 6-2 Material constants for HAZ materials in seawater

Tests	R	C	m	R ²
1	0.1	2.0×10^{-13}	4.3	0.96
2	0.1	1.0×10^{-14}	5.3	0.89

The microstructure variations in the HAZ materials may also be responsible for the difference in values of the material constants derived for the line of best fit through the da/dN vs. ΔK plots. These values are given in Table 6-2 coupled with the corresponding correlation coefficient resulting from the plots. It was also observed that, at ΔK below $15\text{MPa}\sqrt{m}$, crack growth rates in test 2 were slightly higher than in test 1, but beyond this point the crack growth rates in both materials progressed in a similar manner. However, judging from the crack growth curves in Figure 6-9, the difference in the values given in Table 6-2 can be considered to be within experimental scatter.

6.6.3 Comparison of air and seawater data in HAZ materials

Figure 6-10 compares the crack growth curves in HAZ materials in air and in free corrosion conditions. It can be observed from the figure that the crack advancement is relatively higher in seawater than in air across the loading cycles. The number of cycles consumed by the specimens tested in seawater was about $1/3$ of those tested in air due to the environmentally enhanced crack growth mechanism in seawater.

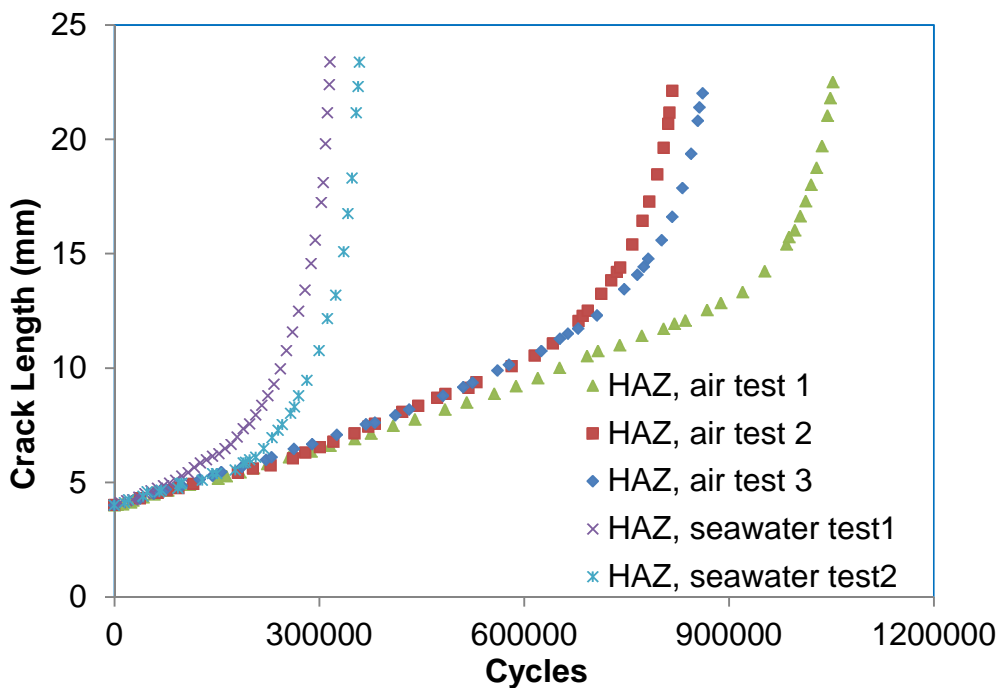


Figure 6-10 Fatigue crack growth in HAZ materials in air and seawater

However, at the early stages of crack growth as shown in the figure, it can be observed that the trends of the air and seawater curves are similar, up to a crack length of approximately 6mm. Subsequently, there was a rapid rise in the seawater curves. This implies that the environmental effect of the seawater was not appreciable until about 40% of the total number of cycles had been consumed in seawater. It also suggests that, the rate of corrosion or metal removal along the crack front is time dependent and at a lower crack opening displacement which occurs at earlier stages of crack growth, this phenomenon should be expected. The implication of this on the integrity of welded structures is that the frequency of inspection on the corrosion enhanced damage areas depends on when the environmentally enhanced crack propagation begins.

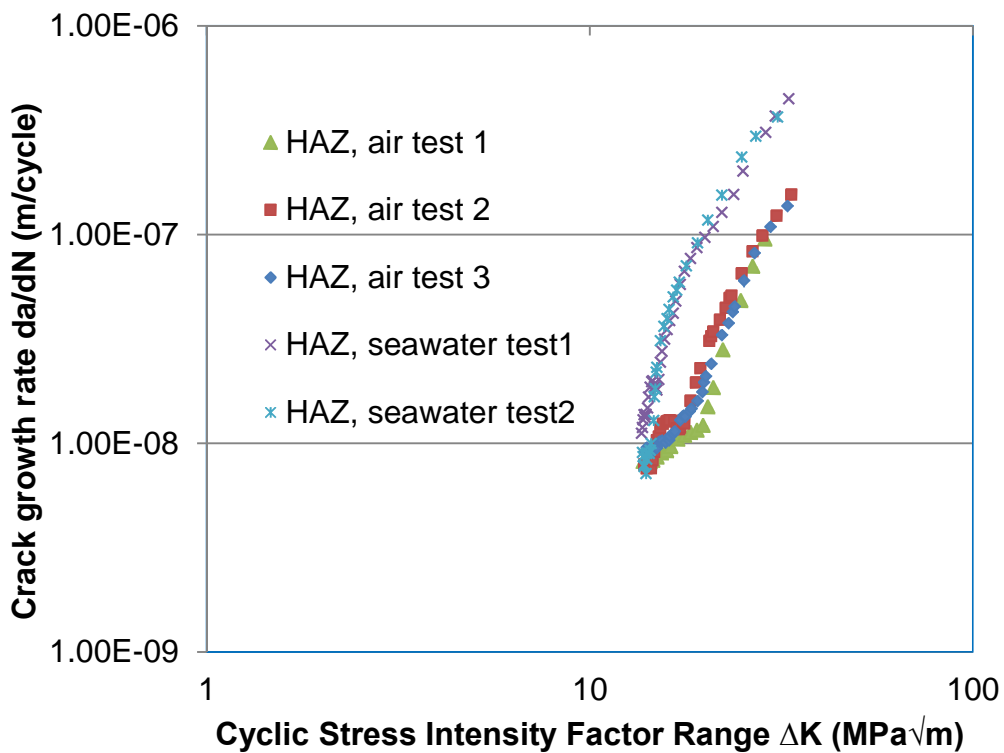


Figure 6-11 Crack growth rates in HAZ materials in air and seawater

The crack growth rates measured in the HAZ materials in air and in seawater are compared in Figure 6-11. It can also be seen that crack growth rates in seawater were higher than in air across all the ranges of ΔK tested. The line of best fit through the mean data in air and seawater produced the Paris equation

of the forms $\frac{da}{dN} = 7.0 \times 10^{-13} \Delta K^{3.5}$ in air, and $\frac{da}{dN} = 6.0 \times 10^{-14} \Delta K^{4.7}$ in seawater. It can be seen that the effect of the corrosive environment has enhanced the C and m values by an order of magnitude.

At $\Delta K < 15 \text{MPa}\sqrt{m}$, crack growth rates in seawater were found to be slightly higher than in air, particularly in HAZ seawater test 2 while in test 1, crack growth rates were found to be twice higher in seawater than in air. Beyond the ΔK of $15 \text{MPa}\sqrt{m}$, nearly at the mid-section of the specimens, crack growth rates in seawater were nearly five times higher than in air. However, at higher ΔK , crack growth rates were four times higher in seawater than in air. It can also be observed that at higher ΔK , the seawater curves have similar shapes to those obtained in air and they deviate towards the air curves. The rates of material removal in the HAZ specimens in a corrosive environment at higher ΔK , might reduce the access of the corrosive media to the crack tip due to the significant deposits of corrosion products. Therefore, the effect of layers of corrosion products at the crack may be responsible for the deviation of the seawater crack growth curves towards the reference air ones at higher ΔK , as shown in Figure 6-11.

6.6.4 Mean stress effects on fatigue crack growth in HAZ materials

In order to understand the response of the HAZ materials to crack growth and to cancel the possible effect of crack closure, some tests were conducted at R-ratios of 0.5 and 0.7 respectively. The results are depicted in Figure 6-12 and included in this figure are the mean air data for the tests conducted at an R-ratio of 0.1. It can be seen that at the higher R-ratio, the form of bi-linear relationships that was observed at an R-ratio of 0.1, which was previously attributed to the effects of residual stress induced crack closure, is absent. This implies that crack closure is less significant at a higher R-ratio due to the degree of opening at the crack tip. A similar phenomenon was also reported in [78]. The crack growth response at an R-ratio of 0.5 was found to be similar to the response at an R-ratio of 0.7, as shown in Figure 6-12, which implies that a crack closure free phenomenon can be achieved at both R-ratios.

However, lower values of ΔK were obtained at an R-ratio of 0.7 compared to an R-ratio of 0.5, as shown in the figure. Two effects were observed from the comparison made with the R-ratio of 0.1 test; first, at all the ΔK ranges tested, crack growth rates were found to be higher at a higher R-ratio than at an R-ratio of 0.1 but this was not more than twice the observed crack growth rates at an R-ratio of 0.1 and secondly, there were reductions in the ΔK values at a higher R-ratio compared to in an R-ratio of 0.1. At an R-ratio of 0.5, the calculated plastic zone sizes were 0.9mm and 2.6mm for plane strain and plane stress, for a final crack length of 22.3mm. However, at an R-ratio of 0.7, the plastic zone sizes were determined to be 0.4mm and 1.4mm for a final crack length of 20mm. These values are also similar to those determined for tests conducted in seawater at the same loading conditions. Comparison of the results presented in this section with those obtained from parent materials will be discussed in a later section.

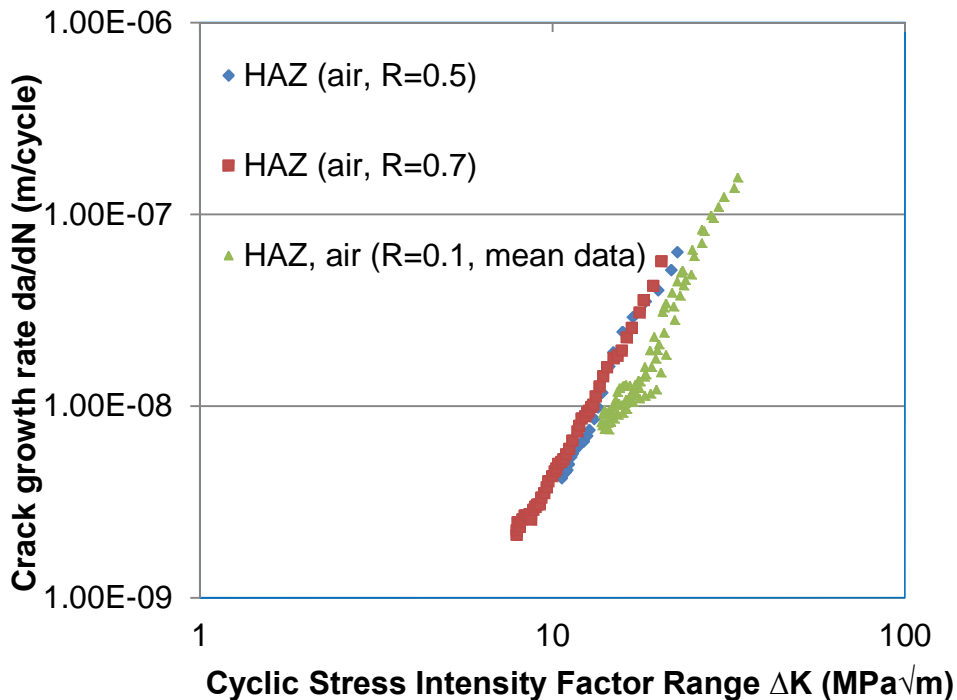


Figure 6-12 Crack growth rates in HAZ material in air at R-ratios of 0.1 to 0.7

Figure 6-13 compares the crack growth rates in the HAZ materials at R-ratios of 0.1 and 0.7 in free corrosion conditions. Crack growth rates were found to increase with an increase in stress ratios from 0.1 to 0.7, as shown in the figure,

but the effect of the mean stress was significantly higher at lower stress intensity factor ranges. At ΔK between $13\text{MPa}\sqrt{m}$ and $18\text{MPa}\sqrt{m}$, crack growth rates were found to be twice higher at an R-ratio of 0.7 than in 0.1 and beyond this point the curves nearly converged. The trend shown, at an R-ratio of 0.7 at higher ΔK , could be attributed to the effect of corrosion debris within the crack accompanied by rates of material removal by corrosion in the HAZ material, as mentioned earlier. In Appleton's work [15], the formation rate of corrosion products in the crack was also reported to be dominant under free corrosion conditions, thus restricting access of the corrosion elements to the crack tip. However, it was mentioned that this effect may be significant in the near threshold region [14].

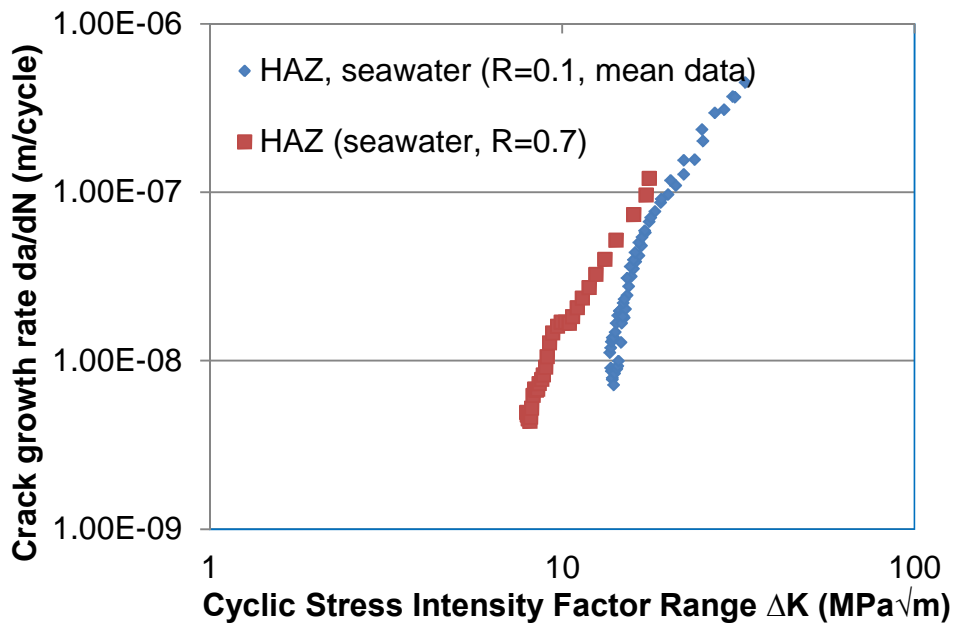


Figure 6-13 Crack growth rates in HAZ materials in seawater at R-ratios of 0.1 and 0.7

In Figure 6-14, the air and seawater data obtained at R-ratios of 0.5 and 0.7 are compared. At all the ranges of ΔK , the enhancement of crack growth rates in seawater was found to be in the order of two to three times faster than the equivalent air curves obtained at R-ratios of 0.5 and 0.7 respectively. It can also be seen that the acceleration in crack growth is more rapid at a lower ΔK

compared to the comparisons made in air. The possible underlying reason for this behaviour is the effect of soaking time, which is expected to be dominant under a fully open crack, leading to a reduction in resistance to crack growth. This behaviour clearly shows the significance of environmental interaction with mean stress effects on crack growth rates in seawater compared to in air (Figure 6-12).

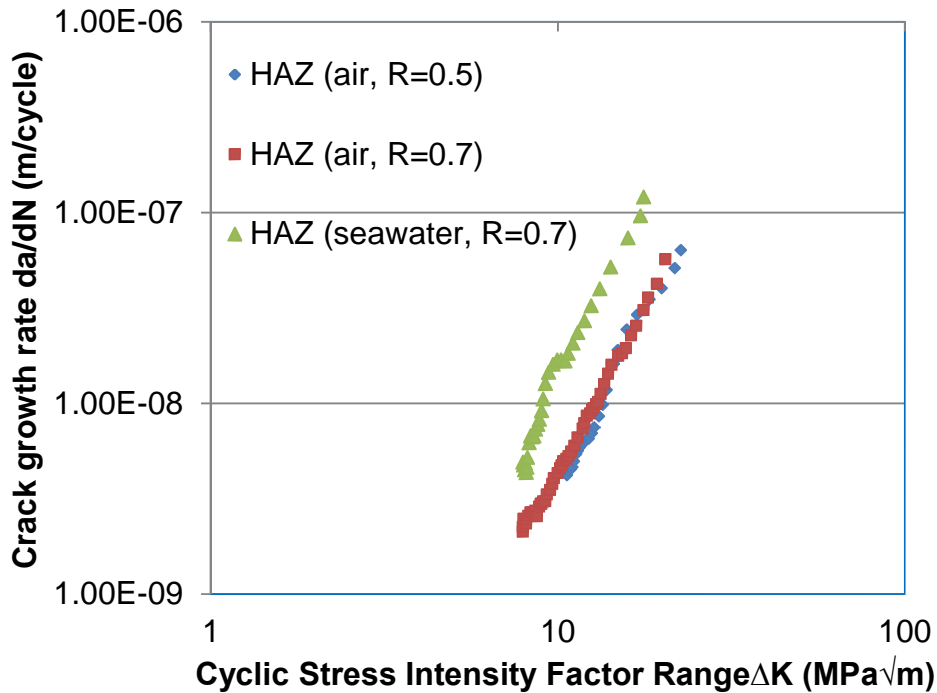


Figure 6-14 Air and seawater data in HAZ materials at R-ratios of 0.5 and 0.7

6.6.5 Comparison and discussion of crack propagation data in HAZ and parent materials

Figure 6-15 compares the crack growth data in HAZ materials with the parent materials data that were discussed in Chapters 4 and 5. Considering the differences in crack initiation lives at the root of the notches, it was found during pre-cracking that the crack initiation time at the notch in HAZ materials was approximately half of the number of cycles expended to crack initiation in the parent materials, which implies the possibility of the existence of the tensile segment of the residual stress distribution during pre-cracking, as mentioned in section 6.6.1. With respect to mean stress effects in welded joints, it appears that if adequately controlled welding sequences and procedures that will

significantly reduce the damaging residual stress distribution are employed during the fabrication of offshore monopile structures, the frequency of inspection and cost of repairs will be significantly reduced.

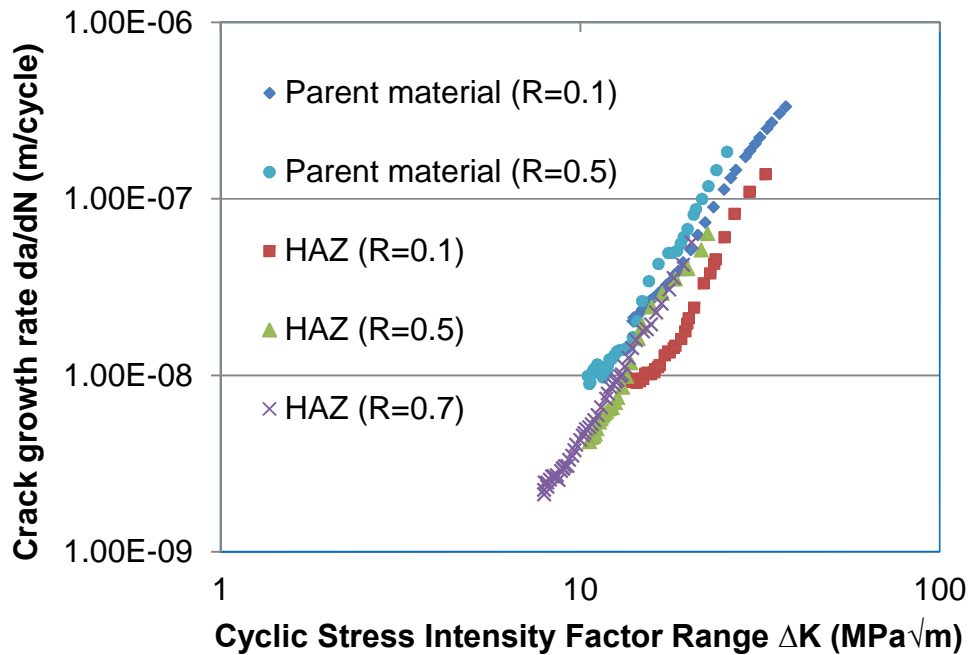


Figure 6-15 Crack growth data comparison in HAZ and parent materials in air

At an R-ratio of 0.1 in Figure 6-15 and at lower values of ΔK , crack growth rates were found to be higher in parent materials than in HAZ materials by approximately a factor of 4, but at higher ΔK , crack growth rates were observed to be approximately twice as fast in the parent material as in HAZ. As the crack deepens, at ΔK above $25\text{MPa}\sqrt{m}$, the crack growth trends in the HAZ and parent materials are similar and the two curves almost converged. In simulating tensile residual stresses in weldments using the response from the base materials, higher R-ratio tests ($R \geq 0.5$) have been suggested [73]. However, this assumption may be limited to near surface tensile residual stresses, but for through thickness situation, it is likely that the crack growth behaviour would be different due to the overall magnitude of the residual stresses accompanied by the welding procedure. It can also be observed in Figure 6-15 that the crack growth rates in the HAZ materials at R-ratios of 0.5 and 0.7 are similar to those

measured at an R-ratio of 0.1 in the parent materials. For the cases considered here, the implication of this is that the crack growth data obtained in parent materials at an R-ratio of 0.1 in air may be used to represent HAZ crack growth behaviour in air at higher R-ratios.

However, under free corrosion conditions slightly different crack growth behaviour was observed. The HAZ crack growth data obtained at lower and higher R-ratios are compared with those obtained in parent materials, as shown in Figure 6-16. At an R-ratio of 0.1 the crack growth trends in HAZ and parent materials are similar. However, at lower ΔK below $15\text{MPa}\sqrt{m}$, crack growth rates in parent material were slightly higher than in HAZ material, but beyond this point, the crack growth response in both materials was nearly the same. A similar crack growth behaviour has also been reported in [81]. It appears from the observation at an R-ratio of 0.1 that the material data of parent materials in seawater can also be used to estimate the corresponding HAZ crack growth behaviour.

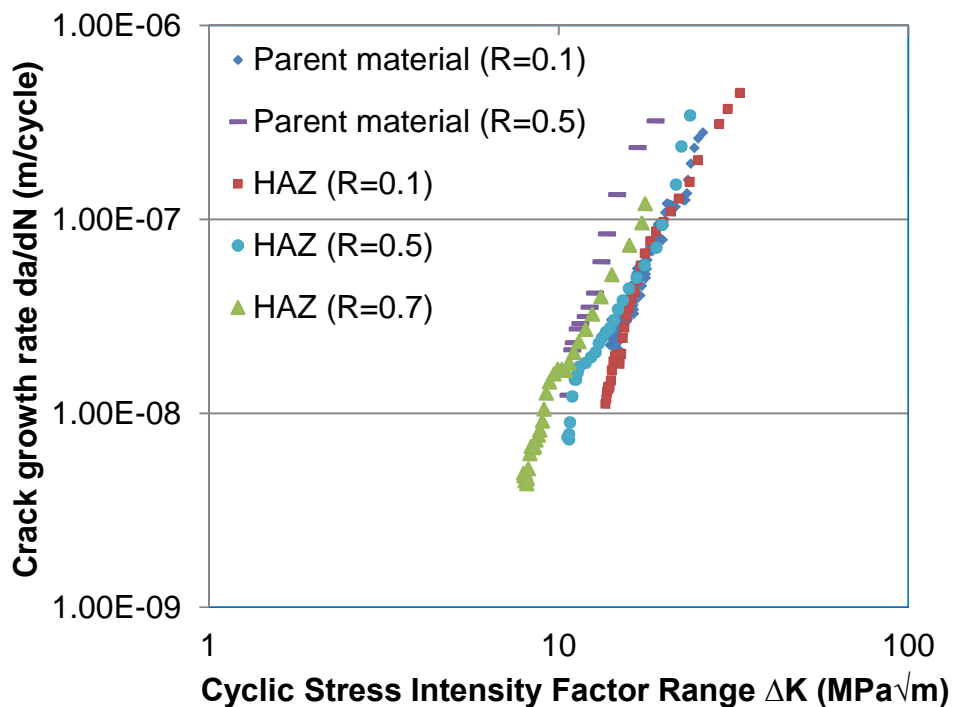


Figure 6-16 Crack growth data comparison in HAZ and parent materials in seawater

The effects of mean stress also led to an increase in crack growth rates in the HAZ materials across all the ranges of ΔK at an R-ratio of 0.7 than at an R-ratio of 0.5. This is in agreement with what was reported in [54] for parent materials. It can also be observed, as shown in Figure 6-16, that the crack growth trends in HAZ at R-ratios of 0.5 and 0.7 progressed in a similar manner. It can be recalled that in air (Figure 6-15), the crack growth mechanisms in HAZ materials were similar under R-ratios of 0.5 and 0.7 which implies that fatigue damage in free corrosion conditions is significant due to environmental interaction. Crack growth rates in the parent material at an R-ratio of 0.5 were also found to be higher than in HAZ material tested under the same R-ratio, but were similar to those obtained from HAZ material at an R-ratio of 0.7 at lower ΔK . At higher ΔK , crack growth rates in the parent material were in the order of approximately three times higher than in HAZ materials, with the latter curves converging with the R-ratio of 0.1 crack growth curves. Considering the presence of possible weld fabrication defects and HAZ microstructure sensitivity to corrosion assisted fatigue damage, crack growth accompanied by deposits of corrosion products within the crack is the most likely explanation of the HAZ behaviour at higher ΔK in free corrosion conditions.

6.6.6 Discussion of HAZ material response with literature data

Crack growth data obtained from the present investigation in air and in seawater are compared with those obtained from other steels used for offshore installations in Figures 6-17 and 6-18. Data related to HAZ materials were collected from [76], [81], [113] and [108] for the comparisons made in the figures. It was found that the line of best fit through the present mean data lies within the lower bounds of Fukuda et al.'s, Thompson's, and Coudert and Renaudin's data [76], [81], [108], while the Bertini data [113] fell below the other data plotted. This can be seen in Figure 6-17. The applied test load in Bertini's investigation is the most likely reason to explain this, considering the level of shift in the crack growth data to the right of the other curves. The type of crack growth trend obtained from the present investigation, particularly the delayed crack growth at lower ΔK followed by a transition to a higher crack growth

manner at higher ΔK , was not evident in the other data regardless of some similarities in the curves. This could be attributed to differences in material, welding procedure, welding sequence, thickness and specimen geometry etc. which are important factors that need careful consideration when data are compared. Details of the aforementioned factors may have significant effects on crack propagation in the HAZ and thus, the derived material constants. Details of the welding procedure, thickness and specimens' geometry relating to the data compared in Figure 6-17 can be found in [76], [81], [108], [113].

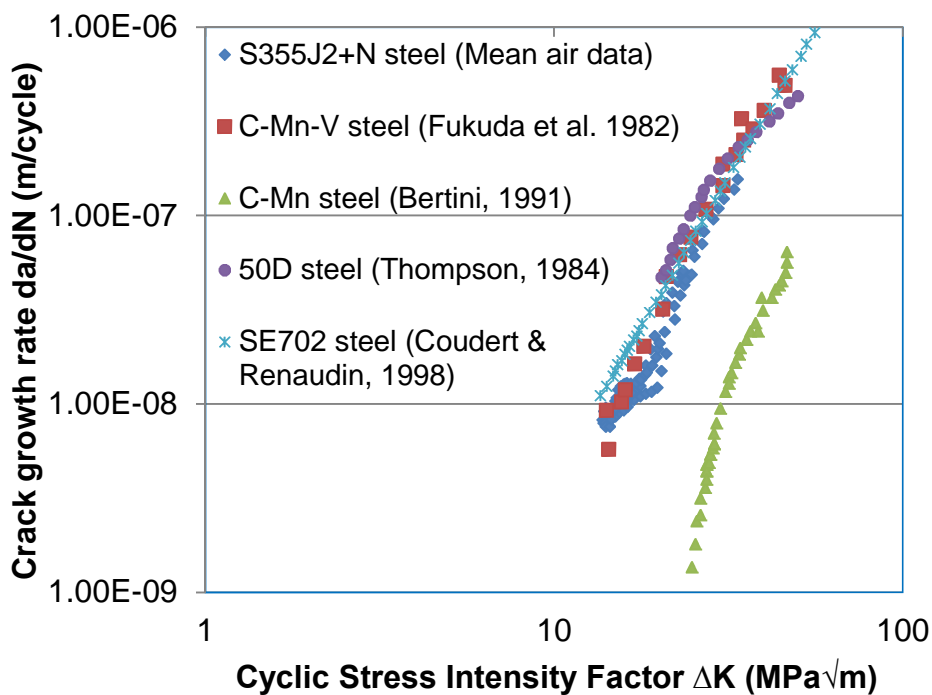


Figure 6-17 Comparison of crack growth rates in HAZ materials in air with literature data

The comparisons of the present data with those obtained from the literature in free corrosion conditions are plotted in Figure 6-18. In spite of the significant number of corrosion fatigue studies that were conducted nearly 30 years ago, almost no data have been obtained from S355J2+N steel material used for the present investigation, particularly at higher stress ratios, and considering the weld plate thickness and tests conditions similar to what is experienced by monopile support structures. Also, the present HAZ materials data were obtained under free corrosion conditions and, as mentioned previously, some

investigations for example in [76] have observed the possibilities of hydrogen enhanced crack growth rates even under a free corrosion potential. The mechanism of environmental enhancement in seawater for BS4360 50D was also explained by hydrogen embrittlement for all the applied potentials including free corrosion potential [3]. This implies that hydrogen embrittlement was not limited to the mechanisms of CP in the reported studies. Therefore, crack growth data derived under a free corrosion potential may not absolutely represent the real effects of free corrosion conditions on fatigue crack growth.

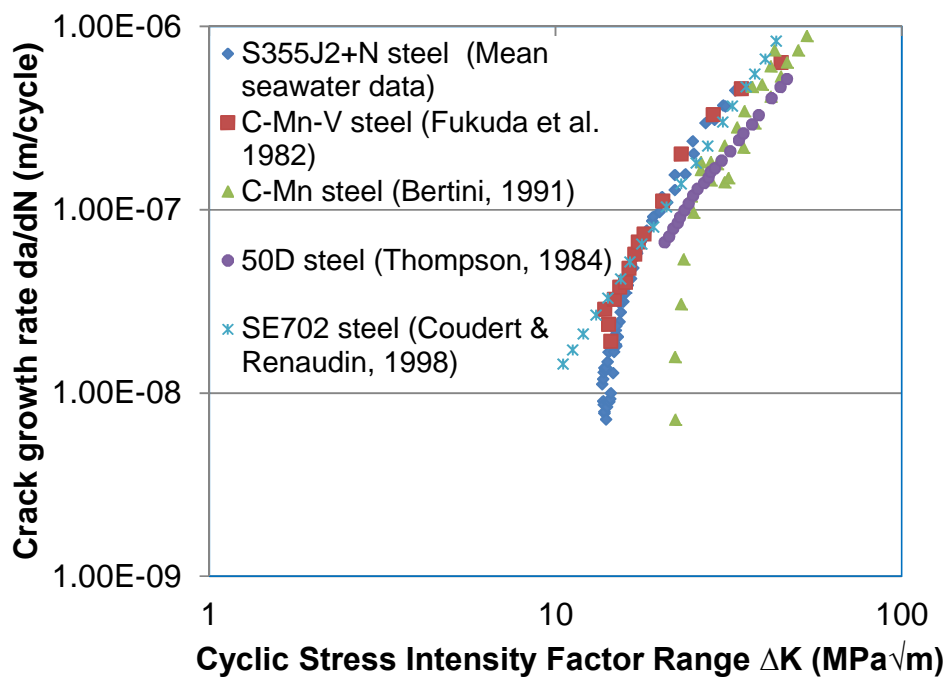


Figure 6-18 Comparison of crack growth rates in HAZ materials in seawater with literature data

The only data having a similar crack growth response to the present HAZ material data, as shown in Figure 6-18, is Fukuda et al.'s data. However, a test load frequency of 0.133Hz corresponding to sea wave frequency was used in their investigation. Therefore, it is expected that crack growth rates would be higher than those reported in the present study due to the longer time the crack tip is exposed to the corrosive environment. The likely explanation for this behaviour is the test temperature of 15°C used as against the temperature range of $8^{\circ}\text{C-}10^{\circ}\text{C}$ used for the present investigations. Another possible reason

is a difference in material with respect to material composition, and mechanical properties coupled with the type of welding procedure used for fabrication, as previously mentioned.

Thompson's data did not agree with the present data, as shown in Figure 6-18 for a number of reasons, but mainly probably due to the higher load frequency of 0.5Hz used for testing with the intention of reducing the test duration. It should be noted that a higher load frequency in seawater would result in lower crack growth rates due to the shorter crack tip opening time. This had also been proved in Vosikovsky's study [74] as mentioned in Chapter 2. Therefore, the assumption made in Thompson's work by increasing corrosion fatigue test load frequency, firstly may not represent the intended sea wave loading frequency and secondly does not comply with the aim of reducing the crack tip opening to the corrosive media. Also, the welding procedure and filler material used in Thompson's work are different from the present work and therefore dissimilar crack growth rates might be expected.

Also, in Thompson's study, crack lengths were measured in a seawater environment using a microscope with external illumination. It should be mentioned that optical measurements of crack lengths in seawater may not be a reliable approach and if attempted, might lead to inaccuracies in data analysis and interpretation. It can also be seen from Figure 6-18 that Bertini's data do not agree with the present data, probably due to the applied test load range.

It should also be mentioned that the interaction of test parameters such as loading frequency, load range, load ratio, test temperature etc. in corrosion fatigue situations should be considered when data comparisons and interpretation are made. However, the agreement between the present HAZ data and those obtained from SE702 was good (Figure 6-18) particularly at ΔK above $14\text{MPa}\sqrt{m}$, which implies that the crack growth behaviour of the present steel in a seawater environment is similar to that in SE702 regardless of its higher strength and the level of CP used. This is also in agreement with the data compared in Chapter 4 for parent materials fabricated from S355J2+N and SE702 steels respectively.

6.7 Fatigue crack growth of weld material in air and seawater

The results discussed in this section were obtained from CT specimens with the notches aligned in the middle section of the weld. The extraction procedure is shown in Appendix E and the specimens were extracted from the same plate that the HAZ specimens were taken from. Depending on the severity of local stress concentrations introduced during welding, it is possible for fatigue crack initiation to occur on welds. This is one of the primary reasons for generating the data discussed in this section. Another reason is to establish a comparison of crack growth rates in welded zones with those in HAZ and parent materials respectively.

6.7.1 Results and discussion of Weld materials crack growth data in air

The crack growth data obtained from the weld materials tested in air are plotted in Figure 6-19 as a plot of crack lengths versus the number of fatigue cycles. It can be seen that the crack growth curves progressed in a similar manner over the applied number of cycles. However, tests 2 and 3 produced a similar crack growth response while in test 1 a difference of about one and half the applied number of cycles in tests 2 or 3 was observed. Weldments are heterogeneous in nature due to temperature variation during cooling, coupled with weld and possible fabrication defects, which may lead to variations in toughness across the weld, regardless of the level of quality control measures employed during the welding process. Therefore, it is possible that in test 1, the crack was propagating through a tougher region or a region of the weld having more resistance to crack growth compared to tests 2 and 3 respectively. Also, the plastic zone sizes for the final crack lengths in the weld materials in air are the same as those determined in HAZ and parent materials for tests conducted at an R-ratio of 0.1 due to the similarity in loading conditions. This also applies to those determined in the seawater tests.

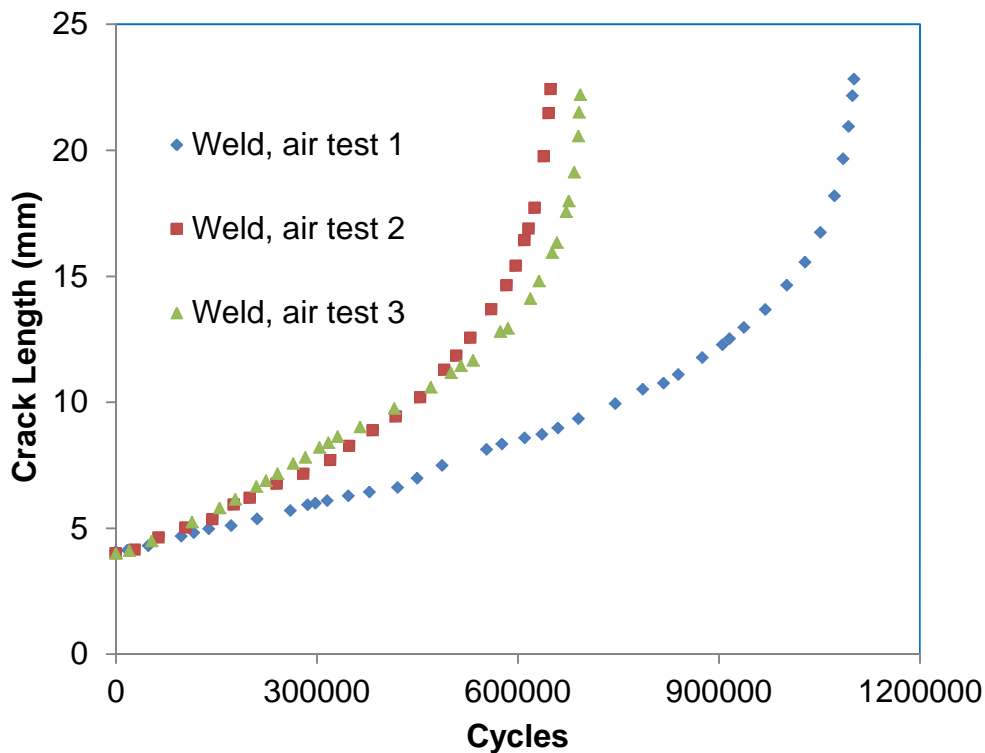


Figure 6-19 Fatigue crack growth in weld materials in air at an R-ratio of 0.1

In Figure 6-20, the crack growth rates obtained in the three specimens are compared. It can be observed that the crack growth curves of the three tests responded in a similar manner regardless of the difference in the number of loading cycles. The observed deviation in the curves occurred at ΔK below $20\text{MPa}\sqrt{m}$ with delayed crack growth rates in test 1 but beyond which the crack growth curves are similar. From microstructural examination of the weld materials' crack surfaces, the degree of crack deviation in an attempt to propagate through a preferred path was marginal compared to what was observed in HAZ materials. Also from the specimens' orientation within the weld plate, the earlier stages of crack growth occurred close to the weld root and, due to subsequent deposits of multiple welding passes, there is a possibility of improvement in the weld toughness as a result of grain refinement by tempering due to subsequent weld layers. Therefore it may be implied that the crack growth mechanism in the weld materials at lower ΔK , particularly in test 1, was related to material variation.

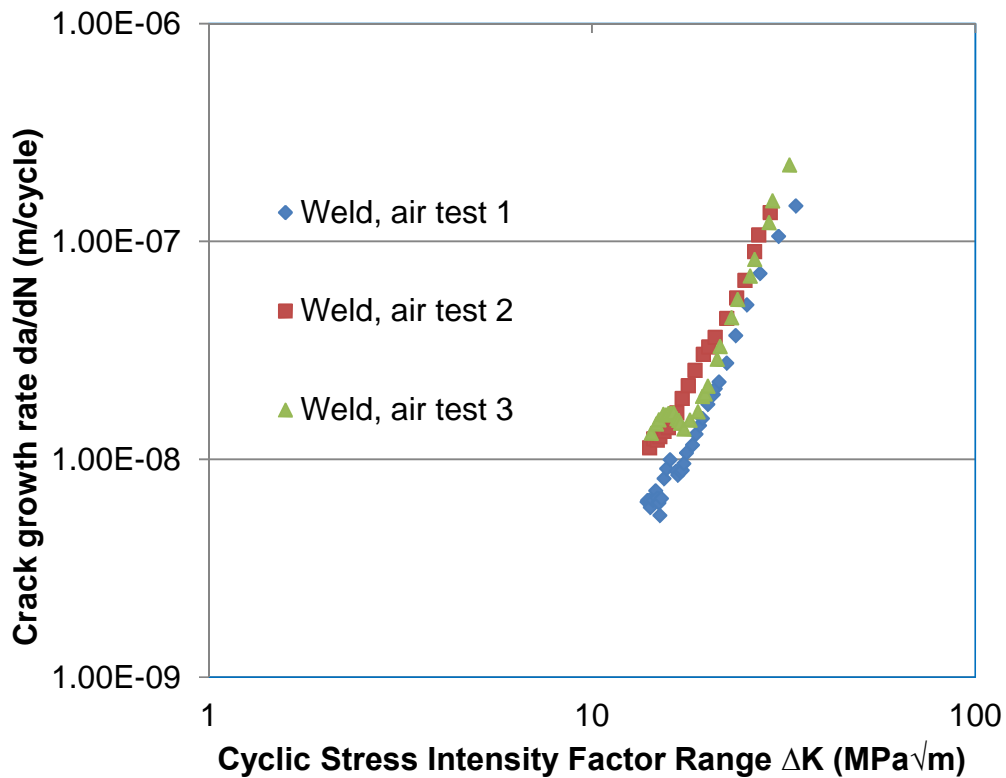


Figure 6-20 Crack growth rates in weld materials in air at an R-ratio of 0.1

The materials constants obtained from the plotted crack growth data shown in Figure 6-20 are set out in Table 6-3. The data correlate with the Paris relationship and the m values obtained from the three tests are similar, while there is a slight change in the corresponding C values. Despite the slight difference in the crack growth curves discussed above, the agreement of the derived constants is quite encouraging which implies the consistency and repeatability of the tests.

Table 6-3 Materials constants in weld materials in air

Tests	R	C	m	R^2
1	0.1	4.0×10^{-13}	3.6	0.97
2	0.1	1.1×10^{-12}	3.4	0.99
3	0.1	1.0×10^{-12}	3.4	0.91

6.7.2 Results and discussion of weld materials crack growth data in seawater

The crack growth data obtained in weld materials in free corrosion conditions are plotted in Figures 6-21 and 6-22 respectively. For the data plotted in Figure 6-21, it was observed that the crack advancements in the specimens were similar until a crack length of approximately 7mm from the notch was attained. This corresponds to about 60% of the total number of cycles. Subsequently, test 1 was found to have a slightly higher resistance than test 2 up to a crack length of about 14mm from the notch, but from this point onward, the two curves began to converge and resulted in a similar total number of cycles consumed. It was challenging to define exactly if the change in the midway crack growth behaviour was related to a change in crack growth mechanism or deviation due to the degree of corrosion products on the specimen surfaces.

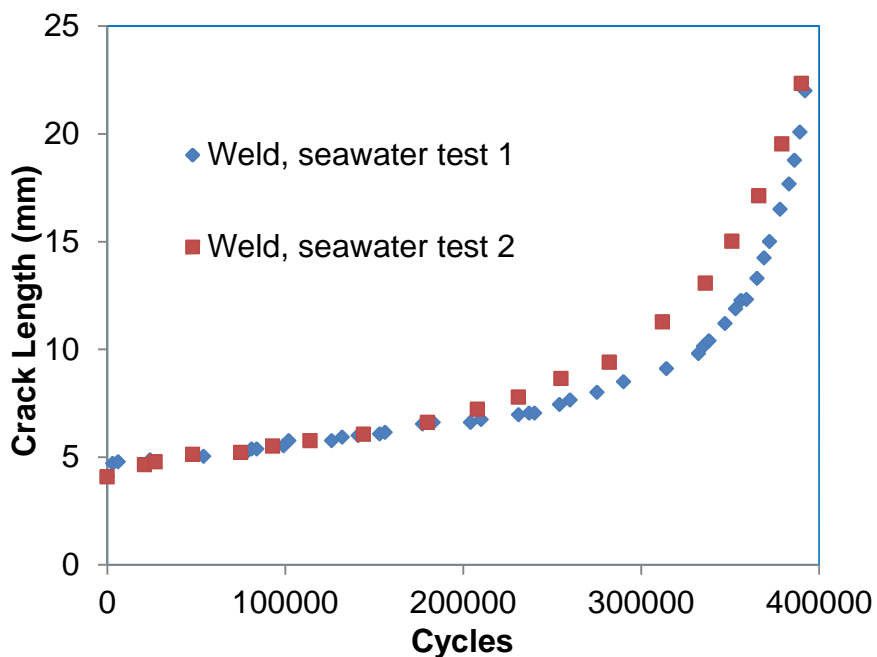


Figure 6-21 Fatigue crack growth in weld materials in seawater at an R-ratio of 0.1

On the da/dN vs. ΔK curves plotted in Figure 6-22, it can be seen that there is a close agreement between the results of the two tests. This indicates that the dominating environmental effect of the seawater within the crack was similar

through the ranges of the applied ΔK . From data analysis, the observed crack growth rates in both specimens were found to be similar at both lower and higher ΔK .

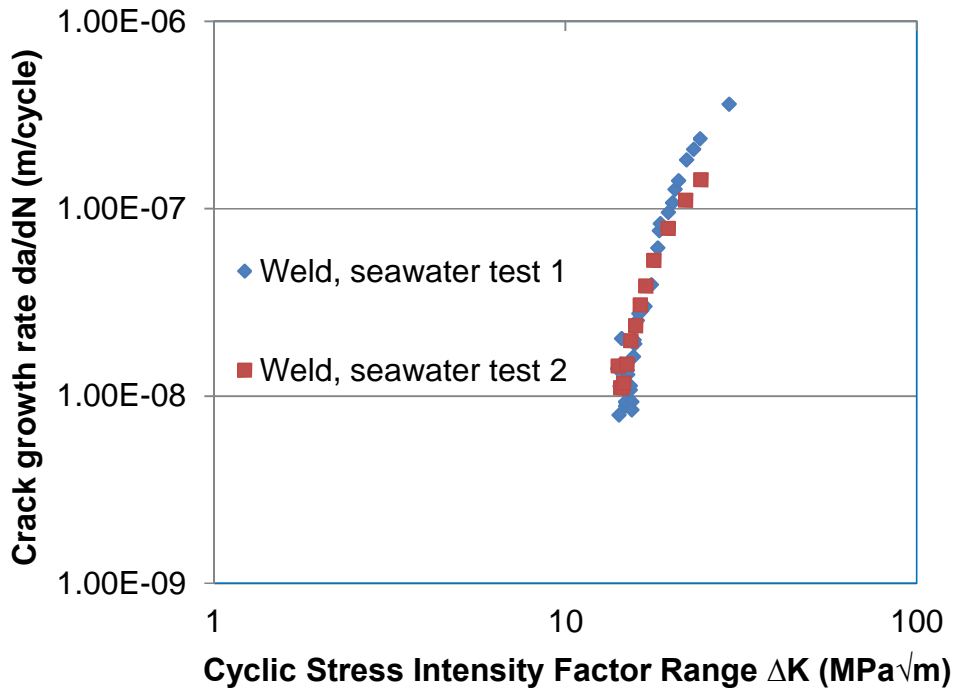


Figure 6-22 Crack growth rates in weld materials in seawater at an R-ratio of 0.1

The material constants derived from the plots (Figure 6-22) are given in Table 6-4. There is a much better agreement between the C and m values when compared with those obtained from the HAZ materials tested under the same loading and environmental conditions. Microstructure changes in the HAZ material may possibly be responsible for the observed difference in the Paris constants, as previously mentioned. This was also observed in the weld materials but was not as significant as in the HAZ materials.

Table 6-4 Material constants in weld materials in seawater

Tests	R	C	m	R ²
1	0.1	2.0×10^{-15}	5.9	0.92
2	0.1	2.0×10^{-14}	5.1	0.95

6.7.3 Comparison of air and seawater data in weld materials

The crack growth curves obtained in seawater are compared with the corresponding air curves, as shown in Figure 6-23. It can be seen that the crack advancement in seawater was similar to in air at the earlier stages of crack growth. The time dependent mechanism of the corrosive environment within the crack at lower opening displacement is the most likely explanation for this. The similarity in crack growth occurred at a crack length of approximately 8mm from the notch. Beyond this point, there was a sharp rise in the seawater crack growth curves over the entire range of loading cycles due to environmental enhancement. At midway in the crack propagation of the specimen, the advancing crack would have been saturated by the corrosive environment; therefore a sudden rise in the crack growth curves should be expected. The difference between the averages of the total number of cycles in the seawater tests and averages of the total number of cycles in the air tests plotted in Figure 6-23 was found to be by a factor of 2. This implies that in free corrosion conditions, the reduction in crack propagation life in the weld material compared with air data was approximately 50% as against 40% in the HAZ material. This also implies that crack propagation was faster in the weld than in the HAZ materials.

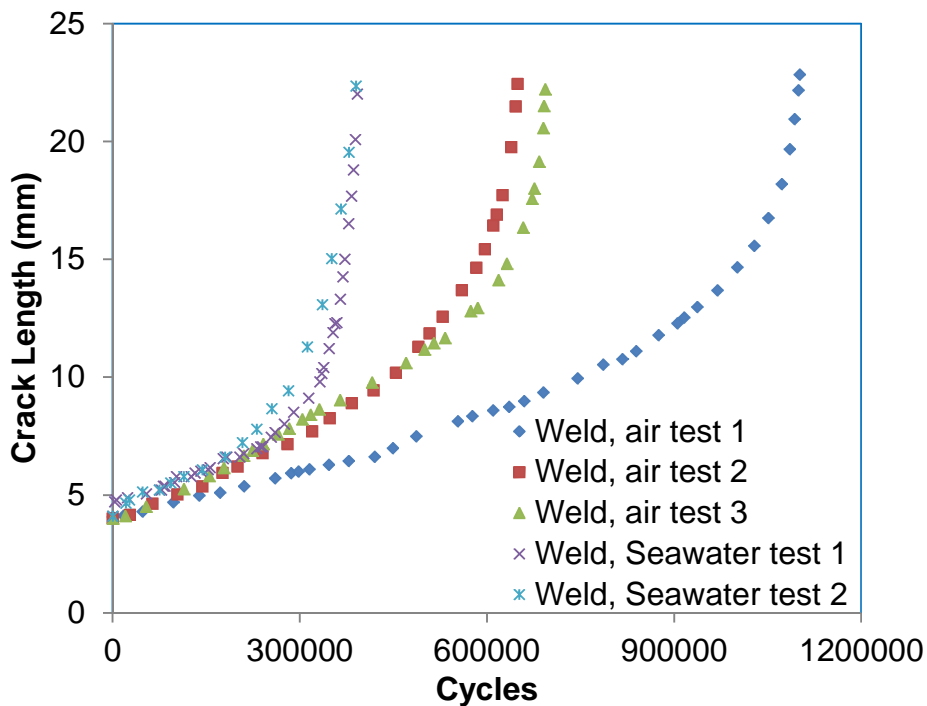


Figure 6-23 Fatigue crack growth in weld materials in air and seawater

The crack growth rates obtained in weld materials in seawater are compared with the air ones in Figure 6-24. At lower ΔK , crack growth rates in seawater were found to be similar to those obtained in air, especially when compared with weld air tests 2 and 3. This was due to the time dependent build-up of the seawater effect within the crack, as previously mentioned. Crack growth rates in seawater were a factor of approximately 3 faster than in air at the intermediate range of ΔK less than $17\text{MPa}\sqrt{m}$. Beyond this point, the order of increase in crack growth rates in seawater was about five to six times higher than in air. At about the ΔK range of $20\text{MPa}\sqrt{m}$, the seawater curves began to deviate towards the air curve and the measured crack growth rates at that instance were about three times higher in seawater than in air. It is possible that the deposit of corrosion products at the crack tip at the higher ΔK was responsible for this effect.

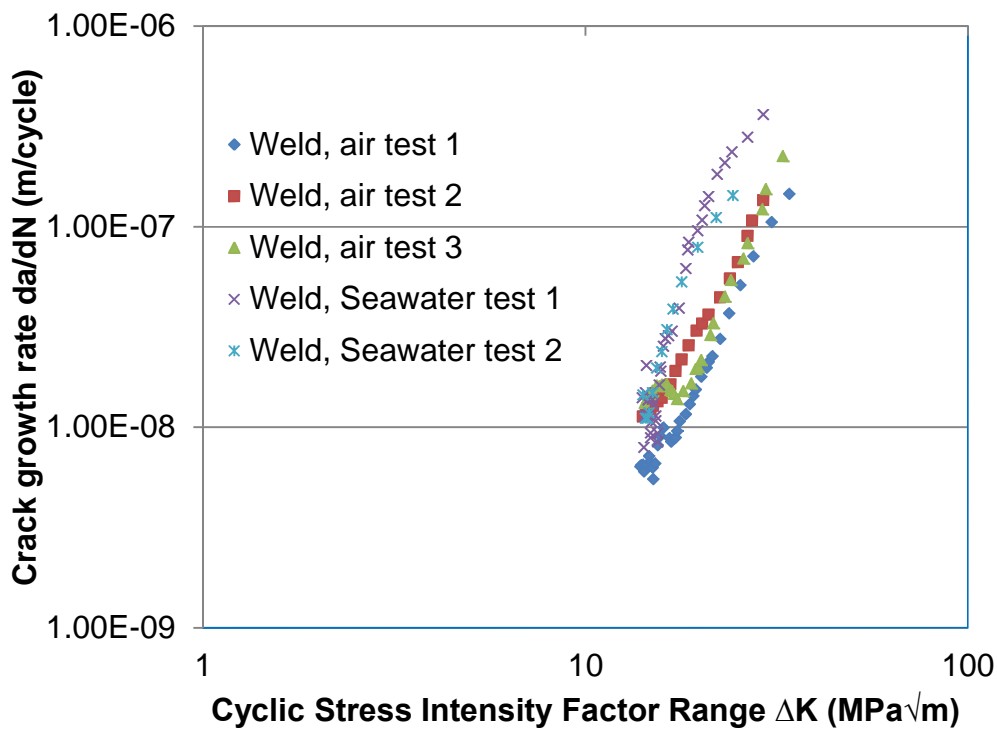


Figure 6-24 Crack growth rates in weld materials in air and seawater

6.7.4 Discussion of weld material response with literature data

In Figure 6-25, the mean data obtained in weld materials at an R-ratio of 0.1 are compared with the results presented by Thompson [76] and Bertini [113] for BS4360 50D and C-Mn steels respectively. It can be seen that the response of the present weld material does not agree well with their results, particularly Bertini's data. In Bertini's work, the behaviour of the weld fusion zone of a steel material with yield strength of 490MPa was investigated. Therefore the data obtained in Bertini's study may be related to differences in yield strength, material and applied load, considering the degree of deviation in the results compared with the data obtained from this work.

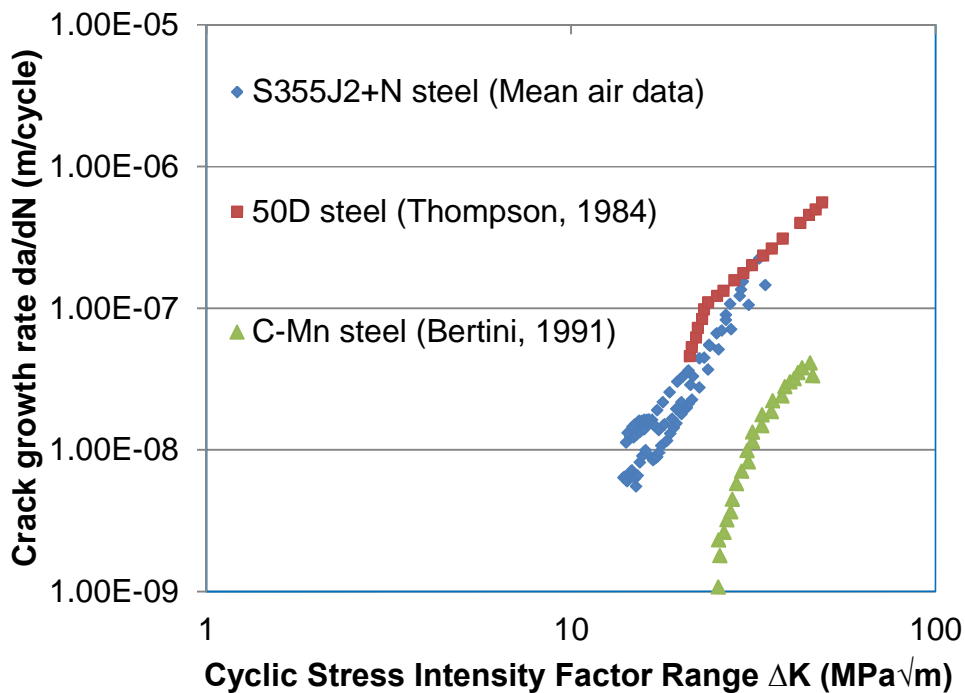


Figure 6-25 Comparison of crack growth rates in weld materials in air with literature data

In Thompson's work, a three point bend single edge notch specimen was used with the notch machined in the mid-section of the weld. The specimen's dimension W was about 30mm measured from the reference plane with an initial uncracked ligament length of 20mm. However, for the CT specimens used in this work, the dimension W was 50mm from the loading axis and the initial uncracked ligament was 40mm. Therefore, it is expected that the difference in the specimen's geometry will have an effect on the response of the material to crack growth.

Apart from the difference in welding procedure, as mentioned in section 6.6.6, another notable difference in the material used for the present work compared with that of Thompson's study is the variation in material composition. The present steel has a reduced level of carbon (0.053%) compared with 0.15% used in Thompson's work. There is also an additional amount of Nickel and Copper with an introduction of Niobium (Nb) and Nitrogen which are not present in the BS4360 50D steel. The reduction in carbon content and introduction of

these new elements would result in improved toughness and weldability [112] while the addition of Aluminium in the presence of Nitrogen to produce nitrides would refine the grains leading to improved toughness [105]. Therefore, it is possible that the crack growth behaviour in Figure 6-25 was related to the material properties in terms of composition and mechanical properties, loading type and specimen geometry. However, it should be noted that for the present steel, higher R-ratios data similar to those discussed in section 6.6.5 are scarce. Also, almost none of the available data in the public domain has been reported under corresponding wind and wave loading conditions using materials that are fabricated from thick welded plates with dimensions and fabrication procedures that represent those of real monopiles as closely as possible.

The mean seawater crack growth data obtained in free corrosion conditions at a temperature of 8°C-10°C are compared with those obtained by both Thompson and Bertini at a temperature of 10°C and 20°C in Figure 6-26. Bertini's data were obtained under CP of -800mV, therefore it is expected that the significant difference in the environmental test conditions would influence the material's crack growth behaviour. It can be seen that the crack growth response of the present data is quite similar to Thompson's data but dissimilar to Bertini's data, as shown in the figure. From the data analysis, it was found that Thompson's crack growth data were measured within ΔK of around $20\text{MPa}\sqrt{m}$ to $50\text{MPa}\sqrt{m}$, while those obtained by Bertini were obtained within the range of $25\text{MPa}\sqrt{m}$ to $71\text{MPa}\sqrt{m}$. The present data were measured at ΔK between $14\text{MPa}\sqrt{m}$ to approximately $30\text{MPa}\sqrt{m}$, which clearly indicates that a higher test load would have been used in both Bertini's and Thompson's studies compared to that used in this work. Therefore the comparisons made here were based on the crack growth rates within the range of the present result, which were found to be slightly higher than Thompson's data particularly at ΔK between $22\text{MPa}\sqrt{m}$ and $30\text{MPa}\sqrt{m}$.

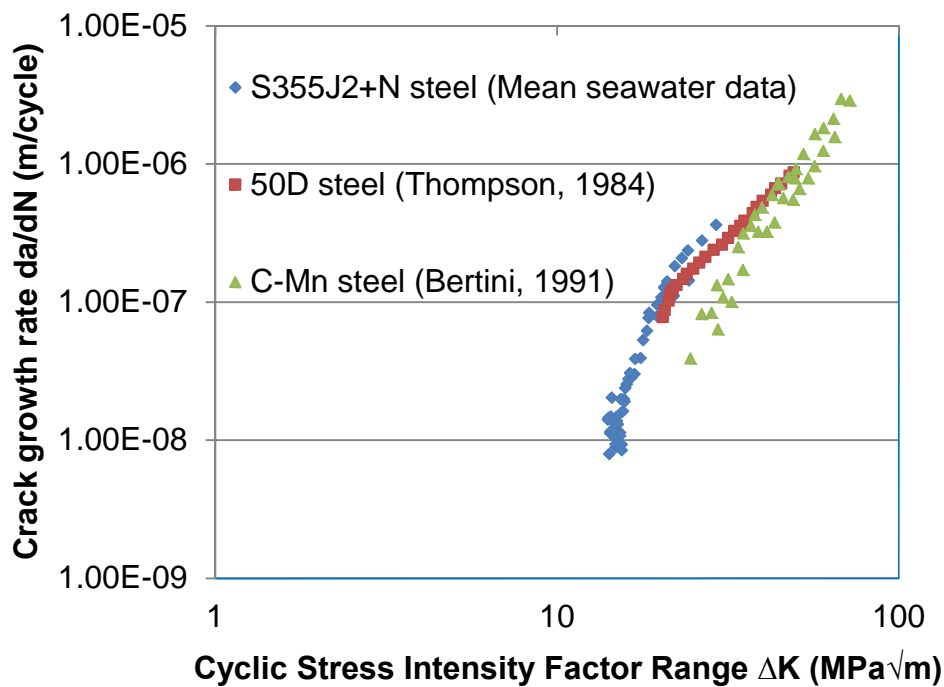


Figure 6-26 Comparison of crack growth rates in weld materials in seawater with literature data

When the C and m values derived for the regression analysis of da/dN vs. ΔK plots were compared, the value of m for C-Mn steel was found to be 5.3 and that of 50D steel was 2.7, while for the present material, the value of m was 3.6. This variation was also applicable to the C values and this implies that C and m values depend on loading conditions such as cyclic load frequency, load range, test environment and type of material.

6.8 Comparison of parent, HAZ and weld materials

The mean air data obtained at an R-ratio of 0.1 in parent, HAZ and weld materials in air are compared in Figure 6-27. It can be seen that the crack growth response of HAZ and weld materials are parallel over the entire ranges of ΔK , while crack growth rates were found to be generally higher in parent materials than in weld and HAZ materials respectively. The manner of crack growth in HAZ and weld materials may be due to the similarity in the composition of the steel plate to that of the filler material used in welding. These compositions are set out in Appendix C. Therefore, it can be suggested that the

response of weld materials may also be used to assess the crack growth behaviour of the HAZ materials if the composition of the base and filler materials are similar. This can also be supported by the similar values of C and m derived for the regression analysis of the HAZ and weld data, as depicted in Table 6-5.

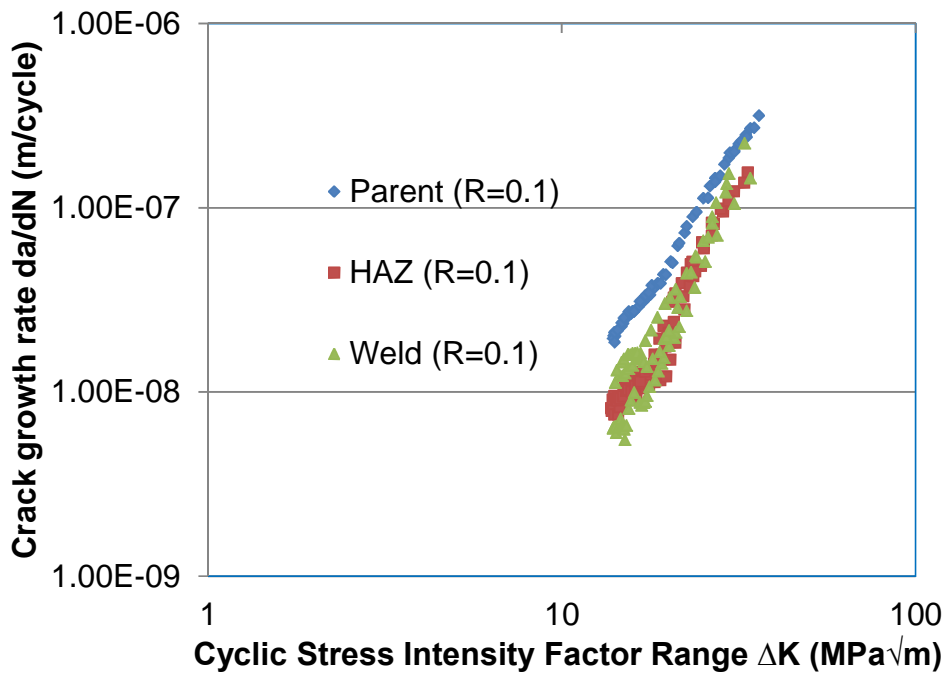


Figure 6-27 Crack growth rates in parent, HAZ and weld materials in air at an R-ratio of 0.1

In Table 6-5, the C and m values derived from parent, HAZ and weld materials at an R-ratio of 0.1 are those corresponding to the mean data. The crack growth rates obtained at R-ratios of 0.5 to 0.7 in parent and HAZ materials are compared in Figure 6-28 where it can be seen that the crack growth rates in parent materials at both R-ratios are similar. The differences between the crack growth rates in parent and HAZ materials at both R-ratios were only evident at the lower ΔK range below $13MPa\sqrt{m}$, but this difference was not more than a factor of 2. Beyond the ΔK range of $13MPa\sqrt{m}$, the crack growth rates in the HAZ were found to be similar to those measured in parent materials. It can also be seen from Table 6-5 that the material constants obtained at an R-ratio of 0.5 in parent materials are the same as those obtained in HAZ at an R-ratio of 0.7.

This implies that the crack growth data obtained in parent materials at higher R-ratios can be applied to assess the integrity of welded joints subjected to high mean stresses. Figure 6-28 also implies that R-ratio effects are not significant either in HAZ or parent materials in an air environment.

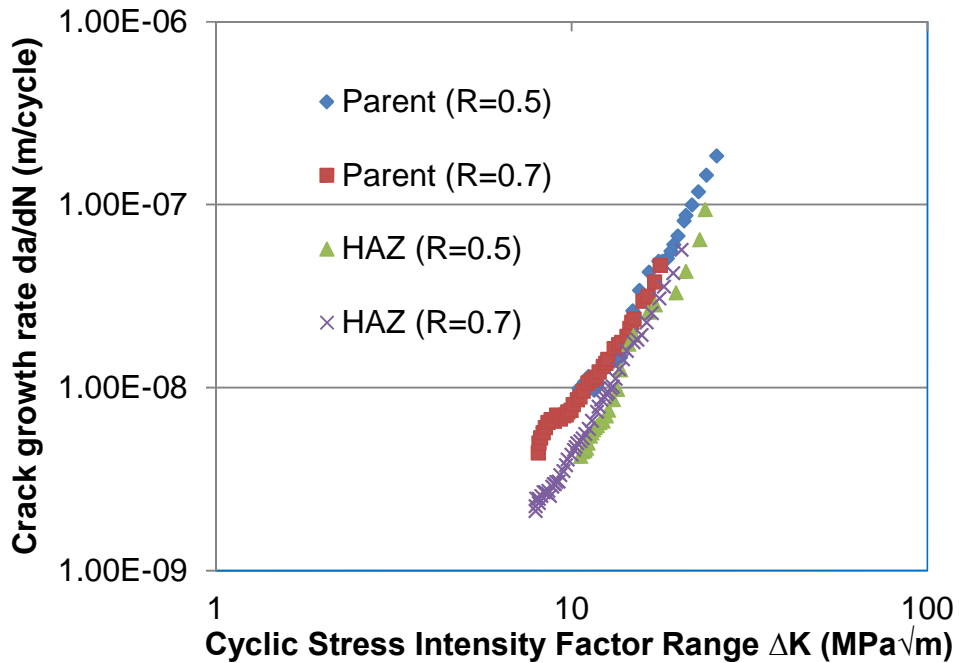


Figure 6-28 Crack growth rates in parent and HAZ materials in air at an R-ratio of 0.5 and 0.7

The parent, HAZ and weld crack growth data obtained at an R-ratio of 0.1 in free corrosion conditions are compared in Figure 6-29. A similar pattern in crack growth rates was found in the three materials, as shown in the figure, with a marginal difference in crack growth rates in parent materials than from those obtained in the HAZ and weld materials. Regardless of the similarity in the crack growth behaviour in the materials, the values of constant C and exponent m , compared in Table 6-5, vary from the parent to weld materials. This implies that material variation and environmental contribution still have some effects on crack growth rates.

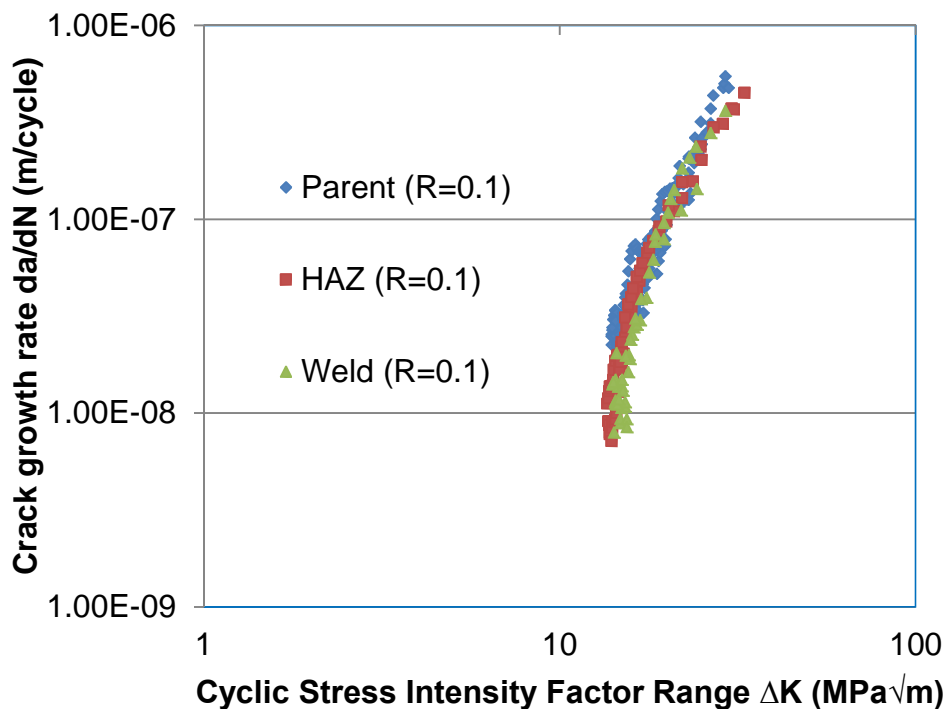


Figure 6-29 Crack growth rates in parent, HAZ and weld materials in seawater at an R-ratio of 0.1

However, on the overall scale, it was found that there was a good agreement in the crack growth response of parent material with those obtained in HAZ and weld materials. A similar mechanism was also reported for high strength steels parent and weld materials with yield strength ranging from 500MPa to 600MPa [54]. It was suggested that proper screening of the crack growth behaviour of parent materials may be applied to evaluate the suitability of weld materials.

The data generated at higher R-ratios in HAZ materials in seawater are compared with those obtained from parent materials, as shown in Figure 6-30. The significant effects of environmental interaction with loading conditions can be seen in the figure for tests conducted at higher R-ratios compared with the crack growth data obtained in air (Figure 6-28). Crack growth rates were found to be higher in parent materials than in the HAZ, particularly at higher ΔK . Mean stress effect was dominant at lower ΔK , but at higher ΔK , crack growth rates at an R-ratio of 0.7 were similar to those obtained at an R-ratio of 0.5. From the material constants compared in Table 6-5, it can be observed that the R-ratios of 0.5 and 0.7 tests produced the same m values but different C values which

implies that mean stress effects in this case only have a significant effect on C values but their effect on m values can be considered marginal.

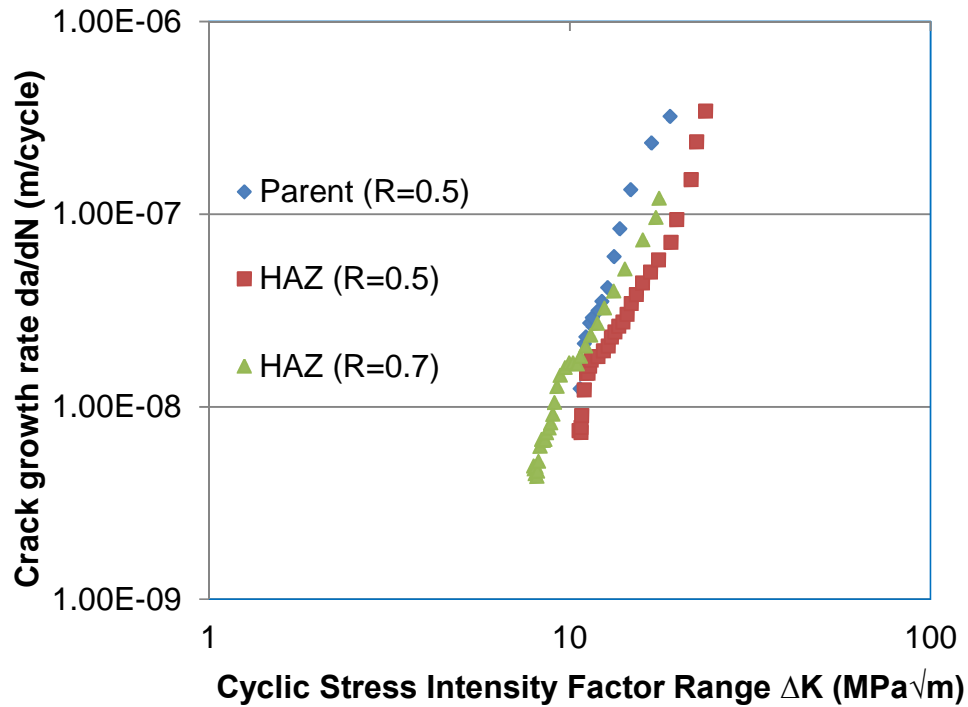


Figure 6-30 Crack growth rates in parent and HAZ materials in seawater at an R-ratio of 0.5 and 0.7

Table 6-5 Material constants for parent plate, HAZ and weld materials

Environment	Material	R-ratio	C	m
Air	Parent	0.1	7.1×10^{-12}	3.0
Air	HAZ	0.1	7.0×10^{-13}	3.5
Air	Weld	0.1	5.0×10^{-13}	3.6
Air	Parent	0.5	2.1×10^{-12}	3.4
Air	Parent	0.7	2.0×10^{-11}	2.6
Air	HAZ	0.5	7.0×10^{-13}	3.7
Air	HAZ	0.7	2.1×10^{-12}	3.4
Seawater	Parent	0.1	4.1×10^{-13}	4.2
Seawater	HAZ	0.1	6.0×10^{-14}	4.7
Seawater	Weld	0.1	3.0×10^{-15}	5.7
Seawater	Parent	0.5	3.1×10^{-14}	5.6
Seawater	HAZ	0.5	8.0×10^{-13}	4.0
Seawater	HAZ	0.7	1.1×10^{-12}	4.0

The crack growth data obtained from this study at an R-ratio of 0.1 are compared with the air and seawater recommendations in BS 7910 [130]. The mean data obtained from parent materials at an R-ratio of 0.1 agree well with the recommended curves and the majority of the data points are encompassed by the weld and parent materials' recommended curves, as shown in Figure 6-31. The seawater data for parent, weld and HAZ materials crossed the base material air curve towards the base material free corrosion curve at lower ΔK , but at higher ΔK the data points generally lie on the free corrosion curve. It can also be seen from Figure 6-31 that the HAZ and weld material air data are below the base material recommended air curve. This also applies to the generated free corrosion data which are quite far away from the recommended weld materials free corrosion curve, as shown in the figure. The implication of this on the comparisons made with the recommended mean+2SD for R<0.5

curves is that the present HAZ and weld materials have good resistance to crack growth.

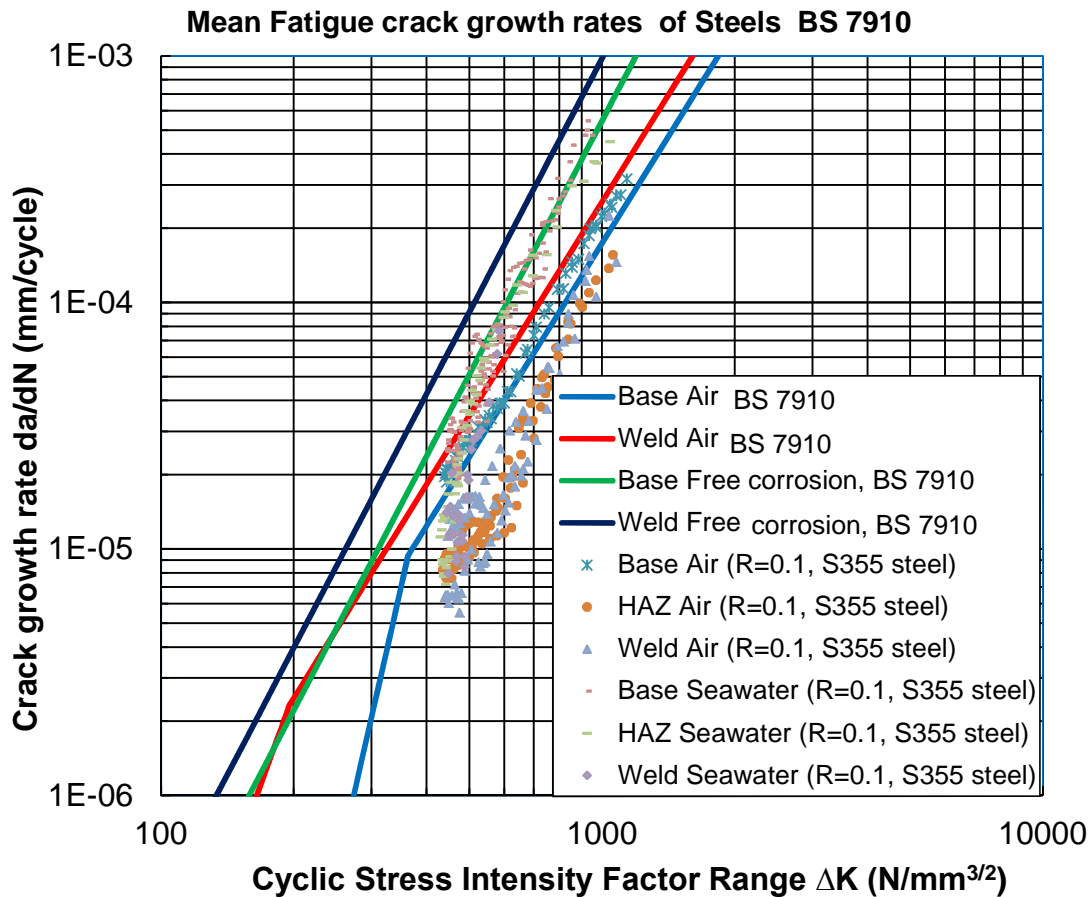


Figure 6-31 Comparison of Parent, HAZ and weld data with BS 7910 in air and seawater at an R-ratio of 0.1

The data obtained at R-ratios of 0.5 to 0.7 are compared with the fatigue crack growth laws recommended in BS 7910 for $R \geq 0.5$ as shown in Figure 6-32. The mean+2SD curve ($R \geq 0.5$) was recommended in BS 7910 for the assessment of welded joints in order to provide room for the effect of residual stresses. It can be observed from the figure that the parent and HAZ crack growth data obtained at R-ratios of 0.5 to 0.7 in air are generally below the recommended base material air curve particularly at lower ΔK , while at the ΔK range above $20\text{MPa}\sqrt{m}$, the parent material R-ratio of 0.5 data lies within the acceptable region of the curve. It can also be observed that the HAZ air data obtained at R-ratios of 0.5 and 0.7 are quite far away from the recommended weld material air

curve, which implies a good resistance to crack growth in the present material, as mentioned earlier. The HAZ seawater data for R-ratios of 0.5 and 0.7 lie below the weld free corrosion curve and were found to be between the base materials' and weld materials' recommended air curves. The seawater data obtained in parent material at an R-ratio of 0.5 crossed the base material free corrosion curve at ΔK below $14\text{MPa}\sqrt{m}$ and later approached the weld free corrosion recommended curves as shown in the figure. However, from the data analysis, it was found that about 70% of the R-ratio of 0.5 seawater data points fell within the acceptable region. Judging by the response of the present materials with respect to the comparisons made in Figures 6-31 and 6-32, it can be submitted that the steel used in this work exhibited good crack growth behaviour in air and in seawater. The resistance to crack growth, particularly the weldments, might be linked to modern material manufacturing and fabrication procedures, such as the welding specification employed in preparing the plate. This suggests that if modern steel fabrication techniques and welding procedures can be improved, with more quality control measures that will significantly reduce associated welding defects, an appreciable level of resistance to damage in offshore structures can be achieved.

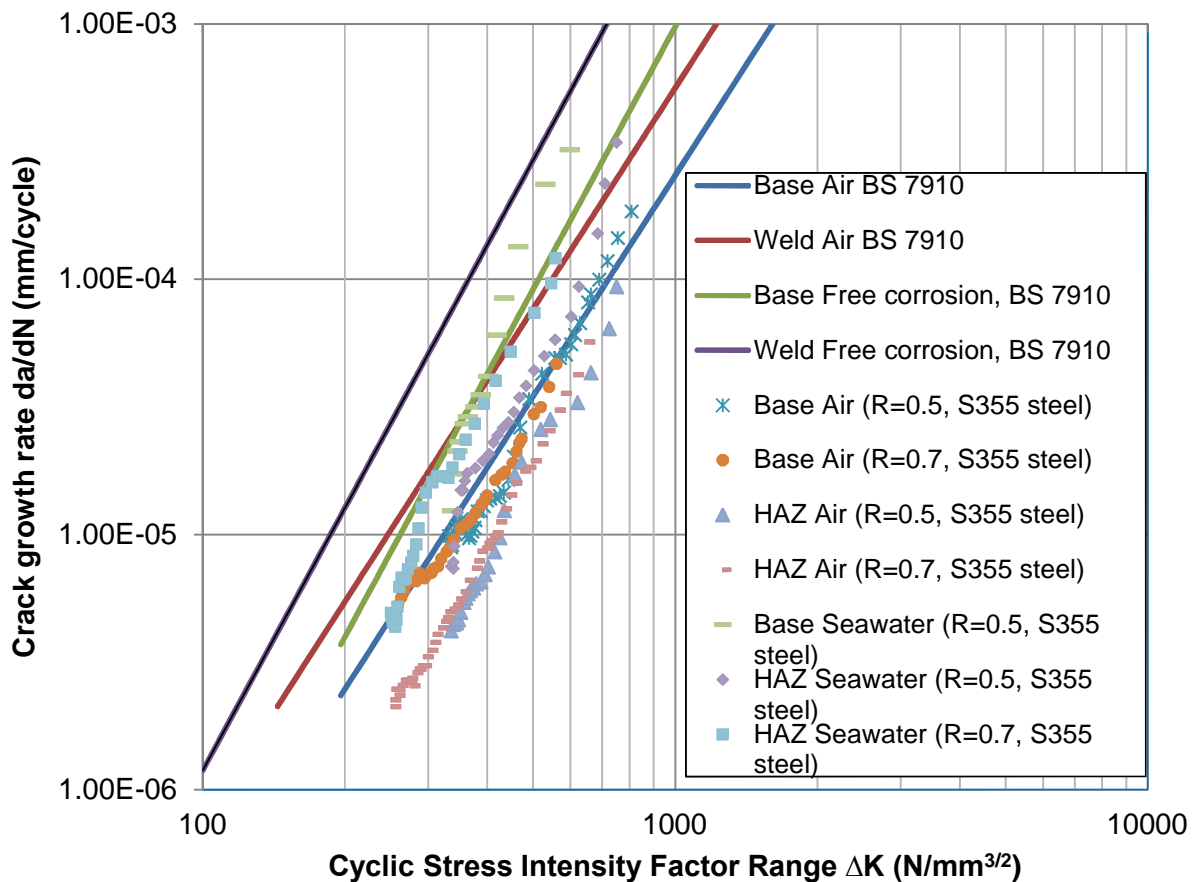


Figure 6-32 Comparison of Parent and HAZ data with BS 7910 in air and seawater at an R-ratio of 0.5 and 0.7

6.9 Implementation of model on HAZ materials

A new crack opening time correlation that accounts for mean stress effects on corrosion fatigue crack growth was presented in Chapter 5. The models for positive and negative R-ratios are given in Equations 5-15 and 5-18. In this section, the models are applied to predict mean stress effects on crack growth rates in weldments. As mentioned in Chapter 5, the experimental data obtained at an R-ratio of 0.1 in air and seawater is used as the baseline data for the model development.

In Figure 6-33, the model is compared with experimental data obtained from HAZ materials in air at R-ratios of 0.1 to 0.7. The model gave a good agreement with the experimental data at an R-ratio of 0.1, as shown in the figure. The material constants derived from the plots of da/dN vs. ΔK in air and seawater for

the positive and negative R-ratios are compared in Table 6-6. It can be observed that the present model produced the same C and m values as those derived from the air data at an R-ratio of 0.1. However, at R-ratios of 0.5 and 0.7 in air, it can be seen from Figure 6-33 that the model overestimated the experimental data. This may be attributed to the resistance of the present materials to crack growth.

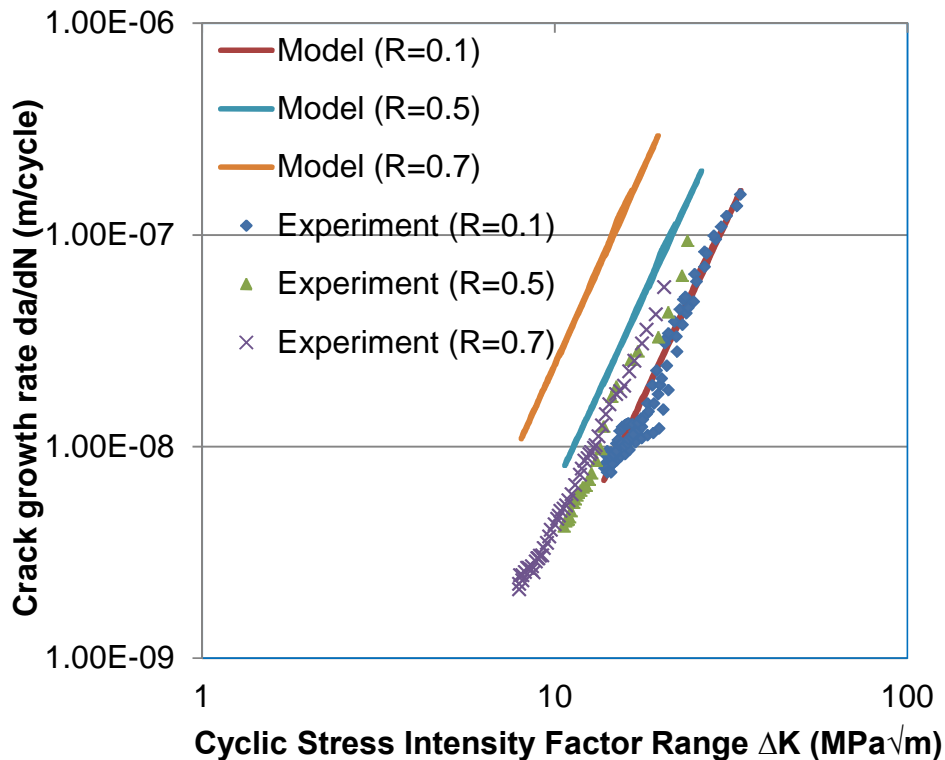


Figure 6-33 Model application to HAZ materials in air at positive R-ratios

It may also be recalled from the literature survey that higher crack growth rates have been attributed to an increase in stress ratios, but the data plotted in Figure 6-33 indicates that the degree of increase in crack growth rates under a higher mean stress may be material dependent. However, from the comparisons made in Table 6-6, between the experimental and theoretical material constants, it can be observed that at R-ratios of 0.5 and 0.7 in air, nearly the same m values but varying C values were obtained. This implies that the effects of material and mean stress on crack growth rates for the case considered in air is more related to the C values compared to their marginal effects on m values.

Table 6-6 Model and experimental data material constants

Environment	R-ratio	Experiment		Model	
		<i>C</i>	<i>m</i>	<i>C</i>	<i>m</i>
Air	0.1	7.0×10^{-13}	3.5	7.0×10^{-13}	3.5
Air	0.5	7.0×10^{-13}	3.7	2.1×10^{-12}	3.6
Air	0.7	2.1×10^{-12}	3.4	5.1×10^{-12}	3.6
Seawater	0.1	6.0×10^{-14}	4.7	2.1×10^{-13}	4.5
Seawater	0.5	8.0×10^{-13}	4.0	6.0×10^{-13}	4.4
Seawater	0.7	1.1×10^{-12}	4.0	2.0×10^{-12}	4.5
Air	-1			5.1×10^{-13}	3.5
Seawater	-1			1.0×10^{-13}	4.3

The seawater data obtained at R-ratios of 0.1 to 0.7 in seawater are compared with the present model in Figure 6-34. The present model gave a good agreement with the experimental data at an R-ratio of 0.1 and produced a similar manner of crack growth as the experimental investigation. The derived *C* and *m* values from the R-ratio of 0.1 data, as compared in Table 6-6, also resulted in fairly good agreement with the present model. At R-ratios of 0.5 and 0.7, it can be seen that the model overestimated the experimental data, while at higher ΔK , the R-ratio of 0.5 and 0.7 data deviated towards the R-ratio of 0.1 data. However, from the material constants compared in Table 6-6 for R-ratios of 0.5 and 0.7, it can be seen that the present model resulted in slightly higher *m* values and similar *C* values, regardless of the degree of deviation in the curves. The influence of material on mean stress effects is the possible explanation for this result, as mentioned earlier.

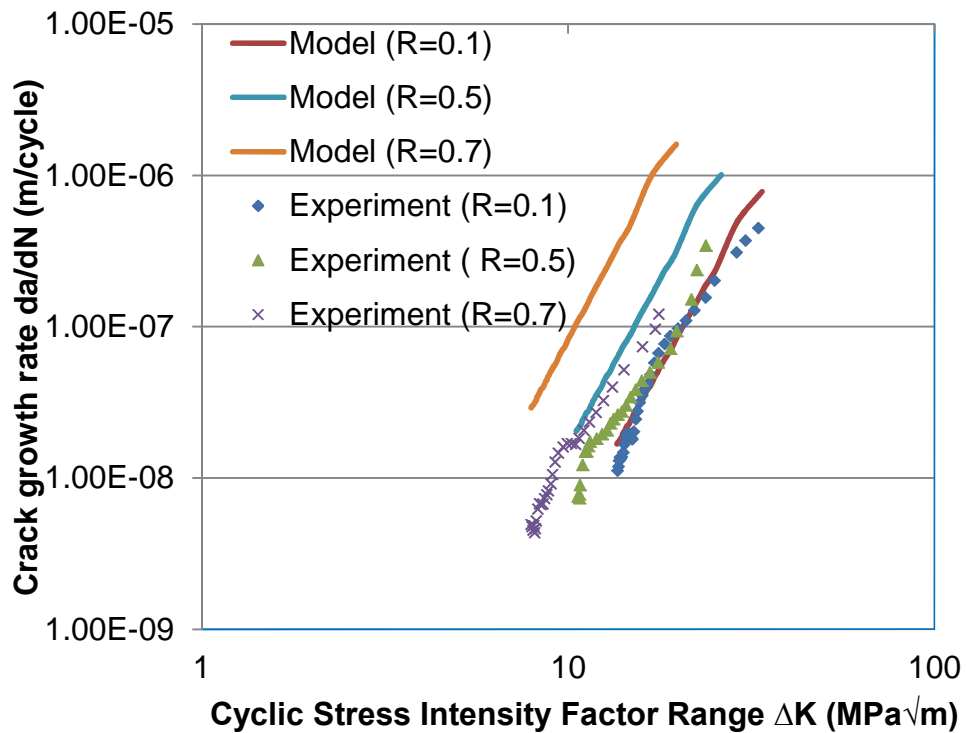


Figure 6-34 Model application to HAZ materials in seawater at positive R-ratios

Tests are conducted at higher stress ratios in order to allow for the influence of residual stresses in weld materials and also to obtain conservative results for fatigue life calculations. However, these may depend on the magnitude of the residual stress distribution accompanied by the type of welding procedure which is likely to be different in relatively thick materials such as the weld plate used in this work. Therefore, increasing mean stresses may not necessarily produce higher crack growth rates, especially when the crack is immersed in a compressive residual stress field.

As mentioned in Chapter 5, due to the self-equilibrating nature of residual stresses, it was anticipated in this work that, with respect to mean stress or R-ratio effects, the magnitude of the residual stress distribution in the weld plate would be negative. The expected crack growth curve in air in such a situation was modelled by Equation 5-17 using the crack growth data at an R-ratio of 0.1 as the baseline data. The result for the negative R-ratio in air is depicted in

Figure 6-35 where it can be seen that the modelled curve obtained using Equation 5-17 shifted to the right of the baseline data, as expected.

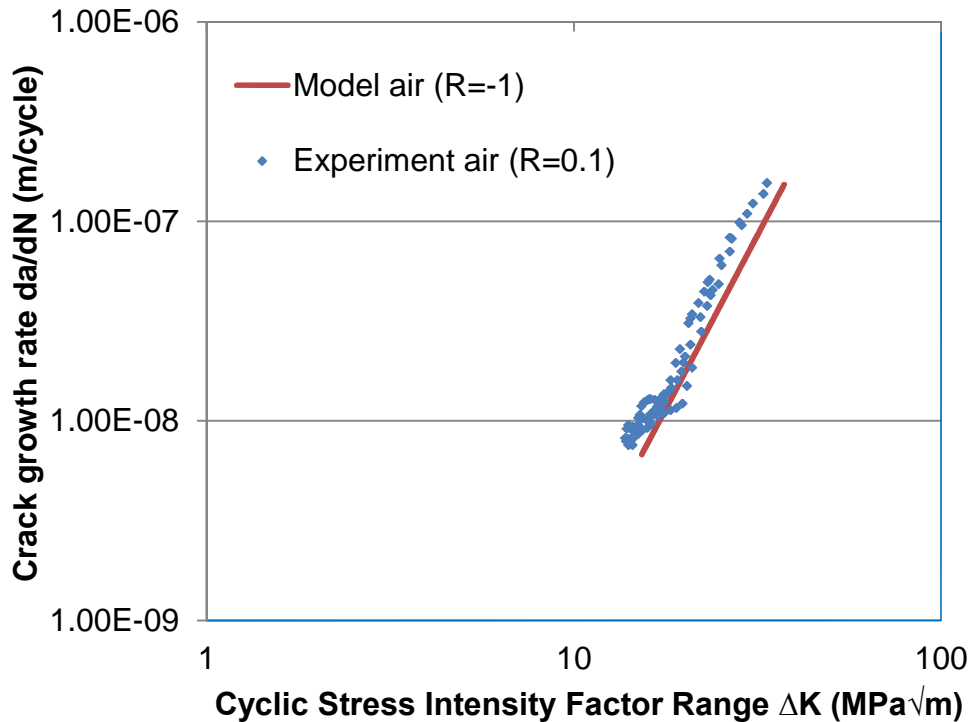


Figure 6-35 Model application to HAZ material in air at negative R-ratio

Equation 5-18 was also used to calculate the crack growth rates in seawater at an R-ratio of -1. The results are plotted in Figure 6-36 where it can be observed that the modelled seawater curve at an R-ratio of -1 lies between the air and seawater data obtained at an R-ratio of 0.1, as postulated in Chapter 5. Crack growth rates were also found to be lower at an R-ratio of -1 than those measured at an R-ratio of 0.1 experimentally, but at higher ΔK , the baseline data almost merged with the modelled curve. However, with respect to the position of the modelled crack growth curve at an R-ratio of -1, as shown in Figure 6-36, it implies that the assumption made in Chapter 5 is in agreement with the model response in HAZ materials, but experimental data obtained at an R-ratio of -1 are needed in areas of further research in order to validate this model and the assumption made.

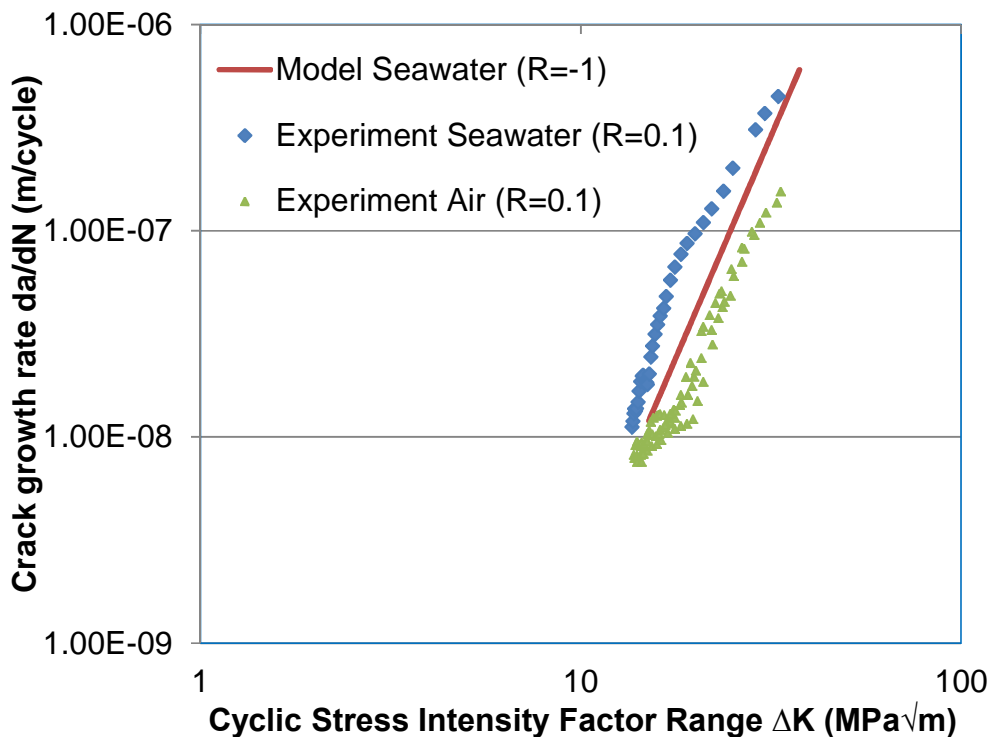


Figure 6-36 Model application to HAZ materials in seawater at negative R-ratio

6.9.1 Discussion of fatigue test results with microstructural analysis

The observed microstructure of the HAZ is depicted in Figure 6-37. The figure shows the position of the notch on the HAZ and the microstructure variations from parent materials to the weld region. It can be seen that the notch is located at the intercritical region closer to the coarse grain microstructure. Figure 6-38 also shows the direction of crack growth as it deviates towards the finer grain microstructure closer to the parent material, probably due to its lower resistance to crack growth. The crack path in the HAZ has also been found to be significantly tortuous with reduced crack growth rates as the crack deviates towards the unaffected parent material in stainless steel welds [147].

The present material also exhibited an irregular crack growth in the HAZ materials based on the examination of the specimens tested at R-ratio of 0.1 in air. A similar crack branching phenomenon was also reported for tests conducted at lower R-ratios in Q345 steel weldments [79], leading to a reduction in crack growth. The direction of the crack path in this study appears to have been influenced by microstructure in the HAZ materials. The

microstructure influence on the preferred crack path in the HAZ of CSN3:8 steel was also reported in [112]. It may therefore be implied that the data presented in section 6.6.1, Figure 6-6, were also significantly influenced by microstructure variation accompanied by crack deviation towards the parent material. This can also be argued by the degree of crack branching in air, which was observed to have increased with an increase in applied ΔK . Previous studies [5], [148], [149] have also shown that the degree of crack branching or deviation depends on the applied ΔK , irrespective of the microstructure or material strength.

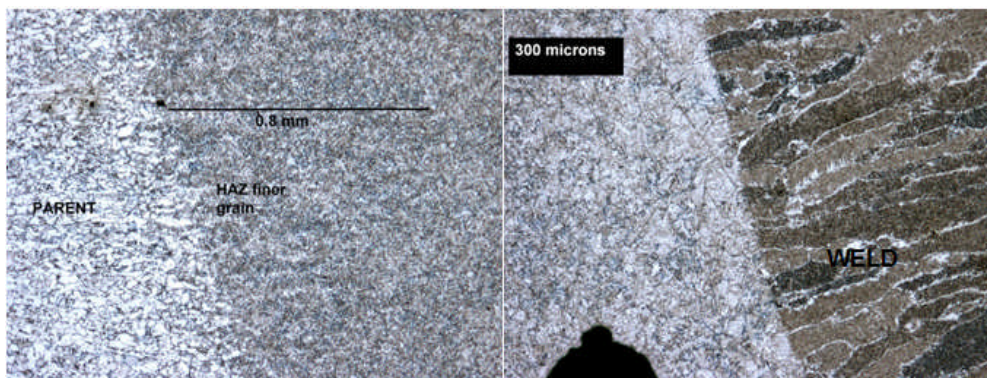


Figure 6-37 Microstructural variation from weld to parent materials (X5)

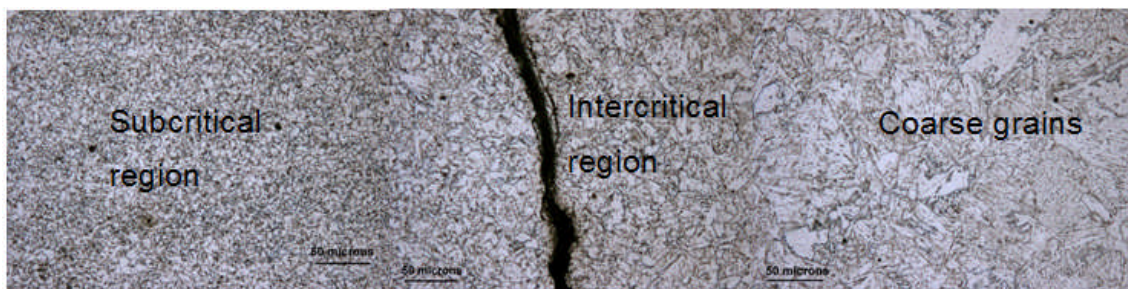


Figure 6-38 Crack growth in the Intercritical HAZ region (X5)

An interesting feature in the manner of crack growth was that the crack propagated only in the HAZ region of the material over the ranges of the applied loading cycles. This can be seen in Figure 6-39 and was also confirmed by measurements taken at intervals along the crack path. At the beginning of the crack propagation, the crack was about 0.4mm from the weld region, at midway of propagation, the crack was about 0.7mm from the weld, and it was about 1mm from the weld towards the end of the propagation. However, the recommended remaining uncracked ligament of the specimen [116], did not

permit the crack from growing into the parent material. The implication of this on an offshore structural member is that if the propagation process had continued, the crack would have grown into the unaffected parent material. Microstructure examination of the crack path in the specimens tested in seawater also revealed that the crack propagated in the HAZ microstructure with a marginal crack deviation. The rate of metal removal associated with the microstructure of the HAZ is the possible explanation for this.

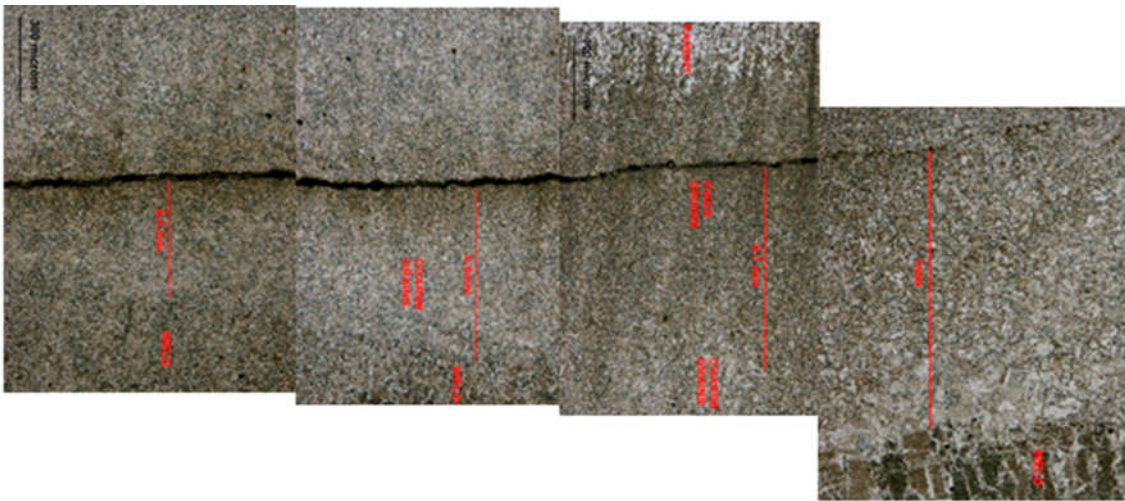


Figure 6-39 Crack growth in HAZ materials in air (X5)

It was also observed that the crack path in the HAZ materials exhibited a tortuous manner, as shown in Figure 6-39. This curvy nature of the crack path as it progresses through the specimen would have also contributed to the manner of crack growth shown in Figure 6-6. The effect of microstructure on crack propagation was also evident in the HAZ materials when the crack path was compared with that of weld material, as shown in Figure 6-40. It can be seen from the figure that the changes in crack path were more in the HAZ microstructure (left) than in the weld material (right). This would also have contributed to the slightly higher crack growth in the weld material than in the HAZ materials, particularly in the air environment. This is in agreement with the explanation given in section 6.7.3 with respect to crack propagation lives in weld and HAZ materials.

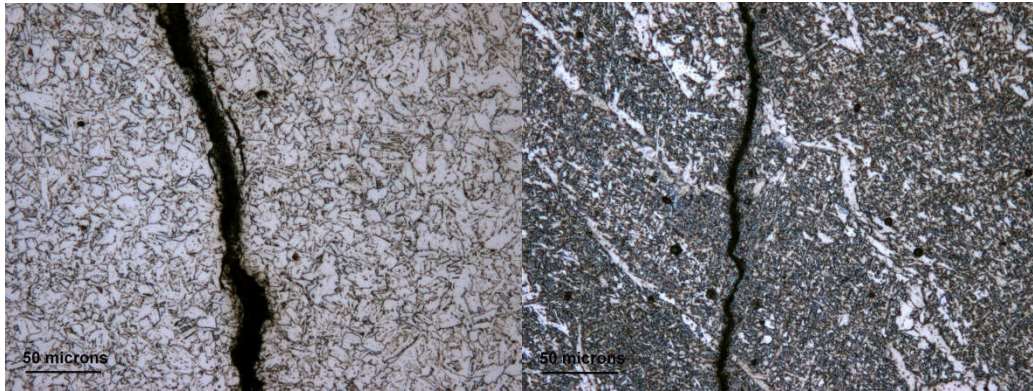


Figure 6-40 Crack growth pattern in left: HAZ and right: weld materials (X20)

6.9.2 Discussion of fatigue test results with fractography analysis

The fractography analysis of the specimens tested in air and in free corrosion conditions are shown in Figures 6-41 to 6-46. Particular areas of interest were examined on the fracture surfaces, but mainly at higher ΔK where the influence of environmental interaction might be more obvious. This was attempted in order to also correlate the degree of striations found on the fracture surfaces with crack advancement. However, examination of all the fracture surfaces with respect to ΔK was not in detail. In air, as shown in Figure 6-41 for the parent material, the fracture surface showed a transgranular mixture of ductile and brittle striation mechanisms.

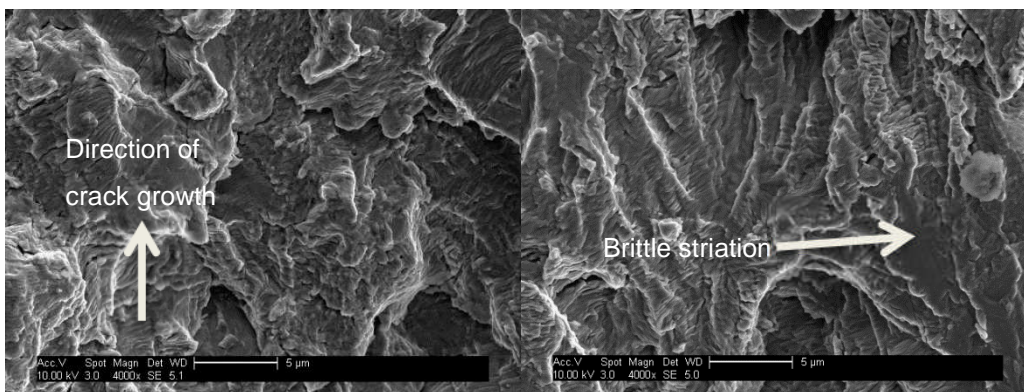


Figure 6-41 Mixture of ductile and brittle striations in parent materials in air at $\Delta K=20\text{MPa}\sqrt{m}$

In order to relate the appearance of the HAZ material fracture surface to the change in slope of the da/dN vs. ΔK plots in air, as discussed in section 6.6.1,

the particular areas of the specimen corresponding to ΔK between $18\text{MPa}\sqrt{m}$ and $19\text{MPa}\sqrt{m}$ were examined, as shown in Figure 6-42. At ΔK of $18\text{MPa}\sqrt{m}$, the bottom right of the figure, it can be observed that a significant amount of fatigue striations are evident compared to a lesser degree of striations as shown at the top right of the figure which corresponds to ΔK of $19\text{MPa}\sqrt{m}$. The degree of striations in the bottom right may be related to the delayed crack growth prior to ΔK below $19\text{MPa}\sqrt{m}$ and the characteristic appearance of the figure at the top right may also be linked to a change in slope prior to transition to the faster crack growth region, as shown in Figure 6-6. However, variation in the surface features of all the specimens tested in air was inconclusive as additional information with respect to the measurements of striation spacing was not obtained during the investigation.

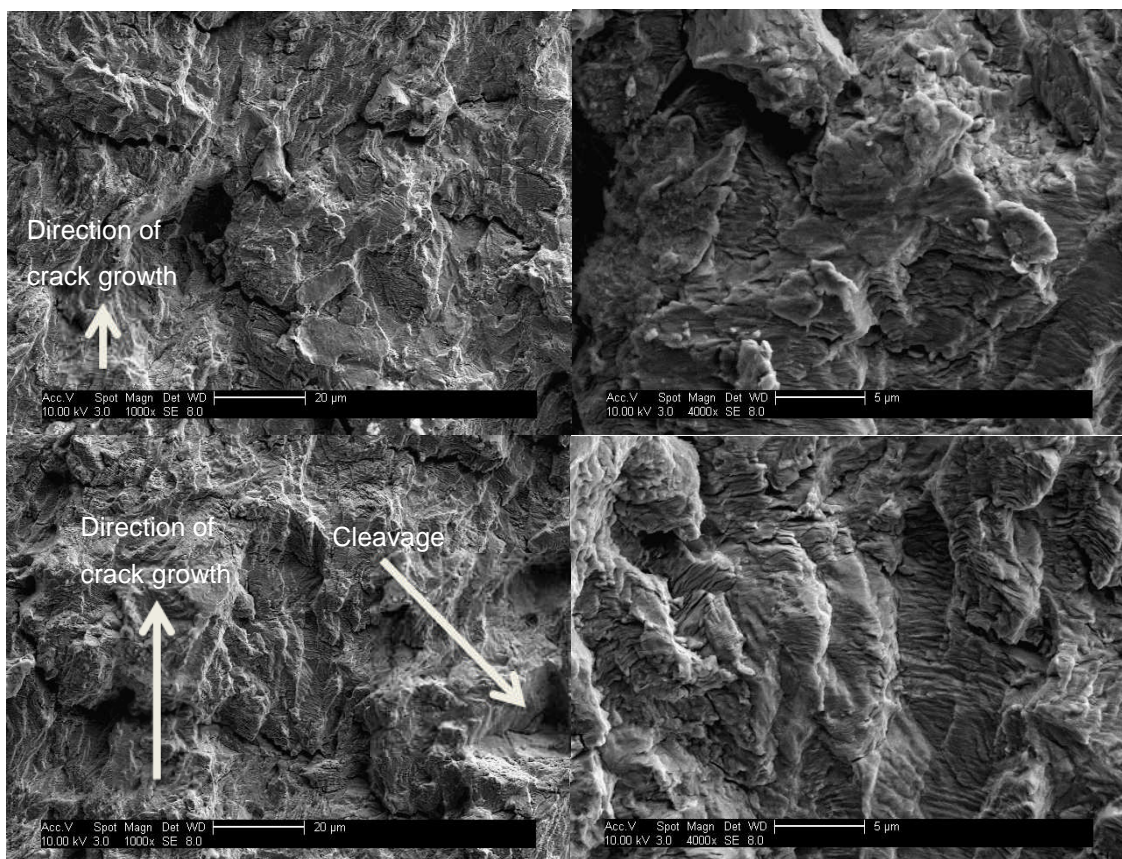


Figure 6-42 Transition region in HAZ material in air at ΔK between $18\text{MPa}\sqrt{m}$ and $19\text{MPa}\sqrt{m}$

Figure 6-43 shows the examined fracture surface of the weld material tested in air. The surface feature shows failure by a mixture of ductile and brittle striations. This feature may be related to the weld inhomogeneity and possible defects introduced during welding.

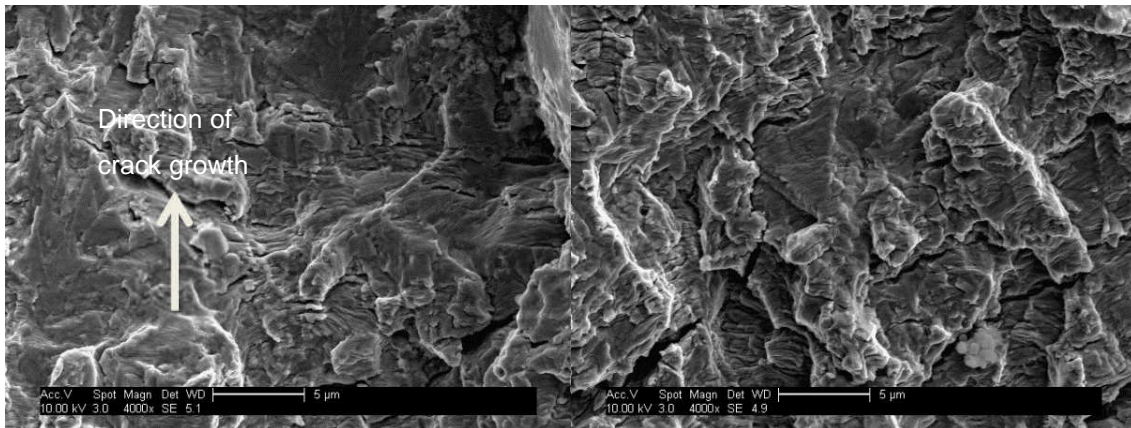


Figure 6-43 Mixture of ductile and brittle striation in weld materials in air at $\Delta K=20\text{MPa}\sqrt{m}$



Figure 6-44 Ductile striations on parent materials in seawater $\Delta K=19\text{MPa}\sqrt{m}$

In the parent material tested in seawater, the fracture surface, as shown in Figure 6-44 at ΔK of $19\text{MPa}\sqrt{m}$ gave a uniform cracking mechanism particularly at the right of the figure. Some cleavage features of the crack surface are also evident at the left of the figure coupled with some corrosion products. From the fracture surface appearance, it is possible that the associated uniform features of the surface shown in Figure 6-44 were related to a minimum level of corrosion enhanced damage introduced on the parent material's microstructure

compared to in HAZ and weld materials. This implies that fracture surfaces accompanied by the type of striations are material dependent, as also mentioned in [150].

This can also be supported by the difference in the appearances of the fracture surfaces of the HAZ and weld materials compared to in the parent materials. It can be observed, as shown in Figures 6-45 and 6-46, that there are considerably massive corrosion enhanced damage features compared to those observed in parent materials (Figure 6-44). Some deposits of corrosion products are still evident on the HAZ surfaces even after cleaning, as shown in Figure 6-45. The density of the corrosion surfaces increased with an increase in ΔK and at ΔK of $20\text{MPa}\sqrt{m}$, the crack growth mechanism showed a mainly brittle form of failure. The fracture surfaces of the HAZ and weld materials were also found to exhibit corrosion pits more severely than in parent materials. This may be attributed to the influence of corrosion on microstructure variations in the weld and HAZ materials. Figure 6-46 shows the fracture surfaces of the weld materials. It was also found that the crack propagated by brittle striation mechanisms and some pits can be observed, as shown in the figure, due to corrosion effects. This implies that both microstructure and environmental factors are responsible for the crack growth mechanisms in free corrosion conditions.

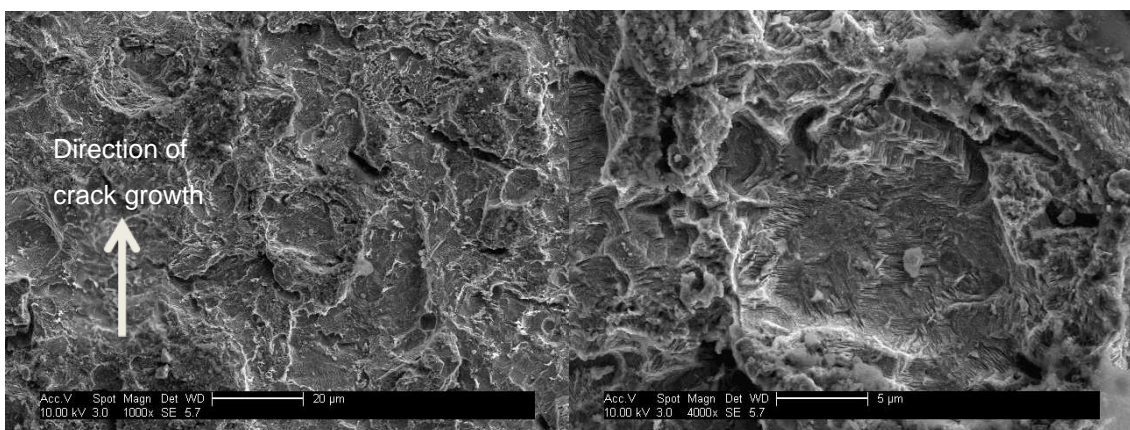


Figure 6-45 Mixture of brittle and ductile striation in HAZ materials in seawater

$$\Delta K=20\text{MPa}\sqrt{m}$$

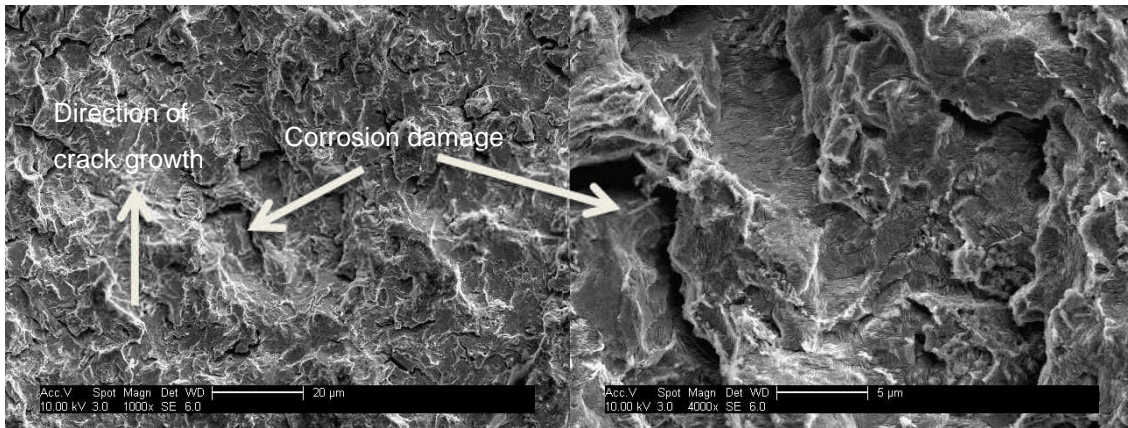


Figure 6-46 Brittle striations in weld materials in seawater $\Delta K=20\text{MPa}\sqrt{m}$

6.10 Summary

The crack growth behaviour in HAZ and weld materials fabricated from S355J2+N steel have been investigated in air and in a laboratory simulated seawater environment similar to what is experienced by offshore installations in service. The following conclusions can be drawn from this chapter.

- In order to reproduce the direction of crack growth in real monopiles as closely as possible, a methodology has been developed for extracting small scale laboratory test specimens, from welded plate with similar thickness and fabrication procedures as those used for offshore wind turbine monopile support structures.
- The crack growth mechanism in HAZ materials tested in an air environment at an R-ratio of 0.1 showed a delayed and accelerated crack growth at lower and higher applied stress intensity factor ranges respectively, resulting in a bi-linear relationship of the da/dN vs. ΔK plots. This was attributed to the possible influence of residual stresses induced crack closure and crack branching. However, for tests conducted at higher R-ratios (R=0.5 and 0.7) in air, the bi-linear crack growth effect was eliminated.
- The crack growth behaviour in HAZ and weld materials at an R-ratio of 0.1 resulted in nearly the same materials constants derived from the da/dN vs. ΔK plots. The HAZ and weld materials used in this work have a higher resistance to crack growth than parent materials at an R-ratio of

0.1, but at higher R-ratios in air, there was no marked difference in crack growth rates in HAZ and parent materials. The implication of this is that the crack growth behaviour of parent materials at a higher R-ratio may be applied to assess the integrity of welded joints subjected to high mean stresses.

- The crack growth behaviour in parent, HAZ and weld materials was found to be similar in free corrosion conditions at an R-ratio of 0.1. This has been attributed to the interaction of the applied loading conditions and the effect of the environment accompanied by rates of material removal in HAZ and weld test specimens.
- The material used for this work showed a good resistance to crack growth, when compared with the crack growth behaviour in other types of steels used for offshore installations, regardless of its lower yield strength.
- Application of the model developed in Chapter 5 for positive R-ratios has shown that mean stress effects on crack growth rates in weldments in air and in free corrosion conditions appear to be material and environmental dependent. It appears that improvement in welding procedures with respect to welding sequences can reduce the effects of high mean stress or tensile residual stress on crack growth rates in welded structures. Therefore, planning related to the frequency of inspection or repairs on the anticipated crack initiation areas of welded monopile structures may be achieved if the suitable welding sequences are designed for prior to monopile fabrications.
- The model developed in Chapter 5 for negative R-ratio responded in a similar manner as in parent materials when applied to HAZ materials tested under the same conditions.
- Through microstructural examination, crack branching or deflection in HAZ materials were found to be due to the effect of microstructure variation leading to crack propagating from the region having a higher resistance to crack growth towards a weaker region.

7 Conclusions, Contribution and Recommendations for Future Work

7.1 Introduction

In this chapter, the deductions made from previous chapters and the conclusions drawn from this research are outlined. The major contributions of this doctoral thesis are highlighted. Other areas outside the scope of this research are also identified and outlined as potential areas for further studies.

7.2 Conclusions

In this thesis, a fracture mechanics approach has been used to study the fatigue and corrosion assisted fatigue damage in a medium strength offshore steel. The major area of interest was to provide a better understanding of the crack growth behaviour of S355J2+N steels in a free corrosion marine environment. Free corrosion conditions in offshore structures are not designed for, but the behaviour of the structures under the real effect of corrosion needs to be known. The behaviour of the investigated steel was not just limited to the associated parent/base materials but also to HAZ and weld materials respectively. The following conclusions can be drawn from this research.

- The free corrosion tests data obtained under the narrow band of frequency range pertinent to offshore wind farm monopile support structures, have shown that there was no consistent trend in the data that suggests a more severe damage situation at a slower cyclic frequency of 0.3Hz compared to cyclic load frequencies of 0.35Hz and 0.4Hz. Similar crack growth rates were exhibited under free corrosion conditions using the three test frequencies. It appears from this study that a frequency of 0.3Hz may be used for testing offshore wind monopiles' representative materials. However, considerations are being given to deeper water depths, larger wind turbines and different types of support structure. Therefore, due to the likely different fatigue behaviours of such structures with respect to structural dynamic response characteristics, the data obtained within the range of frequency used for

testing in this work may not represent the damage mechanisms in their respective marine environments. A small number of tests have been reported within the narrow frequency range, i.e. 0.3Hz to 0.4Hz. Therefore, the crack growth behaviour of the materials within a narrow frequency range might be different compared to a frequency range of 0.1Hz to 1Hz.

- Based on the literature survey, findings have shown the difference between oil and gas structures and wind turbine support structures, with respect to frequency of operational and environmental loadings, manufacturing volumes and reduction in profit margins. Therefore, it may be inferred that the data obtained from this study serve as an update of the nearly 30 year old corrosion fatigue database that was developed based on oil and gas structures. With the use of modern materials, manufacturing techniques, data acquisition techniques and methodologies, the new sets of data obtained from this work may be applied to optimise offshore wind monopile support structures' design requirements.
- Crack growth rates in parent plate, HAZ and weld materials were significantly accelerated under a free corrosion condition, at all the stress ratios studied compared to in air environment. The resistance to crack growth in the present HAZ and weld materials were shown to be higher than in parent materials in air. However, in free corrosion conditions, parent, HAZ and weld materials exhibited similar crack growth behaviours. Results also revealed that the resistance of the present steel materials to crack growth appears similar to, and in some cases better than other types of steels used for offshore installations. The HAZ and weld data comparisons with BS7910 recommendations also suggest that the present steel materials exhibited good resistance to fatigue crack growth in air and in free corrosion conditions.
- The results of the theoretical model developed for predicting mean stress effects on corrosion fatigue crack growth agree fairly well with experimental findings. This suggests that the model can be applied to

predict crack growth rates in air and seawater so that the time and cost involved in conducting experimental tests at all possible stress ratios can be significantly reduced. However, from the comparisons made for higher R-ratios, particularly in weldments, this study has revealed that the mean stress effect may be material and environment dependent. The hypothesis for the model development for a negative R-ratio case was found to produce a similar response in parent and weldments. However, more tests are needed in order to further verify the hypothesis.

7.3 Contribution of this PhD

The contribution of this PhD is outlined as follows:

- Corrosion fatigue load frequency sensitivity analysis has been conducted within a frequency range pertinent to offshore wind turbine monopile support structures.
- The fatigue crack growth behaviour of parent, HAZ and weld steel materials used for offshore structures has been investigated in air and in free corrosion conditions, under lower and higher stress ratios using simulated wind and wave cyclic loading frequencies similar to what might be experienced in offshore wind farm monopile support structures.
- A new theoretical model that predicts mean stress effects on crack growth rates in offshore structures was developed for positive and negative R-ratio cases respectively.
- A BFS calibration developed with respect to optical measurements has been recommended for measuring crack lengths in air and in seawater environments.
- A novel methodology for conducting crack growth tests that permits reliable measurements of crack lengths in seawater has been developed.
- A methodology for extracting small scale laboratory specimens from relatively thick weld plate with similar dimensions to those used for monopile fabrications was presented.

7.4 Recommendations for future work

In the previous section, the main achievements of this doctoral thesis were highlighted. However, some areas of research requiring a better understanding of this subject area have been identified as follows:

- It will be recalled that in Chapter 6 the behaviour of the HAZ materials used in this study was attributed to the effects of residual stresses. Therefore, it is suggested that through thickness residual stresses on both weld materials and the HAZ specimens after extraction should be conducted. This may provide a better understanding of fatigue crack behaviour in the materials.
- A methodology for the calibration of BFS in a laboratory seawater environment is recommended for further studies. This methodology can be accompanied by another cost-effective technique for measurements of crack length in seawater. A sensitivity study of the strain gauge positions with respect to crack lengths obtained from the BFS is also recommended for further studies.
- The theoretical model developed in Chapter 5 for a negative R-ratio was not validated with experimental data. Therefore, middle tension (MT) or centre crack tension (CCT) specimens that accommodate tension-compression loading are recommended for testing in air and seawater environments in order to verify the assumption made in the model development.
- Further improvements to the theoretical model developed in Chapter 5 should be employed so that predictions under random loadings with the associated load interaction effects could be considered. More test data obtained from parent materials are needed at higher R-ratios ($R > 0.5$) in air and in seawater in order to validate the model further and also to verify the applicability of the model within the reported range of validity.
- More tests should be conducted in future test programmes, particularly at higher stress ratios, i.e. greater than 0.7, for a better understanding of the sensitivities of the HAZ and weld materials to higher mean stresses.

- A residual stress relaxation procedure is recommended for the HAZ and weld materials. Investigations of the crack growth behaviour of the residual stress free materials are also recommended for further studies.
- The effect of different waveforms, accompanied with holding time on crack growth rates is recommended for further studies.

REFERENCES

- [1] M. Arshad and B. C. O’Kelly, “Offshore wind-turbine structures : a review,” *Inst. Civ. Eng.*, vol. 166, no. EN4, pp. 139–152, 2013.
- [2] T. W. Thorpe, P. M. Scott, A. Rance, and D. Silvester, “Corrosion fatigue of BS 4360:50D structural steel in seawater,” *Int. J. Fatigue*, vol. 5, no. 3, pp. 123–133, Jul. 1983.
- [3] P. M. Scott, T. W. Thorpe, and D. R. V Silvester, “Rate -determining process for corrosion fatigue crack growth in ferrite steels in seawater,” *Corros. Sci.*, vol. 23, no. 6, pp. 559–575, 1983.
- [4] F. Brennan and I. Tavares, “Fatigue design of offshore steel monopile wind substructures,” *Inst. Civ. Eng.*, pp. 1–7, 2014.
- [5] N. Tantbiroj, “Fatigue testing of weldable high strength steels under simulated service loading,” PhD thesis, University College London, 2002.
- [6] D. A. Shifler, “Understanding material interactions in marine environments to promote extended structural life,” *Corros. Sci.*, vol. 47, no. 10, pp. 2335–2352, Oct. 2005.
- [7] I. Tavares, P. Ernst, G. John, R. Jacob, and B. Wyatt, “Internal cathodic protection of offshore wind turbine monopile foundations,” *Corros. Manag. A J. Inst. Corros.*, vol. 123, pp. 14–17, 2015.
- [8] I. Tavares, P. Ernst, G. John, R. Jacob, and B. Wyatt, “Corrosion threats to offshore wind foundations,” in *European Wind Energy Association (EWEA)*, 2015.
- [9] C. Pawsey, “The importance of corrosion protection on offshore wind farms,” *Wind Energy IQ*, 2015. [Online]. Available: <http://windenergy-iq.com/>. [Accessed: 19-Jun-2015].
- [10] Y. Kondo, “Prediction of fatigue crack initiation life based on pit growth,” *Corros. Sci.*, vol. 45, no. 1, pp. 7–11, 1989.
- [11] A. Turnbull and D. H. Ferriss, “Mathematical modelling of the electrochemistry in corrosion fatigue cracks in steel corroding in marine environments,” *Corros. Sci.*, vol. 27, no. 12, pp. 1323–1350, Jan. 1987.
- [12] L. S. Etube, *Fatigue and fracture mechanics of offshore structures*. Professional Engineering Publishing Limited, London and Bury St Edmunds, UK, 2001.

- [13] J. A. Austin, "The role of corrosion fatigue crack growth mechanisms in predicting the fatigue life of offshore tubular joints," PhD Thesis, University College London, 1994.
- [14] P. T. Myers, "Corrosion fatigue and fracture mechanics of high strength jack up steels," PhD thesis, University College London, 1998.
- [15] R. J. Appleton, "Corrosion fatigue of a C-Mn steel," PhD Thesis, University of Glasgow, 1985.
- [16] P. G. Millar, "Corrosion fatigue crack propagation behaviour of a high strength low alloy steel in a synthetic seawater environment," PhD Thesis, Cranfield Institute of Technology, 1986.
- [17] T. L. Anderson, *Fracture mechanics fundamentals and applications*, Third Edit. Taylor and Francis Group, 2005.
- [18] A. A. Griffith, "The phenomenon of rupture and flow in solids," *Philos. Trans. Ser. A*, vol. 221, pp. 163–198, 1920.
- [19] C. E. Inglis, "Stresses in a plate due to the presence of cracks and sharp corners," *Trans. Inst. Nav. Archit.*, vol. 55, pp. 219–241, 1913.
- [20] P. Zargarzadeh, "Structural integrity of CO2 transportation infrastructures," PhD Thesis, Cranfield University, 2013.
- [21] S. M. Beden, S. Abdullah, and A. K. Ariffin, "Review of fatigue crack propagation models for metallic components," *Eur. J. Sci. Res.*, vol. 28, no. 3, pp. 364–397, 2009.
- [22] G. R. Irwin, "Analysis of stresses and strains near the end of a crack traversing a plate," *Appl. Mech.*, vol. 24, pp. 361–364, 1957.
- [23] R. J. Sanford, *Principles of fracture mechanics*. Prentice Hall, 2003.
- [24] A. E. Chahardehi, "Fatigue crack growth in complex stress fields," PhD Thesis, Cranfield University, 2008.
- [25] Y. Murakami, *Stress intensity factors handbook*. Pergamon Press, 1987.
- [26] A. A. Wells, "Unstable crack propagation in metals: cleavage and fast fracture," in *Proceeding of the crack propagation symposium, Vol. 1, paper 84*, 1961.
- [27] J. R. Rice, "A path independent integral and the approximate analysis of strain concentrations by notches and cracks," *J. Appl. Mech.*, vol. 35, pp. 379–386, 1968.

- [28] P. C. Paris and F. Erdogan, "A critical analysis of crack propagation laws," *J. Basic Eng.*, vol. 85, pp. 528–534, 1963.
- [29] F. P. Brennan, "A framework for variable amplitude corrosion fatigue materials tests for offshore wind steel support structures," *Fatigue Fract. Eng. Mater. Struct.*, vol. 37, no. 6, pp. 1–5, Mar. 2014.
- [30] O. Adedipe, F. Brennan, and A. Kolios, "Corrosion fatigue crack growth in offshore wind monopile steel HAZ material," in *Analysis and Design of Marine Structures V, 5th International Conference on Marine Structures*, Taylor and Francis Group, 2015, pp. 207–212.
- [31] P. Higgins and A. Foley, "The evolution of offshore wind power in the United Kingdom," *Renew. Sustain. Energy Rev.*, vol. 37, pp. 599–612, Sep. 2014.
- [32] Department of Energy and Climate Change, "UK renewable energy roadmap update," 2013.
- [33] Global Wind Energy Council, "Global growth of wind sector," 2014.
- [34] O. Adedipe, F. Brennan, and A. Kolios, "Corrosion fatigue load frequency sensitivity analysis," *Mar. Struct.*, vol. 42, pp. 115–136, 2015.
- [35] 4Coffshore, "www.4coffshore.com," 2014. .
- [36] P. Schaumann, S. Lochte-Holtgreven, and S. Steppeler, "Special fatigue aspects in support structures of offshore wind turbines," *Mater. Sci. Eng. Technol.*, vol. 42, no. 12, pp. 1075–1081, Dec. 2011.
- [37] E. G. Ochieng, Y. Melaine, S. J. Potts, T. Zuofa, C. O. Egbu, A. D. F. Price, and X. Ruan, "Future for offshore wind energy in the United Kingdom: The way forward," *Renew. Sustain. Energy Rev.*, vol. 39, pp. 655–666, Nov. 2014.
- [38] W. Musial, S. Butterfield, and B. Ram, "Energy from offshore wind," in *Offshore Technology Conference*, 2006, pp. 1–11.
- [39] R. Holmes, "The fatigue behaviour of welded joints under sea environment and random loading conditions," in *Offshore Technology Conference*, 1980, pp. 219–224.
- [40] European Wind Energy Association (EWEA), "Deep water: The next step for offshore wind," 2013.
- [41] W. Zhixin, J. Chuanwen, A. Qian, and W. Chengmin, "The key technology of offshore wind farm and its new development in China," *Renew. Sustain. Energy Rev.*, vol. 13, no. 1, pp. 216–222, Jan. 2009.

- [42] M. D. Esteban, J. J. Diez, J. S. López, and V. Negro, "Why offshore wind energy?," *Renew. Energy*, vol. 36, no. 2, pp. 444–450, Feb. 2011.
- [43] O. Salo and S. Syri, "What economic support is needed for Arctic offshore wind power?," *Renew. Sustain. Energy Rev.*, vol. 31, pp. 343–352, Mar. 2014.
- [44] Concerted action on offshore wind energy in Europe, "Offshore wind energy ready to power a sustainable Europe," Report Duwind 2001.006, Delft University of Technology, The Netherlands, 2001.
- [45] W. Musial and B. Ram, "Large-scale offshore wind power in the united states, assessment of opportunities and barriers," NREL/TP-500-40745, National Renewable Energy Laboratory (NREL), 2010.
- [46] M. B. Zaaier, "Foundation modelling to assess dynamic behaviour of offshore wind turbines," *Appl. Ocean Res.*, vol. 28, no. 1, pp. 45–57, Feb. 2006.
- [47] D. Lombardi, S. Bhattacharya, and D. Muir Wood, "Dynamic soil–structure interaction of monopile supported wind turbines in cohesive soil," *Soil Dyn. Earthq. Eng.*, vol. 49, pp. 165–180, Jun. 2013.
- [48] S. Bhattacharya, N. Nikitas, J. Garnsey, N. A. Alexander, J. Cox, D. Lombardi, D. Muir Wood, and D. F. T. Nash, "Observed dynamic soil–structure interaction in scale testing of offshore wind turbine foundations," *Soil Dyn. Earthq. Eng.*, vol. 54, pp. 47–60, Nov. 2013.
- [49] Det Norske veritas, "DNV-OS-J101: Design of offshore wind turbine structures," 2013.
- [50] S. Peder Hyldal Sørensen and L. Bo Ibsen, "Assessment of foundation design for offshore monopiles unprotected against scour," *Ocean Eng.*, vol. 63, pp. 17–25, May 2013.
- [51] T. R. Camp, M. J. Morris, R. van Rooij, J. van der Temple, M. Zaaier, A. Henderson, K. Argyriadis, S. Schwartz, H. Just, W. Grainger, and D. Pearce, "Design methods for offshore wind turbines at exposed sites. Final report of the OWTES project. EU Joule III project JOR3-CT98-0284," Bristol United Kingdom, 2004.
- [52] A. R. Henderson (editor), "Design methods for offshore wind turbines at exposed sites: Hydrodynamic loading on offshore wind turbines," Delft University of Technology, Section Wind Energy, Delft, Netherlands, 2003.
- [53] S. Adhikari and S. Bhattacharya, "Dynamic analysis of wind turbine towers on flexible foundations," *J. Shock Vib.*, vol. 19, pp. 37–56, 2012.

- [54] J. Healy and J. Billingham, "A review of the corrosion fatigue behaviour of structural steels in the strength range 350-900MPa and associated high strength weldments," Health and Safety Executive-Offshore Technology Report (OTH 532), Norwich, United Kingdom, 1997.
- [55] E. Mecozzi, M. Lecca, S. Sorrentino, M. Large, C. Davies, H. Gouveia, C. Maia, M. Erdelen-Pepler, S. Karamanos, and P. Perdikaris, "Fatigue behaviour of high strength steel welded joints in offshore and marine systems," Final Report EUR 24214EN, 2010.
- [56] A. M. P. de Jesus, R. Matos, B. F. C. Fontoura, C. Rebelo, L. Simões da Silva, and M. Veljkovic, "A comparison of the fatigue behavior between S355 and S690 steel grades," *J. Constr. Steel Res.*, vol. 79, pp. 140–150, Dec. 2012.
- [57] A. Chahardehi, F. P. Brennan, and S. K. Han, "Surface crack shape evolution modelling using an RMS SIF approach," *Int. J. Fatigue*, vol. 32, no. 2, pp. 297–301, Feb. 2010.
- [58] D. A. Shifler and D. M. Aylor, "Factors affecting corrosion performance and testing of materials and components in seawater," in *NACE International Corrosion Conference*, 2005, no. 05224, pp. 1–15.
- [59] J. W. Knight, "Corrosion fatigue related to welded steel structures: A literature survey," *Weld. Res. Inst.*, vol. 7, no. 3, pp. 195–239, 1977.
- [60] ASTM D1141, "Standard practice for the preparation of substitute ocean water," 2008.
- [61] O. Vosikovsky, "Frequency, stress ratio and potential effects on fatigue crack growth of HY 130 steel in salt water," *J. Test. Eval.*, vol. 6, no. 3, pp. 175–182, 1978.
- [62] M. B. Kermani and D. Harrop, "The impact of corrosion on oil and gas industry," *Soc. Pet. Eng.*, vol. 11, no. 3, pp. 186–190, 1996.
- [63] Y. W. Cheng, "The fatigue crack growth of a ship steel in seawater under spectrum loading," *Int. J. Fatigue*, vol. 7, no. 2, pp. 95–100, Apr. 1985.
- [64] R. P. Wei and M. O. Speidel, "Phenomenological aspects of corrosion fatigue, critical introduction," in *corrosion fatigue: chemistry, mechanics and microstructure NACE-2*, 1972, pp. 379–380.
- [65] C. E. Jaske, J. H. Payer, and V. S. Balint, *Corrosion Fatigue of Metals in Marine Environments*. Battelle Press, Columbus, Ohio, 1981.
- [66] G. Bhuyan, A. S. J. Swamidas, and O. Vosikovsky, "Influence of environmental and mechanical variables on fatigue crack growth rates in

- CSA G40.21M 350 WT steel," *Int. J. Fatigue*, vol. 10, no. 1, pp. 37–42, Jan. 1988.
- [67] R. Johnson, I. Bretherton, B. Tomkins, P. M. Scott, and D. R. V. Silvester, "The effect of seawater corrosion on fatigue crack propagation in structural steel," in *Paper VI, European Offshore Steels Research Seminar*, 1978, pp. 1–15.
- [68] O. Vosikovsky, "Effects of stress ratio on fatigue crack growth rates in X70 pipeline steel in air and saltwater," *J. Test. Eval.*, vol. 8, no. 2, pp. 68–73, 1980.
- [69] L. S. Etube, P. Myers, F. P. Brennan, W. D. Dover, and A. Stacey, "Constant and variable amplitude corrosion fatigue performance of a high strength jack-up steel," in *International Offshore and Polar Engineering conference*, 1998, vol. IV, pp. 123–130.
- [70] G. S. Booth, "The influence of simulated north sea environmental conditions on the constant amplitude fatigue strength of welded joints," in *Offshore Technology Conference*, 1979, pp. 547–551.
- [71] G. H. G. Vaessen and J. de Back, "Fatigue behaviour of welded steel joints in air and seawater," in *Offshore Technology Conference*, 1979, vol. 510, pp. 555–558.
- [72] A. J. Griffiths and A. Turnbull, "Impact of long term exposure on corrosion fatigue crack growth of alloy steels," in *NACE International Annual Conference and Exposition*, 1996, pp. 2–9.
- [73] T. Havn and H. Osvoll, "Corrosion fatigue of steel in seawater," in *NACE International Corrosion Conference*, 2002, no. 02431, pp. 1–11.
- [74] O. Vosikovsky, "Fatigue crack growth in an X-65 pipeline steel at low cyclic frequencies in aqueous environments," *Trans. ASME, J. Eng. Mater. Technol.*, vol. 97, no. 4, pp. 299–304, 1975.
- [75] B. Huneau and J. Mendez, "Evaluation of environmental effects on fatigue crack growth behaviour of a high strength steel in a saline solution with cathodic protection," *Int. J. Fatigue*, vol. 28, no. 2, pp. 124–131, Feb. 2006.
- [76] J. W. C. Thompson, "Phenomenological investigation of the influence of Cathodic protection on corrosion fatigue crack propagation behaviour, in a BS 4360 50D type structural steel and associated weldment microstructures, in a marine environment," PhD Thesis, Cranfield Institute of Technology, 1984.

- [77] M. Horstmann, J. K. Gregory, and K. H. Schwalbe, "Geometry effects on corrosion-fatigue in offshore structural steels," *Int. J. Fatigue*, vol. 17, no. 4, pp. 293–299, 1995.
- [78] A. Trudel, M. Sabourin, M. Lévesque, and M. Brochu, "Fatigue crack growth in the heat affected zone of a hydraulic turbine runner weld," *Int. J. Fatigue*, vol. 66, pp. 39–46, Mar. 2014.
- [79] Y. Xiong and X. X. Hu, "The effect of microstructures on fatigue crack growth in Q345 steel welded joint," *Fatigue Fract. Eng. Mater. Struct.*, vol. 35, no. 6, pp. 500–512, Jun. 2012.
- [80] K. Sanghoon, K. Donghwan, K. Tae-won, L. Jongkwan, and L. Changhee, "Fatigue crack growth behaviour of the simulated HAZ of 800MPa grade high performance steel," *Mater. Sci. Eng. A*, vol. 528, pp. 2331–2338, 2010.
- [81] T. Fukuda, T. Iwadate, and M. Shimazaki, "Consideration on the scatter of COD and fatigue crack propagation characteristics of heavy section C-Mn-V forged steel for offshore structure," in *Offshore Technology Conference*, 1982, pp. 109–112.
- [82] W. Zhang and R. Brook, "The effect of loading sequence on fatigue crack growth of an offshore structural steel," in *International Offshore and Polar Engineering Conference*, 1993, pp. 98–103.
- [83] O. H. Burnside, S. J. Hudak, E. Oelkers, K. Chan, and R. I. Dextert, "Long-term corrosion fatigue of welded marine steels," Ship Structure Committee, Texas, 1984.
- [84] M. Knop, J. Heath, Z. Sterjovski, and S. P. Lynch, "Effects of cycle frequency on corrosion-fatigue crack growth in cathodically protected high-strength steels," *Procedia Eng.*, vol. 2, no. 1, pp. 1243–1252, Apr. 2010.
- [85] R. G. Forman, "Study of fatigue crack initiation from flaws using fracture mechanics.," *Eng. Fract. Mech.*, vol. 4, no. 2, pp. 333–345, 1972.
- [86] K. Walker, "The effect of stress ratio during crack propagation and fatigue for 2024-T3 and 7076-T6 aluminium. In: Effect of environment and complex load history on fatigue life. ASTM STP 462," Philadelphia, 1970.
- [87] D. Kujawski, "A new driving force parameter for crack growth in aluminum alloys," *Int. J. Fatigue*, vol. 23, pp. 733–740, 2001.
- [88] X. Huang and T. Moan, "Improved modeling of the effect of R-ratio on crack growth rate," *Int. J. Fatigue*, vol. 29, no. 4, pp. 591–602, Apr. 2007.

- [89] W. Zhan, N. Lu, and C. Zhang, "A new approximate model for the R-ratio effect on fatigue crack growth rate," *Eng. Fract. Mech.*, vol. 119, pp. 85–96, Mar. 2014.
- [90] M. Itatani, J. Fukakura, M. Asano, M. Kikuchi, and N. Chujo, "Fatigue crack growth behaviour of weld heat affected zone of type 304 stainless steel in high temperature water," *Nucl. Eng. Des.*, vol. 153, pp. 27–34, 1994.
- [91] G. Pouget and A. P. Reynolds, "Residual stress and microstructure effects on fatigue crack growth in AA2050 friction stir welds," *Int. J. Fatigue*, vol. 30, no. 3, pp. 463–472, Mar. 2008.
- [92] D. A. Lados, D. Apelian, and J. K. Donald, "Fracture mechanics analysis for residual stress and crack closure corrections," *Int. J. Fatigue*, vol. 29, no. 4, pp. 687–694, Apr. 2007.
- [93] Z. Barsoum, "Residual stress analysis and fatigue assessment of welded steel structures," PhD thesis, KTH Royal Institute of Technology, Sweden, 2008.
- [94] K. J. Kirkhope, R. Bell, L. Caron, and R. I. Basu, "Weld detail fatigue life improvement techniques," Ship Structural Committee, USA, 1997.
- [95] J. R. Lloyd, "The effect of residual stress and crack closure on fatigue crack growth," PhD Thesis, University of Wollongong, 1999.
- [96] C. Jang, P.-Y. Cho, M. Kim, S.-J. Oh, and J.-S. Yang, "Effects of microstructure and residual stress on fatigue crack growth of stainless steel narrow gap welds," *Mater. Des.*, vol. 31, no. 4, pp. 1862–1870, Apr. 2010.
- [97] M. B. Kermani and F. Abbassian, "Corrosion fatigue of marine structural steels in saline environments," in *12th International Corrosion Congress*, 1993, pp. 1671–1691.
- [98] C. J. Thomas, R. G. J. Edyvean, R. Brook, and I. M. Austen, "The effects of microbially produced hydrogen sulphide on the corrosion fatigue of offshore structural steels," *Corros. Sci.*, vol. 27, no. 10, pp. 1197–1204, 1987.
- [99] D. Braun, "Fatigue design review of offshore wind turbine generators structures," United State Department of the Interior, Herndon, VA, 2013.
- [100] J. C. P. Kam, "Recent development in the fast corrosion fatigue analysis of offshore structures subject to random wave loading," *Int. J. Fatigue*, vol. 12, no. 6, pp. 458–468, 1990.

- [101] L. R. Hilbert, A. R. Black, F. Andersen, and T. Mathiesen, "Inspection and monitoring of corrosion inside monopile foundations for offshore wind turbines," in *EUROCORR Conference*, 2011, no. 4730, pp. 1–14.
- [102] C. Lindley and W. J. Rudd, "Influence of the level of cathodic protection on the corrosion fatigue properties of high-strength welded joints," *Mar. Struct.*, vol. 14, pp. 397–416, 2001.
- [103] A. Comer and L. Looney, "Corrosion and fatigue characteristics of positively polarised Zeron 100 base & weld metal in synthetic seawater," *Int. J. Fatigue*, vol. 28, no. 8, pp. 826–834, Aug. 2006.
- [104] W. J. D. Jones and A. P. Blackie, "Effect of stress ratio on the cyclic tension corrosion fatigue life of notched steel BS970:976M33 in sea water with cathodic protection," *Int. J. Fatigue*, vol. 11, no. 6, pp. 417–422, Nov. 1989.
- [105] D. R. Callister, "A study of fatigue crack propagation in quenched and tempered and controlled rolled high strength low alloy (HSLA) steels," PhD Thesis, Cranfield Institute of Technology, 1987.
- [106] L. S. Etube, F. P. Brennan, and W. D. Dover, "Modelling of jack-up response for fatigue under simulated service conditions," *Mar. Struct.*, vol. 12, no. 4–5, pp. 327–348, May 1999.
- [107] J. Billingham, J. V. Sharp, J. Spurrier, and P. J. Kilgallon, "Review of the performance of high strength steels used offshore," HSE Research Report 105, School of Industrial and Manufacturing Science, Cranfield University, 2003.
- [108] E. Coudert and C. Renaudin, "Variable amplitude corrosion fatigue behaviour and hydrogen embrittlement of high strength steels for offshore applications," in *International Offshore and Polar Engineering Conference*, 1998, vol. IV, pp. 116–122.
- [109] D. Radaj, "Review of fatigue strength assessment of nonwelded and welded structures based on local parameters," *Int. J. Fatigue*, vol. 18, no. 3, pp. 153–170, 1996.
- [110] D. Kang, S. Kim, C. Lee, J. Lee, and T. Kim, "Corrosion fatigue behaviors of HSB800 and its HAZs in air and seawater environments," *Mater. Sci. Eng.*, vol. 559, pp. 751–758, 2012.
- [111] L. W. Tsay, T. S. Chern, C. Y. Gau, and J. R. Yang, "Microstructures and fatigue crack growth of EH36 TMCP steel weldments," *Int. J. Fatigue*, vol. 21, no. 8, pp. 857–864, Sep. 1999.

- [112] J. Healy, J. P. Chubb, and J. Billingham, "Further assessment of cast steel for use in offshore structures," *Int. J. Fatigue*, vol. 12, no. 3, pp. 191–197, May 1990.
- [113] L. Bertini, "Influence of seawater and residual stresses on fatigue crack growth in C-Mn steel weld joints," *Theor. Appl. Fract. Mech.*, vol. 16, no. 2, pp. 135–144, Nov. 1991.
- [114] M. Beghini and L. Bertini, "Fatigue crack propagation through residual stress fields with closure phenomena," *Eng. Fract. Mech.*, vol. 36, no. 3, pp. 379–387, 1990.
- [115] ASTM E647, "Standard test method for measurement of fatigue crack growth rates," 2008.
- [116] BS EN ISO 11782-2, "Corrosion of metals and alloys- Corrosion fatigue testing-Part 2: Crack propagation testing using precracked specimens," 2008.
- [117] M. C. Lugg, "An introduction to ACPD," Technical Software Consultants Ltd. Milton Keynes, United Kingdom, 2009.
- [118] L. V. Andersen, M. J. Vahdatirad, M. T. Sichani, and J. D. Sørensen, "Natural frequencies of wind turbines on monopile foundations in clayey soils—A probabilistic approach," *Comput. Geotech.*, vol. 43, pp. 1–11, Jun. 2012.
- [119] M. Damgaard, L. B. Ibsen, L. V Andersen, and J. K. F. Andersen, "Cross-wind modal properties of offshore wind turbines identified by full scale testing," *J. Wind Eng. Ind. Aerodyn.*, vol. 116, pp. 94–108, 2013.
- [120] J. M. F. Carter, "North Hoyle offshore wind farm : design and build," *Proc. ICE- Energy*, vol. 160, no. 1, pp. 21–29, 2007.
- [121] W. F. Deans and C. E. Richards, "A simple and sensitive method for monitoring crack and load in compact fracture mechanics specimens using strain gauges," *J. Test. Eval.*, vol. 7, no. 3, pp. 147–154, 1979.
- [122] W. T. Riddell and R. S. Piascik, "A back face strain compliance expression for the compact tension specimen," NASA/TM-1998-208453, Hampton, Virginia, 1998.
- [123] W. J. D. Shaw and W. Zhao, "Back face strain calibration for crack length measurements," *J. Test. Eval.*, vol. 22, pp. 512–516, 1994.
- [124] Y. Huh and J.-H. Song, "Back face strain compliance calibration for the four-point bend specimen," *KSME Int. J.*, vol. 14, no. 3, pp. 314–319, 2000.

- [125] J. C. Newman, Y. Yamada, and M. A. James, "Back-face strain compliance relation for compact specimens for wide range in crack lengths," *Eng. Fract. Mech.*, vol. 78, no. 15, pp. 2707–2711, Oct. 2011.
- [126] P. M. Scott and D. R. V. Silvester, "The influence of seawater on fatigue crack propagation in structural steels," in *United Kingdom Offshore Steel Research Project*, 1975.
- [127] P. M. Scott and D. R. V. Silvester, "The influence of mean tensile stress on corrosion fatigue crack growth in structural steels immersed in seawater," in *United Kingdom Offshore Steel Research Project*, 1977.
- [128] J. K. Musuva and J. C. Radon, "Threshold of fatigue crack growth in a low alloy steel," *Advances in Fracture Research*, Pergamon Press, Oxford, 1982, pp. 1365–1372.
- [129] J. Congleton and Craig I. H., "Corrosion fatigue," in *Corrosion processes*, R. N. Parkins, Ed. Applied Science Publishers, 1982.
- [130] BS 7910, "Guide to methods for assessing the acceptability of flaws in metallic structures," 2013.
- [131] R. N. King, "A review of fatigue crack growth rates in air and seawater," *Offshore Technology Report*, OTH 511, HSE, 1998.
- [132] C. C. Monahan, *Early fatigue crack growth at welds*. Computational mechanics publications, Southampton UK, 1995.
- [133] W. Elber, "The significance of fatigue crack closure. In: Damage tolerance in aircraft structures. ASTM STP 486," Philadelphia, 1971.
- [134] S. J. Maddox, T. R. Gurney, A. M. Mummery, and G. S. Booth, "An investigation of the influence of applied stress ratio on fatigue crack propagation in structural steels.," *TWI Ind. Memb. Rep. Summ.* 72, 1978.
- [135] J. Schijve, "Some formulas for the crack opening stress level," *Eng. Fract. Mech.*, vol. 14, pp. 461–465, 1981.
- [136] R. Kumar and K. Singh, "Influence of stress ratio on fatigue crack growth in mild steel," *Eng. Fract. Mech.*, vol. 50, no. 3, pp. 377–384, 1995.
- [137] D. Kujawski, "A fatigue crack driving force parameter with load ratio effects," *Int. J. Fatigue*, vol. 23, pp. 239–246, 2001.
- [138] D. L. Chen, B. Weiss, and R. Stickler, "Contribution of the cyclic loading portion below the opening load to fatigue crack growth," *Mater. Sci. Eng.*, vol. 208, pp. 181–187, 1996.

- [139] K. Donald and P. C. Paris, "An evaluation of ΔK_{eff} estimation procedures on 6061-T6 and 2024-T3 aluminium alloys," *Int. J. Fatigue*, vol. 21, pp. 47–57, 1999.
- [140] D. Kujawski, "Enhanced model of partial crack closure for correlation of R-ratio effects in aluminum alloys," *Int. J. Fatigue*, vol. 23, pp. 95–102, 2001.
- [141] D. Kujawski and F. Ellyin, "A fatigue crack growth model with load ratio effects," *Eng. Fract. Mech.*, vol. 28, no. 4, pp. 367–378, 1987.
- [142] R. C. McClung, "The influence of applied stress, crack length, and stress intensity factor on crack closure," *Metall. Trans.*, vol. 22, no. 7, pp. 1559–1571, 1991.
- [143] S. Dinda and D. Kujawski, "Correlation and prediction of fatigue crack growth for different R-ratios using K_{max} and ΔK_+ parameters," *Eng. Fract. Mech.*, vol. 71, no. 12, pp. 1779–1790, Aug. 2004.
- [144] A. H. Noroozi, G. Glinka, and S. Lambert, "A study of the stress ratio effects on fatigue crack growth using the unified two-parameter fatigue crack growth driving force," *Int. J. Fatigue*, vol. 29, no. 9–11, pp. 1616–1633, Sep. 2007.
- [145] L. Weng, J. Zhang, S. Kalnaus, M. Feng, and Y. Jiang, "Corrosion fatigue crack growth of AISI 4340 steel," *Int. J. Fatigue*, vol. 48, pp. 156–164, 2013.
- [146] ESAB, "Fluxes and wires for joining non and low-alloyed steels, stainless steels and nickel-base alloys," *Submerged Arc Welding Technical Handbook*, 2008.
- [147] A. Trudel, M. Lévesque, and M. Brochu, "Microstructural effects on the fatigue crack growth resistance of a stainless steel CA6NM weld," *Eng. Fract. Mech.*, vol. 115, pp. 60–72, Jan. 2014.
- [148] G. C. Maden, "Corrosion fatigue of high strength low alloy steel under conditions likely to promote hydrogen embrittlement," MPhil thesis, Cranfield University, 1994.
- [149] J. Drury, "An investigation into the fatigue and corrosion fatigue properties of two high strength low alloy steels and their HAZs," PhD thesis, Cranfield University, 1992.
- [150] J. Schijve, "Fatigue of structures and materials in the 20th century and the state of the art," *Int. J. Fatigue*, vol. 25, no. 8, pp. 679–702, Aug. 2003.

APPENDICES

Appendix A Crack growth results comparison

In this appendix, results of the 355 steel grades obtained in air are compared with those obtained from the material used in this research. A consistent comparison of crack growth behaviour in S355J2+N steel and in other types of steels in air and in free corrosion condition have been discussed in Chapters 4 and 6. However, the purpose of the comparisons made in this section is to relate the crack growth behaviour of S355J2+N steel to other 355D steel grades. The results are depicted in Figures A-1 and A-2. Included in the figures are data obtained from RQT 701 steels [55]. It can be seen from Figure A-1 that the data obtained in S355J2+N steel falls between the 355D steel [57] and S355 [56] steel, while the 355 EMZ [55] steel crack growth manner is different from the other 355 steel grades but similar to those obtained from RQT 701 steel. It appears from the results that material variability with respect to the chemical composition of the materials has a significant effect on the response of the materials.

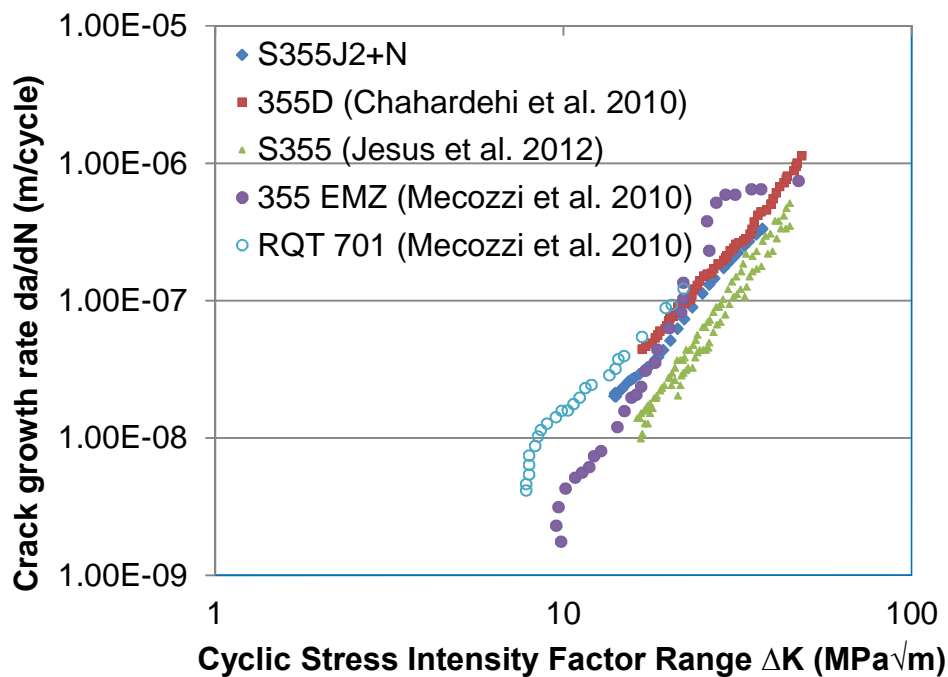


Figure A- 1 Crack growth rates in parent materials in air

The data obtained from S355J2+N steel HAZ material are also compared with those obtained from 355 EMZ and RQT 702 steels in Figure A-2. Regardless of the similarity between S355J2+N steel and 355 EMZ steel, it can be seen that their crack growth behaviours are different. At lower ΔK , crack growth rates in RQT 702 are similar to 355 EMZ but at higher ΔK , it can be seen that the 355 EMZ steel produced a bump shape curve and deviated towards the RQT 702 curve above ΔK of $43\text{MPa}\sqrt{m}$. Material variability is the most likely explanation for the difference in behaviour of the steels.

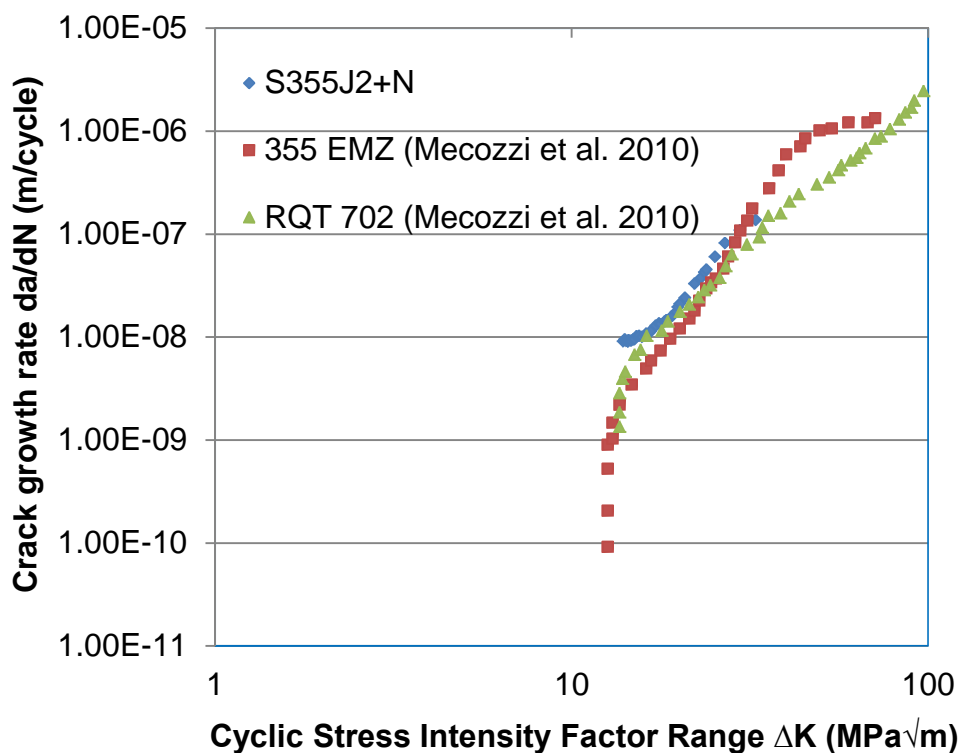


Figure A- 2 Crack growth rates in HAZ materials in air

Appendix B Clevis and loading pins

The design of the clevis and loading pins are shown in Figures B-1 to Figure B-2. The loading clevis and pins were manufactured from 2205 duplex stainless steel. All the dimensions set out in the figures are in mm. The dimensions of the Perspex tank used for the corrosion fatigue experiments are given in Figure B-3, also in mm.

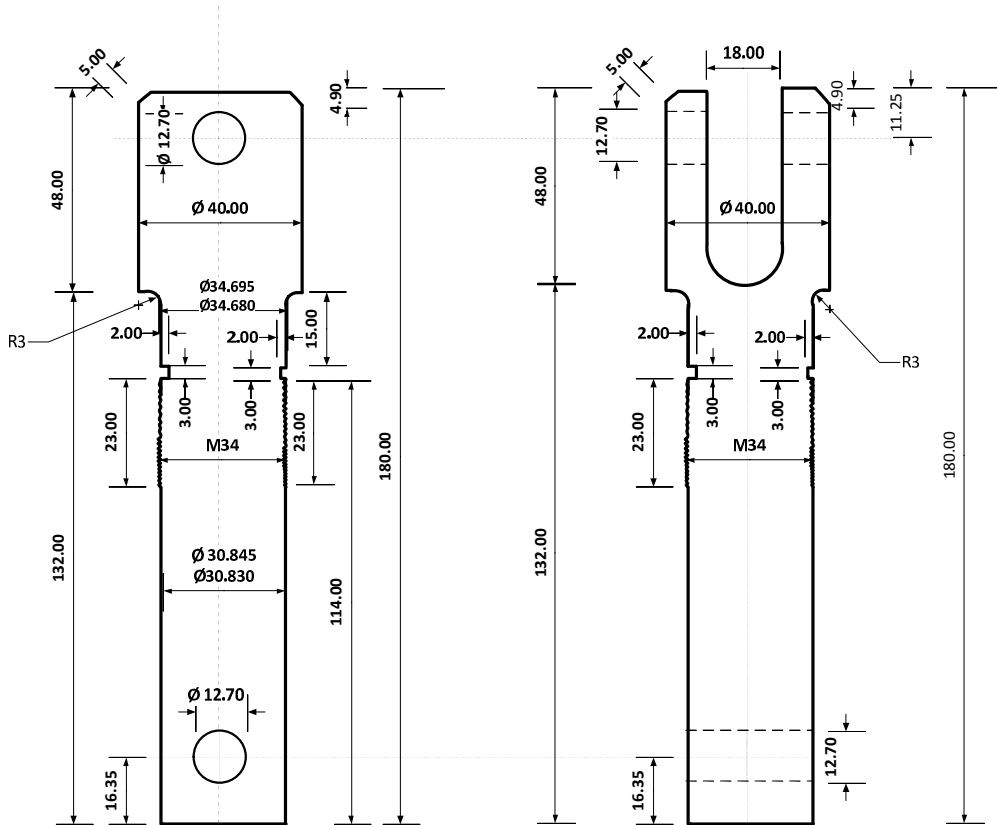


Figure B- 1 Loading clevis dimensions

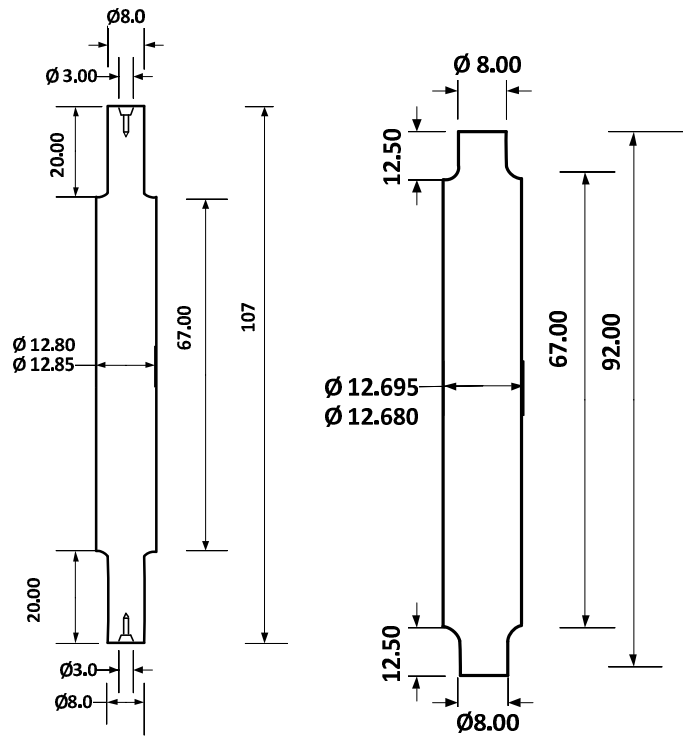


Figure B- 2 Loading pins dimensions

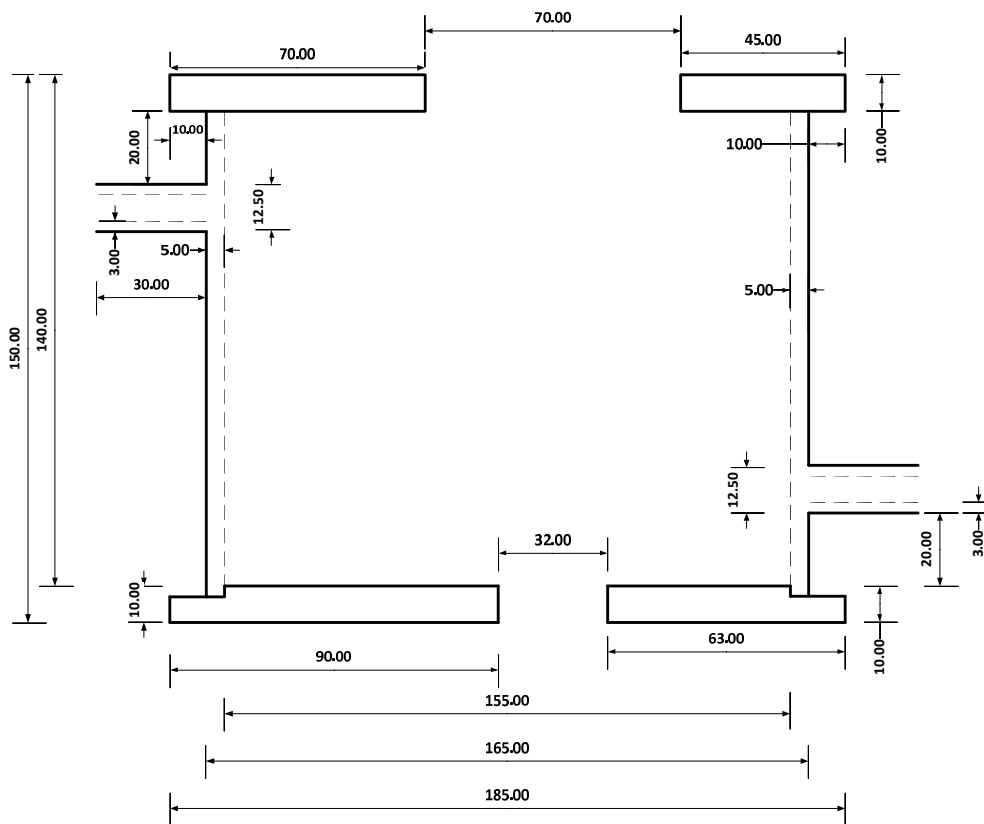



Figure B- 3 Perspex chamber dimensions


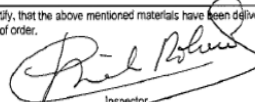
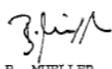

Appendix C Material Certificate

The chemical composition provided by the steel manufacturer is shown in Table C-1. In comparison with the chemical composition of the filler materials shown in Table D-2, it can be seen that the two materials are similar considering the composition of C, Mn, Si, S, P and Cu. Therefore, it appears that the similarity in the observed crack growth rates in HAZ and weld materials as discussed in Chapter 6 was related to the similarity in the chemical compositions of the steel and filler materials.

Table C-1 Test material certificate


DILLINGER HÜTTE

Erläuterungen siehe Rückseite/Explications voir au verso/See reverse for explanations (www.dillinger.de/certificate)

A02 INSPECTION CERTIFICATE 3.2 AS PER EN 10204:2004 INSPECTION REPORT 3.2 AS PER EN 10204:1991+A1:1995 + AS PER ISO 10474:1991		A10 Advice of dispatch No./ Date of dispatch 309311-26.07.08	A08/ Manufacturer's order/ A03 Certificate No. 339313-001	Sheet 4/...												
A05 Established inspecting body GL	A06 Purchaser SALZGITTER, GLADBECK Final receiver ERNDTEBR., ERNDTEBRUE	A07.1 No. 41016-04-08/3093 A07.2 No. 41016-04	B01 Product HOT ROLLED PLATES													
B02/ Steel design. S355G8+M																
B03 Any suppl. requirements EN-10225:01																
C70-C99 Chemical composition % - Heat analysis																
B07.2 Heat	C70	C	SI	MN	P	S	N	CU	MO	NI	CR	V	NB	AS	SN	
324298	Y	0,053	0,276	1,54	0,013	0,0007	0,0046	0,243	0,008	0,326	0,029	0,001	0,021	0,002	0,001	
324300	Y	0,052	0,276	1,54	0,011	0,0010	0,0039	0,240	0,016	0,332	0,028	0,001	0,020	0,004	0,002	
324301	Y	0,052	0,289	1,55	0,010	0,0009	0,0043	0,238	0,011	0,332	0,025	0,001	0,020	0,003	0,001	
B07.2 Heat	C70	TI	PB	B	SB	CA	BI	AL-T								
324298	Y	0,001	0,000	0,0003	0,0007	0,0021	0,0001	0,036								
324300	Y	0,002	0,000	0,0001	0,0009	0,0026	0,0001	0,038								
324301	Y	0,002	0,000	0,0003	0,0006	0,0020	0,0001	0,035								
C94 Heat analysis Carbon equivalent / Alloying restrictions																
B07.2 Heat		FO-A1=	FO-02=	FO-51=	FO-52=	FO-55=										
324298		7,83	0,36	0,02	0,02	0,61										
324300		9,74	0,36	0,02	0,02	0,62										
324301		8,14	0,36	0,02	0,02	0,61										
C95 Ladle treatment																
ITEM NO. : 01 HEAT OF THE INDICATED ITEM: VACUUM DEGASSED																
C70-C99 Chemical composition % - Product analysis																
B07.2 Heat	B07.1 Test No.	C01	C	SI	MN	P	S	N	CU	MO	NI	CR	V	NB	TI	B
324298	48147	K4	0,053	0,269	1,52	0,012	0,0007	0,0036	0,236	0,007	0,318	0,028	0,001	0,020	0,001	0,0001
324298	48149	K4	0,052	0,265	1,52	0,011	0,0006	0,0036	0,230	0,007	0,320	0,028	0,002	0,020	0,001	0,0000
324298	48154	K4	0,056	0,267	1,53	0,013	0,0007	0,0033	0,234	0,009	0,322	0,036	0,002	0,020	0,002	0,0001
324300	48137	K4	0,052	0,270	1,54	0,010	0,0010	0,0028	0,232	0,018	0,324	0,028	0,001	0,019	0,001	0,0000
A04	Z01/Z02/Z03 We hereby certify, that the above mentioned materials have been delivered in accordance with the terms of order.										A01					
 Manufacturer's mark	 Inspector					 B. MUELLER Test House Manager					 Inspector's stamp	AG der Dillinger Hüttenwerke Postfach 1580, D-66748 Dillingen/Saar Inspection department	Date 28.07.08 EDI ML 1			

Appendix D Welding procedure and specification

Table D- 1 Welding procedure specification


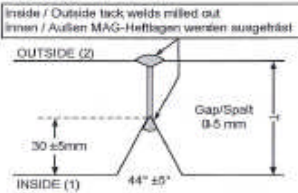
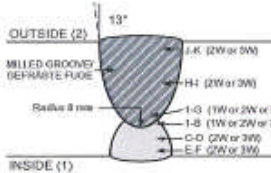
		EEW - SCHWEISSANWEISUNG WELDING PROCEDURE SPECIFICATION (WPS)				DOKUMENT/DOCUMENT WPS 49041/1											
		SPEZIFIKATION SPECIFICATION		WERKSTOFF PARENT METAL		LN LONGWELD		X RN CIRCWELD		X							
QUALIFIKATION QUALIFIED		POR 730/1		QUALIFIZIERTE DICKE QUALIFIED THICKNESS		30 -120 mm		QUALIF. DURCHM. QUALIFIED DIAMETER		LW N.A.							
AKTUELLE DICKE ACTUAL THICKNESS		50 mm		AKTUELLER DURCHM. ACTUAL DIAMETER		N.A.											
FUGENVORBEREITUNG / EDGE PREPARATION						SCHWEISSNAHTAUFBAU / WELD RUN SEQUENCE											
																	
VORWÄRMUNG PREHEAT		°C 60		METHODE METHOD		GAS/ Electric		LAGE TEMP. INTERPASS TEMP.		< 250 °C		PRÜFUNG CHECK		TEMP. STICK OR THERMOMETER			
KANTENVORBEREITUNG EDGE PREPARATION		MECHANICAL/ FLAME CUT		AUSFUGEMETHODE GOUGING METHOD		MILLING		PRÜFUNG DER FUGE CHECK OF GOUGE		Visual Examination optional DT Check							
SEITE SIDE	LAGE PASS	SCHWEISS- VERFAHREN WELDING PROCESS	SCHWEISS- POSITION WELDING POSITION	DRAHT / ELEKTRODE WIRE / ELECTRODE		PULVER / GAS FLUX / GAS		GAS Fluß Flow l/min		AMPS (A)		VOLTS (V)		SCHWEISSG. SPEED mm/min		WÄRMEEIN- BRINGUNG HEAT INPUT kJ/mm	
				DIA	MARKENNAME / TRADE NAME	POLUNG / POLARITY	MARKENNAME / TRADE NAME			VON - BIS FROM - TO	VON - BIS FROM - TO	VON - BIS FROM - TO	VON - BIS FROM - TO	VON - BIS FROM - TO	VON - BIS FROM - TO		
1	1-B	SAW-2W	PA (1G)	4	S3Si	DC+	OP121TT	590	650	28	30	820	880	2,2	2,9		
	E-F			4	S3Si	AC-		530	620	29	32						
oder/or																	
1	1-B	SAW-3W	PA (1G)	4	S3Si	DC+	OP121TT	590	650	27	29	1150	1250	2,4	3,0		
	C-D			4	S3Si	AC-		570	630	29	30						
	E-F			4	S3Si	AC-		550	610	30	32						
oder/or																	
1	C-D	SAW-4W	PA (1G)	4	S3Si	DC+	OP121TT	580	630	28	29	1450	1550	2,5	3,0		
				4	S3Si	AC-		560	610	29	30						
				4	S3Si	AC-		540	590	30	31						
				4	S3Si	AC-		520	570	31	33						
VON AUSSEN FRÄSEN / EXTERNAL MILLING																	
2	1-G	SAW-2W	PA (1G)	4	S3Si	DC+	OP121TT	590	650	28	30	850	880	2,2	2,8		
	H-I				S3Si	AC-		560	620	29	33						
	J-K																
oder/or																	
2	1-G	SAW-3W	PA (1G)	4	S3Si	DC+	OP121TT	600	650	28	29	1150	1250	2,4	3,0		
	H-I			4	S3Si	AC-		580	630	29	30						
	J-K			4	S3Si	AC-		560	610	30	33						
WIRE STICKOUT = 25-35mm, Distance between welding wires = 14-20 mm, TRAVEL ANGLE = 0° - 8° / - 20° / - 20°																	
ZFP / NDE GEMÄSS AUFTRAG / AS SPECIFIED						TOLERANCES ACC. DIN EN ISO 5817, Level B											
WÄRMENACHBEHANDLUNG POST WELD HEAT TREATMENT (PWHT)				BEWERTUNGEN / NOTES													
X NEIN / NO JA / YES				WPS LONGWELDS AND CIRCWELDS MP+TP / WPS Längsnähte und Rundnähte MP+TP SMOOTH TRANSITIONS WITHOUT NOTCHES/ Weiche- Kantfreie Übergänge TACKWELDING ACCORDING WORK PROCEDURE INTERNAL WPS/ Heften nach interner WPS MILLING OUTSIDE ACCORDING WORK PROCEDURE/ Fräse nach Arbeitsanweisung INTERPASS CLEANING MECHANICAL/ Zwischenlagerreinigung mechanisch													
TEMPERATUR / TEMPERATURE °C HALZEIT / HOLDING MIN.				schweisszus. / WIRE: EN ISO 14171; S3 Si - SUPPLIER: DRAHTZUG-STEIN (SDA D3) CONSUMABLES FLUX: EN ISO 14174; SA FB 1 55 AC H - SUPPLIER: OERLIKON (OP 121 TT IE)													
DETAILS SIEHE / SEE HT																	
FIRMA / FIRM		ERSTELLT / PREPARED		GEPRÜFT / APPROVED		REV.		BESCHREIBUNG / DESCRIPTION									
EEW		EEW		EEW		0		FOR APPROVAL / COMMENTS									
UNTERSCHRIFT / SIGNATURE		DORGE		DROBEK		1		AFTER COMMENTS									
NAME / PRINT NAME		DORGE		DROBEK													
DATUM / DATE		05.05.2014		05.05.2014													

Table D- 2 Chemical composition of S3Si filler material [146]

C	Mn	Si	S	P	Cu
0.06-0.15	1.50-2.00	0.25-0.65	0.025	0.025	0.35

Appendix E Weld and HAZ specimens' orientation

The extracted HAZ and weld specimens' orientations within the weld plate are shown in Figures E-1 and E-2 with dimensions.

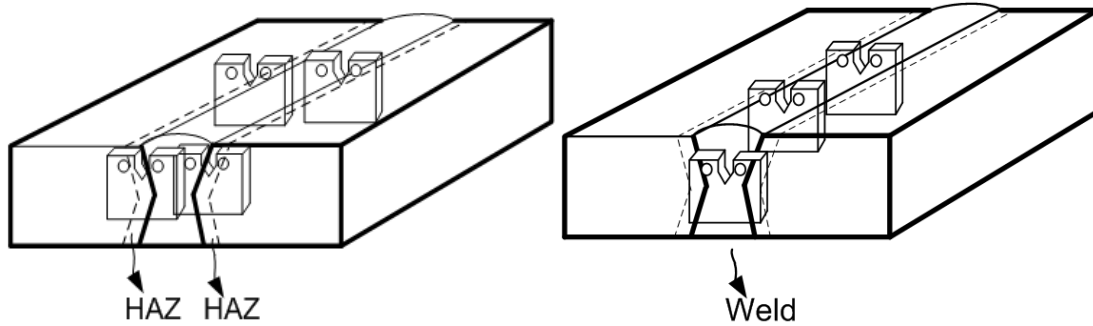
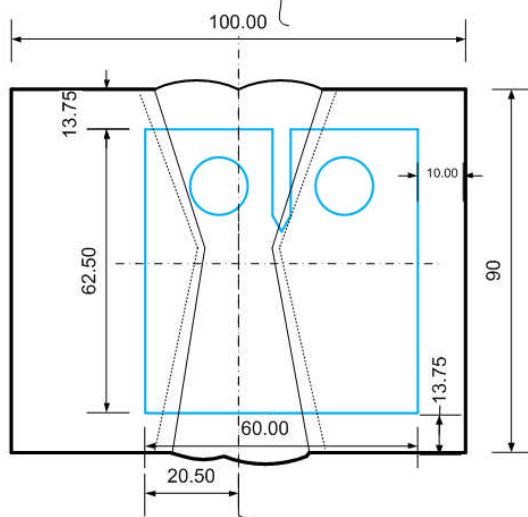


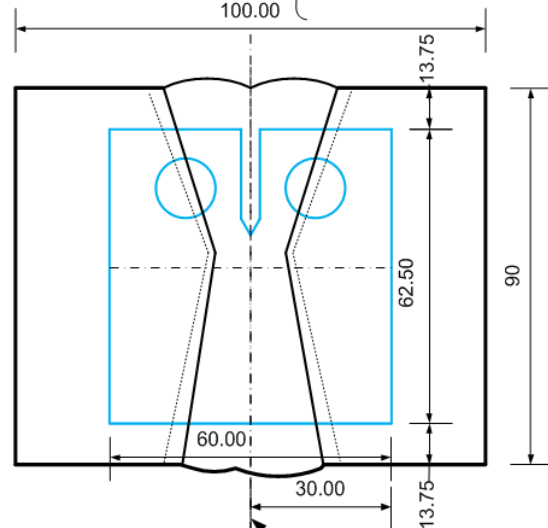
Figure E- 1 CT specimen's extraction from HAZ and weld regions

HAZ specimens: Notch tip machined at the centre of the heat affected zone as shown below (1mm from the fusionzone)



Position of centre line determined by examination of polished and etched surface. Note: All dimensions in (mm)

Weld specimens: Notch tip machined at the centre of weld as shown below



Position of centre line determined by examination of polished and etched surface: All dimensions in (mm)

Figure E- 2 CT specimen's locations in HAZ and weld regions

Some of the polished and etched specimens are shown in Figure E-3 with the notches located at the HAZ.

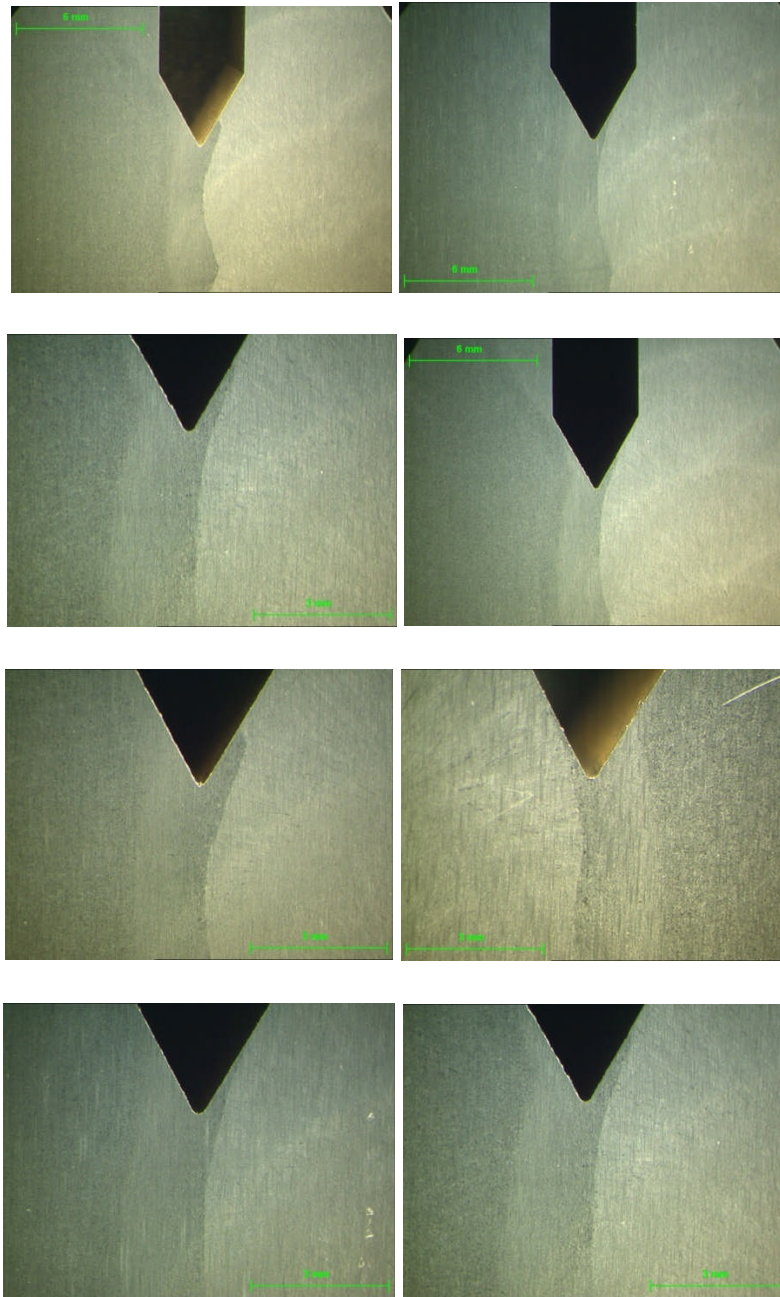


Figure E- 3 Characterised CT specimens with the notch located in HAZs

The direction of crack growth in the HAZ is schematically shown in Figure E-4. The figure shows the approximate crack length where the change in slope of the da/dN vs. ΔK plots occurred. As discussed in Chapter 6, the change in slope occurred when the crack length was about 11.25mm from the notch tip, which is approximately 47.5mm through the thickness of the weld plate

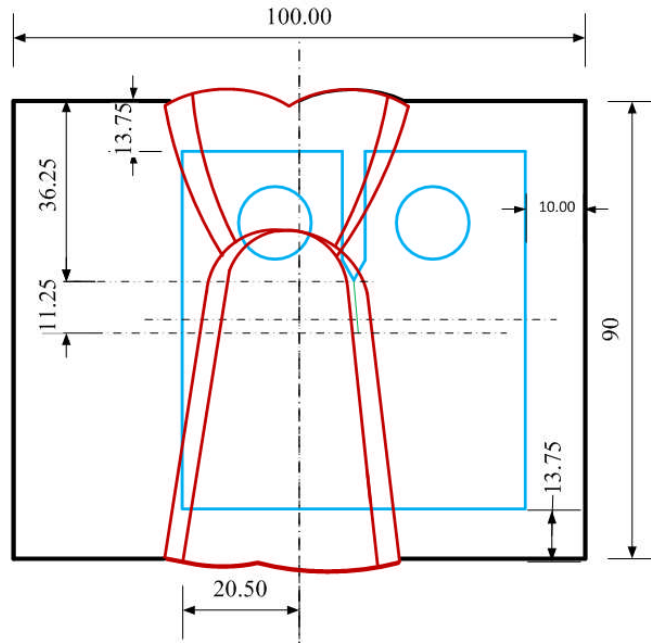


Figure E- 4 Direction of crack growth in HAZ

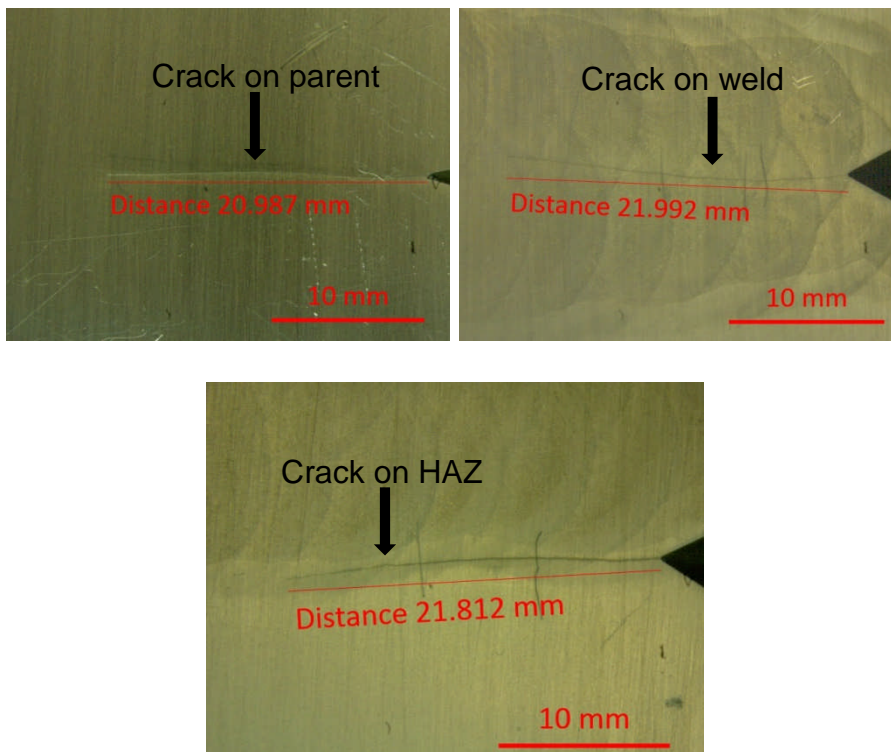


Figure E- 5 Crack growth in parent, weld and HAZ materials

In Figure E-5, crack propagating in the parent, weld and HAZ materials is shown while Figures E-6 and E-7 show typical examples of fatigue surfaces of materials tested in air and in seawater.

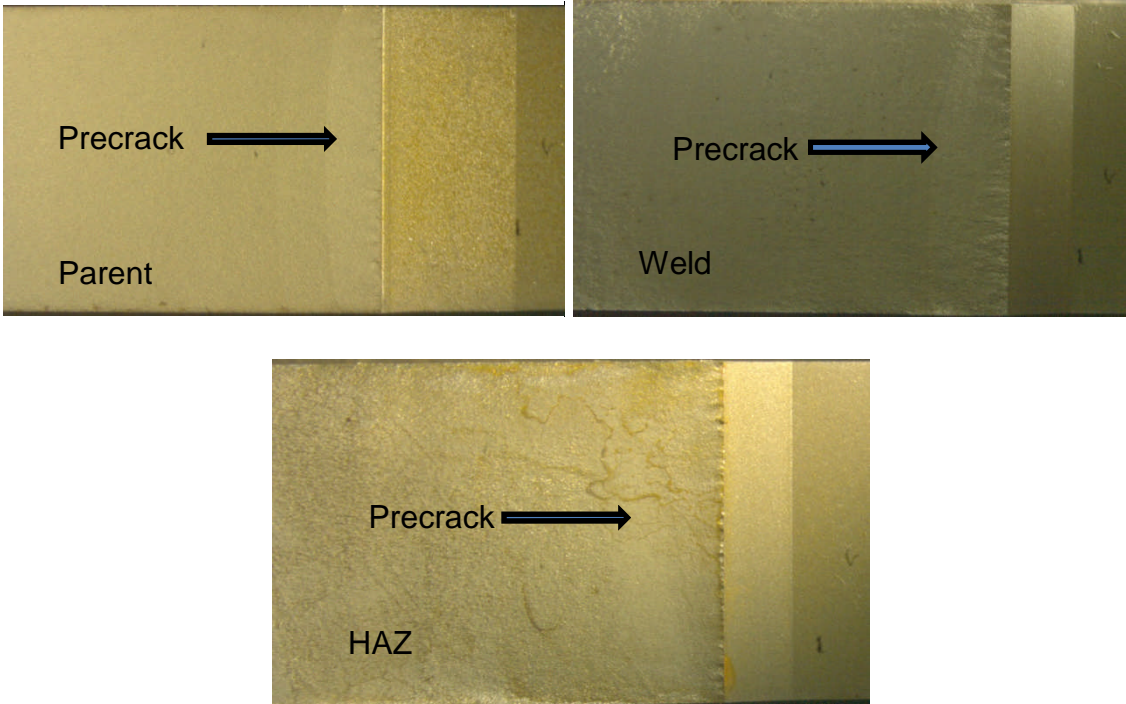


Figure E- 6 Typical fatigue surfaces

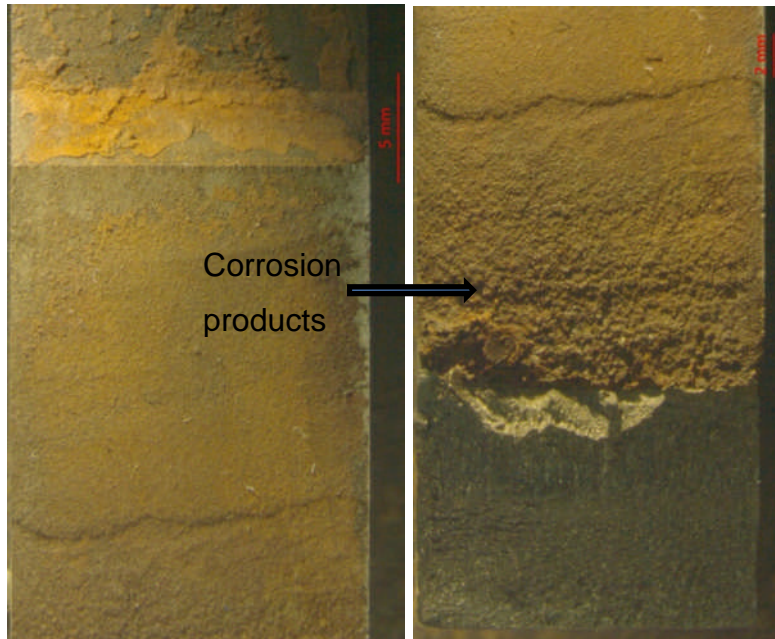


Figure E- 7 Typical corrosion fatigue surfaces

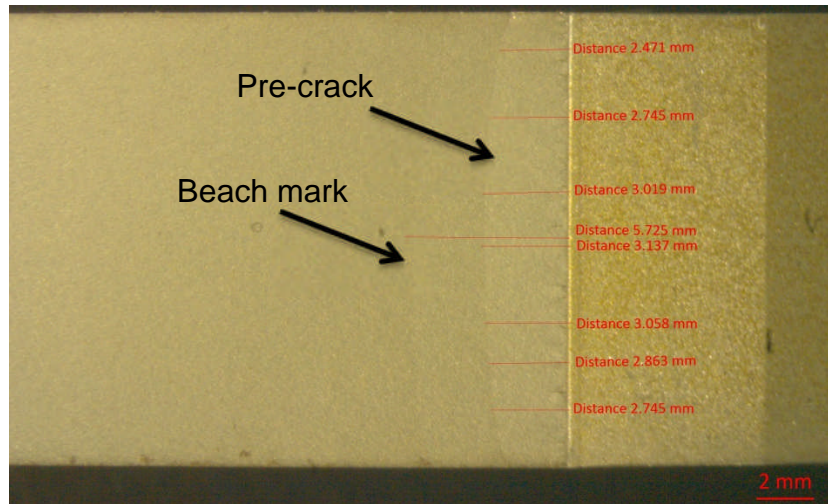


Figure E- 8 Crack measurements in parent material

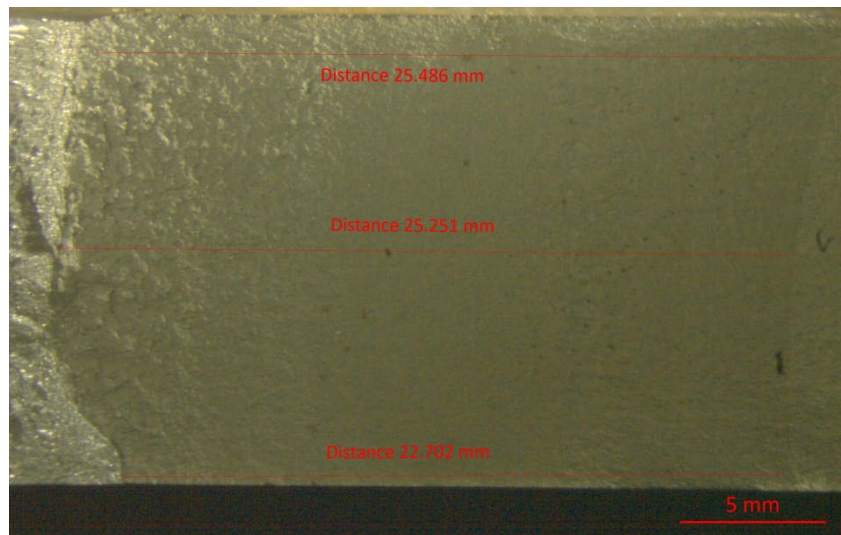


Figure E- 9 Crack measurements in HAZ material

The dimensions of crack length measured near the surface and the middle sections of the parent material are shown in Figure E-8, while those measured from the pre-crack length towards the fractured region in HAZ material are shown in Figure E-9. From Figure E-8, it can be seen that the length of the crack increased from the surface towards the centre of the specimen. However, the difference in the surface crack length and through thickness crack length was not more than 0.67mm. This implies that the accuracy of optical measurement of the surface crack length was appreciable. However, measurement of the through thickness crack length may be a more appreciable

approach for monitoring crack lengths and this can be considered as a potential area for further research.

In Figure E-9, the crack shape was also found to be similar to what was observed in parent material. The difference between the final surface crack length and the through thickness crack length was not more than 0.78mm.

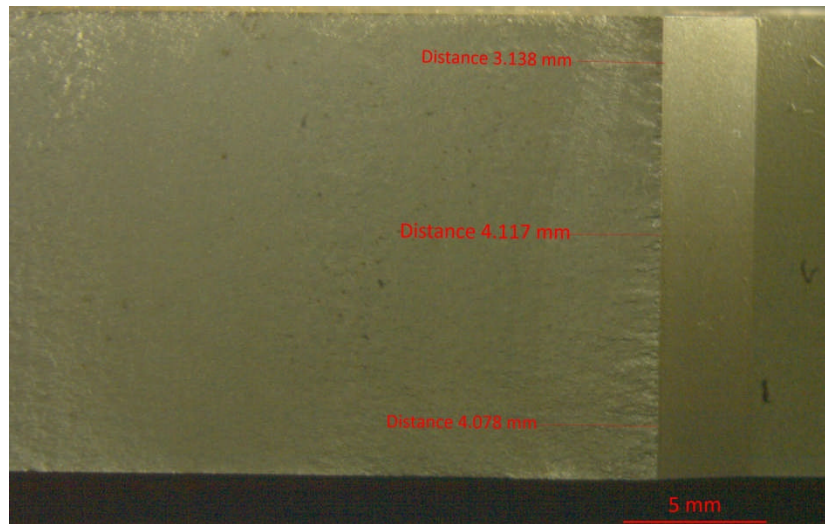


Figure E- 10 Crack measurement in weld material

The dimensions of the advancing crack measured from the machined notch in a weld material are shown in Figure E-10. The difference between the through thickness crack length and the optically measured surface crack length was also found to be less than 1mm.

Appendix F Hardness measurements

The hardness measurements were made using the Zwick computer assisted Vickers micro hardness tester with diamond indenters. A load of 200g was applied through the indenter at intervals of 15 seconds. The hardness values were taken in four sets and directions; firstly, from parent across the weld to parent at every 0.5mm interval, secondly, from the notch through the weld centre line at every 1mm interval. The third set of hardness values were measured from the parent material across the HAZ to the weld at intervals of 0.2mm. In order to verify the hardness values of the HAZ further, hardness measurements were taken at every 0.2mm along the HAZ from the coarse grain microstructure towards the subcritical region closer to the parent material. These measurements were taken from the notch to a distance of 4mm along the crack path.

F.1 Micro hardness results

The hardness values taken from different directions on the test specimens used in this work are shown in Figures F-1 and F-2. The highest hardness value measured from the parent material and across the weld region as shown in the left of Figure F-1 was 240HV, while the lowest hardness value of 186HV was observed in the parent material. It was found that the hardness values decrease from the weld region across the HAZ to the parent materials. The right of Figure F-1 shows the variation in hardness values measured from the notch tip across the weld centre line, with a mean hardness value of 214HV. It can be seen that the hardness varied along the crack path, which may be due to the effects of different weld passes and cooling rates.

In the left of Figure F-2, the hardness values of the parent material are compared with those measured at the HAZ and weld zones. The hardness values of the HAZ decrease from the weld towards the parent material and with a mean hardness value of 209HV, while in the parent materials, the mean hardness value was found to be 200HV. The right of Figure F-2 also shows that the hardness values decrease from the coarse grain towards the finer grain

microstructure. The data plotted in the figure with respect to the examined crack path, as shown in Figures F-1 and F-2, imply that the crack deviated from the harder region of the HAZ to the weaker region closer to the parent material. The variation in hardness values in the HAZ region was also in agreement with what was observed in a similar material [76] and also from the investigated hardness profiles in some other types of steel [78], [105], [112], [147].

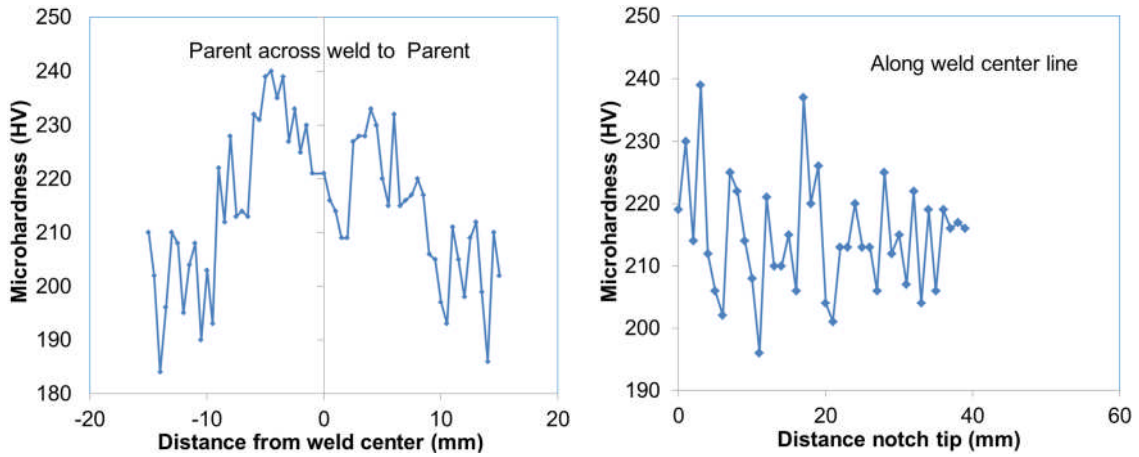


Figure F- 1 Vickers hardness values, left: parent to parent, right: along weld centre line

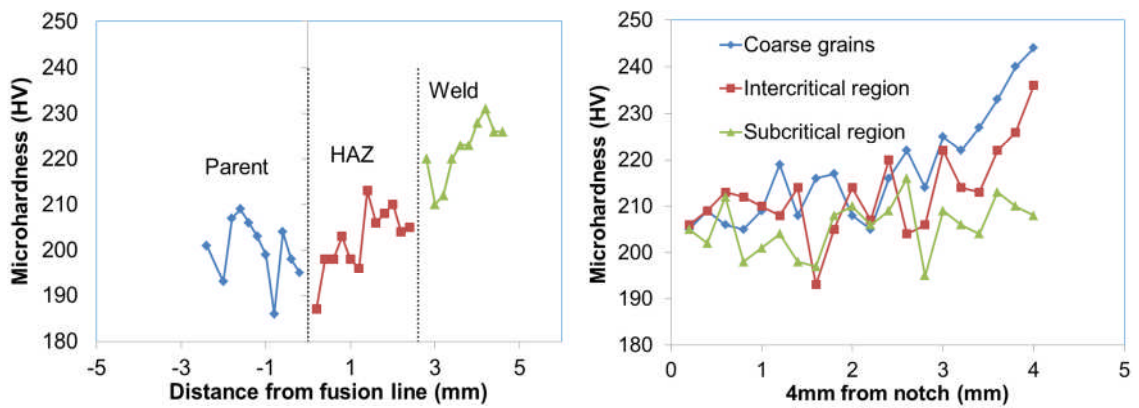


Figure F- 2 Vickers hardness values, left: parent to weld, right: along HAZ

Appendix G Analysis of crack growth results with incremental polynomial and secant methods

The secant method was used to calculate the crack growth rates corresponding to the first and last three data points of the crack lengths vs. number of cycles data. These data were combined with those analysed using the incremental polynomial method. The results are depicted in Figures G-1 and G-2 respectively.

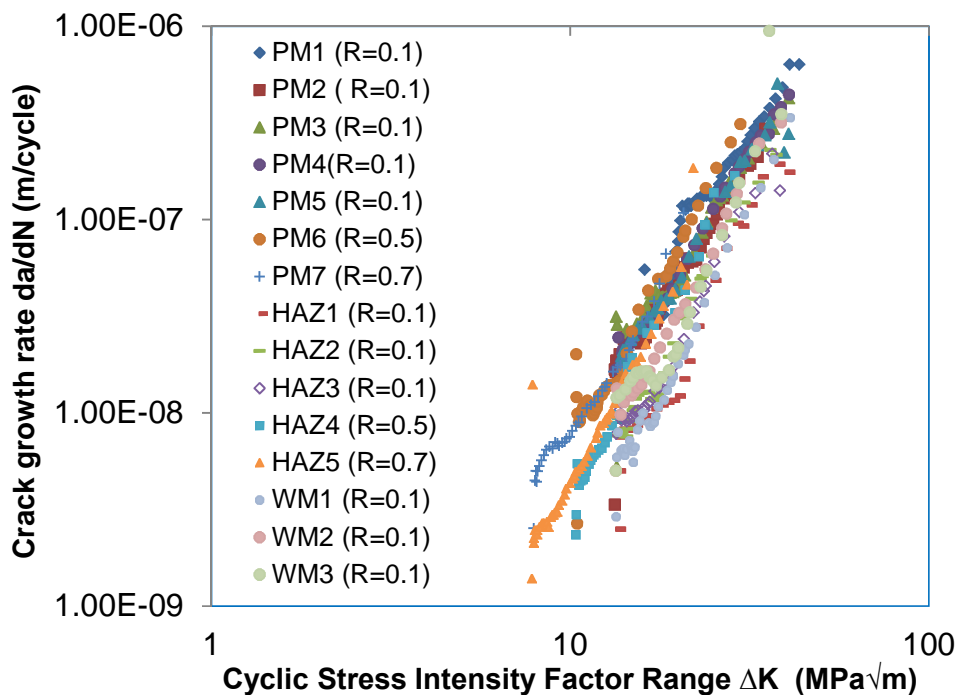


Figure G- 1 Crack growth rates in air using incremental polynomial and secant methods

Figure G-1 compares the air data obtained in parent materials (PM), HAZ and weld (WM). It can be seen that the trends of the plots are consistent with those reported in chapters 4, 5 and 6. However, the few data points that fell outside the trends are those obtained using the secant method. The seawater data are plotted in Figure G-2, where it can be seen that there are fewer number of points that fell outside the crack growth trends compared with the air plot.

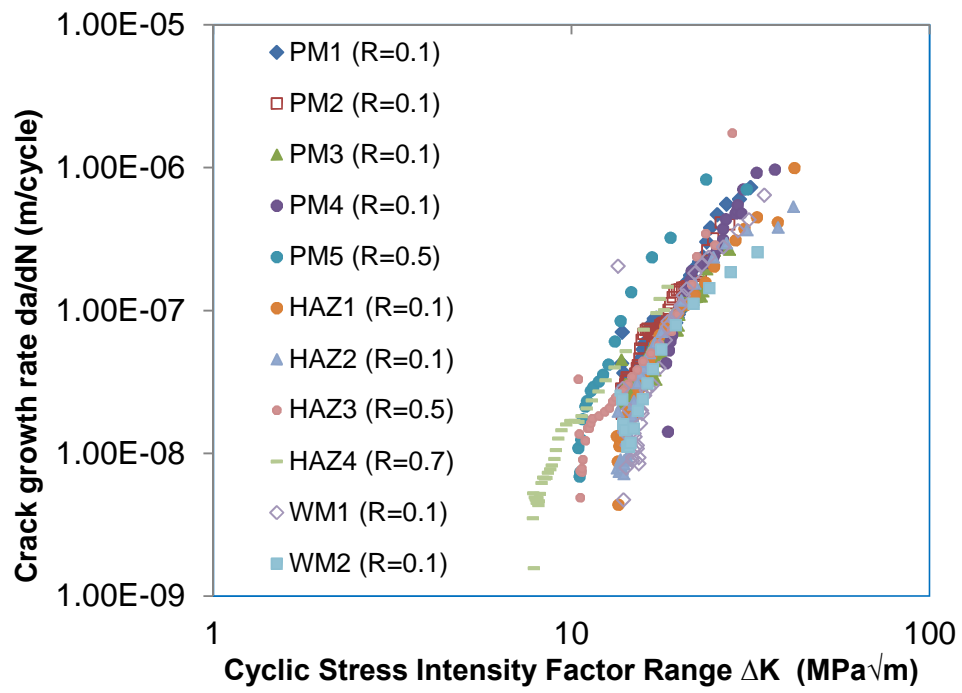


Figure G- 2 Crack growth rates in seawater using incremental polynomial and secant methods

Appendix H Experimental test matrix

Table H- 1 Experimental test matrix

Test ID	Material	Frequency (Hz)	Load Range (kN)	Environment	Initial crack length (mm)	Final crack length (mm)	R-ratio
PM1	Parent	2	10.8	Air	4	22.5	0.1
PM2	Parent	2	9	Air	3.9	21.13	0.1
PM3	Parent	2	9	Air	4	22.5	0.1
PM4	Parent	5	9	Air	4	22.5	0.1
PM5	Parent	2	9	Air	4	22.5	0.1
PM6	Parent	5	7	Air	4	22.35	0.5
PM7	Parent	5	5.25	Air	4	22	0.7
PM8	Parent	0.3	9	Seawater	4.3	20.1	0.1
PM9	Parent	0.35	9	Seawater	4.25	18	0.1
PM10	Parent	0.4	9	Seawater	4.25	18	0.1
PM11	Parent	0.3	12	Seawater	4.3	19	0.1
PM12	Parent	0.3	7	Seawater	4.1	22.5	0.5
HAZ1	HAZ	5	9	Air	4	22.5	0.1
HAZ2	HAZ	5	9	Air	4	22	0.1
HAZ3	HAZ	5	9	Air	4	22	0.1
HAZ4	HAZ	5	7	Air	4	22.3	0.5
HAZ5	HAZ	5	5.25	Air	4	22.1	0.7
HAZ6	HAZ	0.3	9	Seawater	4	22.3	0.1
HAZ7	HAZ	0.3	9	Seawater	4	22.3	0.1
HAZ8	HAZ	0.3	7	Seawater	4	22.5	0.5
HAZ9	HAZ	0.3	5.25	Seawater	4	20	0.7
WM1	Weld	5	9	Air	4	22.5	0.1
WM2	Weld	5	9	Air	4	22.5	0.1
WM3	Weld	5	9	Air	4	22.2	0.1
WM4	Weld	0.3	9	Seawater	4	22	0.1
WM5	Weld	0.3	9	Seawater	4	22	0.1